University of South-Eastern Norway
Faculty of Technology, Natural Sciences and Maritime Sciences

Doctoral dissertation no. 35

2019

Cornelius Emeka Agu

Bubbling Fluidized Bed Behaviour for Biomass Gasification

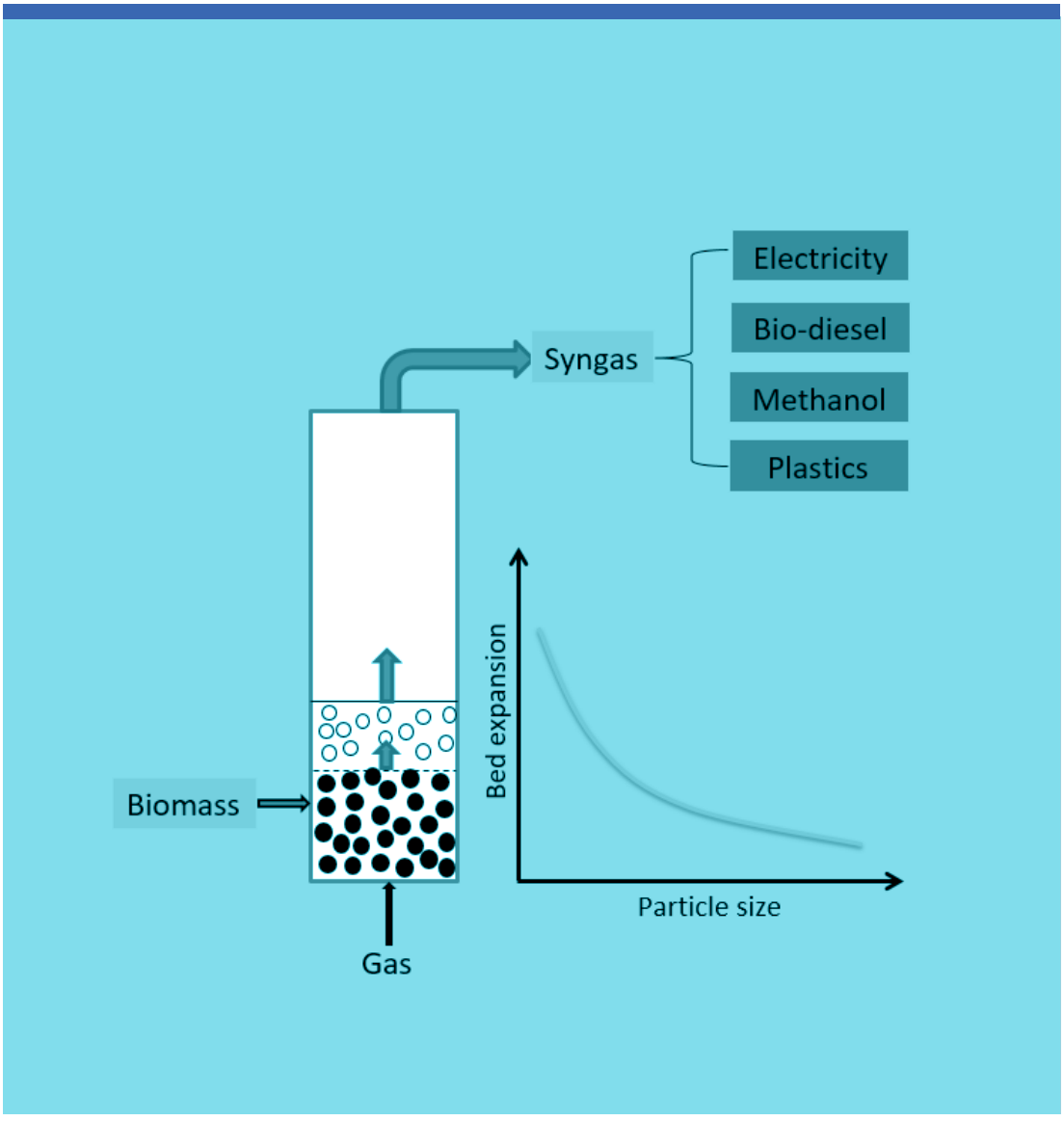

Cornelius Emeka Agu

Bubbling Fluidized Bed Behaviour for Biomass Gasification

A PhD dissertation in
Process, Energy and Automation Engineering

Faculty of Technology, Natural Sciences and Maritime Studies
University of South-Eastern Norway
Porsgrunn, 2019

Doctoral dissertations at the University of South-Eastern Norway no. 35

ISSN: 2535-5244 (print)
ISSN: 2535-5252 (online)

ISBN: 978-82-7206-526-2 (print)
ISBN: 978-82-7206-527-9 (online)

Print: University of South-Eastern Norway

Preface

This thesis is about the application of bubbling fluidized bed behaviour to biomass gasification processes. The research was carried out in partial fulfilment for the award of a doctoral degree in the field of Process, Energy and Automation Engineering at University of South-Eastern Norway (USN). The topic was initiated by the Energy and CO_2 Capture (ECC) research group of the university under the supervision of Prof. Britt M.E. Moldestad. The main focus of this research is to investigate the hydrodynamic behaviour of fluidized beds and the effects on the sustainable thermochemical conversion of biomass into a gaseous form of high energy value.

This work is a continuation of previous studies carried out under the ECC research group as documented in [1, 2], and is based on different experimental setups (cold and hot flow setups) and on the models developed in the course of this study. Several literature were studied, and their results were used to make this thesis successful. The report is also based on my analytical, modelling and simulation skills, and on my previous research experiences. All the results presented in this report were analysed and simulated using the MATLAB software.

In regards to my background, I graduated from Nnamdi Azikiwe University, Nigeria in 2004 as a mechanical engineer and obtained a master degree in Process Technology at University of South-Eastern Norway in 2014. Before my PhD studies, I have carried out a number of research projects, leading to designs of Venturi rig and Beer processing rig, both currently installed at USN, Porsgrunn. In my previous research, some publications were also recorded, which include “Algorithm with improved accuracy for real-time measurement of flow rate in open channel systems” [3], “Model-based drilling fluid flow rate estimation using Venturi flume” [4] and “ Simulation of transcritical flow in hydraulic structures” [5].

The research work lasted from September 1, 2015 to April 15, 2019, and was carried out at University of South-Eastern Norway, Porsgrunn campus. At successful defence of this thesis, I am awarded a doctoral degree in Process, Energy and Automation Engineering.

In this report, the reader can find a brief background of the study, the methods employed, the summary of the findings, and the detailed analysis of the results as also contained in the different publications enclosed and freely available online. The thesis is organized to collect all the papers I published in relation to the focus of my research. Hence, the literature survey given in this report is a summary of those contained in the different papers. All the symbols used in this report are the same as those in the relevant

papers, and therefore no symbol list is provided. Where new symbols are introduced, they are clearly defined in the text.

I would like to thank my supervisor, Prof. Britt Moldestad for her mothering advice, encouragement and provision of different aids for the success of this thesis. My sincere appreciation also goes to my co-supervisors, Prof. Christoph Pfeifer of BOKU Vienna, Prof. Lars-Andre Tokheim and Dr. Marianne Eikeland of USN for their supports and professional guidance in the course of my research.

I also extend my gratitude to Prof. Bernt Lie and Prof. Carlos Pfeiffer of USN, who have stood as my mentors since my admission into this university. My previous research activities with them added much value to my knowledge to achieve this greatness. I equally appreciate the head of the department, Prof. Klaus J. Jens, whose fathering advice and mentorship are immeasurable. Having participated in his course, Chemical Gas Processing enhanced my interest to follow this path of career.

I thank the 2011 international admission team, especially Unni S. Kaasin and Prof. Lars-Andre Tokheim, without whom I would have missed the chance of completing my research today in this great institution. I also thank other staff members of this university including the dean, Prof. Morten C. Melaaen, Dr. Randi T. Holta and Prof. Saba K. Mylvaganam for discovering my interest in research and provided me with the needed supports.

I also appreciate all my friends and colleagues for their assistances, supports and words of encouragement throughout my studies. Among others, my humble appreciation goes to Ambrose Ugwu of NTNU, Dr. Christian Ahobasam of UiO, Arome Okpanachi of Kvaerner, Dr. Rajan Thapa, Rajan Jaiswal, Janitha Bandara and Ramesh Timsina of USN.

In all, my special thanks go to my parents, my wife and my children, Obioma, Ifechukwu and Nwasinachi Agu for their daily prayers and sacrifices to see to the end of this success. I therefore dedicate this my piece of work to my dear wife, Victoria Agu who stood by me all the time until this moment.

Cornelius E. Agu, April 2019

Abstract

The need to cut down the high dependency on the fossil fuels requires sustainable alternative energy resources. Aside that the stock of fossil fuels is depreciable, the energy source also accounts for the major contribution of greenhouse gas effects. Biomass in the categories of woody, herbaceous, marine and manure biomasses, are among the renewable energy sources, which can be grown everywhere in a sustainable manner. Biomass currently contributes to more than 10% global energy consumption in the different forms of application: direct combustion and conversion into a gaseous form for chemical synthesis. Gasification is a means of converting biomass into a higher energy gas containing mainly CO, CH_4, H_2 and CO_2 for sustainable utilization.

Among different technologies applied in biomass gasification, fluidized bed has wide industrial advantages in that a variety of feedstock can be gasified in addition to that the process can be easily controlled. To explore the numerous benefits of fluidized bed technology, an in-depth understanding of the fluid-particle interactions in the reactor at different operating conditions is necessary. This thesis investigates the behaviour of different powders in fluidized beds. The effects of particle size, bed height and gas velocity on the bubbling bed behaviour and on the transition from bubbling to slugging regime are outlined. The mixing and segregation patterns of biomass particles in binary mixtures with inert particles are also investigated. In addition, the study covers the measurement of residence time of biomass during conversion in an air-blown bubbling bed reactor and the yield of char particles during the devolatilization phase. The gasification of biomass in a laboratory scale reactor using different bed particle sizes, air-fuel ratios, steam-biomass ratios and biomass loading rates are also characterized.

These studies are performed using two different experimental setups and a one-dimensional (1D) model developed for bubbling fluidized bed reactors. The two experimental setups have close internal diameter of 10 cm and effective total height in the range 1 – 1.4 m. The first setup is equipped with two electrical capacitance tomography (ECT) sensors, which measure the distribution of solids fraction at different bed positions for a given gas flowrate. At the ambient conditions, the ECT setup is used to characterize the behaviour of different particles at different gas velocities. The information from the two plane ECT sensors are also used to develop methods for determining different bubble properties, and the gas velocity and bed voidage at the onset of slugging regime. The second setup is used for hot flow processes and it is equipped with five different thermocouples and pressure transducers for monitoring the reactor performance along the vertical axis. The bubbling bed reactor model is developed to capture the average flow properties and product gas species at any position in the reactor. The model is unsteady and developed based on the conservation

of mass, momentum and energy within and across the reactor. The basic assumption underlying the model is that the mean circulation velocity of the bed material is zero, which reduces the computational complexities in using the model.

The results show that the ratio of superficial gas velocity to the minimum fluidization velocity at the onset of slugging regime increases with decreasing particle size. As the particle size increases, changes in the bed height has a negligible effect on the transition velocity. The bubble growth rate with increasing gas velocity increases with the particle size, resulting in the earlier occurrence of slugs in the beds of large particles. The bubble frequency increases with increasing gas velocity only when the bubble diameter is below a threshold value. The maximum bubble frequency over the range of operating gas velocities also indicates the transition from bubbling to slugging regime. For a mixture of biomass and bed material, the bubble diameter decreases with increasing amount of biomass, leading to a delay in the slug flow. The minimum fluidization velocity increases with increasing biomass load but for a high density biomass ($\sim$1000 kg/m^3), the gas velocity slightly decreases due to a reduction in the bed voidage when the biomass load is below 20 vol.%. The sinking of biomass at a given gas velocity also increases with the biomass density while the spreads of biomass towards the walls decreases with increasing biomass density. The minimum gas velocity required to achieve a mixing over the bed increases with increasing biomass load, decreasing bed diameter and slightly unaffected by changes in the bed height. During conversion, the segregation pattern of the char particles is similar to the parent biomass in the cold condition. When introduced in a bubbling bed, the initial distribution of biomass particles is greatly influenced by the combined effects of the particle bulk density and the rising bubbles. As biomass devolatilizes, the particles rise upwards. The time for complete devolatilization increases with the amount of biomass charged and with decreasing air flowrate. Moreover, the amount of char released at the completion of devolatilization and the char residence time before complete conversion decrease with increasing air flowrate and decreasing amount of biomass loaded in the bed. The gasification of wood pellets with air shows that at the same air-fuel ratio, the particle size of the bed material has insignificant effect on the gas composition. With an increase in the air-fuel ratio, H_2 yield increases and the yields of CO and CH_4 decrease. Increasing the biomass flowrate from 2.7 to 3.6 kg/h increases the yields of CO and CH_4 and decreases that of H_2 at the same air flowrate. Similar behaviour with different particle sizes are also observed in the gasification of the same biomass with steam using the proposed 1D model. The model results also show that both H_2/CO and CO_2/CO ratios attain minimal values at certain bed temperatures. The method used in obtaining the bed expansion and bed voidage influences the model results. With an increase in the bed expansion within a certain range, the yields of CO and CH_4 increase due to increasing char conversion. The increase in the biomass flowrate at a constant steam to biomass ratio increases the char accumulation. The

biomass density also has a great influence on the particle distribution, and thus on the product quality. The higher the biomass density, the better the conversion efficiency.

Different correlations are also proposed for prediction of bubble properties (bubble diameter, bubble flux, bubble velocity and bubble frequency), bed expansion, bed voidage of a binary mixture and the minimum gas velocity required to achieve particle mixing over a segregated layer of biomass. The proposed models for the bubble diameter and volumetric bubble flux averaged over the bed height account for the effect of particle and fluid properties on these variables. Applying the particle dependent-bubble diameter on the bed expansion model gives a good prediction for a given bed. The bubble velocity model gives better predictions for Geldart B and D particles than those in the existing literature. Using the proposed model for the bed voidage, accurate predictions can be achieved for different binary systems. The application of the voidage model to the Ergun equation shows that the minimum fluidization velocity of binary mixtures can be predicted with error of 15% for two inert materials and 7% for a mixture of biomass and an inert material. New correlations based on the air flowrate, biomass flowrate, mass of the bed material and the minimum fluidization velocity of the bed particles at the operating temperature are also proposed for the biomass residence time, the amount of char accumulated during the conversion and the total heat loss at the completion of devolatilization process.

The results of this thesis can be useful for optimization of design and operational control of biomass gasification reactors. The proposed 1D model can also be incorporated into a circulating fluidized bed reactor to obtain the dynamic behaviour of the so-called dual fluidized bed reactors. As the model can accept all the possible inputs to a gasifier, it can be used to determine the optimum operating point for efficient conversion of biomass in a given bubbling fluidized bed reactor.

Keywords: Fluidized bed; Binary mixture; Biomass; Bubbling bed; Slugging bed; Bubble properties; Gasification; One-dimensional model; Segregation

List of papers

Article 1 [A1]

Agu, C.E.; Tokheim, L.-A.; Eikeland, M.; Moldestad, B.M.E. Determination of onset of bubbling and slugging in a fluidized bed using a dual-plane electrical capacitance tomography system. *Chemical Engineering Journal* 328 (2017) 997 – 1008.

Article 2 [A2]

Agu, C.; Eikeland, M.; Tokheim, L.; Moldestad, B.M.E. Simulation of bubbling fluidized bed using a one-dimensional model based on the Euler-Euler method. *9th EUROSIM Congress on Modelling and Simulation, EUROSIM 2016, and 57th SIMS Conference on Simulation and Modelling, SIMS 2016*, Oulu, Finland, 12 – 16 September, 2016.

Article 3 [A3]

Agu, C.; Tokheim, L.-A.; Halvorsen, B. Measurement of bubble properties in a fluidized bed using electrical capacitance tomography. *12th International Conference on Fluidized Bed Technology*, Krakow, Poland, 23 – 26 May, 2017.

Article 4 [A4]

Agu, C.E.; Ugwu, A.; Pfeifer, C.; Eikeland, M.; Tokheim, L.-A.; Moldestad, B.M.E. Investigation of Bubbling Behavior in Deep Fluidized Beds at Different Gas Velocities using Electrical Capacitance Tomography. *Industrial & Engineering Chemistry Research* 58 (2019) 2084 - 2098.

Article 5 [A5]

Agu, C.E.; Pfeifer, C.; Eikeland, M.; Tokheim, L.-A.; Moldestad, B.M.E. Models for predicting average bubble diameter and volumetric bubble flux in deep fluidized beds. *Industrial & Engineering Chemistry Research* 57 (2018) 2658 – 2669.

Article 6 [A6]

Agu, C.E.; Tokheim, L.-A.; Eikeland, M.; Moldestad, B.M.E. Improved models for predicting bubble velocity, bubble frequency and bed expansion in a bubbling fluidized bed. *Chemical Engineering Research and Design* 141 (2019) 361 - 371.

Article 7 [A7]

Agu, C.E.; Tokheim, L.-A.; Pfeifer, C.; Moldestad, B.M.E. Behaviour of biomass particles in a bubbling fluidized bed: A comparison between wood pellets and wood chips. *Chemical Engineering Journal* 363 (2019) 84 - 98.

Article 8 [A8]

Agu, C.E.; Pfeifer, C.; Moldestad, B.M.E. Prediction of void fraction and minimum fluidization velocity of a binary mixture of particles: Bed material and fuel particles. *Powder Technology* 349 (2019) 99 - 107.

Article 9 [A9]

Agu, C.E.; Pfeifer, C.; Eikeland, M.; Tokheim, L.-A.; Moldestad, B.M.E. Measurement and characterization of biomass mean residence time in an air-blown bubbling fluidized bed gasification reactor. *Fuel* 253 (2019) 1414 – 1423.

Article 10 [A10]

Agu, C.E.; Pfeifer, C.; Eikeland, M.; Tokheim, L.-A.; Moldestad, B.M.E. Detailed One-Dimensional Model for Biomass Gasification in a Bubbling Fluidized Bed. Submitted and currently under review in *Energy & Fuels*.

List of tables

List of figures

Table of contents

1 Introduction

Similar to thermochemical conversion of coal, biomass gasification via fluidized bed has great advantages for industrial application. To explore the benefits of a fluidized bed in biomass conversion, an in-depth understanding of the hydrodynamics of beds of different particle types is required. This thesis investigates the effect of different particle properties on bubbling fluidized bed behaviour. The investigation also includes the mixing and segregation patterns of biomass particles in different mixtures with sand particles. In addition, the performance of a biomass gasification process under different operating parameters including the particle size of the bed material and biomass-loading rate is studied. The finding of this study can be a useful tool for the initial design phase, operational control and parameter optimization of bubbling fluidized bed reactors.

1.1 Research overview

In recent years, there is increasing number of researches in the field of biomass conversions destined for different uses, which include direct combustion for heat production, and gasification for power generation and synthesis of chemicals such as methanol, biodiesel and bioethanol. Biomass, as a source of energy, is an ancient technology where wood was burned in homes, primarily for heat production. The conversion of biomass such as grains and oil into ethanol and biodiesel can be traced as far back as the Second World War.

Generally, biomass includes all the energy sources, which are derived from animal and plant matters. In this definition, the so-called “first generation” of bioenergy technology was described to include different feedstock such as food grains, forest wastes, forest plants, soya bean and palm oil. The forest-based biomass are widely distributed across the globe as shown in Figure 1.1, and are the most commonly used due to their consistent properties. The municipal solid wastes and animal manure are also regarded as biomass. The growing interest in biomass research and technology today is widely attributed to the belief that biomass is a greener energy source when compared to the fossil fuels. Biomass is also believed to be a renewable source of energy because it can be re-grown after used. The plant-based biomass is grown all year round and once removed for food or energy, new ones are re-grown artificially or naturally. As a renewable energy source, the plant-based biomass (which are the most reliable form of biomass) remove approximately the same amount of carbon dioxide (CO_2) they emit when burned during their lifecycles. Biomass is widely available and can easily be stored and transported. It is ranked among the top four-world energy sources, providing more than 10% global energy supply [6, 7] as shown in Figure 1.2.

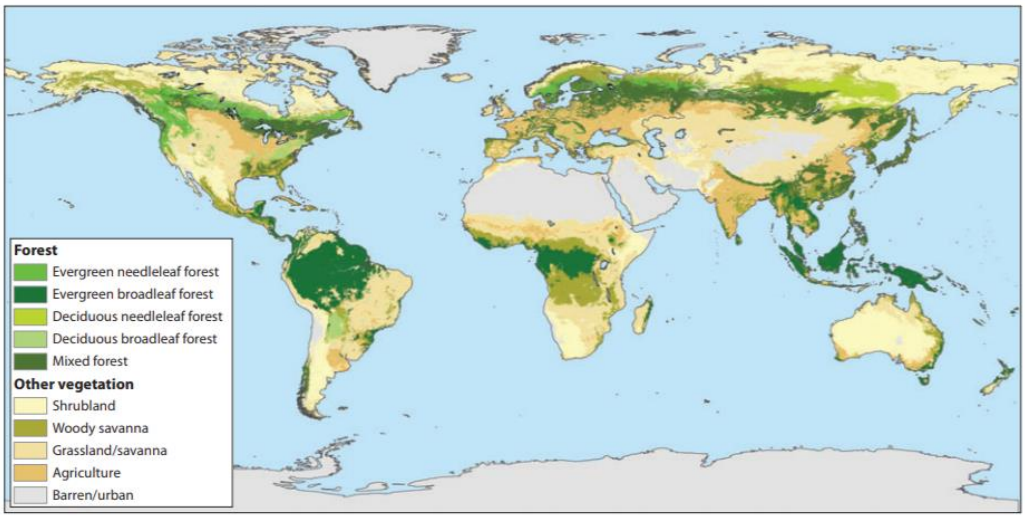

Figure 1.1. Global map showing the distribution of forest-based biomass [8].

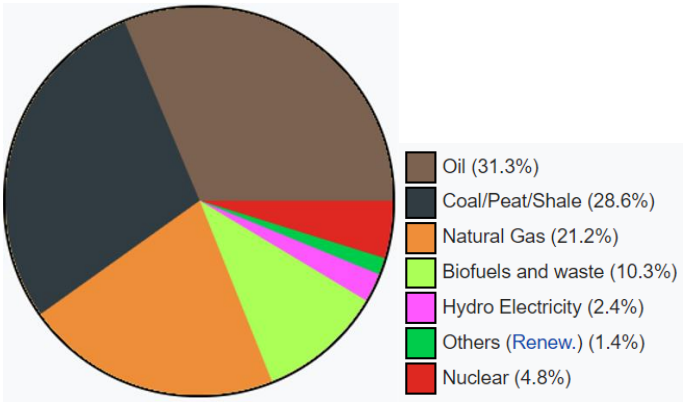

Figure 1.2. Contribution of different energy sources to the world energy consumption. [IEA World Energy Outlook 2014].

Biomass powered plants can be found in some countries today. Some chemical companies also use biomass as feedstock. Biomass makes up 4.8% of United States (US) total energy consumption and 12% of all the renewable energy sources, where wood is the largest biomass energy resource. In US, there are 227 plants running on biomass, while in the United Kingdom, about 35 plants exist [9]. Globally, biomass is viewed as a solution to the world projected energy crisis due to depletion of fossil fuels. Because of this, a large number of researches has been devoted to improving on the overall usage of biomass. For efficient use, biomass is converted into gaseous form by means of gasification. As shown in Figure 1.3, the main steps involved in the biomass conversion and utilization are classified into upstream processing, gasification and downstream processing. In the upstream processing, the biomass is made suitable for the gasification process by means of drying, size reduction and densification [10]. Biomass gasification involves drying and thermochemical degradation of the feedstock by pyrolysis, partial

oxidation and gasification of the resulting char particles. The gasification of char particles is achieved through their reactions with air, pure oxygen, carbon dioxide, steam or their combination. The energy value and quality of the product gas depend on the gasifying agent, biomass properties, temperature, pressure and reactor design [11]. With the use of catalyst and sorbents, the gasification process can also be improved.

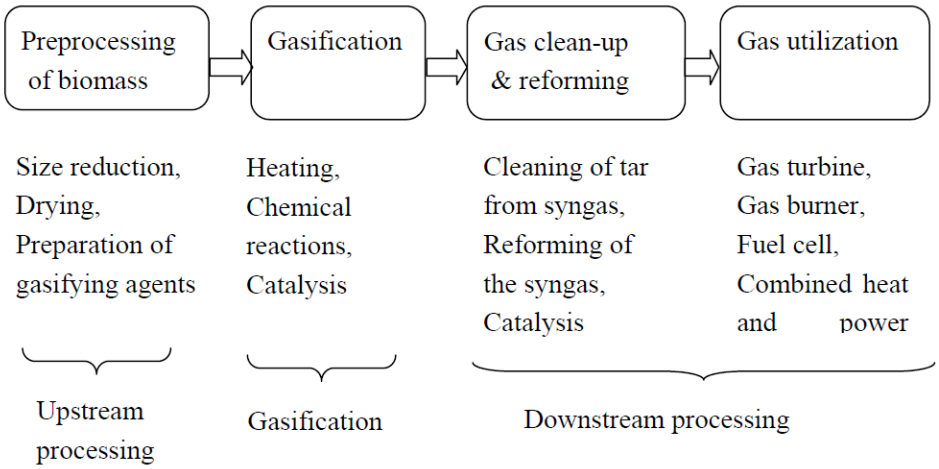

Figure 1.3. Different process steps for conversion and utilization of biomass [10].

Biomass gasification can accept a wide variety of feedstock, thus generating multiple useful products. For gasification with air, the calorific value of the product gas is in the range 4 – 7 MJ/Nm^3, and with pure oxygen a value of 12 – 28 MJ/Nm^3 can be achieved. The gasification process reduces the carbon to hydrogen mass ratio, thereby increasing the calorific value of the product gas [12]. A gasification reactor is usually designed for a specific feedstock type classified into woody biomass, herbaceous biomass, manures and marine biomass. The first biomass gasification plant was constructed and installed in US in 1999 under the Wabash River Coal Gasification project [13]. Since then, more advancement has been recorded in the gasification projects towards achieving the global energy demands and reduction in the greenhouse gas emissions.

One major challenge in biomass gasification is the tar content of the product gas, which degrades the gas quality and often results in reduction of the process efficiency. Tar is a thick viscous liquid of aromatic hydrocarbon with some traces of heavy metals [14] formed during biomass pyrolysis. The yield of tar can be minimized by thermal cracking, partial oxidation and reforming processes. To some extent, the quality of product and efficiency of the process depend on the type of gasification technology employed. The most common technologies used are the fixed bed, fluidized bed and the entrained flow gasifiers, depicted in Figures 1.4 – 1.6.

In a fixed bed gasifier, biomass is fed from the top of the reactor, and as shown in Figure 1.4, the different stages of gasification can clearly be distinguished in this type of gasifier. As a single column reactor, air is often used for the gasification process such that the partial combustion of char particles provides the necessary heat required during the reduction stage. Depending on the flow of air in relation to the direction of the biomass flow, fixed bed reactors are classified into downdraft and updraft gasifiers. Air is blown upwards through the biomass bed in the updraft design and downwards in the downdraft configuration. The updraft gasifier operates within 750 – 1000℃, resulting in a high tar yield in the range 10 - 20 wt% of the product gas compared to the yield of about 5 g/Nm^3 in the downdraft gasifier. The low tar content in a downdraft fixed bed system is due to its higher operating temperature 1200 – 1400℃ that enhances the cracking of the heavy hydrocarbon [15]. However, the ash content of the product gas from a downdraft gasifier is on a high side and the requirement for the moisture content of the feedstock is very low (< 25 wt.%) compared to other technologies, limiting the use of variety of biomass types.

Fluidized bed gasifiers employ inert bed material that is fluidized to aid the distribution of heat and fuel particles. In the fluidized state, the superficial velocity of the incoming gas is greater than the minimum gas velocity required to lift the bulk material against the bed weight. As shown in Figure 1.5, fluidized bed gasifiers are divided into bubbling fluidized bed (BFB), circulating fluidized bed (CFB) and dual fluidized bed (DFB) gasifiers. In a BFB gasifier, biomass is fed from either the top or side of the bed. The gas velocity is usually within twice the minimum fluidization velocity to reduce particle elutriation effects, and a wide distribution of particle size can be used. On the other hand, a CFB gasifier requires a higher gas velocity, a lower bed height and a smaller particle size. The solid particles in a CFB reactor are circulated through a cyclone system to increase their contact time with the gasifying agents. In a dual fluidized bed configuration, two interconnected reactor columns (BFB column and CFB riser) are used. The biomass gasification takes place in the BFB column while combustion of char residue and additional fuel takes place in the CFB riser. While the bed material is circulated between the separate reactors, it transfers the heat released during combustion in the riser to the bubbling bed column to aid the gasification process. This reactor design is usually applied for steam gasification, as the process is highly endothermic.

An entrained flow gasifier as shown in Figure 1.6 is highly energy efficient, operating above 1000℃ and has the least tar yield among the known gasification technologies. For coal gasification, the reactor design is widely applied. However, the requirement that the feedstock must be pulverized poses some operational challenges when biomass is used as the feed.

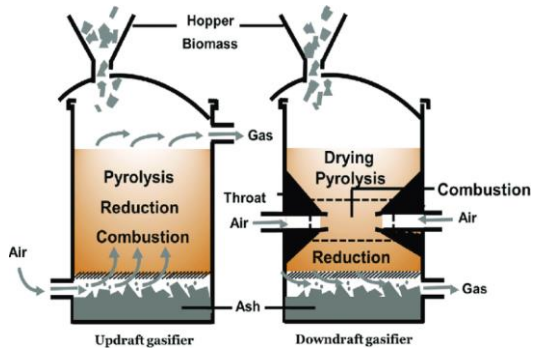

Figure 1.4. Updraft and downdraft configuration of fixed bed biomass gasifier[16].

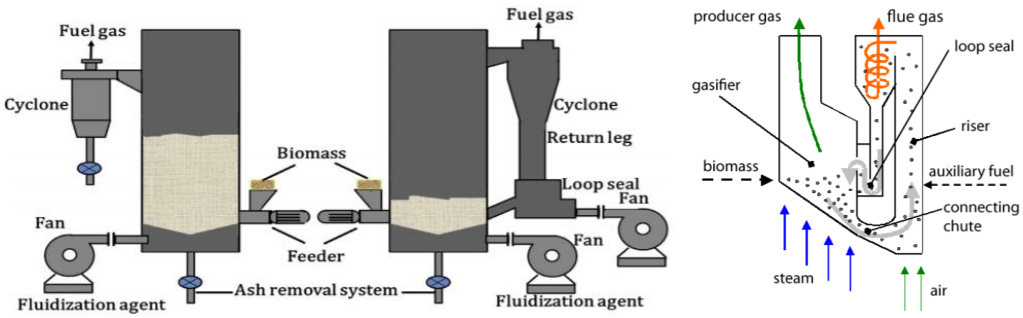

(a) (b) (c)

Figure 1.5. Fluidized bed biomass gasifier showing different configurations (a) bubbling bed (b) cirgulating bed [17] (c) dual-fluidized bed [18].

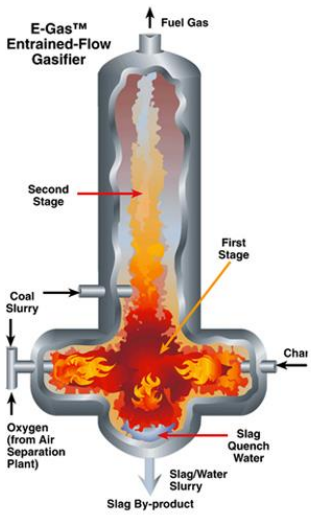

Figure 1.6. Configuration of entrained flow reactor as applied for coal gasification [From http:// biofuelsacademy.org, retrieved on March 25, 2019].

This thesis focuses on the bubbling fluidized bed reactors, which are common among the three different fluidized bed designs shown in Figure 1.5. The fluidized bed

technology offers a number of advantages for thermochemical conversions, and thus has a wide industrial application. Due to rapid mixing of solids and better heat distribution, a continuous feed and operational control can be achieved easily in a fluidized bed reactor.

1.2 Objective

No matter the regime of operation, biomass gasification in a fluidized bed is achieved with the help of inert particles. A clear investigation into the fluidized bed behaviour of different materials and their mixtures with biomass particles, is a route to achieving efficient biomass gasification. The main objectives of this study are outlined as follows.

- To enhance the understanding of the effect of bed hydrodynamics on the biomass gasification.
- To provide a more refined information for efficient design and operation of biomass gasifiers.

1.3 Scope

To achieve the above objectives, this thesis focuses on the following broad areas.

- Investigation of the effect of particle properties on fluidized bed regime transition.
- Investigation of the effect of particle properties and operating gas velocity on bubble flow properties.
- Investigation of mixing and segregation behaviour of binary mixtures of biomass and inert particles in fluidized state.
- Measurement of biomass residence time before it is completely converted in a bubbling bed.
- Evaluation of biomass gasification performance at different operating parameters.

1.4 Limitation

While trying to achieve the overall objectives, this study is still limited to a certain number of investigations. The following list highlights the limitation of this thesis due to the limited time and challenges with the experimental setup.

- Only the particles in the Geldart [19] B and D solid groups are investigated.
- The experimental measurements are based on air as the fluidizing and gasifying agent.

- A relatively small bed diameter, 10 cm is used, thus requiring investigation into the scaling up of the results obtained.
- The beds investigated are relatively deep (bed height to diameter larger than 2).
- The gasification is based on the woody biomass, limiting the generalization of the behaviour observed.
- Tar and CO_2 measurements, which also give indication about the quality of the gasification, are not obtained.
- Entrainments of fuel particles and bed materials are not quantified, limiting the evaluation of efficiency of the conversion and quality of the product yield.

1.5 Outline

In the following chapters, the detailed experimental setups and analysis of results are presented. Chapter 2 reviews some of the relevant literature. The review briefly describes the previous studies on fluidized bed behaviour at different gas velocities, bed geometries and particle properties. The mixing and segregation behaviour of the beds containing different amounts of biomass particles are reviewed. Previous contributions on biomass gasification in fluidized beds including the modelling approaches are also covered in this chapter.

The experimental setups are described in Chapter 3. The setups include those used in the cold flow and hot-reacting flow measurements. The methods employed in the reconstruction of sensor data and acquisition of the necessary information for analysis are also clearly described. The cold flow experimental setup is used to study the fluidized bed regime transition, and to measure the bubble properties and mixing and segregation behaviour of biomass particles in different binary mixtures with inert bed material. Using the hot flow setup, measurement of biomass residence time over the conversion period is obtained. By measurement of axial temperature distribution, the hot bed setup is also used to investigate the axial mixing and segregation pattern of biomass over the conversion period. The gasification of woody biomass at different air-fuel ratios and biomass flow rates are also studied using this hot bed setup.

In Chapter 4, both the zero (0) and one (1) -dimensional hydrodynamic models describing the behaviour of fluidized beds are presented. The 0D models are correlations of the experimental data describing the average behaviour of the bed, and can be used for scaling up of the bed behaviour and validation of complex computational fluid dynamic models. A semi-empirical expression for predicting the average void fraction of a bed mixture containing two different solid types are developed and presented. The procedure for applying the bed voidage model for determining the mixture minimum fluidization velocity is outlined. To properly account for the material

and energy distribution in a fluidized bed, a detailed 1D model is developed. The 1D hydrodynamic model is further simplified to provide a model applicable for bubbling fluidized bed gasifiers by eliminating the bed material mass and momentum exchanges with the rest of the bed. The gasifier model assumes that the bed material has zero mean velocity over one cycle of circulation period. The accompanied changes in the bed voidage is obtained by incorporating the bed expansion model developed in this work.

The results are analysed and discussed in Chapter 5. The experimental results obtained from gasification of wood pellets using air as the gasifying agent at different air-fuel ratios and different bed particle sizes are presented. The steam gasification behaviour simulated using the developed 1D model is also analysed and compared with the gasification using air. Chapter 5 also presents the conclusions drawn from this study and recommendations for further studies.

2 Literature Review

Several studies can be found on the bed behaviour and gasification process. This chapter gives an overview of the previous studies conducted in these fields. The chapter includes the fluidized bed behaviour and influence of different operating parameters on the bed. A brief state of the art of biomass gasification is also presented.

2.1 Fluidized bed behaviour

This section presents a summary of the previous studies on the fluidized bed behaviour performed at the ambient conditions, and with different bed aspect ratios and particle sizes. This also includes the effects of these variables on the transition from bubbling to slugging regimes and on the bubble properties.

2.1.1 Fluidized bed regimes

Chemical conversion via fluidized bed requires a well-defined flow regime [20]. The transition of a bed from one regime to another may occur when the gas velocity is increased above the minimum fluidization velocity of the bed. The fluidized bed regimes include particulate, bubbling, slugging, turbulent fluidization, fast fluidization and pneumatic conveying regimes [21]. At a transition between two regimes, the bed is often characterized by a certain void fraction and a certain superficial gas velocity. The overview of the previous works on the relevant bed regime transitions between the fixed state and slugging regimes including the effects of particle properties and bed dimension is given in Article [A1]. To characterize the behaviour at the transition, the signals acquired from the bed are analysed using a statistical data analysis such as the probability density function distribution and the standard deviation. Different signals like pressure, solids/void fraction and temperature fluctuations can be acquired from the fluidized beds using probes and tomographic techniques.

The minimum fluidization velocity is usually measured from the plot of the mean pressure drop against the superficial gas velocity. For large particles, analysis of the absolute pressure fluctuations as well as the solids/void fraction fluctuations can also be used. The visual observation is the most common technique for obtaining the gas velocity at which bubbles begin to flow in a fluidized bed. On the assumption that the bed fluctuation arises due to flow of bubbles, the minimum bubbling velocity can also be obtained as the point at which the fluctuation of pressure or solids fraction begins to rise above zero. Due to the chaotic behaviour of slug flow, different studies have been conducted to characterize the slugging behaviour. The minimum slugging velocity can be obtained by visual observation, statistical method or a combination of the two techniques. In the article [A1], the minimum slugging velocity was measured using two-plane ECT sensors. Based on the data analysis, the onset of slugging regime is defined

as the point where the difference in the solids fraction fluctuation between the two sensor positions is maximum. Moreover, in Article [A2], a one-dimensional model developed based on the Euler-Euler method was employed to characterize the fluidized bed regimes.

2.1.2 Bubbling bed behaviour and properties

The bubble growth and the resulting bubble properties depend on a number of parameters including the gas velocity, the bed height to diameter ratio, the particle and the fluid properties. By proper analysis, the bubble properties such as bubble diameter, rise velocity, bubble frequency and volumetric bubble flux can be measured at a given gas velocity. A clear description of how these properties can be measured using the ECT sensors is given in Article [A3]. Different experimental studies report the dependency of these variables on the bed dimension and particle properties. Depending on the bed aspect ratio (the bed height to bed diameter ratio), bubbles can grow into slugs at a much higher velocity above the minimum fluidization velocity. The flow of slugs in a bed is accompanied with excessive pressure fluctuation and escapes of gas with the slugs, which in turn reduces the efficiency of the fluidized bed for chemical synthesis. For fine particles, slugs rarely flow when the bed aspect ratio is less than 2 [22]. In Article [A4], a number of studies related to this behaviour are clearly outlined. In addition to the ECT technique, the bubble properties can be measured using different measurement methods such as probe, X-ray and camera imaging techniques. Further investigations into the bubbling behaviour in deep beds are presented in the article [A4]. The results as outlined in this article [A4] show that the bubble growth and bed distribution are also affected by the particle sphericity. The bubble growth increases with increasing particle size. The effect of bed height on the bubble diameter decreases with increasing gas velocity. With an increase in the gas velocity, the bubble frequency increases within the bubbling regime and decreases in the slugging regime.

There are also a number of correlations for predicting the bubble diameter and velocity [23], which are mainly developed for a freely bubbling bed. For the bubble/slug frequency, only few correlations are available [24, 25]. The overview of these correlations are also presented in this study as can be found in Articles [A5, A6]. Although particle properties influence the bubble growth rate, most existing models rarely account for this. For particles with higher Archimedes number (>400), correlations for predicting the bubble diameter and volumetric flux averaged over the bed height while incorporating the particle and fluid properties are proposed in the article [A5]. Following the analysis of a single bubble flow, a set of semi empirical models for the bubble velocity, bubble frequency and bed expansion are proposed in the article [A6].

The proposed models can be applied to beds of different particle properties but strongly depend on the bubble diameter.

2.2 Biomass behaviour in bubbling bed

Biomass is difficult to be fluidized due to its peculiar shape, size and cohesive nature. In a fluidized bed reactor involving biomass, a bed material such as sand of considerable higher density and smaller particle size is used to aid the fluidization. The summary of some studies on the behaviour of biomass particles in fluidized bed is given in Article [A7]. The relative differences between the sizes and densities of the two different materials usually lead to particle segregation in the bed mixture. The difference in the particle properties also affects the bed voidage and minimum fluidization velocity. As described in most studies, the minimum fluidization of a binary mixture containing biomass increases with increasing biomass load, although this may also depend on the density of the biomass [A8]. The minimum fluidization velocity decreases with increasing amount of biomass in the range 0 – 20 vol.% for wood pellets of density 1132 kg/m^3, but slightly increases for wood chips of density 423 kg/m^3 [A7]. For prediction of minimum fluidization velocity of binary mixtures of biomass and an inert material, a number of correlations including the approach proposed in the article [A8] can be found in literature. Since the minimum fluidization velocity depends on the bed voidage, which is usually difficult to be predicted, a semi-analytical model for predicting the bed voidage involving mixtures of two different particle types and how it can be combined with the Ergun [26] equation to predict the minimum fluidization velocity, is proposed in the article [A8].

Depending on the density difference, biomass can flow up or down the bed when the binary mixture of particles is fluidized. As shown in the article [A7], the low density biomass such as wood chips tends to move upwards when fluidized, but downwards at a much higher gas velocity. The extent to which a bed behaviour is influenced by biomass particles depends on the amount of biomass charged. The minimum gas velocity required to achieve an effective particle mixing over the bed surface increases with the biomass load and decreases with increasing bed diameter. Changes in the bed height at a given bed diameter have an insignificant effect on the minimum mixing velocity [A7]. Moreover, biomass with a low sphericity value tends to sink faster and rises slower in a fluidized bed [27]. With a decrease in the biomass particle size, a better mixing can be obtained in the bed [28]. In addition to the particle morphology, the biomass segregation in a thermochemical conversion process is also influenced severely by the rise of volatile bubbles formed around the particles during devolatilization [29].

The distribution of biomass in a fluidized bed is attributed to the rise of bubbles [30, 31], and the bubble growth rate depends on the amount of biomass present. Increasing the

biomass load decreases the bubble size in the transition region between the bubbling and slugging regimes, thereby delaying the flow of slugs in the bed [A7].

The flow of bubbles also influences the residence time distribution of the fuel particles, and consequently their conversion rate as reviewed in Article [A9]. The mean particle residence time decreases with increasing gas velocity and decreasing bed height [32]. Due to the segregation effect, it may take a longer time than required for a given amount of biomass to be completely converted. For an air-blown bubbling bed reactor, the biomass residence time before a complete conversion is achieved decreases with increasing air flowrate and decreasing biomass load [A9]. The amount of char particles released after devolatilization also decreases with increasing air flowrate due to the partial oxidation.

2.3 Biomass gasification

Biomass gasification usually takes place in the temperature range of 600 – 900℃ and in the presence of a gasifying agent including steam, air/oxygen, carbon dioxide or their combination. In the absence of an oxidizing agent, biomass particles undergo pyrolysis, which involves their decomposition into light gases, char, tar and other contaminant. The thermal degradation of biomass in the atmosphere of nitrogen can be measured using the thermogravimetric analysis (TGA). During the pyrolysis, the fuel particles first go through the heating up and drying process when the temperature < 125℃. Within 125 – 500℃, an active pyrolysis takes place, where most of the volatiles are released. Above 500℃, the passive stage (secondary pyrolysis) sets in, leading to cracking of tar molecules into light gases and inert tar component. The composition and product yields from the biomass pyrolysis depend on the heating rate, biomass composition and the degree of nitrogen flux [33 - 36].

There are several studies on the biomass gasification in fluidized bed based on different heating methods, which include direct and indirect means. In an air/oxygen-blown gasifier, the required heat is generated internally due to partial oxidation of fuel species by the available oxygen, giving rise to an auto-thermal process. For the gasification with pure steam, an allothermal process is used where the required heat is supplied from an external source. The heat supplied for a steam-biomass gasification can be provided by a discontinuous intermittent operation of a single fluidized bed [37, 38], a circulation of particles between two interconnected fluidized bed [39 - 41] and an indirectly heated fluidized bed [42, 43]. The review of Karl and Pröll [17] provides a summary of the state of the art with respect to the layout and dimensioning of indirect heating processes for biomass gasification.

The gasification efficiency, gas composition, product yield and quality depend on a number of factors such as biomass type, amount of oxidizer relative to the biomass supply, gasification temperature and bed material used. In addition to Karl and Pröll [17], Kumar et al. [10] also presents a summary of effects of these parameters on the gasification behaviour as observed in different studies. The amount of gasifying agent influences the superficial gas velocity in the bed. The gas velocity in a bubbling bed gasifier is often within 5 – 10 times the minimum fluidization velocity [17]. Due to the increasing gas volume during gasification, which thus increases the superficial gas velocity, most designs introduce a gradual increase in the bed diameter along the reactor axis [17].

The composition of biomass influences the gasification performance. Hanaoka et al. [44] showed that for cellulose, xylan and lignin based biomasses, the carbon conversion efficiencies at 900 ℃ are 97.7, 92.2 and 52.8%, respectively. The compositions of the product gas are similar in the last two-biomass types. While the CO and CH_4 mole fractions are higher in the cellulose material, the amounts of CO_2 and H_2 are lower than in the xylan and lignin materials. The use of biomass with a high moisture content (> 10%) increases the energy requirement but reduces the amount of steam required in the gasifier [45]. The energy input for gasification also increases when using biomass with low carbon content due to the low char generation and high tar yield [46, 47]. Decreasing the biomass particle size increases the energy efficiencies and yield of CO [48 - 50]. In addition, Lv et al. [48] observed increasing amounts of CH_4 and C_2H_4, and decreasing amounts of CO_2 and H_2 as the particle size is decreased. However, Rapagna and Latif [49] observed a decreasing trend in the yield of CO_2 while Luo et al. [50] observed an increasing trend for H_2 yield. Decreasing the fuel particle size increases the specific surface area, which enhances the heat transfer, and thus the process efficiency.

The biomass flow rate also affects the gasification performance. Over feeding of biomass leads to plugging of the bed and a reduced conversion efficiency while under feeding results in lower gas yields. The optimum biomass flowrate depends on the gasifier design and the amount of the gasifying agent applied. For gasification with air, the equivalence ratio (ER) is used to relate the fuel supply with the amount of air applied. The total gas yield and lower heating value increase with increasing value of ER, although different trends of the gas composition have been reported in different studies [51 - 54]. With an increase in the equivalence ratio within 0 - 0.45, the amounts of CO, H_2, CH_4 and tar decrease [51], H_2 yield varies slightly until the optimum ER = 0.23 value [52], and CO and H_2 yields increase [54]. For gasification with steam, a high steam flowrate decreases the cold gas efficiency and tar content of the product gas. A high steam flowrate also promotes char conversion and prevents the downstream soot and coke formations when the temperature is above 700 ℃ [17, 55]. Naraez et al. [51] showed that by

increasing H/C ratio (where hydrogen are derived from the moisture content, the external steam supply and the biomass composition) from 1.6 to 2.2, the hydrogen yield increases while the lower heating value increases from 4 to 6 MJ/Nm^3 and tar content decreases from 18 to 2 g/Nm^3. By varying the mass of steam to biomass ratio above 2.7, Lv et al. [52] observed that the gas composition does not vary significantly, but with an increase in the steam-biomass ratio from 1.35 to 2.7, the CO and CH_4 yields decrease whereas the CO_2 and H_2 yields increase.

The bed material size and properties influence the reactor dimension and gas composition [17]. Due to slow gasification rate of char particles, high reactor volume is required to increase the residence time for effective conversions. The catalytic nature of some bed materials can also enhance the tar decomposition and CO shift for a higher H_2 production [56, 57]. The most commonly used bed materials are olivine, silica sand and calcites due to their high specific heat capacity and ability to withstand high temperature [58].

Moreover, different models have been proposed for simulation of biomass gasification behaviour. As briefly highlighted in Article [A10], the models can be based on the thermodynamic equilibrium, reaction kinetics and a combination of the two. The procedures for modelling a gasifier are recently summarized by Mazaheri et al. [59]. For detailed analysis, models based on the computational fluid dynamics and computational fluid-particle dynamics are applied. Due to complexities of the multi-dimensional computational models, several one-dimensional models are available for prediction of the gas composition and studying of the effects of different operating parameters on the gasifier performance. Most of the existing one-dimensional models are based on the two-phase theory, which assumes that the gas flow through a fluidized bed exists in two separate phases (bubble and emulsion). In addition to the one-dimensional hydrodynamic model based on the computational fluid dynamics presented in the article [A2] for predicting the behaviour across different regimes in a non-reacting fluidized bed, a detailed 1D model based on the conservation of mass, momentum and energy for biomass gasification in a bubbling bed is also proposed in [A10]. As illustrated in the article [A10], the model can be used to study the effect of gasifier design choices and operating conditions.

3 Experimental Setups

There are two different experimental setups used in this study. The first is operated in the cold flow conditions to investigate the behaviour of fluidized beds at different gas velocities, particle sizes and bed heights. This setup is easy to control, and due to the cold operating environment, advanced measurement techniques such as ECT (electrical capacitance tomography) could be applied. The second setup is used to study the bed behaviour in hot flow conditions, and gasification of biomass under the atmospheric pressure condition. This chapter presents the detailed descriptions of the different setups and the methods employed in the measurement of the bed dynamic properties, which include the bubble dimeter, bubble velocity, bubble frequency, mixing and segregation pattern, and the biomass residence time over the conversion period.

3.1 Cold flow behaviour

The setup used under this study consists of a cylindrical Perspex column of diameter 10.4 cm and height 1.4 m as shown in Figure 3.1. Two ECT sensors are positioned at a space of 13 cm for measurement of solids fraction distributions across the bed diameter and along the bed axis. The lower sensor is mounted 15.7 cm above the gas distributor plate made of a highly porous stainless steel material with effective flow area, 40%. Detailed description of this setup is given in the articles [A1, A4, A5, A7]. ECT measures the relative permittivity between two non-conducting media. Different materials have different permittivity, making it possible to measure the distribution of different solid materials in a fluidized bed using the ECT system. Each plane of the ECT sensors is divided into 32x32 pixels of which 812 pixels lie within the bed. The pixels hold the normalized permittivity of the denser material relative to the lighter material in the scale of 0 – 1. A value of 0 indicates that the bed is filled with the light material (air) and 1 indicates that the bed contains only the denser material (bed particles). The setup was used to measure the minimum fluidization and slugging velocity [A1] as well as the bubble properties [A4, A5, A6] based on the different materials and properties listed in Table 3.1. The setup was also used to investigate the mixing and segregation behaviour of biomass in a binary mixture [A7] using the materials given in Table 3.2.

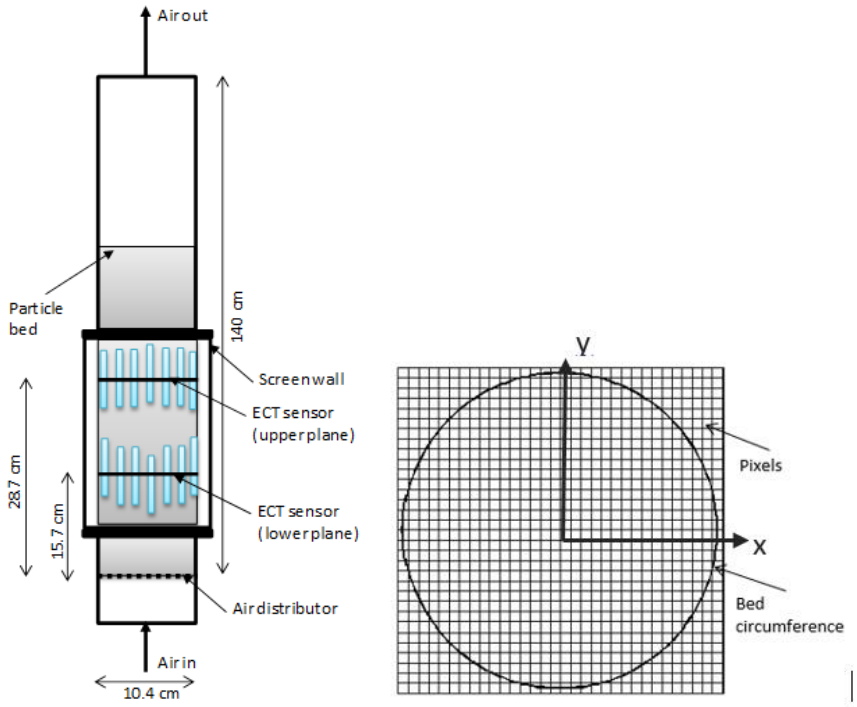

(a) (b)

Figure. 3.1. (a) Schematic illustration of a cold fluidized bed equipped with ECT sensors for measurement of solids fraction distribution (b) bed cross-section divided into 812 pixels.

Table 3.1. Properties of particles used in the cold bed behaviour studies.

Materials	Mean size [µm]	Density [kg/m^3]	ε_{mf} [-]	U_{mf} [cm/s]
Glass	188	2500	0.430	3.80
Glass	261	2500	0.450	8.15
Limestone	293	2837	0.530	13.80
Sand	483	2650	0.460	16.50
Glass	624	2500	0.488	23.20
Limestone	697	2837	0.607	39.24
Molecular sieve	2170	1300	0.472	76.85

Table 3.2. Properties of particles used in the study of biomass behaviour at cold flows.

Materials	Shape	ρ_p [kg/m^3]	$d_{p,sph}$ [mm]	φ_p [-]	ε [-]	ε_{mf} [-]	U_{mf} [m/s]
Wood pellets	Cylindrical	1139	8.96	0.82	0.43	0.46	1.99
Wood chips	Rectangular	423	6.87	0.75	0.49	0.57	1.27
Sand	Angular	2650	0.293	0.86	0.42	0.46	0.079

3.1.1 Identification of flow regime transition

Figure 3.2 shows the average solid fraction fluctuations measured as described in the article [A1] at different superficial air velocities and bed positions. The results show that the solids fluctuations in both planes begin to increase above 0 after a certain velocity. The increase in the solids fluctuation at a higher gas velocity is attributed to the flow of bubbles. By considering that bubbles begin to rise in a bed of Geldart B particles as soon as it is fluidized, the minimum fluidization velocity U_{mf} is measured at the point where the fluctuations begin to increase from 0.

The figure also shows that the difference in the solids fluctuations between the upper and lower planes attains a peak value as the gas velocity is increased. At the peak point, the rate of change in the solids fluctuation with gas velocity is the same in both planes. As clearly described in the article [A1], slugs flow across the two planes in the region where the difference in the fluctuation curves decreases with increasing velocity. Below the peak fluctuation point, both planes bubble freely at a lower gas velocity, but at a velocity closer to the peak fluctuation (where the slope of the curve is lower), slugs flow only in the upper plane. The mean minimum slugging velocity U_{ms} over the bed is therefore obtained at the point where the fluctuation between the two planes is maximum.

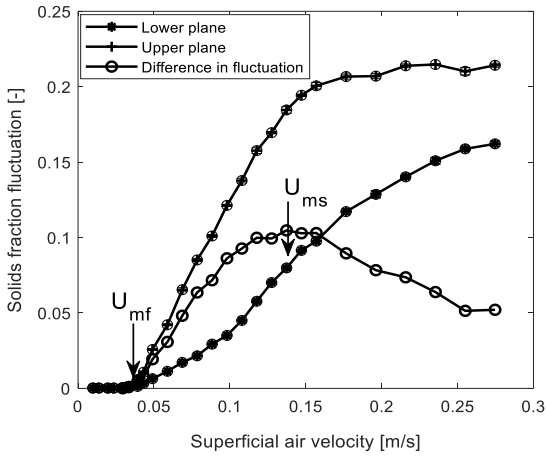

Figure 3.2. Solids fraction fluctuation at different gas velocities and two positions in a bed, showing the procedure of determining the minimum fluidization and slugging velocities. Particle: 188 µm glass particles and bed height, 58 cm.

3.1.2 Measurement of bubble properties

Figure 3.3(a) shows the distribution of solids fraction measured with the lower plane ECT sensor in a bed containing 188 µm glass beads. The number in the colorbar indicates the normalized relative permittivity (solids fraction) of the particles due to flow of air at a velocity of 0.137 m/s in the bed with initial height, 58 cm. From the figure, a bubble is identified as a region where the solids fraction is less than 0.2 [A3]. Figure 3.3(b) displays a typical time evolution of the bubble-projected area in the deep bed, where due to bubble coalescence only a single bubble is observed at the measurement planes. The figure also shows that the projected bubble area rises to a peak value and then falls to zero when the bubble has completely passed the plane. Between two successive bubble passages, the bed is idle, giving rise to periodic fluctuation of the bed.

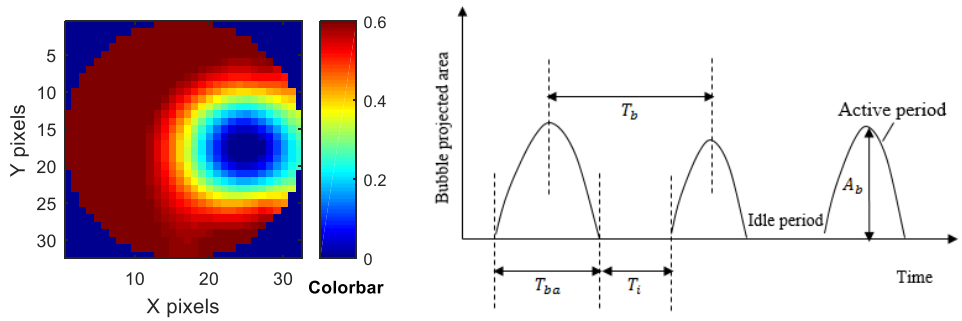

(a) (b)

Figure. 3.3. (a) Contour showing the distribution of solids fraction at the lower plane for a bed of the 188 µm glass particles at $U_0 = 0.137$ m/s; bed height = 58 cm. Increasing colour scale from 0 to 0.6 increases the solids concentration; in the bubble region, the solids fraction is less than 0.2 [69] (b) evolution of the bubble-projected area with time.

The peak of the projected area represents the bubble cross-sectional area through its centre. Assuming a spherical bubble, the bubble diameter d_b is measured from

$$d_b = \frac{1}{N}\sum_i \left(\sqrt{\frac{4A_{b,i}}{\pi}}\right) \tag{3.1}$$

where N is the number of bubble passages observed over the measurement period and $A_{b,i}$ is the maximum projected area recorded during each bubble passage.

The bubble frequency f_b is obtained from Eq. (3.2), where T_b is the mean bubble period measured as the time between two successive bubble passages.

$$f_b = \frac{1}{T_b} \tag{3.2}$$

The volumetric bubble flux G defined as the volume of bubbles passing in a unit time across a unit cross-sectional area of the bed is therefore determined from

$$G = \frac{\pi d_b^3}{6AT_{ba}} \tag{3.3}$$

where A is the bed cross-sectional area and T_{ba} is the average time required for a complete passage of the bubbles through the plane.

By measurement of the time taken for a single bubble to move from the lower to the upper plane, the average bubble velocity can be determined. However, due to the spacing between the two ECT planes, the bubble may coalesce with another bubble or split into smaller bubbles before reaching the upper plane. This makes it difficult to trace a single bubble between the two planes and then difficult to compute the bubble travel time by any statistical method. Since the void or solids fraction can be measured at a given plane in the bed, the local bubble velocity can be computed by applying the two-phase theory [A6].

$$u_b = G/\delta_b \tag{3.4}$$

where

$$\delta_b = \frac{\varepsilon_f - \varepsilon_{mf}}{1-\varepsilon_{mf}} \tag{3.5}$$

3.1.3 Biomass distribution in a binary mixture

Because different solid materials have different relative permittivity, the concentration of biomass in a bed of binary mixture with inert particles can be determined by comparing the solids fraction of the mixture with that of the pure bed material at the

same measurement position and gas velocity. The detail of this procedure is given in the article [A7]. Assuming $\alpha_{i,j,s}$ is the solids fraction of the pure inert material (sand for example) and $\alpha_{i,j,m}$ is the solids fraction of the mixture containing biomass at a given pixel (i,j), Eq. (3.6) can be derived for computing the mass concentration $X_{i,j,b}$ of the biomass particles at the same pixel position.

$$X_{i,j,b} = \frac{(\alpha_{i,j,s}-\alpha_{i,j,m})^2}{\alpha_{i,j,m}+\alpha_{i,j,s}(\alpha_{i,j,s}-\alpha_{i,j,m})\left(\frac{\rho_s}{\rho_b}-1\right)} \tag{3.6}$$

where ρ_s and ρ_b are the densities of the bed material and biomass particles, respectively. In terms of volume fraction, the concentration of biomass in the bed can be obtained from

$$Y_{i,j,b} = \frac{X_{i,j,b}}{X_{i,j,b}+\frac{\rho_b}{\rho_s}(1-X_{i,j,b})} \tag{3.7}$$

A typical result of Eq. (3.7) is shown in Figure 3.4. The figure compares the distribution of wood pellets with that of wood chips of close volumetric equivalent spherical diameter but smaller density (about 2.5 times smaller) at different gas velocities. Each bed contains 20 vol.% biomass and 80 vol.% sand particles. As can be seen, the homogeneity of pellets across the bed height increases with increasing gas velocity as more of the biomass particles move upwards from the bottom of the bed. The sinking of the wood chips from the upper part of the bed increases with increasing gas velocity, but the axial dispersion is more pronounced than in the pellet bed. The results also show that the tendency of biomass to move towards the walls is higher with the wood chips than with the wood pellets.

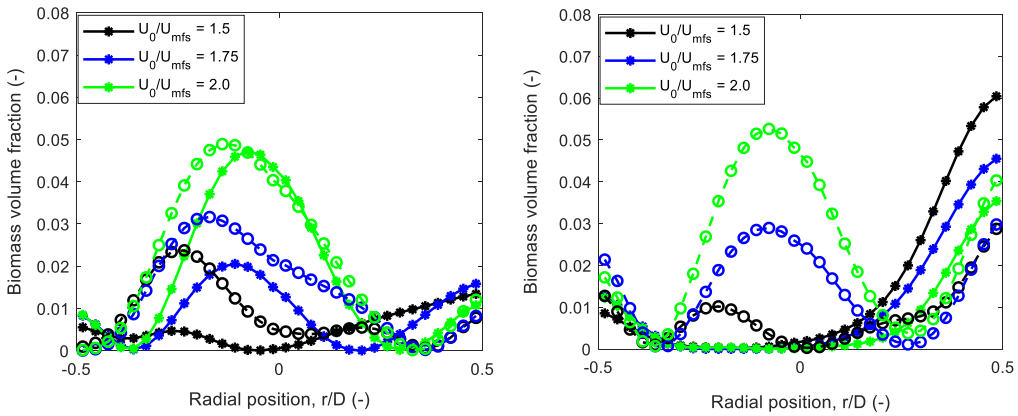

(a) (b)

Figure 3.4. Radial distribution of biomass in a bed mixture of sand and 20 vol.% of (a) wood pellets (b) wood chips. Upper plane = star data points with solid lines; lower plane = circle data points with broken lines. Particles, see Table 3.2; Initial bed height = 50 cm.

3.2 Hot flow behaviour

Figure 3.5 describes the setup used in the hot flow studies. The reactor column is made of stainless steel material and has internal diameter of 10 cm and a length of 1.0 m. The column is fitted with five temperature and five pressure sensors along the axis. The test rig is described in detail in the article [A9]. The setup was used to study the biomass residence time before a complete conversion is attained, the mixing and segregation behaviour of the fuel particles during the conversion, and the influence of air-fuel ratio and bed material particle size on the product gas composition in a biomass gasification process. As shown, air is supplied through a heater while the product gas goes through the flare before exiting to the atmosphere. Biomass is fed at the position 21.2 cm above the bed base. Gas is also sampled above the bed for offline analysis. The gas analyser comprises a gas chromatography with helium as the carrier gas. From the gas analysis, the mole fractions of nitrogen, oxygen, hydrogen, carbon monoxide and methane are determined in each gas sample. The materials used under this study are listed in Table 3.3.

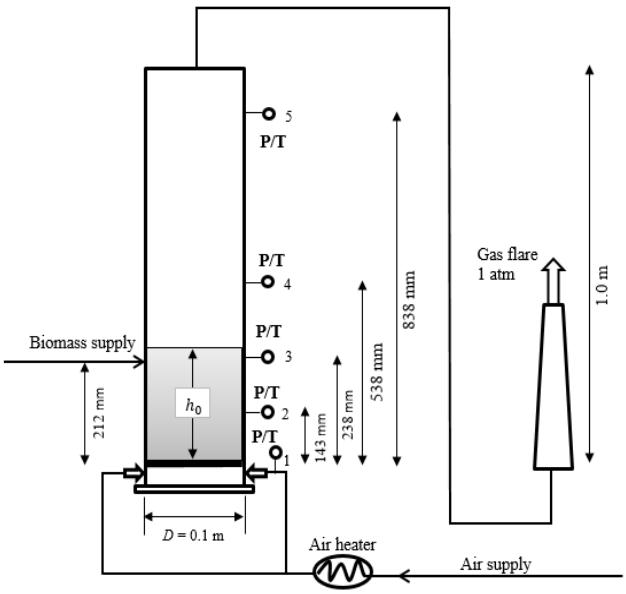

Figure 3.5. Schematic illustration of a biomass gasification reactor. Symbols **P/T** indicate pressure and temperature sensor probes; h_0 is the initial bed height above air introduction points.

Table 3.3. Properties of different particles used in the hot flow experiments.

Materials	Shape	ρ_p [kg/m^3]	$d_{p,sph}$ [mm]	φ_p [-]	ε [-]	ε_{mf} [-]	U_{mf} [m/s]
Wood pellets	Cylindrical	1139	8.96	0.82	0.43	0.46	1.99
Wood chips	Rectangular	423	6.87	0.75	0.49	0.57	1.27
Sand	Angular	2650	0.293	0.86	0.42	0.46	0.079
Sand	Angular	2650	0.615	0.72	0.454	0.454	0.245

3.2.1 Biomass residence time and char yield

In this study, a batch process is used to determine the residence time before a given amount of biomass is completely converted and the amount of char released at the end of the devolatilization phase in an air-blown bubbling fluidized bed. The detailed procedure employed is presented in the article [A9]. As shown in Figure 3.6, the bed pressure drop increases to a peak value (point **O**) shortly after the desired amount of biomass is introduced in the fluidized bed of sand particles. The bed pressure rapidly drops to point **D** due to release of volatiles during the devolatilization of the biomass particles, which is completed at point **D**. At the instant of complete devolatilization, the bed temperature drops to the minimum. The temperature increases above **D** due to partial combustion of combustible gases and the residual char particles. At point **E**, nearly all the char particles are consumed and the pressure drop tends towards the initial value corresponding to that of the pure sand particles.

Starting from point A where the desired amount of biomass is introduced, t_d is the biomass devolatilization time and t_e is the extinction time of the fuel particles in the bed. The difference $(t_e - t_d)$ defines the char residence time before it is completely converted, and t_* is the mean biomass residence time over the conversion process. The amount of char γ_{char} released after devolatilization as a fraction of mass of the biomass loaded can be obtained by the mass balance over the bed.

$$\gamma_{char} = \frac{p_D - p_s}{p_O - p_s} \tag{3.8}$$

where p_s is the mean pressure drop over the bed of pure sand particles at the same air flowrate. The detailed derivation of Eq. (3.8) is presented in [A9].

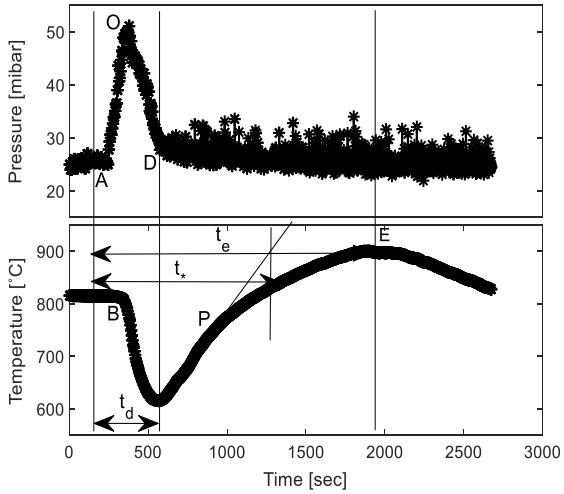

Figure 3.6. Pressure drop (over the bed height) and temperature (measured at 14.3 cm from the bed base) curves, showing the different phases during biomass conversion in a batch bubbling fluidized bed operation for a bed containing 26.4 vol.% wood pellets and 293 µm sand particles (mass = 2.2 kg) at an air flowrate of 1.0 kg/h.

The value of p_s in Eq. (3.8) is obtained as an average value over a measurement period, and the measurement uncertainty can be neglected. The pressure drops p_O and p_D are obtained at instances of time. Due to fluctuation of fluid pressure, these quantities are difficult to be measured via graphical method. As an approximation, the values of p_O and p_D can be obtained by fitting a line across the pressure data over the measurement periods O-D. Assuming that the variance is uniformly distributed over the measurement interval, the uncertainty σ_p^2 in the pressure measurement is computed as

$$\sigma_p^2 = \left(\sqrt{\frac{1}{N}\sum_i (p_i - \bar{p}_i)^2} - \sigma_s\right)^2 \tag{3.9}$$

Here, σ_s is the standard deviation of the pressure drop fluctuation in the bed without biomass, $\bar{p}_i$ is the estimated pressure drop from the fitting line and p_i is the actual pressure drop measured at the given time. The uncertainty σ_{char}^2 in the measurement of char yield is then given by

$$\frac{\sigma_{char}^2}{\gamma_{char}^2} = \left[\frac{1}{(\bar{p}_D - p_s)^2} + \frac{1}{(\bar{p}_O - p_s)^2}\right]\sigma_p^2 \tag{3.10}$$

The rate of total heat loss over the devotilization period can be ascertained from the temperature drop between points **B** and **D**.

$$\dot{q}_L = \frac{T_B - T_D}{t_D - t_B} \tag{3.11}$$

Here, $\dot{q}_L$ [K/s] is the net heat loss during devotilization and T_B can be approximated to the initial bed temperature.

3.2.2 Mixing and segregation behaviour

Using the measurement of temperatures along the bed axis, the mixing and segregation behaviour of biomass particles in the batch process can be determined. In a well-mixed bed, the distributions of material and temperature are approximately uniform over the bed height. This means that the heat released in the lower part of the bed due to higher availability of oxygen is quickly transported up the bed by the hot gas and bed material while the unburnt fuel particles quickly move downwards by the circulation of the bed material. When there is a temperature gradient along the bed axis, it indicates a non-uniform distribution of the particles.

Figure 3.7 shows the variation of axial temperature difference normalized with the peak temperature recorded over the measurement period in each of the different beds at different air velocities. The positive value of the temperature difference indicates that the temperature inside the bed is higher than that near the bed surface, and vice versa. At the introduction of a given amount of biomass, the results show that the degree of sinking of the fuel particles increases with decreasing air velocity as similarly observed in the cold flow behaviour [A7]. The initial sinking behaviour can be attributed to the strength of the bubble flux across the bed. In addition to the lower density, the bubble flux is higher in the wood chip bed, resulting in upward flow of the biomass particles at increasing air velocity. At the lower velocity, most of pellets lie closer to the bottom of the bed due to the higher gravity effect compared to the flux of the rising bubbles. With an increase in the gas velocity, the amount of pellets moving upwards increases, resulting in a much higher temperature within the bed than near the bed surface.

The temperature difference decreases as the biomass moves upwards due to devolatilization. At the completion of devolatilization, the pellet char tends to move back into the bed and mix uniformly over the bed height before it is completely converted. However, the wood char particles remain segregated near the bed surface until the conversion is complete. The figure also shows that with increasing air velocity, the sinking behaviour of the char particles is enhanced.

Based on these results, the behaviour of char particles in the hot bed can be viewed similar to the behaviour of the parent biomass in the cold bed [A7]. However, to evaluate the mixing and segregation behaviour of the fuel particles using this technique, a detailed analysis of heat balance needs to be incorporated. The temperature gradient in the bed of pure sand particles at the same air flowrates as used in the biomass conversion is to be considered. Decoupling the heat flow in the individual pure

component bed from that of the bed mixture will give a better quantitative assessment of the bed behaviour during the biomass conversion.

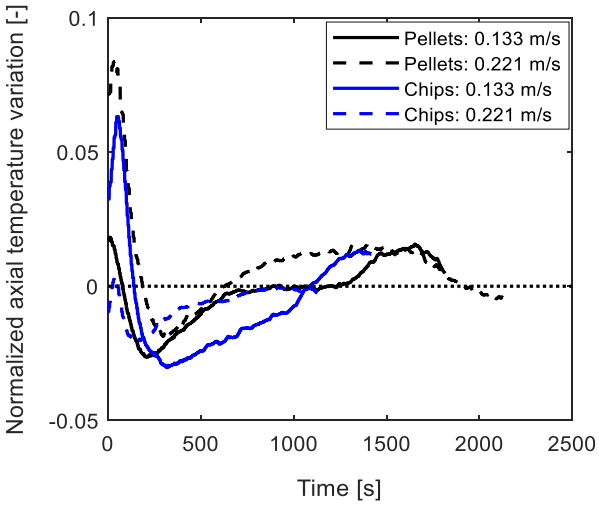

Figure 3.7. Normalized axial temperature difference across the bed of 20.2 vol.% wood pellets and 21.3 vol.% wood chips with 293 µm sand particles (mass = 2.2 kg), illustrating the effect of gas velocity on the distribution of temperature (fuel particles) during biomass conversion in a bubbling bed. Initial bed temperature = 820 ℃.

4 Modelling and Simulation

In this chapter, correlations of the experimental data are given. The 0D models describe the average behaviour of a bed at a given operating condition, and thus can be used in scaling up the observations. This chapter also presents a detailed 1D hydrodynamic model that describes the fluid-particle interactions in a bubbling fluidized bed reactor.

4.1 0D bed averaged models

The 0D models include the correlations for predicting the volumetric bubble flux, bubble diameter, minimum slugging velocity and the bed voidage of a binary mixture averaged over the bed height. Included in this section are also the proposed models for predicting the bubble velocity and bubble frequency at any position in the bed. An analytical model for predicting the minimum gas velocity required to achieve an effective mixing over the surface of a binary mixture containing biomass is proposed as well as the bed expansion at a given gas velocity in a fluidized bed.

4.1.1 Models for average volumetric bubble flux, bubble diameter and minimum slugging velocity

The detail derivation and description of these models are given in the article [A5]. The models are also validated as discussed in the article. Following the expression proposed by Grace and Cliff [60], the volumetric bubble flux can be expressed as

$$G = U_0 - kU_{mf} \tag{4.1}$$

where k is the correction factor accounting for the deviation of a bubbling bed behaviour from the two-phase theory. Figure 4.1(a) shows the plot of $\log(k)$ against $\log(U_0/U_{mf})$ for different particles based on the average volumetric bubble flux over the bed height. In the figure, each set of the experimental data is fitted with two different lines of different slopes and intersections. The description of the behaviour is also given in the article [A5]. The behaviour in the bubbling regime is represented by the solid lines while that in the slugging regime is given by the dashed lines.

Each line in Figure 4.1(a) is represented by

$$k = c\left(\frac{U_0}{U_{mf}}\right)^a \tag{4.2}$$

The fitting parameters a and c depends on the particle properties and the bed regime as shown in Table 4.1. Substituting Eq. (4.2) in (4.1), the average bubble flux can be expressed as given in Eq. (4.3).

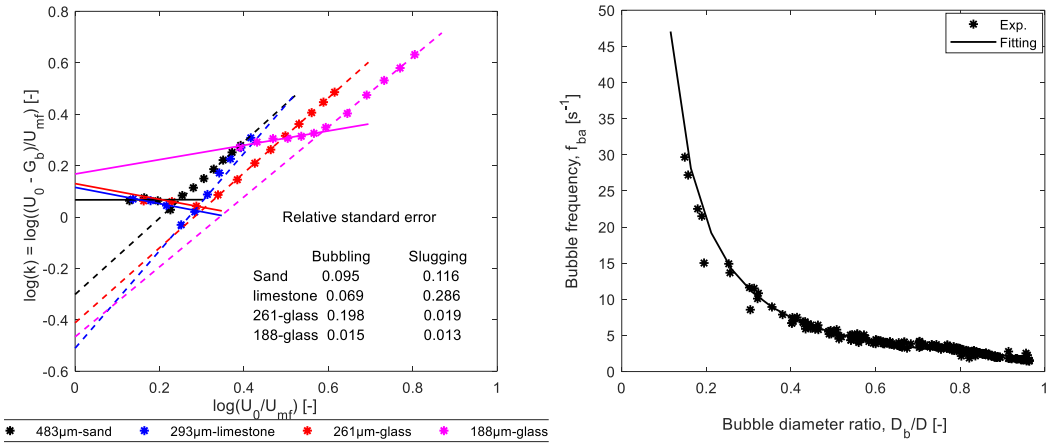

(a) (b)

Figure 4.1. (a) Two-phase theory deviation coefficient showing bubbling behaviour of different particles at different gas velocity ratios; solid lines – bubbling regime; dashed lines – slugging regime (b) relationship between the active bubbling frequency and bubble diameter.

Table 4.1. Correlations for the model parameters a and c in the bubbling and slugging regimes.

Parameters	Expressions	Validity
	Bubbling regime	
a	$\varphi^{1.5}(4.168 - 1.389\log(Ar))$	$\log(Ar) < 3.5$
	$\varphi^{1.5}(0.329 - 1.156 \cdot 10^{3} Ar^{-0.9})$	$\log(Ar) \geq 3.5$
c	$(1.321 + 8.161 \cdot 10^{4} Ar^{-1.04})^{0.083}$	$\log(Ar) > 0$
	Slugging regime	
a	$0.725 + 0.230\log(Ar)$	$\log(Ar) < 3.9$
	$1.184 + 8.962 \cdot 10^{4} Ar^{-1.35}$	$\log(Ar) \geq 3.9$
c	$0.042 + 0.108\log(Ar)$	$\log(Ar) < 4.0$
	$(0.978 - 1.964 \cdot 10^{2} Ar^{-0.8})^{4.88}$	$\log(Ar) \geq 4.0$

$$\boldsymbol{G = U_0 - c\left(\frac{U_0}{U_{mf}}\right)^{a} U_{mf}} \tag{4.3}$$

Based on Figure 4.1(a), the transition between the bubbling and slugging regimes occurs at the intersection of the two different lines in each bed. Applying Eq. (4.2), the minimum slugging velocity ratio U_{ms}/U_{mf} can be obtained as

$$\frac{U_{ms}}{U_{mf}} = c_t^{a_t} \tag{4.4}$$

Here, $c_t = c_b/c_s$ and $a_t = 1/(a_s - a_b)$, where "b" and "s" denote parameters in the bubbling and slugging regimes, respectively. In general, the minimum slugging velocity depends on the bed aspect ratio h_0/D. From further analysis using different beds at different bed heights [A5], Eq. (4.4) is improved, leading to

$$\boldsymbol{\frac{U_{ms}}{U_{mf}} = 1 + 2.33 U_{mf}^{-0.027}\left(\varphi^{0.35} c_t^{a_t} - 1\right)\left(\frac{h_0}{D}\right)^{-0.588}} \tag{4.5}$$

Figure 4.1(b) shows the dependency of the active bubble frequency $f_{ba} = 1/T_{ba}$ on the bubble diameter. The curve correlating the data is given by

$$1/T_{ba} = 1.927\left(\frac{D}{d_b}\right)^{1.48} \tag{4.6}$$

Substituting Eq. (4.6) in (3.3), the bubble flux becomes

$$G = 1.285\left(\frac{d_b}{D}\right)^{1.52} D \tag{4.7}$$

Combining Eqs. (4.3) and (4.7), the average bubble diameter $\bar{d}_b$ over the bed height can then be obtained as

$$\boldsymbol{\bar{d}_b = 0.848\left(U_0 - c\left(\frac{U_0}{U_{mf}}\right)^{a} U_{mf}\right)^{0.66} D^{0.34}} \tag{4.8}$$

Equations (4.3), (4.5) and (4.8) are applicable to particles for which the Archimedes number, $Ar > 400$. The minimum bubbling velocity $\left(U_0/U_{mf}\right)_{min}$ above which these equations are also valid is given by

$$\left(\frac{U_0}{U_{mf}}\right)_{min} = c_b^{1/(1-a_b)} \tag{4.9}$$

4.1.2 Models for bubble velocity, bubble frequency and bed expansion

The bubble frequency and bed expansion depends on the bubble velocity. Following the trajectory of a single bubble rising through a fluidized bed, a set of semi-analytical models can be developed for prediction of these bubbling fluidized bed properties as clearly described in the article [A6]. Moreover, these quantities also depend on the bed

dimension and particle properties. Based on the bubble growth rate, two classes (A and B types) of bubbling behaviour as summarized below are identified to aid the analysis [A6].

• "***Type A**: Bed with a slow bubble growth rate and a smooth transition from bubbling to slugging regime. Slugs rise along the central axis with a full-grown size less than the bed diameter; this behaviour is typical for fine and smooth Geldart B particles*."

• "***Type** B: Bed with a rapid bubble growth rate or a sharp transition from bubbling to slugging regime. Slugs spread across the bed cross-section and attach to the wall while rising. Slugs can grow to the bed size; this behaviour is typical for large particles or rough smaller particles*."

4.1.2.1 Bubble velocity

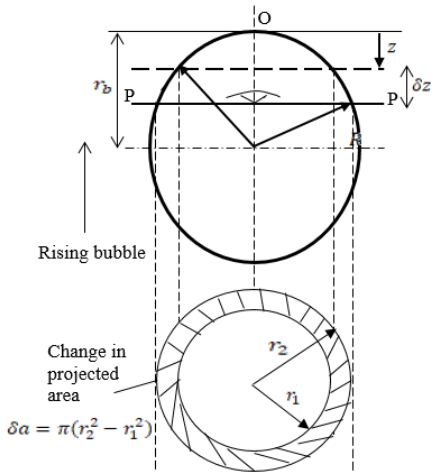

Figure 4.2. Trajectory of a single bubble rising in a fluidized bed at an observer plane.

Considering Figure 4.2 for a single bubble passing an observer placed on the plane **P-P** in a fluidized bed, the rate of change of the projected area of the bubble as viewed by the observer can be expressed as

$$\frac{\delta a}{\delta t} = \pi(2r_b - 2z - \delta z)\frac{\delta z}{\delta t} \tag{4.10}$$

where $r_b = d_b/2$ is the bubble radius. Taking the limit: when $\delta t \to 0$, $\delta z \to 0$, $\delta a/\delta t \to da/dt$ and $\delta z/\delta t \to dz/dt$. Defining the bubble rise velocity as $u_{br} = dz/dt$, Eq. (4.10) leads to

$$\frac{da}{dt} = \pi(2r_b - 2z)u_{br} \tag{4.11}$$

Normalizing Eq. (4.11) by diving through with the bed cross-sectional area, gives

$$\frac{1}{4A}\frac{da}{dt} = \left(\frac{2r_b - 2z}{D}\right)\left(\frac{u_{br}}{D}\right) \tag{4.12}$$

Setting $k = \frac{2(r_b - z)}{D}$, the bubble rise velocity becomes

$$u_{br} = \left(\frac{D}{4Ak}\right)\frac{da}{dt} \tag{4.13}$$

Equation (4.13) suggests that for a given bed geometry, the bubble rise velocity is proportional to the rate of change of the projected area with time, where k is a constant value depending on the fluid flow properties. Referring to Figure 3.3(b), a bubble passes the observer after the period T_{ba}. Assuming that the change in the bubble projected area within this period is parabolic, the mean value of da/dt can be derived as

$$\frac{da}{dt} = \frac{2A_b}{T_{ba}} \tag{4.14}$$

Substituting Eq. (4.6) in Eq. (4.14) and then in (4.13), u_{br} can be expressed as

$$u_{br} = \frac{0.9635}{k}\left(\frac{d_b}{D}\right)^{0.52} D \tag{4.15}$$

Analysis of the experimental data shows that k can be correlated with the excess gas velocity $U_0 - U_{mf}$ as expressed in Eq. (4.16).

$$k = 0.077(U_0 - U_{mf})^{-0.362} \tag{4.16}$$

Using Eq. (4.16) in (4.15), the following expression is therefore proposed for the bubble rise velocity.

$$\boldsymbol{u_{br} = 12.51(U_0 - U_{mf})^{0.362}\left(\frac{d_b}{D}\right)^{0.52} D} \tag{4.17}$$

With further analysis and comparison with literature data, it can be shown that the bubble velocity u_b due to existence of more than one bubble in a bed is given by [A6].

$$\boldsymbol{u_b = \varphi_N(U_0 - U_{mf}) + 12.51\varphi_D(U_0 - U_{mf})^{0.362} d_b^{0.52}} \tag{4.18}$$

Where

$$\varphi_N = \begin{cases} 1 & \text{for Geldart A and A/B} \\ 0 & \text{for Geldart B and D} \end{cases}$$

$$\varphi_D = \begin{cases} D^{0.48} & \text{for type A behaviour (Geldart A and small Geldart B particles)} \\ 0.337 & \text{for type B behaviour (large Geldart B particles)} \\ 0.26 & \text{for Geldart D} \end{cases}$$

4.1.2.2 Bubble frequency

From Figure 3.3(b), the bubble frequency can be expressed as

$$f_b = 1/(T_{ba} + T_i) \tag{4.19}$$

The bed idle period T_i decreases with increasing bubble velocity. As discussed in the article [A6], T_i can be correlated with the bubble velocity in the following equation.

$$T_i = m u_b^n d_b \tag{4.20}$$

Where

Bubbling regime, $\frac{d_b}{D} \leq \left(\frac{d_b}{D}\right)_{fm}$: $\begin{cases} m = 0.05\,; n = -3.475 & \text{for type A} \\ m = 0.05\,; n = -4.379 & \text{for type B} \end{cases}$

Slugging regime, $\frac{d_b}{D} > \left(\frac{d_b}{D}\right)_{fm}$: $\begin{cases} m = 0.631\,; n = -1.187 & \text{for type A, } \frac{d_b}{D} \leq 0.6 \\ m = 3.382\,; n = -0.122 & \text{for type A, } \frac{d_b}{D} > 0.6 \\ m = 5.277\,; n = -0.366 & \text{for type B} \end{cases}$

$(d_b/D)_{fm}$ can be obtained from Eq. (4.21) and is defined as the bubble diameter at which the bubble frequency is maximum, and which also corresponds to the bubble diameter at the local transition between the bubbling and slugging regimes as discussed in the article [A4].

$$(d_b/D)_{fm} = \left(2.90 - 36.66 \exp\left(-2.80 \frac{U_{ms}}{U_{mf}}\right)\right)^{-1} \tag{4.21}$$

Substituting Eqs. (4.6) and (4.20) in Eq. (4.19) gives the bubble frequency as

$$\boldsymbol{f_b = \left(0.52 \left(\frac{d_b}{D}\right)^{1.48} + m u_b^n d_b\right)^{-1}} \tag{4.22}$$

4.1.2.3 Bed expansion

The bed expansion Δe in a fluidized bed can be defined as

$$\Delta e = \frac{H_f - H_{mf}}{H_{mf}} \tag{4.23}$$

where H_f is the total bed height at the fluidized state and H_{mf} is the bed height at the minimum fluidization condition. By the mass balance of solid particles in the bed,

$$\Delta e = \frac{1-\varepsilon_{mf}}{1-\varepsilon_f} - 1 \tag{4.24}$$

Substituting Eq. (3.5) in Eq. (4.24), Δe can be expressed as

$$\Delta e = \frac{1}{1-\delta_b} - 1 \tag{4.25}$$

Combining Eqs. (3.4), (4.7), (4.17) and (4.25) for a single rising bubbling behaviour over the bed height yields

$$\Delta e = \left[1 - 0.103\left(U_0 - U_{mf}\right)^{-0.362}\left(\frac{\bar{d}_b}{D}\right)\right]^{-1} - 1 \quad (4.26)$$

Within the range of its validity, Eq. (4.8) can be applied in Eq. (4.26) to obtain the particle-dependent bed expansion as demonstrated [A6].

4.1.3 Model for minimum mixing velocity in a binary mixture

For a bed containing biomass of low density, the particles usually segregate to the surface of the bed when the gas velocity is slightly above the minimum fluidization velocity of the bed. The accumulation of biomass particles at the bed surface prevents the rise of bubbles and circulation of sand particles over the bed height as discussed in the article [A7]. Without circulation of bed material over the bed height, particle mixing in the bed will be poor. However, at a sufficiently higher velocity, the biomass layer breaks, allowing the eruption of bubbles and consequently the circulation of the bed particles. The minimum gas velocity required to achieve mixing over the bed height can be obtained by establishing a force balance across the biomass layer as shown in Figure 4.3, where l_{max} is the maximum thickness of the biomass layer.

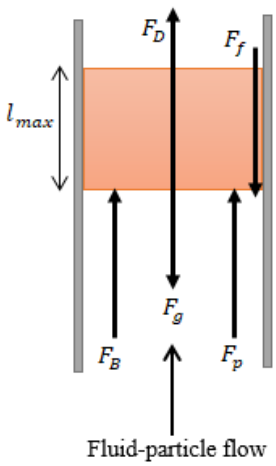

Figure 4.3. Different forces acting on a layer of biomass segregated to the surface of a bed.

At static condition, the force balance across the layer at the top of the bed is given by

$$F_g + F_f = F_B + F_p + F_D \quad (4.27)$$

where

$F_g = \varepsilon_b \rho_b g A l_{max}$ and $F_f = \tau_w \pi D l_{max}$

$F_B = \left(\rho_g + \varepsilon_s f_{wake} \rho_s\right) G u_b A$, $F_p = \varepsilon_b \Delta p_g A$ and $F_D = \beta A l_{max}$.

The fluid pressure drop Δp_g across the layer is modelled as in Eq. (4.28a). The wall frictional stress τ_w can be obtained by applying the Coulomb's law, $\tau_w = \mu_w \sigma$, where the normal stress σ can be based on the Rankine [61] model of dense powder flow as given in Eq. (4.28b).

$$\Delta p_g = \gamma \delta_b \varepsilon_s \rho_s g l_{max} \tag{4.28a}$$

$$\sigma = \frac{1}{2} \varepsilon_b \rho_b g l_{max} k \tag{4.28b}$$

Here, $k = \left(\frac{1-sin\theta_i}{1+sin\theta_i}\right)$, where θ_i is the internal frictional angle of the biomass particles. As considered in [A7], the pressure correction factor $\gamma = (1 - y_b)h_0/D$ can be assumed the same as the bed aspect ratio corresponding to the bed material, where y_b is the volume fraction of biomass in the bed. Simplification after substituting all the above expressions in Eq. (4.27) yields Eq. (4.29), which relates the maximum thickness of the biomass layer with the particle and flow properties in the bed.

$$\boldsymbol{\frac{2}{D}\mu_w k l_{max}^2 + (1 - \gamma \frac{\rho_s}{\rho_b} \delta_b \varepsilon_s - \frac{\beta}{\varepsilon_b \rho_b g}) l_{max} = \frac{(\rho_g + \varepsilon_s f_{wake} \rho_s)}{\varepsilon_b g \rho_b} G u_b} \tag{4.29}$$

Equation (4.29) has been validated [A7], where by using the relevant correlations in the literature, the bubble properties are evaluated at the bottom part of the layer interfacing with the bed material. At the minimum mixing gas velocity, $l_{max} \approx 0.5 y_b h_0$.

4.1.4 Model for bed voidage in a binary mixture

One major challenge in the prediction of minimum fluidization velocity of a binary mixture of particles is the difficulty in obtaining the appropriate value for the bed voidage. In the article [A8], a model for predicting the bed voidage of a binary mixture at any packing condition is proposed. The approach to developing this semi-analytical model is summarized in this section. The basic assumption underlying the model development is that the smaller particles in the mixture first fill the available space within the larger particles without changing the total volume occupied by their host particles. The excess of the smaller particles then fill the available space above the packed layer of the solid mixture. This assumption leads to introduction of a packing factor since there is a maximum limit to which solids can be packed in a given space.

For a mixture of two solid types with the respective pure component properties α_i, d_{si}, φ_{si} and ρ_{si} (denoting the solids fraction, particle diameter, sphericity and particle density), where i ∈ [S,L] is the index describing the smaller particle size (S) and the larger particle size (L), the packing factor θ is defined as the following.

$$|\theta| = \frac{m_*}{(1-\alpha_L)\rho_{sS}V_0} \tag{4.30}$$

where m_* is the mass of the smaller particles contained in the void space of the larger particles with initial volume V_0. The modulus $|\theta|$ indicates that θ can be negative or positive. When $\theta < 0$, the bed contracts, i.e. the volume of the solid mixture is lower than the sum of the volume of the mixture components. On the other hand, $\theta > 0$ indicates that the bed expands, i.e. the volume of the bed at the given condition is greater than the volume of the bed when it was well mixed. By assuming that each particle of the individual solid type has the same mass, and noting that $\alpha_i + \varepsilon_i = 1$, where ε_i is the void fraction of the corresponding pure component, the packing factor can be expressed as

$$\theta = \left(1 - \frac{\varepsilon_L - \alpha_*}{\varepsilon_L}\right)\left(\frac{d_{sS}}{d_{sL}}\right) \tag{4.31}$$

Based on the assumption underlying the packing factor, it follows that $m_* = 0$ when $d_{sS}/d_{sL} = 1$. This means that the term $(\varepsilon_L - \alpha_*)/\varepsilon_L$ must be a function of d_{sS}/d_{sL} for this condition to be always true in Eq. (4.31). Hence, Eq. (4.31) can be re-expressed as

$$\theta = \left(1 - \left(\frac{d_{sS}}{d_{sL}}\right)^{\beta x_S}\right)\left(\frac{d_{sS}}{d_{sL}}\right) \tag{4.32}$$

Here, x_S is the mass fraction of the smaller particles in the mixture and β is the interaction parameter between the two particle types in the bed. For a contracting bed, $\beta < 0$ wheares $\beta > 0$ when the bed expands. From analysis of a set of data in literature, the particle interaction parameter can be obtained from

$$\beta = 0.623\left(\frac{d_{sS}\rho_{sS}}{d_{sL}\rho_{sL}}\right)^{-0.61} \tag{4.33}$$

Based on the mass balance, the total mass m of solids in the mixture is expressed as

$$m = (1 - \varepsilon_m)\rho_{sm}(V_0 + \Delta V) \tag{4.34}$$

where ε_m is the mixture voidage, ρ_{sm} the mixture density and ΔV is the volume occupied by the smaller particles above the packing volume of the larger particle as expressed in Eq. (4.35).

$$\Delta V = \frac{m_S - m_*}{\alpha_S \rho_{sS}} \tag{4.35}$$

Combining Eqs. (4.32), (4.34) and (4.35) and noting that $V_0 = m_L/(\alpha_L\rho_{sL})$, the mixture void fraction after simplification can be expressed as in Eq. (4.36), where y_L and y_S are the volume fractions of the large and small particles, respectively.

$$\varepsilon_m = 1 - \frac{\alpha_S}{\left[\left(\alpha_S - (1-\alpha_L)\left(1 - \left(\frac{d_{sS}}{d_{sL}}\right)^{\beta x_S}\right)\left(\frac{d_{sS}}{d_{sL}}\right)\right)\frac{y_L}{\alpha_L} + y_S\right]} \tag{4.36}$$

The performance of Eq. (4.36) is demonstrated in the article [A8]. The application of the void fraction model in the Ergun [26] equation for prediction of the minimum fluidization velocity of a binary mixture is also presented in [A8].

4.1.5 Models for biomass residence time and char accumulation

The data obtained from the setup described in Section 3.2.1 can be correlated for prediction of devolatilization time, char release and heat loss after devolatilization, and the nominal biomass accumulation at a given operating condition in a continuous flow biomass gasification process. To be able to apply the behaviour observed in the current setup to a different system, biomass loading, air flowrate and particle properties need to be properly scaled as described in the article [A9]. Figure 4.4 shows the plots of $\log_{10}(x_b^a t_d)$ and $\log_{10}(x_b^a t_e)$ against the gas velocity ratio $\log_{10}(U_0/U_{mf})$, where x_b is the mass of biomass to mass of sand particles in the bed and $U_0 = \dot{m}_{air}/(\rho_{air}A)$ is the superficial air velocity obtained at the temperature corresponding to the respective time in the bed. The particle minimum fluidization velocity U_{mf} is predicted using the Wen and Yu [62] model. The value of a for each figure is obtained by minimizing the sum of the square error between the fitting line and the experimental data.

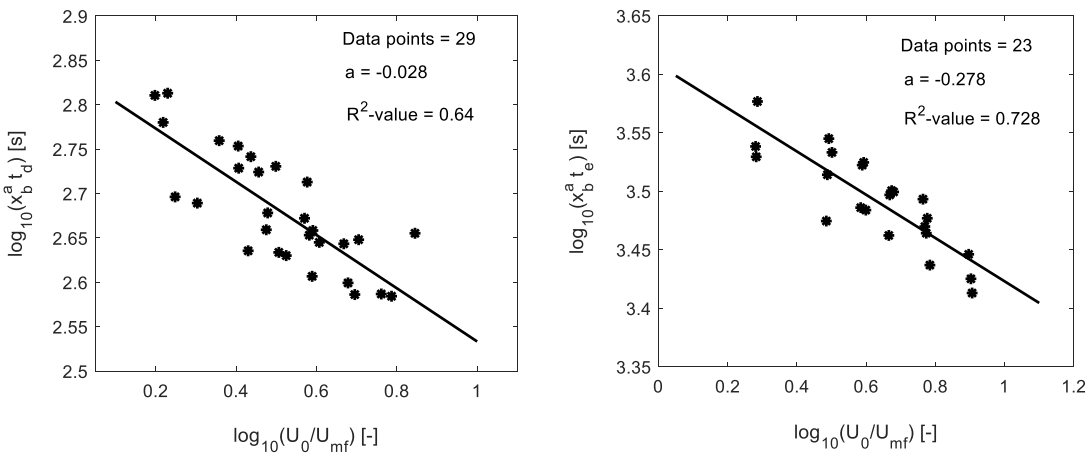

(a) (b)

Figure 4.4. Characteristic residence time for biomass conversion in an air-blown batch bubbling fluidized bed correlated with biomass mass load and air velocity (a) devolatilization (b) extinction.

From the fitting lines, the biomass devolatilization time t_d [min] and extinction time t_e [min] can be modelled by

$$\boldsymbol{t_d = 11.35 x_b^{0.028} \left(\frac{U_0}{U_{mf}}\right)^{-0.3} \pm 7.7\%} \quad (4.37)$$

$$\boldsymbol{t_e = 67.58 x_b^{0.278} \left(\frac{U_0}{U_{mf}}\right)^{-0.185} \pm 7.6\%} \quad (4.38)$$

The amount of char released after devolatilization also increases with decreasing air flowrate and amount of biomass charged in the bed as presented in the article [A9]. Figure 4.5(a) shows how the fraction of the char yield γ_{char} varies with the operating parameters.

From the relationship shown in Figure 4.5(a), γ_{char} can thus be determined from

$$\boldsymbol{\gamma_{char} = 0.414 x_b^{0.245} \left(\frac{U_0}{U_{mf}}\right)^{-0.463} \pm 18\%} \quad (4.39)$$

The change in the bed temperature over the dvolatilization time, which measures the net heat loss during this conversion phase, is also correlated as given in Figure 4.5(b). Based on the fitting line, the devolatilization heat loss $\dot{q}_L$ [K/s] can be expressed as

$$\boldsymbol{\dot{q}_L = 1.664 \left(\frac{U_0}{U_{mf}} x_b\right)^{0.767} \pm 25\%} \quad (4.40)$$

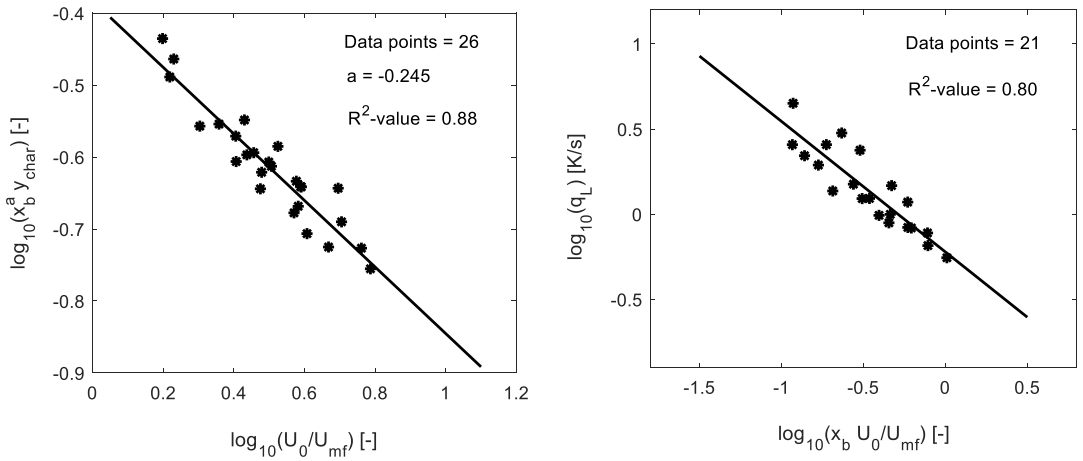

(a) (b)

Figure 4.5. (a) Char yields (b) net heat loss at the end of biomass devolatilization phase in an air-blown batch bubbling fluidized bed correlated with biomass mass load and air velocity.

For application of these equations, (4.37) – (4.40) to a continuous air-blown biomass gasification process in bubbling beds, the extent of the char conversion α at a given air flowrate needs to be defined.

$$\alpha = \frac{t_* - t_d}{t_e - t_d} \tag{4.41}$$

The analysis of the experimental data shows that α lies in the range 0.45 – 0.7, where the mean value of α is 0.55 for the wood pellets and 0.6 for the wood chips. Assuming a plug flow, the amount of biomass x_b supplied over the extinction time t_e at a constant biomass flowrate $\dot{m}_b$ can be obtained from Eq. (4.42) derived from Eq. (4.38).

$$x_b = \left[4055 \frac{\dot{m}_b}{m_p} \left(\frac{U_0}{U_{mf}}\right)^{-0.185}\right]^{1.385} \tag{4.42}$$

where m_p is the mass of the bed material. The amount of char accumulated x_{char} (mass of char to mass of the bed material ratio) in the bed over an extinction cycle can thus be obtained from

$$\boldsymbol{x_{char} = (1 - \alpha)\gamma_{char}(t_e - t_d)\frac{\dot{m}_b}{m_p}} \tag{4.43}$$

Equation (4.43) can be applied for determining the necessary bed properties including the minimum fluidization velocity, bubble properties and bed expansion of the solid mixture at a given operating condition. For decongesting the bed to avoid pressure build-up, the solids circulation rate $\dot{m}_{sc}$ can also be derived from this equation as given below.

$$\boldsymbol{\dot{m}_{sc} = \frac{m_p}{(1-\alpha)(t_e - t_d)}(x_{char} + 1)} \tag{4.44}$$

4.2 1D model for bubbling bed reactor

Based on the Euler-Euler modelling approach, a one-dimensional model describing the fluid-particle behaviour in a fluidized bed is presented in Article [A2] as described below.

$$\frac{\partial}{\partial t}(\varepsilon_s \rho_s v) = -\frac{\partial}{\partial z}(\varepsilon_s \rho_s v.v) + \frac{\partial}{\partial z}\left(\mu_{es}\frac{\partial v}{\partial z}\right) - \varepsilon_s \frac{\partial P_g}{\partial z} - \frac{2 f_s \varepsilon_s \rho_s v|v|}{D_h} - \varepsilon_s \rho_s g - \frac{\partial P_s}{\partial z} + \beta_d(u - v) \tag{4.45}$$

$$\frac{\partial}{\partial t}\left(\varepsilon_g \rho_g u\right) = -\frac{\partial}{\partial z}\left(\varepsilon_g \rho_g u.u\right) + \frac{\partial}{\partial z}\left(\mu_{eg}\frac{\partial u}{\partial z}\right) - \varepsilon_g \frac{\partial P_g}{\partial z} - \frac{2 f_g \varepsilon_g \rho_g u|u|}{D_h} - \varepsilon_g \rho_g g + \beta_d(v - u) \tag{4.46}$$

Equations (4.45) and (4.46) respectively describe the particle and fluid momentum balances in a dense fluidized bed where the solids ε_s and fluid ε_g volume fractions are related by

$$\varepsilon_s + \varepsilon_g = 1 \tag{4.47}$$

The propagation of the bed void fraction ε_g along the axis, Eq. (4.48) is derived based on the mass balances of the different phases across a given volume.

$$\alpha_m \frac{\partial \varepsilon_g}{\partial t} + v_m \frac{\partial \varepsilon_g}{\partial z} = \varepsilon_s \varepsilon_g \rho_{rg} \frac{\partial v_r}{\partial z} \quad (4.48)$$

Here, $v_r = v - u$ is the relative velocity between the particle and the fluid, and $\rho_{rg} = \rho_g/\rho_{ref}$ is the reduced gas density. The mixture mass velocity v_m and relative mass fraction α_m are given by

$$v_m = \varepsilon_g \rho_{rg} v + \varepsilon_s u \quad (4.49)$$

$$\alpha_m = \varepsilon_g \rho_{rg} + \varepsilon_s \quad (4.50)$$

The constitutive equations for closing the governing equations are also given in the article [A2]. The hydrodynamic model described above was used to study the bubbling fluidized bed behaviour of an inert bed material. By including the reaction rate terms, the model can also be applied for thermochemical conversion of solid fuel particles in fluidized beds. In this case, some simplifications can be introduced to reduce the complexities in applying the model for bubbling bed reactors. The description and detailed procedure employed in simplifying the model are given in Article [A10].

The proposed thermochemical conversion model is also based on the conservations of mass and momentum in addition to the energy conservation across a given volume in the direction of fluid flow. For simplicity, the model assumes that the net velocity of the inert bed material is zero. The solids fraction of the bed particle due to flow of gas is therefore computed using the correlation in the literature. The fluid flow is modelled based on the Euler approach following the continuum mechanism, but the viscous force and energy transport due to fluid viscous stress are neglected. The fuel particles are assumed dispersed and their motion is tracked by considering the Lagrangian approach. The changes in the kinetic energy of the particle is also incorporated due to possible changes in the particle mass along the bed axis as the reactions proceed.

The assumption that the fuel particles are dispersed helps to eliminate the interactions between the fuel particles in the model. This assumption is reasonable in normal operations where the concentration of the biomass particles is negligible compared to the bed material. On the contrary, Eq. (4.45) is based on the particle bulk density where the particle number density is very high. For this reason, the momentum transfers due to viscous stress and pressure forces on the particles are considered. In the model developed in [A10], these momentum terms are neglected, resulting in a different form of equation presented in the article and by Eq. (4.55). Figure 4.6 describes the

computational volume of the model, and the flow of fluid and particles within and across the reactor. All the symbols are as described in the article [A10].

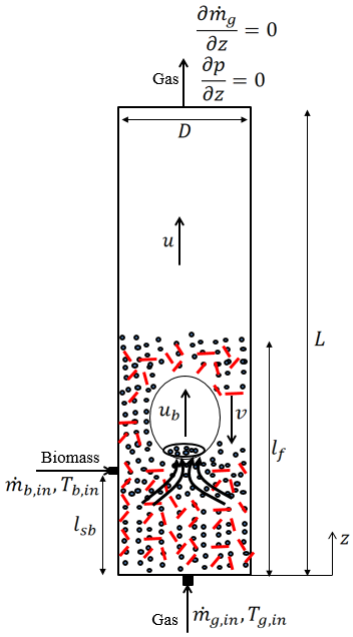

Figure 4.6. Schematic Illustration of a bubbling fluidized bed behaviour in a binary solid mixture (red = biomass, black = bed material), showing biomass and gas boundary conditions and drag of solids into bubble wakes.

It should be noted that the zero pressure gradient ($\partial p/\partial z = 0$) implies that the gauge pressure, $p - p_{\mathrm{atm}} = 0$ at the outlet boundary. Based on this, the pressure outlet boundary condition specified in Figure 4.6 is the same as that given in Article [A2] under the atmospheric bubbling fluidized bed condition. For the simplified model, most of the assumptions introduced are highlighted below.

- There are no variations of temperature and species in the radial directions. Hence, the model is one-dimensional, i.e. there are only gradients in the axial direction.
- The bed expands uniformly, resulting in an even distribution of the bed material particles. With this assumption, the complex computation of mass flow of the particles is eliminated while the average solids fraction of the material is obtained from the available empirical correlations.
- The bed material remains inert over a clearly defined volume, and there is no mass loss due to elutriation. Hence, the net velocity of the particles is considered zero over one cycle of the solids circulation.
- The ash content of biomass is negligible.
- The unconverted tar is in vapour phase.

- The gas species move upwards while the fuel solids move downwards.
- The solid fuel particles are dispersed and the motion of each particle is independent of the others.
- The mass distribution of both gas and solid phases are continuum.
- The properties of biomass and char particles are constant.
- The momentum change of the bed particles as they are dragged into the bubble wake is transferred to the biomass particles.
- The fluid pressure drop over the bed is hydrostatic.
- The amount of fuel particles in the bed is relatively small compared to the bed material, hence does not influence the solid mixture density.
- The gas behaviour follows the ideal gas law.
- The contact and radiation heat exchanges between the fuel particles and the reactor walls are negligible.
- The gas and reactor walls are in thermal equilibrium.

Based on the outlined assumptions, the proposed model for thermochemical conversions in a bubbling bed is therefore given as follows.

4.2.1 Species mass balance

The rate of change of solid concentration $\bar{\rho}_{s,j}$ in the reactor, where $S_{s,j}$ is the rate of generation of the species and j ∈ (b, c) denotes biomass (b) and char (c), is given by

$$\frac{\partial \bar{\rho}_{s,j}}{\partial t} = -\frac{\partial (v\bar{\rho}_{s,j})}{\partial z} + S_{s,j} \tag{4.51}$$

Similarly, the concentration of each gas species j ∈ (H_2, CO, CO_2, CH_4, H_2O, tar, etc.) is modelled by

$$\frac{\partial \bar{\rho}_{g,j}}{\partial t} = -\frac{\partial (y_j \dot{m}_g'')}{\partial z} + S_{g,j} \tag{4.52}$$

where $\dot{m}_g'' = u\bar{\rho}_g$ is the gas flux and y_j is the mass fraction of the species in the gas mixture defined as

$$y_j = \frac{\bar{\rho}_{g,j}}{\bar{\rho}_g} \tag{4.53}$$

The mass concentration $\bar{\rho}_g$ of the bulk gas is given by

$$\frac{\partial \bar{\rho}_g}{\partial t} = -\frac{\partial (\dot{m}_g'')}{\partial z} + \sum S_{g,j} \tag{4.54}$$

4.2.2 Momentum balance

The velocity v of the solid fuel particles is obtained from the following force balance

$$\rho_s \frac{\partial v}{\partial t} = -2\rho_s v \frac{\partial v}{\partial z} + g\left(\rho_s - \rho_g\right) + \beta_{g,s}(-u - v) + F_b' + \beta_{p,s}(-v) + v\sum S_{s,j} \tag{4.55}$$

with the following expressions

$$\beta_{g,s} = \frac{3}{4d_s}\rho_g c_d |u + v| \tag{4.56}$$

$$d_s = \frac{d_b}{\left[1+\left(1.25\sqrt[3]{n_1 \Psi(1-X_c)}-1\right)y_{s,c}\right]} \tag{4.57}$$

$$\rho_s = \left(\frac{y_{sc}}{\rho_c} + \frac{(1-y_{sc})}{\rho_b}\right)^{-1} \tag{4.58}$$

$$y_{s,c} = \frac{\bar{\rho}_{s,c}}{\bar{\rho}_s};\ \ \bar{\rho}_s = \bar{\rho}_{s,c} + \bar{\rho}_{s,b} \tag{4.59}$$

$$c_d = \frac{24}{Re_s}\left[1 + (8.1716\exp(-4.0655\varphi_s))Re_s^{0.0964+0.5565\varphi_s}\right] + \frac{73.69 Re_s \exp(-5.0748\varphi_s)}{Re_s + 5.378\exp(6.2122\varphi_s)} \tag{4.60}$$

$$Re_s = \frac{\rho_g d_s}{\mu_g}|u + v| \tag{4.61}$$

$$\beta_{p,s} = \frac{3\pi(1+e)\left(\frac{1}{2}+\frac{\mu_c \pi}{8}\right)(1-\varepsilon_f)\left(d_s+d_p\right)^2}{\left(\rho_p d_p^3 + \rho_s d_s^3\right)}\rho_p \bar{\rho}_s g_0 |v| \tag{4.62}$$

$$g_0 = \frac{1}{\varepsilon_f} + \frac{3 d_s d_p}{\varepsilon_f^2 (d_s + d_p)}\left(\frac{\bar{\rho}_s}{\rho_s d_s} + \frac{1-\varepsilon_f}{d_p}\right) \tag{4.63}$$

$$F_b' = -(1 - \varepsilon_{mf})\rho_p \theta_w G_b \frac{\partial u_b}{\partial z} \tag{4.64}$$

Here, φ_s is the mean sphericity of the fuel particles, e the coefficient of restitution between the bed and fuel particles, μ_c the Coulomb friction coefficient and g_0 the radial distribution function.

For computation of the gas flux $\dot{m}_g''$ and velocity $u = \dot{m}_g''/\bar{\rho}_g$, the gas momentum equation is described below:

$$\frac{\partial \dot{m}_g''}{\partial t} = -\frac{\partial\left(\dot{m}_g''.u\right)}{\partial z} + g\left[\varepsilon_f\left(1-\varepsilon_f\right)\rho_p - \bar{\rho}_g\right] - \frac{\bar{\rho}_s}{\rho_s}\beta_{g,s}(-u - v) - u\left(\beta_{g,p} - \sum S_{gj}\right) - \varepsilon_f \frac{\partial p}{\partial z} - \frac{2 f_g \bar{\rho}_g}{D} u.|u| \tag{4.65}$$

where

$$\beta_{g,p} = 150\frac{\left(1-\varepsilon_f\right)^2}{\varepsilon_f\left(\varphi_p d_p\right)^2}\mu_g + 1.75\frac{\left(1-\varepsilon_f\right)}{\varphi_p d_p}\rho_g|u| \tag{4.66}$$

$$\rho_g = \frac{\bar{\rho}_g}{\varepsilon_f} \tag{4.67}$$

$$p = \frac{\rho_g R T_g}{M_g} \tag{4.68}$$

$$f_g = \begin{cases} \frac{16}{Re_D}; & Re_D \le 2300 \\ 0.079 Re_D^{-0.25}; & Re_D > 2300 \end{cases} \tag{4.69}$$

$$Re_D = \frac{\rho_g D}{\mu_g}|u| \tag{4.70}$$

4.2.3 Energy balance

To achieve a realistic behaviour of a fluidized bed reactor, the heat exchange within and across the reactor need to be properly accounted for. Considering that the different materials (gas, fuel particles and bed materials) in the reactor as well as the surrounding walls have different capacity to retain and release heat, there will always be temperature differences between the materials. Following the outlined assumptions, the developed models for the fuel particle temperature T_s, the gas temperature T_g and the bed particle temperature T_p are as described below:

$$\bar{\rho}_s \bar{c}_{p,s}\frac{\partial T_s}{\partial t} = -\bar{\rho}_s \bar{c}_{p,s} v\frac{\partial T_s}{\partial z} + \frac{6}{d_s}\left(\frac{\bar{\rho}_s}{\rho_s}\right)\left[h_{g,s}\left(T_g - T_s\right) + \epsilon_s\sigma\left(T_p^4 - T_s^4\right)\right] + h'_{p,s}\left(T_p - T_s\right) - \left(\sum\left(r_i \Delta H^0_{r,i}\right) + r_{pyr}\Delta H^0_{pyr}\right) \tag{4.71}$$

$$\bar{\rho}_g \bar{c}_{p,g}\frac{\partial T_g}{\partial t} = -\bar{\rho}_g \bar{c}_{p,g} u\frac{\partial T_g}{\partial z} - \frac{6}{d_s}\left(\frac{\bar{\rho}_s}{\rho_s}\right)h_{g,s}\left(T_g - T_s\right) - \frac{6}{\varphi_p d_p}\left(1-\varepsilon_f\right)h_{g,p}\left(T_g - T_p\right) - K_r\sigma\left(T_g^4 - T_p^4\right) - \frac{4}{D}U_a\left(T_g - T_a\right) - \sum\left(r_i \Delta H^0_{ri}\right) \tag{4.72}$$

$$\left(1-\varepsilon_f\right)\rho_p \bar{c}_{p,p}\frac{\partial T_p}{\partial t} = \frac{6}{\varphi_p d_p}\left(1-\varepsilon_f\right)h_{g,p}\left(T_g - T_p\right) - \frac{6}{d_s}\left(\frac{\bar{\rho}_s}{\rho_s}\right)\epsilon_s\sigma\left(T_p^4 - T_s^4\right) - h'_{p,s}\left(T_p - T_s\right) + K_r\sigma\left(T_w^4 - T_p^4\right) \tag{4.73}$$

where

$$h_{g,s} = \frac{\lambda_g}{d_s}\left(2 + 0.6 Re_s^{0.5} Pr^{0.33}\right) \tag{4.74}$$

$$h_{g,p} = \frac{\lambda_g}{d_p}\left[\left(7 - 10\varepsilon_f + 5\varepsilon_f^2\right)\left(1 + 0.7 Re_p^{0.2} Pr^{0.33}\right) + \left(1.33 - 2.4\varepsilon_f + 1.2\varepsilon_f^2\right)Re_p^{0.7} Pr^{0.33}\right] \tag{4.75}$$

$$Re_p = \frac{\rho_g d_p}{\mu_g}|u| \tag{4.76}$$

$$K_r = \frac{4}{D}\left[\frac{1-\epsilon_p}{\epsilon_p(1-\varepsilon_f)^2} + \frac{1}{\epsilon_w}\right]^{-1} \tag{4.77}$$

$$h'_{p,s} = \frac{4.88(1-\varepsilon_f)(d_s+d_p)^2}{d_s^3 d_p^3\left((\rho_s \bar{c}_{p,s}\lambda_s)^{-\frac{1}{2}}+(\rho_p \bar{c}_{p,p}\lambda_p)^{-\frac{1}{2}}\right)}\left(\frac{\bar{\rho}_s}{\rho_s}\right)\left(\frac{m}{E}\right)^{3/5}(dv)^{7/10}\sqrt{8\pi(\emptyset_s+\emptyset_p)} \tag{4.78}$$

and

$$m = \frac{\pi}{6}\left(\frac{\rho_s\rho_p d_s^3 d_p^3}{\rho_s d_s^3+\rho_p d_p^3}\right) \tag{4.79}$$

$$E = \frac{4/3}{\frac{(1-\gamma_s^2)}{G_s}+\frac{(1-\gamma_p^2)}{G_p}} \tag{4.80}$$

$$d = \frac{d_s d_p}{2(d_s+d_p)} \tag{4.81}$$

$$\emptyset_s = \frac{2(u-v_{t,s})^2}{15(1-e)}\left(\frac{d_s}{D}\right)^2 \tag{4.82}$$

$$\emptyset_p = \frac{2(u-v_{t,p})^2}{15(1-e)}\left(\frac{d_p}{D}\right)^2 \tag{4.83}$$

Here, λ_s and $\lambda_p$are the respective thermal conductivity of the fuel particles and the bed material, γ_s and γ_p the respective Poison's ratios, G_s [GPa] and G_p [GPa] the corresponding Young's modulus, and $v_{t,s}$ and $v_{t,p}$ the respective terminal velocities. The particle granular temperatures $\emptyset_s$ and $\emptyset_p$ are obtained in m^2/s^2. The mixing rules applied in predicting the appropriate mixture properties are given in the article [A10].

5 Discussion and Conclusion

This chapter presents the results from gasification of different biomass types using the hot flow setup described in Chapter 3. For the gasification with air, the experimental data are reported. The gasification of the same type of biomass using steam as the gasifying agent is demonstrated based on the 1D model developed in this study. The model has been validated as presented in the article [A10], and thus can be used to study the performance of the gasifier at different operating parameters. This chapter also includes the final conclusions drawn in this thesis and the recommendations for further works.

5.1 Discussion

The yield and quality of the produced gas from a gasification process depend on the amount of biomass relative to the gasifying agent introduced in the reactor. The minimum amount of the gasifying agent, air-fuel ratio ($\mathrm{AF_{min}}$) for air and steam-biomass ratio ($\mathrm{SB_{min}}$) for steam required can be obtained from the stoichiometry of the reactions. Neglecting the sulphur content, the global biomass reactions with oxygen (present in air) and with pure steam can be represented by

$$\text{Air: } CH_nO_m + \frac{1}{2}\left(2+\frac{n}{2}-m\right)O_2 \rightarrow CO_2 + \frac{n}{2}H_2O \tag{5.1}$$

giving

$$AF_{min} = \frac{68.67\left(2+\frac{n}{2}-m\right)}{12+2n+16m} \tag{5.2}$$

$$\text{Steam: } CH_nO_m + (1-m)H_2O \rightarrow CO + \left(1+\frac{n}{2}-m\right)H_2 \tag{5.3}$$

giving

$$SB_{min} = \frac{18(1-m)}{12+2n+16m} \tag{5.4}$$

For a typical wood-based biomass, $AF_{min} \approx 6$ and $SB_{min} \approx 0.55$. When the actual air-fuel ratio $\mathrm{AF}>\mathrm{AF_{min}}$, the process tends towards combustion. For gasification, $\mathrm{AF}<\mathrm{AF_{min}}$, giving the equivalence ratio $\mathrm{ER}\ (=\mathrm{AF}/\mathrm{AF_{min}})<1.0$. On the other hand, the steam gasification gets better when a higher steam-biomass ratio (i.e. $\mathrm{SB}>\mathrm{SB_{min}}$) is used. The effect of these quantities among other parameters on the product gas yield and composition are demonstrated in this section.

5.1.1 Gasification with air

The biomass gasification with air was carried out using the reactor described in Section 3.2. One peculiar feature of the setup is the mode of biomass supply. Biomass is fed through a screw conveyor positioned at about 21 cm above the bed base. For each experimental run, a bed of sand particles was initially formed to a height of 22 cm, resulting in a top biomass feed configuration. The minimum feeding rate at the lowest speed of the conveyor drive in a continuous mode is 10 kg/h based on wood chips. However, this amount of biomass supply rate is too high for the 10 cm id reactor. To achieve the desired feed rate in the process, the screw speed is pulsed at intervals. The longer the pulse rate, the lower the mean biomass feed rate.

Figure 5.1 shows the variation of wood pellets delivered into the reactor with time at different fractions of the conveyor full speed. As shown, the peak mass of biomass delivered increases while the idle (waiting) interval decreases with increasing motor speed.

The mean biomass flowrate corresponding to the motor speeds: 3% and 4% are 2.67 and 3.6 kg/h. With 2% motor speed, the estimated mean biomass flowrate is 1.8 kg/h. Although on average, this range of feed rates is suitable for the reactor, the flow pattern of the fuel particles may have consequences in the product gas yield and quality. Figure 5.2 shows the variations of the bed temperature and the combustible gases in the product stream obtained from the gasifier at 1.8 kg/h wood pellets and 2.6 kg/h air flowrates. The bed temperature varies significantly with time due to the varying biomass flowrate, resulting in the variation of the gas composition. While the mole fraction of H_2 is slightly unaffected, the mole fractions of CO and CH_4 increase with an increase in the temperature. The trends of CO and CH_4 change when the temperature decreases with time. This behaviour may not represent the optimum desired for industrial application, but its potential benefit can still be studied further. For the purpose of this report, the time-averaged values of the gas composition are used to illustrate the effects of particle size and biomass flowrate on the gasifier performance.

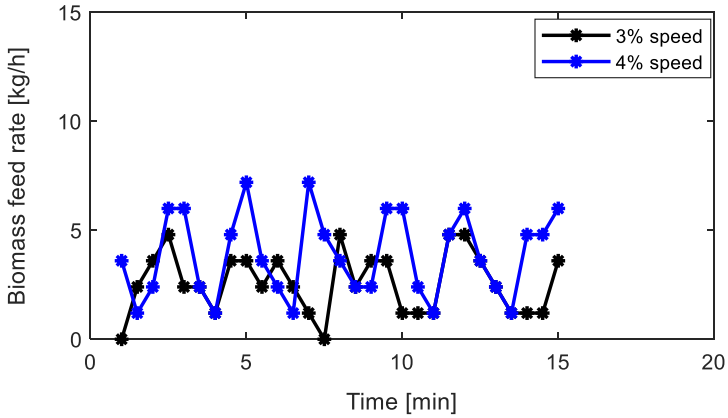

Figure 5.1. Biomass feed rate at different speeds of conveyor drive, showing the effect of ramping of the drive.

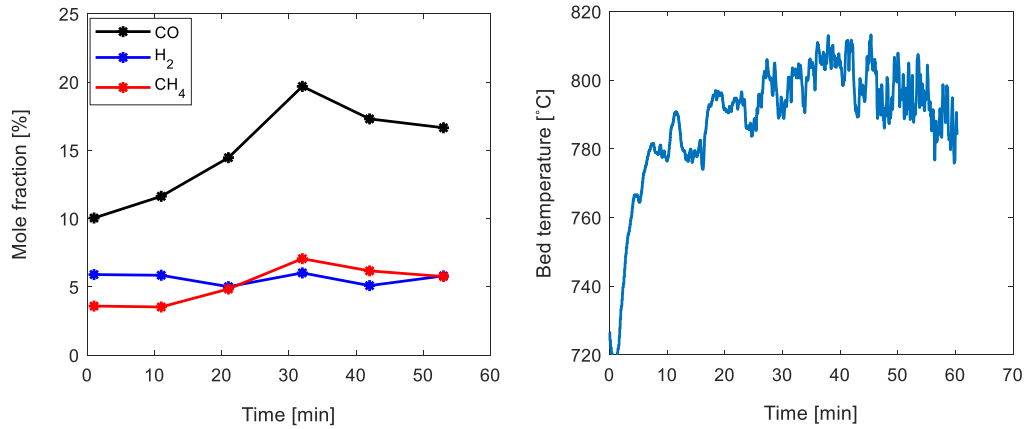

(a) (b)

Figure 5.2. Behaviour of air-blown biomass gasification at 2.6 kg/h air flowrate and 1.8 kg/h biomass mean feed rate with 293 µm sand particles (a) gas composition (b) bed temperature.

Figure 5.3 shows that within the air-fuel ratio 1 – 3, the mole fractions of CO and CH_4 decease while for $AF>1.5$, the amount of H_2 increases to 7.5%. This behaviour may be explained in terms of the oxygen enrichment as the amount of air supply is increased. Increasing the air flowrate at constant biomass flowrate increases the consumption of CO and CH_4 by the partial oxidation. The increase in the temperature due to the partial combustion of the fuel gases and char particles may increase H_2 yields from the devolatilization of the biomass and favourable steam reactions.

Moreover, Figure 5.3(a) shows that changes in the particle size over the range 290 – 620 µm does not affect the H_2 and CH_4 concentrations within $1.5 < AF < 2.5$ but may slightly affect that of CO. With an increase in the biomass flowrate from 2.7 to 3.6 kg/h at the same air-fuel ratio, Figure 5.3(b) shows that the compositions of CO and CH_4 slightly

increase while that of H_2 slightly decreases. This behaviour may be associated with the decrease in the bed temperature due to the flow of larger amount of air and biomass.

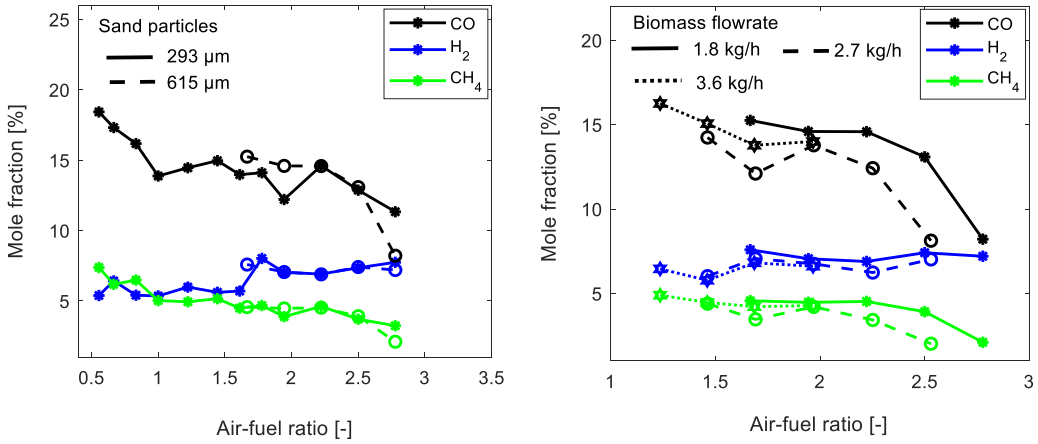

(a) (b)

Figure 5.3. Time-averaged gas composition at different air-fuel ratios, showing (a) effect of particle size with 1.8 kg/h biomass feed rate (b) effect of biomass feed rate with 615 µm sand particles.

5.1.2 Gasification with steam

The 1D unsteady state model described in Section 4.2 was applied to study the effects of different operating parameters on the steam gasification of biomass using the same reactor dimension as described in Figure 3.5. Simulation of the bubbling bed model requires the kinetic rate constants of different conversion phases in the reactor. For the biomass pyrolysis, the parallel kinetic model shown in Figure 5.4 can be applied.

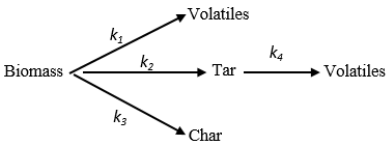

Figure 5.4. Illustration of biomass pyrolysis in parallel steps [63].

The kinetic rate constant, k_i for each stage (i = 1,2,3,4) of the pyrolysis is expressed as follows.

$$k_i = A_i \exp\left(-\frac{E_i}{RT}\right) \tag{5.5}$$

where the respective frequency factor A_i and the activation energy E_i are as given in Chan et al. [64]. The composition of the volatiles released in step 1 is correlated with

temperature as proposed by Gopalakrishnan [65], where j ∈ (H_2, CO, CO_2, CH_4) and the values of the fitting parameters α_j and c_j are listed in Table 5.1.

$$\vartheta_j = \frac{\Lambda_j}{\sum_j \Lambda_j};\ \Lambda_j = c_j T^{\alpha_j} \tag{5.6}$$

The composition γ_j of the tar cracking [64] in step 4 is also given in Table 5.1. The parameters related to the reactor geometry, bed material and biomass properties as well as the different reactions applied in this study for the gasification phase are outlined in Tables 5.2 - 5.4.

Table 5.1. Composition of tar and parameters correlating the yields of volatiles with temperature during biomass pyrolysis [64, 65].

Gas species, j	c_j	α_j	γ_j
H_2	1.34×10^{-16}	5.73	0.02
CO	1.80×10^{7}	-1.87	0.56
CO_2	2.48×10^{3}	-0.70	0.11
CH_4	4.43×10^{5}	-1.50	0.09
Inert tar	-	-	0.22

Table 5.2. Parameters related to the model heat and momentum exchanges.

Parameters		Units
Heat transfer coefficient, U_a	0.018	W/m^2.K
Ambient temperature, T_a	27	˚C
Wall emissivity, ϵ_w	0.13	-
Thermal conductivity, (λ_s, λ_P)	(0.25, 0.26)	W/m.K
Young's modulus, (G_s, G_P)	(36.5, 50.0)	GPa
Poison's ratios, (γ_s, γ_p)	(0.425, 0.25)	-
Emissivity, (ϵ_S, ϵ_p)	(0.95, 0.76)	-
Collision parameters, (e, μ_c)	(0.9, 0.62)	-

Table 5.3. Different reaction routes and rate constants in steam biomass gasification.

i	Reactions	ΔH_{ri}^{0} [kJ/mol]	Rate constant, r_i [mol/m^3.s]	Ref.
			Heterogeneous	
1	C+H_2O → CO+H_2	+131	$r_1 = \frac{k_{r1,1}x_{H_2O}}{1/p + k_{r1,2}x_{H_2} + k_{r1,3}x_{H_2O}}(1 - X_c)[C]$ $k_{r1,1} = 1.25\text{x}10^5 \exp\left(-\frac{28000}{T}\right)$ $k_{r1,2} = 3.26\text{x}10^{-4}$ $k_{r1,3} = 0.313 \exp\left(-\frac{10120}{T}\right)$	[66]
2	C+CO_2 → 2CO	+172	$r_2 = \frac{k_{r2,1}}{1 + \frac{x_{CO}}{k_{r2,2}x_{CO_2}}}[C]$ $k_{r2,1} = 3.6\text{x}10^5 \exp\left(-\frac{20130}{T}\right)$ $k_{r2,2} = 4.15\text{x}10^3 \exp\left(-\frac{11420}{T}\right)$	[67]
3	C+2H_2 → CH_4	-75	$r_2 = 6.11\text{x}10^{-3} \exp\left(-\frac{80333}{RT}\right)[H_2][C]$	[68]
			Homogeneous	
4	CO+H_2O ↔ CO_2+ H_2	-41	$r_4 = 0.278 \exp\left(-\frac{12560}{RT}\right)\left\{[H_2O][CO] - \frac{[H_2O][CO]}{k_{eq,4}}\right\}$ $k_{eq,4} = 0.022 \exp\left(\frac{34730}{RT}\right)$	[69]
5	CH_4+H_2O → CO+ 3H_2	+206	$r_5 = 312 \exp\left(-\frac{15098}{T}\right)[CH_4]$	[70]

Table 5.4. Parameters related to the reactor geometry and operating conditions.

Parameters	
Reactor diameter, D (m)	0.1
Reactor height, L (m)	1
Biomass feeding position, l_{sb} (m)	0.212
Sand particle diameter, d_p (µm)	200 - 650
Sand particle density, ρ_p (kg/m^3)	2650
Sand void fraction, ε_0 (-)	0.42, 0.46
sphericity, φ_p (-)	0.86, 0.72
Minimum fluidization, ε_{mf} (-)	0.43, 0.46
Biomass size (diameter x length), (mm)	6 x 13.3
Biomass moisture content (wt%)	6.2
Biomass density, ρ_b (kg/m^3)	1139, 423
Char density, ρ_c (kg/m^3)	660, 150
Biomass flowrate, $\dot{m}_{b,in}$ (kg/h)	1.5 – 4.5

In addition to the gas composition, the performance of the gasification process can also be ascertained by using the predicted cold gas yield Y, the overall process efficiency η_{th} and the steam conversion efficiency η_{sc} as expressed in the following equations.

$$Y = \frac{\pi D^2}{4}\frac{(1-x_{\mathrm{H2O}})}{\dot{m}_{b,in}(1-y_{moist})}\left(\frac{T_{std}}{T_g}\right)\left(\frac{\dot{m}_g''}{\bar{\rho}_g}\right) \tag{5.7}$$

$$\eta_{\mathrm{th}} = \frac{\dot{V}_g \sum_i x_i \hat{q}_{Lv,i}}{\dot{m}_{b,in}\bar{q}_{Lv,b}+\dot{m}_{st,in}(h_T-h_{fa})} \tag{5.8}$$

$$\eta_{\mathrm{sc}} = 1 - \frac{x_{\mathrm{H2O}}\left(\frac{\dot{m}_g''}{\bar{\rho}_g}\right)\left(\frac{\pi D^2}{4}\right)}{\left(\frac{\dot{m}_{st,in}}{\rho_{st,in}}\right)+y_{moist}\left(\frac{\dot{m}_{b,in}}{\rho_{moist}}\right)} \tag{5.9}$$

Here, $T_{std} = 273$ K is the standard temperature, y_{moist} is the mass fraction of moisture in the biomass, ρ_{moist} is the density of moisture at the feeding condition, $\rho_{st,in}$ the density of steam at inlet and $\dot{V}_g$ [Nm^3/s] is the volume flowrate of the product gas. $\hat{q}_{Lv,i}$ [J/Nm^3] is the lower calorific value of the individual fuel gas (CO, H2, CH4) in the product, $\bar{q}_{Lv,b}$ [J/kg] is the lower calorific value of the biomass, and h_T and h_{fa} are the enthalpy of steam at the operating temperature and ambient condition, respectively.

The model simulation was configured as described in Article [A10] to simulate the gasification behaviour at different operating parameters. For each case, the simulation was run for 30000 s to ascertain the steady state solution.

To avoid the unrealistic bed expansion predicted by the combination of bubble dimeter and bed expansion models given in Eq. (4.26), the maximum permissible bubble diameter in the bed has to be considered. In reality, bubbles do not grow beyond the bed diameter. As the bubble size approaches the bed diameter, the bed slugs. Depending on the fluid and particle properties, the bubble diameter averaged over the bed height at the transition to the fully-developed slug flow can be equal or less than the bed diameter as presented in [A4, A5]. The maximum bubble diameter ratio $(\bar{d}_b/D)_{max}$ at the transition to the fully-developed slug can be obtained as described below.

$$\left(\frac{\bar{d}_b}{D}\right)_{max} = \min\left(1, \left(\frac{\bar{d}_b}{D}\right)_{bs}\right) \tag{5.10}$$

where $(\bar{d}_b/D)_{bs}$ is the bubble diameter evaluated at the minimum slugging velocity [A5] as given in Eq. (5.11).

$$\left(\frac{\bar{d}_b}{D}\right)_{bs} = 0.848\left(\frac{U_{mf}\varphi^{0.35}c_t^{a_t}}{D}\right)^{0.66}\left(1 - c\left(\varphi^{0.35}c_t^{a_t}\right)^{a-1}\right)^{0.66} \tag{5.11}$$

When $\bar{d}_b/D < (\bar{d}_b/D)_{max}$, the bed expansion Δe is determined as described in Section 4.1.2 using the bubble diameter $\bar{d}_b/D$ evaluated from Eq. (4.8) where applicable. For a fully-developed slugging regime, the value of Δe can be obtained as proposed bellow. Considering that the bed expansion ratio $\Delta e_r = (\Delta e + 1)$ can be expressed as

$$\Delta e_r = \frac{H_f}{H_{mf}} = \left(\frac{H_{max}}{H_{mf}}\right)\left(\frac{H_f}{H_{max}}\right) \tag{5.12}$$

the expansion ratios $\Delta e_{rb} = H_{max}/H_{mf}$ in the bubbling regime is determined by substituting Eq. (5.10) into Eq. (4.26) with the superficial gas velocity, U_0 the same as the minimum slugging velocity, U_{ms}. By following the same approach used in developing

Eq. (4.26), the expansion ratio $\Delta e_{rs} = H_f/H_{max}$ in the slugging region can be derived as given in Eq. (5.13).

$$\Delta e_{rs} = \left[1 - 0.305D^{0.48}\left(U_0 - U_{mf}\right)^{-0.362}\right]^{-1} \tag{5.13}$$

In addition to the method described in the article [A10] for predicting the bed expansion, Eq. (5.12) is also applied in this section to investigate the sensitivity of the proposed reactor model to the bed voidage and expansion. In the following section, the results of the different simulations are presented and analysed. For the results shown in Figures 5.5 – 5.7, the Werther [71] bubble diameter model as given in [A10] is used for the bed expansion while Eq. (5.12) is applied in the subsequent results.

5.1.2.1 Effect of temperature

Figure 5.5(a) shows that the mole fractions of CO and H_2 increase with increasing bed temperature at a fixed supply rate of biomass and steam. The decreasing trends of CO_2 and CH_4 concentrations indicate that both reaction routes 2 and 5 favour the yields of CO and H_2 in the product gas. However, Figure 5.5(b) shows that the H_2/CO and CO_2/CO ratios decrease to minimum values, although at different temperatures. The cold gas yield increases to a maximum value at about 720 ℃. A higher value of H_2/CO ratio indicates a better steam conversion while a lower value of CO_2/CO ratio shows a better conversion of carbon to a useful gaseous fuel. To maximize the gas yield, thereby achieving a better energy efficiency, Figure 5.5(b) shows that a threshold temperature close to the minimum syngas ratio (H_2/CO) can be applied.

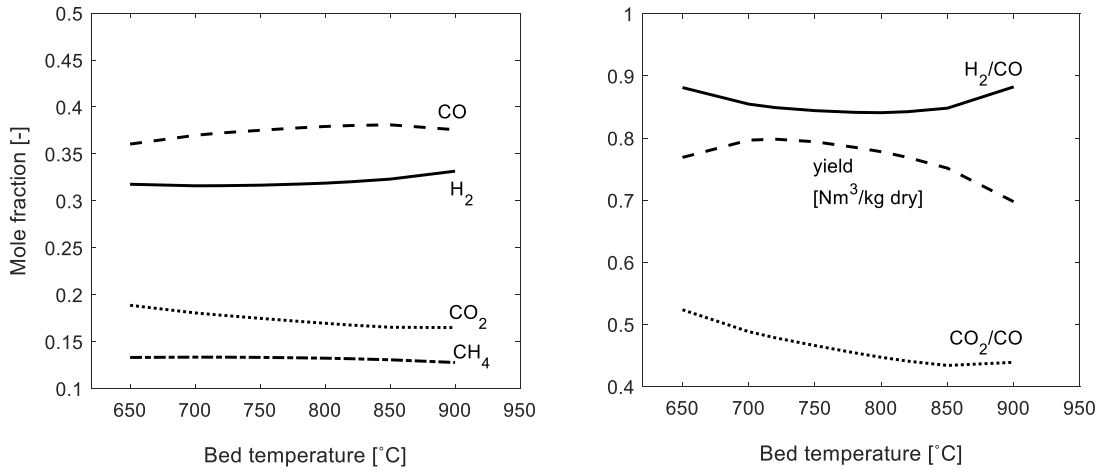

(a) (b)

Figure 5.5. Simulated temperature effect on the steam-biomass gasification behaviour at SB = 0.55, 3.6 kg/h biomass feed and 293 µm sand particles (a) dry gas composition (b) performance indicators.

5.1.2.2 Effect of steam-biomass ratio

Figure 5.6 shows the effect of steam-biomass ratio on the gasification at 800 ℃. Increasing the steam supply rate at a constant biomass feed rate increases the H_2 and CO_2 yields, and decreases those of CO and CH_4 as shown in Figure 5.6(a). With a higher steam flowrate, the water-gas shift (route 4) and steam reforming (route 5) reactions are enhanced, decreasing the mole fractions of CO and CH_4. Figure 5.6(b) shows that both the ratios H_2/CO and CO_2/CO as well as the total gas yield also increase with increasing steam-biomass ratio. The increasing CO_2/CO ratio indicates a shift of carbon to non-combustible species, which reduces the product gas quality.

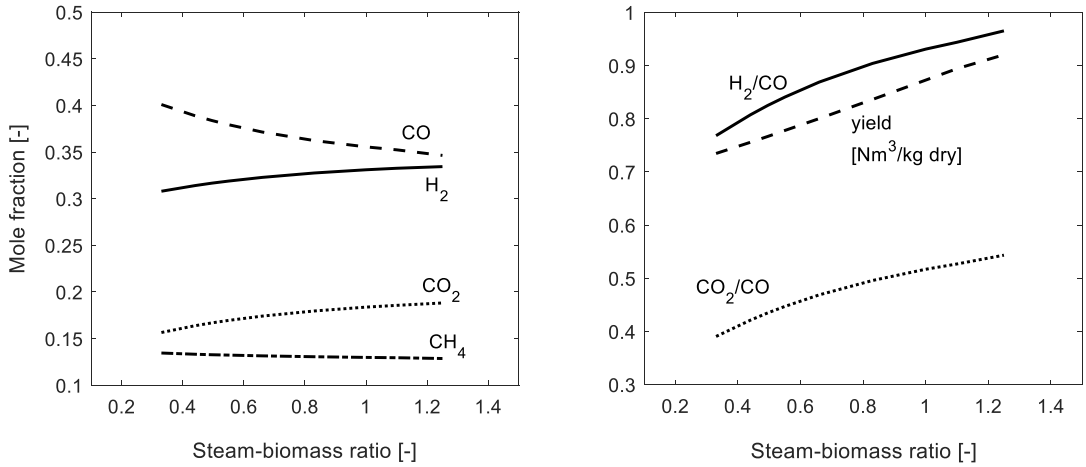

(a) (b)

Figure 5.6. Simulated biomass gasification behaviour at 800℃ for different steam-biomass ratio with 3.6 kg/h biomass feed and 293 µm sand particles (a) dry gas composition (b) performance indicators.

5.1.2.3 Effect of bed material particle size

Similar to the behaviour shown in Figure 5.3(a) for the gasification with air, Figure 5.7 shows that the bed material particle size also has a less significant effect on the gas composition, particularly at the lower particle size, $d_p < 400$ µm. For higher particle sizes, CO and CH_4 slightly decrease while H_2 and CO_2 slightly increase. With increasing particle size, the bed voidage decreases due to poor expansion of the bed, reducing the heat transfer and consequently the char conversion. The homogeneous gas phase reactions are therefore enhanced due to higher steam availability, resulting in the decrease in CO and CH_4 (only in a close watch).

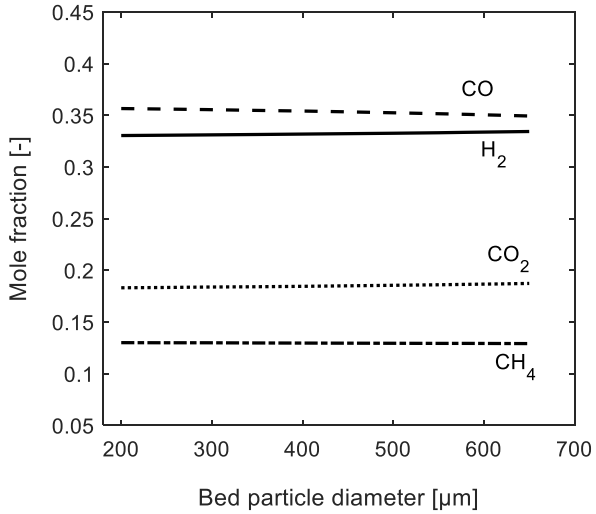

Figure 5.7. Simulated dry gas composition, showing the effect of bed material particle size on the steam-biomass gasification behaviour at 800℃, SB = 1.0 and 3.6 kg/h biomass feed rate.

5.1.2.4 Effect of biomass load

Figure 5.8 shows the gas composition at different biomass flowrates based on the 615 µm sand particles with properties given in Table 3.3. The bed expansion at each steam flowrate was obtained based on the method represented by Eqs. (5.10) – (5.13) contrary to the above results where the bubble diameter used in the expansion model, Eq. (4.26) was predicted based on the Werther [71] model as described in the article [A10]. Figure 5.8(a) shows that there is a significant difference in the model predictions between the two bubble diameter models. While CO and CH_4 are higher, H_2 and CO_2 mole fractions are lower when Eq. (4.8) is used. The two bubble diameter models give different bed expansions, which influence the conversions in the bed. The prediction based on the Werther bubble diameter model gives a value of 0.09 for the bed expansion (corresponding to bed voidage of 0.5) at the gas velocity $U_0/U_{mf} = 4.2$ (or $U_0 - U_{mf} = 0.42$ m/s), which seems too low for the gas velocity comparing with the behaviour observed in the cold flow studies [A6]. Based on Eq. (4.8), the bed is fully expanded at such gas velocity in that there is no physical bubble flow, and hence Eqs. (5.10) – (5.13) are applied for the bed expansion. The bed voidage predicted at the biomass flowrate of 3.6 kg/h is 0.6, which is reasonable considering the gas velocity.

In addition, Figure 5.8(a) shows that increasing the biomass feed rate below 2.6 kg/h affects the gas composition significantly. At a higher feed rate, the composition becomes more or less constant. However, by closely observing the results in the figure when the biomass feed rate > 2.6 kg/h, it can be seen that the amounts of CO and CH_4 slightly decrease while those of H_2 and CO_2 increase. This can be attributed to the excessive expansion of the bed, which reduces the gas residence time and thus decreasing the

char conversion by the available gasifying gases. As expected, the cold gas volume flowrate increases with increasing biomass feed rate. In the region of full bed expansion, Figure 5.8(b) shows that the gas yield increases approximately linearly as the biomass flow is increased, indicating a constant specific char conversion rate. At this constant char conversion rate, increasing the biomass feed rate greatly increases the char accumulation, which may lead to a reduced bed expansion and eventually to de-fluidization of the bed at a very high biomass flowrate. For example, the char accumulation increases from 0.23 to 1.35 kg/m^3 at the bottom of the bed with the increase in the biomass flowrate from 1.8 to 4.0 kg/h. It should be noted that the effect of this behaviour is not considered in the simulations. The char accumulation effect can be accounted for by incorporating the average properties of the solid species in the bed expansion model as described in Article [A7] while the minimum fluidization velocity of the solid mixture is predicted as described in Article [A8]. By considering this effect, the simulated gas composition and yield may be different from those shown in Figure 5.8.

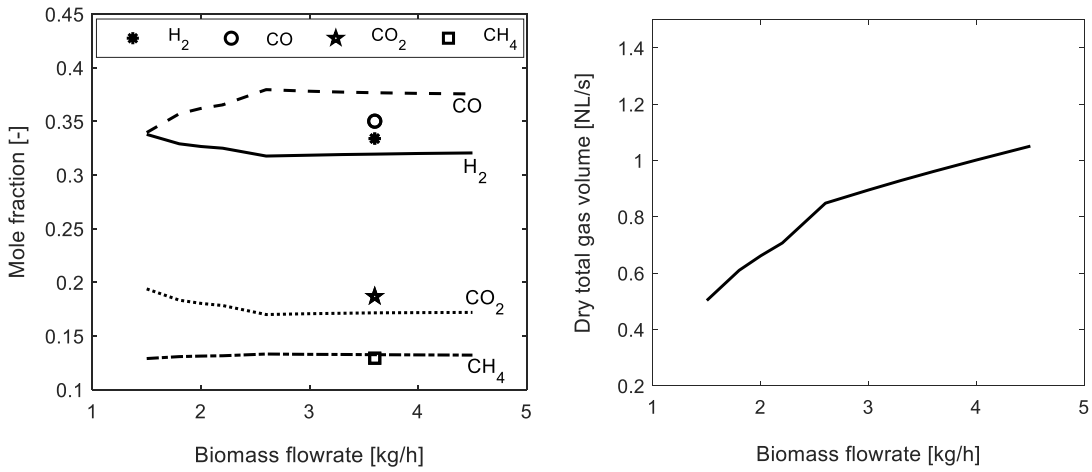

(a) (b)

Figure 5.8. Effect of biomass feeding rate on the gasification behaviour at 800℃, SB = 1.0 and 615 µm sand particles based on model simulations (a) dry gas composition; data points representing behaviour using the Werther [71] model at 3.6 kg/h biomass feed (b) product gas volumetric flowrate.

5.1.2.5 Effect of biomass particle density

The results shown in Figures 5.9 – 5.12 compare the gasification behaviour between two different biomass densities 1139 and 423 kg/m^3 for the same biomass particle size and moisture content. The difference in the two densities influences the heat transfer between the fuel particles and the gas stream as shown in Figure 5.9(a). For the lower biomass density, the particle temperature near the bottom of the bed is lower and the gas temperature in the freeboard is higher compared to those of the higher density. The

variation in the axial temperature can be attributed to the differences in the axial distribution of the fuel particles as shown in Figure 5.9(b). When introduced in the reactor, the 1139 kg/m^3 biomass sinks into the bed while the lower density biomass floats around the feeding position. It should be noted that the flow of biomass to the upper part of the bed is neglected in the simulation since devolatilization occurs very fast at the operating temperature. Figure 5.9(b) also shows that larger amount of char particles accumulates in the bed with lower biomass density, increasing the resistance to heat exchange with the rest of the bed. The lower accumulation of char particles for the higher density biomass indicates a better conversion, which is influenced by the higher availability of different gasifying agents (CO2, H2 and H2O) in the bed as shown in Figure 5.10.

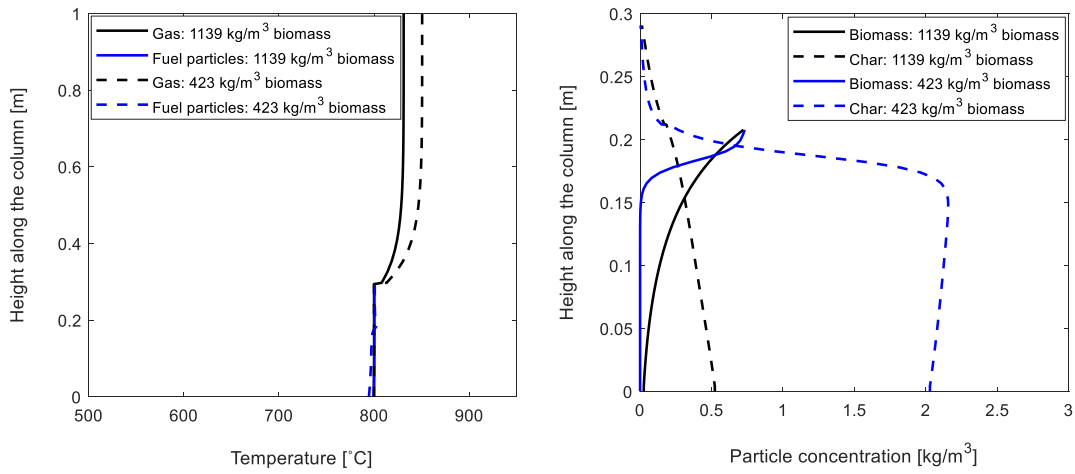

(a) (b)

Figure 5.9. Effect of biomass density on the gasification behaviour at 800℃, SB = 1.0, 2.6 kg/h biomass and 615 µm sand particles (a) simulated axial temperature distribution (b) simulated biomass and char axial distribution.

Figure 5.10 shows that the concentrations of the different gas species in the lower part of the bed are higher for the higher density biomass. With considerable amount of biomass in the bed, the different gas species released during the devolatilization participate actively in the char conversion, increasing the CO and CH_4 yields while decreasing CO_2 and H_2 yields. The water concentration is also lower in the higher density biomass due to the enhanced conversion since the residence time and particle temperature are higher.

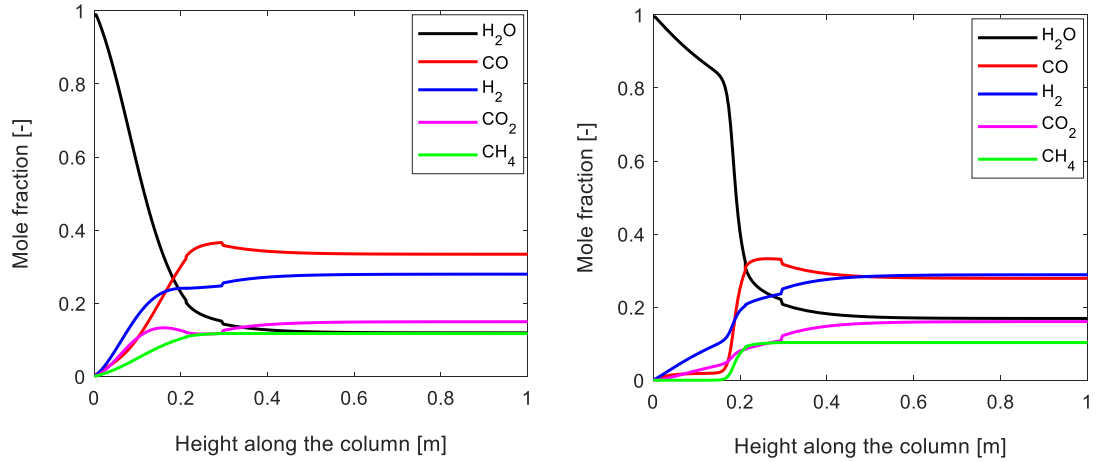

Figure 5.10. Simulated axial distribution of gas composition at 800℃, SB = 1.0, 2.6 kg/h biomass and 615 µm sand particles, showing the effect of biomass density (a) 1139 kg/m^3 biomass (b) 423 kg/m^3 biomass.

Figure 5.11 shows that at increasing bed temperature, CO decreases and CO_2 increases for the biomass with higher density while those of the lower density show opposite trends. The trends of H_2 and CH_4 are the same for both types of biomass, although their values differ significantly. As the temperature increases, the sinking rate of the higher density biomass decreases, reducing the concentration of gases participating in the char conversion. This thus leads to a higher increasing rate of H_2 with temperature. For the lower density biomass, the increase in temperature enhances the reverse water-gas shift, thus decreasing the CO_2 mole fraction and increasing the CO value. The higher temperature in the freeboard also significantly favours the steam reforming reaction, leading to a higher decreasing rate of CH_4 with temperature for the biomass with lower density.

Moreover, the steam conversion efficiency η_{sc} decreases with increasing temperature but increases with increasing biomass density as shown in Figure 5.12. For the overall process efficiency η_{th} (based on biomass with lower calorific value of 18 MJ/kg), the results also show that the composition of CO influences the behaviour. While η_{th} value increases with temperature for the lower density biomass, it decreases for the higher density in the same trend as CO shown in Figure 5.11. The overall efficiency of the denser biomass is considerably higher compared to the lighter biomass due to the higher CO and CH_4 contents of the product gas. This implies that with a higher char conversion, the efficiency of a gasification process is greatly improved. Depending on the downstream application of the product gas, it also follows that a lower gasification temperature is better when the biomass density is high, which indirectly offsets the possible energy

used in densifying the biomass particles. The energy saved in using a lower biomass density in the gasifier will be incurred in using a higher temperature to generate gas with high-energy value. However, for detailed analysis of the process efficiency, the energy flow from the biomass preparation to the final product in the downstream process needs to be considered also.

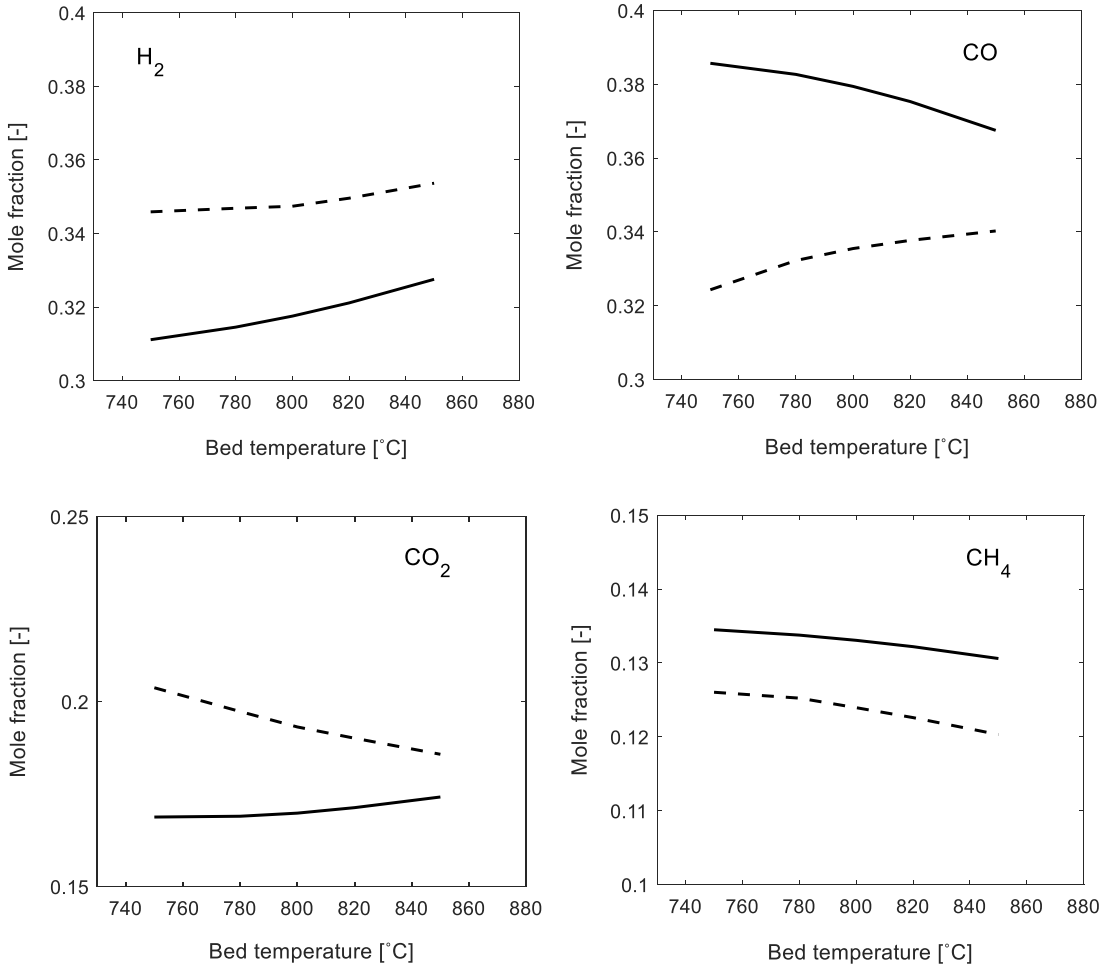

Figure 5.11. Simulated dry gas composition at different temperatures, and SB = 1.0, 2.6 kg/h biomass and 615 µm sand particles, comparing the behaviour with two different biomass densities; solid line = 1139 kg/m^3 biomass; dashed line = 423 kg/m^3 biomass.

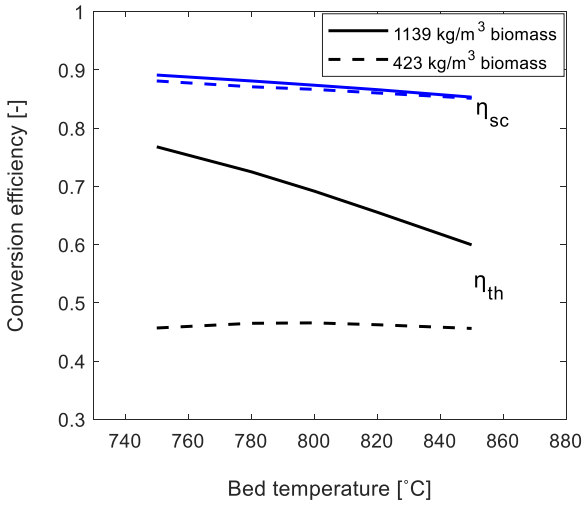

Figure 5.12. Simulated conversion efficiencies at different temperatures, and SB = 1.0, 2.6 kg/h biomass and 615 µm sand particles, comparing the behaviour with two different biomass densities.

5.2 Conclusion and recommendations

This study presented an elaborate analysis of fluidized bed behaviour and the influence on the biomass gasification based on experimental data and model simulations. The bubbling behaviour of bed materials was first investigated using a cold bed setup equipped with two plane ECT sensors. The biomass residence time and char accumulation during conversion in an air-blown bubbling bed were measured using a hot bed reactor of similar dimension as the cold bed rig. The composition of gas produced during the biomass gasification in the reactor at different bed particle sizes, air flowrates and biomass flowrates were measured and analysed. The behaviour of biomass gasification with steam at different operating parameters was investigated using a 1D unsteady state model developed in this study for bubbling fluidized bed reactors. The development of the reactor model was based on the conservation equations of mass, momentum and energy. The gas phase model was based on the continuum mechanism while the fuel particle motion was assumed dispersed. The interactions between the fuel and bed material particles were also considered. The motion of the bed material particles was neglected but the bed voidage at a given gas velocity was accounted for by incorporating the correlation proposed in this study for bed expansion. Other correlations related to the average bed properties at a fluidized state were also proposed.

The findings of this study shows that the hydrodynamic of a bed of particles plays a significant role in the fluidized bed thermochemical conversion of biomass. The shape and size of the bed material particles influence the bed expansion and distribution of

heat and particles, and thus the gasification process. The interaction between the different solid types in the bed also influences the performance of the reactor. Increasing the biomass density, increases the sinking behaviour and the amount of gasifying agents available for effective conversion of char particles near the bottom of the bed. A higher char conversion increases the product gas yield and the process energy efficiency. Moreover, steam gasification of a high-density biomass requires low temperature. Increasing the bed temperature decreases the biomass-sinking rate, thereby reducing the char conversion in the bed due to limited gasifying agents. However, with a low biomass density, increasing the temperature increases the CO and H_2 yields. A gasification using steam or air gives similar trend in the gas composition when the flowrate of the gasifying gas is increased at a fixed biomass supply. While the mole fractions of CO and CH_4 decrease, the concentration of H_2 increases with increasing air-fuel ratio or steam-biomass ratio.

The proposed one-dimensional reactor model has to be validated against the gasification process with air. The behaviour obtained at different operating parameters using the model should be further investigated experimentally. As the model reveals that the bed expansion and bed voidage greatly influence the gasification behaviour, the correlations obtained from the cold bed behaviour should be validated at the elevated temperatures.

The effect of different biomass types and properties should be evaluated. Most of the inert materials used in this study belong to Geldart B group. For wider understanding of the influence of bed hydrodynamics on the gasification, this study should be extended to finer particles, particularly those belonging to group A behaviour. It should be noted that at different temperatures, the fluid-particle behaviour changes between those of different solid classes as noted in the literature. Hence, the behaviour observed in a cold bed for a given particle may differ in the hot environment. Based on this, a systematic approach for scaling up the behaviour from cold to hot bed condition without affecting the bed material type should be investigated.

The mixing and segregation behaviour of biomass particles have been widely studied in cold flow systems. Such behaviour should be investigated in the hot flow to enhance the modelling scheme of a biomass fluidized bed reactor. In this study, a method using the temperature variation measured along the bed axis was introduced. The analysis of this technique needs to be given further attention.

The studies in this thesis did not account for the particle entrainment and tar generation during biomass conversion. As these two variables are very important in determining the quality and efficiency of the conversion, they should be considered in the further work. The energy analysis of a given gasification process should be extended to different

biomass types and gasifying agents. The influence of bed height as well as the biomass feeding position should not be left out in the subsequent studies.

Finally, an attempt should be made to repeat the various experimental studies conducted in this thesis with beds of larger diameter, at least in the range 30 – 50 cm.

References

[1] Rautenbach, C. *An Experimental and Theoretical Study of Dense Fluidized Bed Fluid Dynamics*. PhD Thesis, Telemark University College, 2012.

[2] Thapa, R.K. *Optimization of Flow Behavior in Biomass Gasification Reactor*. PhD Thesis, Telemark University College, 2015.

[3] Agu, C.E.; Hjulstad, A.; Elseth, G.; Lie, B. Algorithm with improved accuracy for real-time measurement of flow rate in open channel systems. *Flow Meas. and Instrum.* 57 (2017) 20.

[4] Berg, C.; Malagalage, A.; Agu, C.E.; Kaasa, G.-O.; Vaagsaether, K.; Lie, B. Model-based drilling fluid flow rate estimation using Venturi flume. *IFAC-PapersOnLine* 48:6 (2015) 171.

[5] Agu, C.E.; Elseth, G.; Lie, B. Simulation of transcritical flow in hydraulic structures. *56th SIMS Conference on Simulation and Modelling, SIMS 2015*, Linkoping, Sweden, 7 – 9 October, 2015.

[6] Saidur, R.; Abdelaziz, E. A.; Demirbas, A.; Hossain, M. S.; Mekhilef, S. A review on biomass as a fuel for boilers. *Renew. Sust. Energ. Rev.* 15 (2011) 2262.

[7] Heidenreich, S.; Foscolo, P. U. New concepts in biomass gasification. *Prog. Energy Combust. Sci*. 46 (2015) 72.

[8] Pan, Y.; Birdsey, R.A.; Phillips, O.L.; Jackson, R.B. The Structure, Distribution, and Biomass of the World's Forests. *Annu. Rev. Ecol. Evol. Syst.* 44 (2013) 593.

[9] Cho, R. Is Biomass Really Renewable? State of the Planet, Earth Institute, Columbia University, October 19, 2016. www.global-greenhouse-warming.com.

[10] Kumar, A.; Jones, D.D; Hanna, M.A. Thermochemical Biomass Gasification: A Review of the Current Status of the Technology. *Energies* 2 (2009) 556.

[11] Parthasarathy, P.; Narayanan, K. S. Hydrogen production from steam gasification of biomass: Influence of process parameters on hydrogen yield – A review. *Renew. Energ.* 66 (2014) 570.

[12] Rapagna`, S.; Jand, N.; Kiennemann, A.; Foscolo, P. U. Steam-gasification of biomass in a fluidised-bed of olivine particles. *Biomass Bioenergy* 19 (2000) 187.

[13] Wabash River Coal Gasification Repowering Project, https://www.netl.doe.gov/research/Coal/energy-systems/gasification/gasifipedia/wabash, retrieved on April 12, 2019.

[14] Basu, P. In *Biomass Gasification and Pyrolysis,* ed. P. Basu, Boston: Academic Press, 2010, pp. 97–116.

[15] Basu, P. *Biomass Gasification and Pyrolysis*, Oxford: Elsevier, 2010.

[16] Martin, H. Wärmeübergang an Wirbelschichten. VDI Wärmeatlas. 10. Auflag, Berlin Heidelberg: Springer-Verlag; 2006. p. 1–9.

[17] Karl, J.; Pröll, T. Steam gasification of biomass in dual fluidized bed gasifiers: A review. *Renew. Sust. Energ. Rev.* 98 (2018) 64.

[18] Wilk, V.; Kitzler, H.; Koppatz, S.; Pfeifer, C.; Hofbauer, H. Gasification of residues and waste wood in a dual fluidised bed steam gasifier. In: Proceedings of the *International Conference on Polygeneration Stategies* (ICPS 10), 2010.

[19] Geldart, D. Types of Gas Fluidization. *Powder Technol.* 7 (1973) 285.

[20] Alberto, C.; Felipe, S.; Rocha, S.C.S. Time series analysis of pressure fluctuation in gas-solid fluidized beds. *Braz. J. Chem. Eng.* 21 (2004) 497.

[21] Kunii, D.; Levenspiel, O. *Fluidization Engineering*, second ed., Butterworth – Heinemann, Washington Street, USA, 1991.

[22] Grace, J. R. Contacting modes and behaviour classification of gas-solid and other two-phase suspensions. *Can. J. Chem. Eng.* 64 (1986) 353.

[23] Karimipour, S.; Pugsley, T. A critical evaluation of literature correlations for predicting bubble size and velocity in gas-solid fluidized beds - A review. *Powder Technol*. 205 (2011) 1.

[24] Lee, S.H.; Lee, D.H.; Kim, S.D. Slug characteristics of polymer particles in a gas-solid fluidized bed. *Korean J. Chem. Eng.* 19 (2002) 351.

[25] Noordergraaf, I.W.; VanDijk, A.; Van Den Bleek, C.M. Fluidization and slugging in large-particle systems. *Powder Technol.* 52 (1987) 59.

[26] Ergun, S. Fluid Flow through Packed Column. *Chem. Eng. Prog.* 48 (1952) 89.

[27] Fotovat F.; Ansart R.; Hemati, M.; Simonin, O.; Chaouki J. Sand-assisted fluidization of large cylindrical and spherical biomass particles: Experiments and simulation. *Chem. Eng. Sci.* 126 (2015) 543.

[28] Cluet, B.; Mauviel, G.; Rogaume, Y.; Authier, O.; Delebarre, A. Segregation of wood particles in a bubbling fluidized bed. *Fuel Process Technol*. 133 (2015) 80.

[29] Salatino, P.; Solimene, R. Mixing and segregation in fluidized bed thermochemical conversion of biomass. *Powder Technol*. 316 (2017) 29.

[30] Baeyens, J.; Geldart, D. Solid mixing in: Gelart, G. (Ed.), *Gas Fluidization Technology*; Willey: New York, 1986, p.97.

[31] Yang, S.C. Density effect on mixing and segregation processes in a vibrated binary granular mixture. *Powder Technol.* 164 (2006) 65.

[32] Ghaly, A.E.; MacDonald, K.N. Mixing patterns and residence time determination in a bubbling fluidized bed system. *Am. J. Engg. & Applied Sci.* 5 (2012) 170.

[33] Mansaray, K.G.; Ghaly, A.E. Physical and thermochemical properties of rice husk. *Energy Sources Part A* 19 (1997) 989.

[34] Kumar, A.; Wang, L.; Dzenis, Y.A.; Jones, D.D.; Hanna, M.A. Thermogravimetric characterization of corn stover as gasification and pyrolysis feedstock. *Biomass Bioenergy.* 32 (2008) 460.

[35] Varhegyi, G.; Antal, M.J.; Jakab, E.; Szabó, P. Kinetic modeling of biomass pyrolysis. *J. Anal. Appl. Pyrolysis* 42 (1997) 73.

[36] Biagini, E.; Barontini, F.; Tognotti, L. Devolatilization of biomass fuels and biomass components studied by TG/FTIR technique. *Ind. Eng. Chem. Res.* 45 (2006) 4486.

[37] Winkler, F. Verfahren zum Herstellen von Wassergas. DE437970; 1922.

[38] Winkler, F. Verfahren zur Herstellung von Wassergas und anderen brennbaren Gasen aus körnigen Brennstoffen. DE487886; 1926.

[39] Rayner, J.W.R. Gasification by the moving-burden technique. *Gas Times* 70 (1952).

[40] Kagayama, M.; Igarashi, M.; Hasegawa, M.; Fukuda, J.; Kunii, D. Gasification of solid waste in dual fluidized-bed reactors. *ACS Symp. Ser. (U S)* 130 (1980).

[41] Hofbauer, H.; Rauch, R.; Bosch, K.; Koch, R.; Aichernig, C. Biomass CHP plant güssing-a success story. In: Bridgwater AV, editor. *Pyrolysis Gasification Biomass Waste*. Newsbury, UK: CPL Press; 2003. p. 371– 383.

[42] Jüntgen, H.; van Heek, K.H. Gasification of Coal with steam using heat from HTRs. *Nucl. Eng. Des*. 34 (1985) 59.

[43] Karl, J.; Schmitz, W.; Hein, D. Allothermal gasification in fluidized bed gasifiers. In: *Proceedings of the Proceedings 10th Engineering Foundation Conference on Fluids*, UEF, New York, 2001.

[44] Hanaoka, T.; Inoue, S.; Uno, S; Ogi, T.; Minowa, T. Effect of woody biomass components on air-steam gasification. *Biomass Bioenergy* 28 (2005) 69.

[45] Brammer, J.G.; Bridgwater, A.V. The influence of feedstock drying on the performance and economics of a biomass gasifier-engine CHP system. *Biomass Bioenergy* 22 (2002) 271.

[46] Wilk, V.; Hofbauer, H. Conversion of mixed plastic wastes in a dual fluidized bed steam gasifier. *Fuel* 107 (2013) 787.

[47] Kuhn, S. Funktions-und Betriebssicherheit eines druckaufgeladenen Wirbelschichtvergasers. Verlag Dr. Hut, 2007.

[48] Lv, P.; Chang, J.; Wang, T.; Fu, Y.; Chen, Y. Hydrogen-rich gas production from biomass catalytic gasification. *Energy Fuels* 18 (2004) 228.

[49] Rapagna, S.; Latif, A. Steam gasification of almond shells in a fluidised bed reactor: The influence of temperature and particle size on product yield and distribution. *Biomass Bioenergy* 12 (1997) 281.

[50] Luo, S.; Xiao, B.; Guo, X.; Hu, Z.; Liu, S.; He, M. Hydrogen-rich gas from catalytic steam gasification of biomass in a fixed bed reactor: Influence of particle size on gasification performance. *Int. J. Hydrogen Energy* 34 (2009) 1260.

[51] Narváez, I.; Orío, A.; Aznar, M.P.; Corella, J. Biomass gasification with air in an atmospheric bubbling fluidized bed. Effects of six operational variables on the quality of the produced raw gas. *Ind. Eng. Chem. Res.* 35 (1996) 2110.

[52] Lv, P.M.; Xiong, Z.H.; Chang, J.; Wu, C.Z.; Chen, Y.; Zhu, J.X. An experimental study on biomass air- steam gasification in a fluidized bed. *Bioresour. Technol.* 95 (2004) 95.

[53] Wang, Y.; Yoshikawa, K.; Namioka, T.; Hashimoto, Y. Performance optimization of two-staged gasification system for woody biomass. *Fuel Process. Technol.* 88 (2007) 243.

[54] Turn, S.; Kinoshita, C.; Zhang, Z.; Ishimura, D.; Zhou, J. An experimental investigation of hydrogen production from biomass gasification. *Int. J. Hydrogen Energy* 23 (1998) 641.

[55] Lucas, C.; Szewczyk, D.; Blasiak, W.; Mochida, S. High-temperature air and steam gasification of densified biofuels. *Biomass Bioenergy* 27 (2004) 563.

[56] van Heek, K.H.; Mühlen, H.-J.; Jüntgen, H. Progress in the kinetics of coal and char gasification. *Chem Eng Technol.* 10 (1987) 411.

[57] Berrueco, C.; Montané, D.; Matas Güell, B.; del Alamo, G. Effect of temperature and dolomite on tar formation during gasification of torrefied biomass in a pressurized fluidized bed. *Energy* 66 (2014) 849.

[58] Pfeifer, C.; Koppatz, S.; Hofbauer, H. Steam gasification of various feedstocks at a dual fluidised bed gasifier: impacts of operation conditions and bed materials. *Biomass-Convers. Biorefinery* 1 (2011) 39.

[59] Mazaheri, N.; Akbarzadeh, A.H.; Madadian, E.; Lefsrud, M. Systematic review of research guidelines for numerical simulation of biomass gasification for bioenergy production. *Energy Convers. Manage.* 183 (2019) 671.

[60] Grace, J.R.; Cliff, R. On the two-phase theory of fluidization. *Chem. Eng. Sci*. 29 (1974) 327.

[61] Rankine, W.J.M. On the stability of loose earth. *Phil. Trans. R. Soc. Lond.* 147 (1857) 145.

[62] Wen, C.Y.; Yu, Y.H. A Generalized Method for Predicting the Minimum Fluidization Velocity. *AIChE J.* 12 (1966) 610.

[63] Shafizadeh, F.; Chin, P.P.S. Thermal deterioration of wood. *ACS Symp. Ser.* 43 (1977) 57.

[64] Chan, W-C. R.; Kelbon, M.; Krieger, B. B. Modelling and experimental verification of physical and chemical processes during pyrolysis of a large biomass particle. *Fuel* 64 (1985) 1505.

[65] Gopalakrishnan, P. *Modelling of biomass steam gasification in a bubbling fluidized bed gasifier*. PhD. Thesis, The University of Canterbury, 2013.

[66] Matsui, I.; Kunii, D.; Furusawa, T. Study of fluidized bed steam gasification of char by thermogravimetrically obtained kinetics. *J. Chem. Eng. Jpn.* 18 (1985) 105.

[67] Braun, R.L.; Mallon, R.G.; Sohn, H.Y. Analysis of Multiple Gas-Solid Reactions during the Gasification of Char in Oil Shale Blocks. In Proceeding, *14th Oil Shale Symposium*, Colorado School of Mines Press, Golden, Colo. 1981, 289.

[68] Babu, B.; Sheth, P. Modeling and simulation of reduction zone of downdraft biomass gasifier: effect of char reactivity factor. *Energy Convers. Manage.* 47 (2006) 2602.

[69] Bıba, V.; Macak, J.; Klose, E.; Malecha, J. Mathematical model for the gasification of coal under pressure. *Ind. Eng. Chem. Process Des. Dev.* 17 (1978) 92.

[70] Zahradnik, R.L.; Grace, R.J. Chemistry and physics of entrained coal gasification. *Ind. Eng. Chem. Proc. Des. Dev.* 126 (1974) 203.

[71] Werther, J. Influence of the bed diameter on the hydrodynamics of gas fluidized beds. *AIChE Symp. Ser.* 70 (1974) 53.

Article 1 (A1)

Determination of onset of bubbling and slugging in a fluidized bed using a dual-plane electrical capacitance tomography system

By

Cornelius Emeka Agu, Lars-André Tokheim, Marianne Eikeland and Britt M.E. Moldestad

Published in

Chemical Engineering Journal 328 (2017) 997 – 1008

Chemical Engineering Journal 328 (2017) 997–1008

Contents lists available at ScienceDirect

Chemical Engineering Journal

journal homepage: www.elsevier.com/locate/cej

Determination of onset of bubbling and slugging in a fluidized bed using a dual-plane electrical capacitance tomography system

Cornelius Emeka Agu *, Lars-André Tokheim, Marianne Eikeland, Britt M.E. Moldestad

Department of Process, Energy and Environmental Technology, University College of Southeast Norway, 3918 Porsgrunn, Norway

HIGHLIGHTS

- Fluidization index decreases with an increasing Archimedes number.
- The bed height for stable slug flow depends on the particle size distributions.
- Both the particle size and the bed height influence the transition from bubbling to slugging.
- The dependency of slug index on the bed height decreases with an increasing Archimedes number.

ARTICLE INFO

Article history:
Received 7 March 2017
Received in revised form 5 July 2017
Accepted 15 July 2017
Available online 18 July 2017

Keywords:
Fluidized bed
Solids fraction
Slugging regime
Bubbling regime

ABSTRACT

For a successful application of fluidized beds in chemical reactions and solids circulation, the boundary of regime of operation such as bubbling and slugging regimes, needs to be clearly defined. This study provides a method for determining the onset of fluidized bed regimes using a two-plane electrical capacitance tomography (ECT) sensor. The method involves computation and analysis of standard deviations of the solids fraction recorded at each plane of the ECT sensor for different superficial gas velocities. The experimental study is based on two different samples of 100–550 μm glass particles and one sample of 150–450 μm limestone particles. The results show that the onset of bubbling is determined when a bubble is first observed in the upper plane. The onset of slugging is obtained at the peak of the difference in the solids fraction fluctuation between the two planes, which is determined at the point where the rates of increase in the fluctuations are the same in both planes. The method developed in this study provides a means of obtaining accurate superficial gas velocities at the onset of slugging in fluidized beds.

1. Introduction

1.1. Background

Application of fluidized beds in processes involving chemical reactions and solids circulation, for example catalyst regeneration or heat transfer, requires a well-defined and stable contact regime [1]. Maintaining the appropriate regime is a major challenge in optimizing the design of fluidized bed reactors due to limited understanding of the dynamics characteristics of fluidized beds [2]. The properties describing the dynamic behaviour of a fluidized bed include the variation of bubble shape, bubble size and solids fraction distribution at different regimes [3].

When a bed is fluidized, it may transit from one flow regime to another depending on the gas velocity. The fluidized bed regimes include bubbling, slugging, turbulent fluidization, fast fluidization and pneumatic conveying regimes [4]. The transition from one regime to another is characterized with a certain superficial gas velocity and a certain bed void fraction. Being able to determine when transition occurs is important for the design of fluidized bed reactors. The most common method to determine the minimum fluidization velocity is by taking measurement of pressure drop in the bed at different superficial gas velocities. The onset of fluidization corresponds to the point where the pressure drop across the bed reaches a maximum value. The minimum fluidization velocity may vary with temperature, pressure or both depending on the properties of the bed [4].

The understanding of transition from the fluidized state to the bubble regime is not as good as that of minimum fluidization [5]. In a bed of larger particles, for example 100–1000 μm, many researchers have observed that bubbles appear as soon as the

* Corresponding author.
E-mail addresses: cornelius.e.agu@usn.no (C.E. Agu), Lars.A.Tokheim@usn.no (L.-A. Tokheim), Marianne.Eikeland@usn.no (M. Eikeland), britt.moldestad@hit.no (B.M.E. Moldestad).

http://dx.doi.org/10.1016/j.cej.2017.07.098
1385-8947/

bed is fluidized. For fine particles such as fluid catalyst cracking particles, the bed expands significantly after the minimum fluidization before bubbles appear. This means that the superficial gas velocity at which bubbling occurs is higher than the minimum fluidization velocity. The difference between the minimum bubbling velocity and the minimum fluidization velocity is attributed to the significant magnitude of inter-particle forces between the fine particles [5].

With further increase in the gas velocity, the bubbles grow in size, and when the bubble size is in the order of the bed diameter, the bed slugs [6–8]. The superficial gas velocity at which a slug appears in the bed is the onset of slugging. The occurrence of slugs depends on the bed aspect ratio defined as the ratio of bed height to bed diameter, and on the particle size. In a large diameter bed, slugs rarely occur because the bubbles will not be able to grow in size up to the bed diameter. When a bed contains fine particles, it will be difficult for it to slug. This is because the stable bubble size in the bed is lower than the bed diameter due to competitive bubble coalescence and bubble splitting [4,5]. Slugs can be in the form of round-nosed structure in beds of materials that can be fluidized easily, or in form of square-nosed structure in difficult-to-fluidize bed materials [9].

The transition between regimes in fluidized beds is accompanied by the solids fraction fluctuation, pressure fluctuation and bed expansion [5]. Different techniques used in fluidized bed studies measure these properties directly or indirectly. Such measurement techniques include pressure transducers, capacitance probes, optical fibre probes, etc. Since different techniques may provide different information about the bed [10], a systematic analysis is required to evaluate the information from the different measurement methods [11]. Among other statistical tools, standard deviation is widely used in analysing the measurement data. The standard deviation can be used to measure the fluctuation of dynamic behaviour of a fluidized bed. In this paper, the fluctuation of the solids fraction is used to determine the behaviour of the fluidized beds. The solids fraction is measured using electrical capacitance tomography (ECT). ECT is a non-intrusive sensor used to measure the relative permittivity between two non-conducting phases. It is non-intrusive as it does not interrupt the flow or bed it measures. In addition to being relatively cheap, fast and flexible to use, ECT can be used in real-time applications, and this makes it more versatile compared to other tomographic methods such as X-ray, γ-ray and ultrasonic tomography [2]. Despite its numerous advantages, the temperature and size of the bed limit its application. In a bed with diameter larger than 30 cm, ECT is not reliable due to the nature of the soft field on which the measurement principle depends [12].

1.2. Previous works

Several studies have been published on different fluidized bed regimes and their transitions. Different techniques employed in identifying a fluidized bed regime are visual detection and analyses of bed property signals such as pressure fluctuation, voidage fluctuation and bed expansion. In a bubbling fluidized bed, the fluctuations arise due to propagation of pressure waves generated during bubble formation, bubble movement, bubble coalescence/splitting and bubble eruption at the surface of the bed [5]. These fluctuations are often analysed in terms of standard deviation, power spectra distribution and probability density function obtained over the measurement period.

The onset of transition from fixed bed to particulate regime (non-bubbling fluidized state) has been widely obtained from the measurement of pressure drops or their fluctuations at different gas velocities [4]. This method has been found to give consistent results independent on the particle size, bed diameter and bed static height. The minimum fluidization velocities have also been obtained from analyses of absolute pressure fluctuation [13–15], and void or solids fraction fluctuation for larger particles [16,17] on the assumption that the minimum fluidization condition coincides with that of bubbling regime.

The transition into bubbling regime is usually visualized as the gas velocity where the first bubble is seen erupting from the bed surface [18]. On the assumption that the fluctuations in fluidized beds are due to bubble formation and passages, different researchers have obtained the onset of bubbling regime at the gas velocity where the pressure [19] or solids fraction [17] fluctuations begins to rise from zero. Leu and Tsai [19] also observed that the minimum bubbling velocity is independent on the bed static height but on the location of the sensors for measurement of the absolute pressure fluctuations.

Slugging fluidized beds have been widely studied due to inconsistencies in the results presented by several authors. Different factors may be responsible for this variation, and these include sensor position during the measurement, variation in the bed diameter, bed height, particle size and particle shape [20]. Broadhurst and Becker [21] used visual detection to identify slugs, where the onset of slugging regime was obtained as the minimum gas velocity at which a bubble is seen to have a continuous floor around the bed circumference before arriving the surface of the bed. This method was shown to produce successful results where the bed height is above twice the bed diameter. Ho et al. [22] measured the minimum slugging velocity at a point where the absolute bubble rise velocity is locally minimum near the transition zone. The bubble rise velocity was obtained from the cross correlation of two different pressure fluctuation signals measured in the bed. In different beds of glass and sand particles, 358 – 1112 μm, Ho et al. found that the minimum slugging velocity is independent on the bed diameter and bed height.

Dimattia et al. [20] used the same technique as Baeyens and Geldart [7] to predict the onset of slugging regime. Baeyens and Geldart [7] identified the flow of slugs in a fluidized bed as either a single slug or a complete slugging. A single slug is observed when the pressure fluctuation spike passes through the datum established at the minimum fluidization condition while complete slugging is obtained when the slug frequency is constant for any change in the gas velocity. For larger particles (diameter above 500 μm), Dimattia et al. [20] observed that the minimum slugging velocity is independent on the bed height due to low resistance to gas flow offered by these particles. In a similar technique, Kong et al. [18] identified a slug flow when a negative amplitude followed by a positive amplitude of the pressure fluctuation crosses a datum line. In their results, Kong et al. concluded that the minimum slugging velocity for fine particles (diameter below 100 μm), is independent on the initial bed height.

Noordergraaf et al. [23] distinguished slugging from bubbling regime by the occurrence of single predominant frequency and a more regular pressure fluctuation pattern. The predominant frequencies are due to passage of single chain of bubbles when the bubble diameter is more than half of the bed diameter. In large particle systems, Noordergraaf et al. obtained the minimum slugging velocity at the point where the curve of predominant frequency versus gas velocity is minimum. For glass particles, 450–540 μm, no predominant frequency was found. The authors concluded that even for fine particles the method will not give results since the pressure fluctuations associated with their fluidization are too small to be sensed by the pressure transducers.

Du et al. [2] used ECT sensors to measure the solids fraction fluctuation at different gas velocities above the minimum bubbling velocity in different beds with diameters: 0.05, 0.1 and 0.3 m and initial bed height 0.5 m. The authors obtained the minimum slugging velocity at the peak of the solids fraction fluctuation. For the

FCC particles, 60 μm, the authors showed that the fluidized bed passes through slugging to the turbulent regime only in the 0.05 m bed. In the larger bed diameters, the system moved from bubbling to turbulent regime, where the onset of turbulent fluidization was obtained at the peak of the solids fraction fluctuation. These results are not in agreement with Baeyens and Geldart [7] observations. Baeyens and Geldart [7] correlated data from different beds: mean particle size ranging from 55 to 3380 μm, particle density in the range of 850 to 2800 and bed diameter in the range of 0.05 to 0.3 m. Their correlation have been widely used for predicting the minimum slugging velocity for different particle properties, bed heights and diameters.

In the bed of 216 μm glass particles (bed height to diameter ratio of 9.8), Bi [5] measured the voidage fluctuation using optical fibre probes. The experiment was conducted to illustrate the transition to turbulent fluidization through slugging regime. Bi [5] noted that the minimum velocity at transition to turbulent flow is obtained at the peak of the voidage fluctuation. Although there is a gradual drop in their results before the peak, the boundary between the bubbling and slugging zones is not clearly marked.

Considering the discrepancies among the results from different literatures, the study of regime transition in fluidized beds is still an ongoing process. In this paper, the method of using information from both planes of a two-plane ECT system for determining the onset of fluidized bed regimes is applied. Finding the actual point at the onset of every regime is vital for a successful fluidized bed application. In systems where the transition is gradual, it may be difficult to determine the exact velocity and void fraction at the onset of the regime. The aim of this paper is to exploit a possible way to combine the information from both planes of the ECT sensor to determine the exact velocities at the onset of slugging.

The study is carried out applying a cold fluidized bed rig using different particle size distributions, bed materials and bed heights. The statistical analysis is based on the standard deviation of the solids fraction, and all the computations are done in MATLAB. The minimum fluidization velocities of the particles used in this study are first obtained from the pressure drop measurement across the bed. This set of values is used to validate the measurements from the ECT sensors. The superficial gas velocities obtained at the onset of fluidization, bubbling and slugging are compared with the values calculated based on the empirical expressions for the respective regimes.

In the remaining parts of this paper, the empirical correlations for prediction of the onset of regime transition in a fluidized bed are presented first, then a description of the experimental setup is given, and finally the results are presented and discussed.

2. Minimum superficial gas velocities at fluidization, bubbling and slugging

In this study, the velocity at the onset of fluidization, referred to as the minimum fluidization velocity is denoted by U_{mf} [m/s]. U_{mf} is obtained by balancing the net weight of the bed with the drag force between the fluid and the particles in the bed.

$$(1-\varepsilon_{mf})(\rho_s-\rho_g)g=\frac{\beta_d U_{mf}}{\varepsilon_{mf}^2} \tag{1}$$

Here, ε_{mf} is the void fraction at minimum fluidization [-], ρ_s is the particle density [kg/m^3], ρ_g is the fluid density [kg/m^3] and g [m/s^2] is the acceleration due to gravity. β_d [kg/(m^3 s)] is the momentum transfer coefficient between the two phases. The accuracy of the U_{mf} calculation depends on the drag model used. A number of drag models have been published in the literature [24–26]. The simpler and more common one is that given by Gidaspow [27]. It was derived from Ergun's equation of pressure drop in fixed beds and is shown in Eq. (2).

$$\beta_d=150\frac{(1-\varepsilon_{mf})^2\mu_g}{\varepsilon_{mf}(\varphi_s d_s)^2}+1.75\frac{\rho_g U_{mf}(1-\varepsilon_{mf})}{\varepsilon_{mf}\varphi_s d_s} \tag{2}$$

Here, μ_g is the fluid dynamic viscosity [Pa.s], d_s the average diameter of the particles [m] and φ_s the particle sphericity [-]. According to Ergun [28], the pressure drop in a fixed bed can be obtained from

$$\frac{\Delta P}{\Delta L}=150\frac{\varepsilon_{s0}^2}{(1-\varepsilon_{s0})^3}\frac{\mu_g U_0}{(\varphi_s d_s)^2}+1.75\frac{\varepsilon_{s0}}{(1-\varepsilon_{s0})^3}\frac{\rho_g U_0^2}{\varphi_s d_s} \tag{3}$$

where $\frac{\Delta P}{\Delta L}$ is the pressured drop per unit length across the bed [Pa/m] and ε_{s0} is the volume fraction of the solid particles in a fixed state [-]. Ergun's model is developed for a dense phase system where the solids concentration is greater than 0.2. The drag model based on the correlation of Gibilaro et al. [29] can be used for the entire range of solids fraction, and may be described as

$$\beta_d=C_d\frac{\varepsilon_{mf}(1-\varepsilon_{mf})}{\varphi_s d_s}\rho_g U_{mf}\varepsilon_{mf}^{-1.80} \tag{4}$$

where C_d is the single particle drag coefficient [-], given by

$$C_d=0.336+\frac{17.3}{Re_{s,mf}} \tag{5}$$

Here, $Re_{s,mf}$ is the modified particle Reynolds number [-] at minimum fluidization conditions, expressed as

$$Re_{s,mf}=\frac{(1-\varepsilon_{mf})}{\varepsilon_{mf}}\frac{\rho_g U_{mf}\varphi_s d_s}{\mu_g} \tag{6}$$

In addition to the momentum transfer coefficient, the void fraction at minimum fluidization is another parameter that determines the accuracy of the U_{mf} calculation. Similar to U_{mf}, ε_{mf} is a bed property, thus its accurate measurement or evaluation is important. ε_{mf} has been observed to strongly depend on the particle sphericity, and according to Wen and Yu [30] its approximate value can be obtained through Eqs. (7) or (8), depending on the particle Reynolds number at minimum fluidization conditions.

$$\varepsilon_{mf}^3=0.091\frac{(1-\varepsilon_{mf})}{\varphi_s^2};\ Re_{mf}<20 \tag{7}$$

$$\varepsilon_{mf}=\left(\frac{0.071}{\varphi_s}\right)^{1/3};\ Re_{mf}>20 \tag{8}$$

The onset of bubbling depends on the particle size. For larger particles, the minimum superficial gas velocity U_{mb} in the bubble regime is about the same as the minimum fluidization velocity [31]. However, with fine particles, Geldart and Abrahamsen [32] found that U_{mb} strongly depends on the fraction of particles smaller than 45 μm that are present in the bed. The ratio $\frac{U_{mb}}{U_{mf}}$ for these types of particles may be expressed as

$$\frac{U_{mb}}{U_{mf}}=\frac{2300\rho_g^{0.13}\mu^{0.52}}{d_s^{0.8}(\rho_s-\rho_g)^{0.93}}\exp(0.72w_{45}), \tag{9}$$

where w_{45} is the weight fraction of particles smaller than 45 μm [-].

Geldart and Abrahamsen [32] also correlated the void fraction at minimum bubbling condition [33] as given by

$$\frac{1-\varepsilon_{mb}}{1-\varepsilon_{mf}}=\left(\frac{U_{mb}}{U_{mf}}\right)^{0.22} \tag{10}$$

where ε_{mb} is the average void fraction of the bed at minimum bubbling condition.

The transition from bubbling to slugging strongly depends on the bed aspect ratio h_0/D_b, where h_0 is the bed height [m] in a fixed state, and D_b is the bed diameter [m]. Yang [34] showed that in addition to ensuring sufficiently high superficial gas velocity, slugging will occur if $h_0/D_b \geqslant 2$. According to Geldart [35], the superficial gas velocity U_{ms} at the onset of slugging can be obtained from

$$U_{ms} = U_{mf} + 0.0016(60D_b^{0.175} - h_{mf})^2 + 0.07(gD_b)^{0.5} \quad (11)$$

where all the length units are in centimetres, and h_{mf} is the bed height at minimum fluidization conditions.

When the bed contains particles of different sizes, the mean particle diameter used in Eqs. (1)–(11) is obtained as given in Eq. (12), which ensures that the total surface area of the particles for the same total bed volume remains the same [4].

$$d_s = \frac{1}{\sum \left(\frac{w_s}{d_s}\right)_i} \quad (12)$$

Here, d_{si} is the diameter of the individual particle having a weight fraction w_{si} in the bed.

3. Experimental

3.1. Experimental setup

The setup used in this work consists of a cylindrical column of diameter 10.4 cm and height 1.4 m. The bottom of the column is fitted with a porous plate and an air supply hose. The porous plate ensures even distribution of air in the bed. The measuring equipment is a dual-plane ECT sensor. The system is shown in Fig. 1. The sensors are located at two different positions, 15.7 cm and 28.7 cm above the distributor. Each sensor consists of 12 electrodes, uniformly distributed around the plane circumference. The cross-section of each sensor is divided into 32 × 32 square pixels, of which 812 pixels lie within the bed as shown in Fig. 1b. Each pixel holds a normalized relative permittivity between 0 and 1. When the sensors are energized by the applied voltage, the capacitance between each pair of electrodes is measured and converted into permittivity values according to the relationship $C = SP$ [36]. Here, C is an M × 1 capacitance matrix with M = 66 (number of inter-electrode pairs), P is an N × 1 relative permittivity matrix with N = 1024 (number of pixels) and S is an M × N sensor sensitivity matrix. The relative permittivity is evaluated based on the Linear Back Projection algorithm [36].

The experiments were performed with limestone and glass particles using compressed air at ambient temperature. These materials were chosen because the difference in their properties gives different behaviour in the fluidized beds. The glass particles may exhibit smooth fluidization, as they are close to spherical in shape and are not adhesive in nature. On the contrary, limestone particles are adhesive and irregular in shape, which may influence fluidization behaviour negatively. In spite of this, limestone may be a good bed material for chemical synthesis due to its catalytic property and ability to withstand high temperature. Using glass particles of different size distributions will also help to investigate the influence of particle size distribution on the fluidized bed regime transition. For each set of particles, the experiments were conducted with three different bed heights: 52, 58 and 64 cm.

Table 1 shows the properties of the bed materials and the range of superficial air velocities used in the experiment. In the experiments, the ECT sensors were first calibrated for the lower permittivity when the column was empty, and then for the higher permittivity value by filling up with the appropriate particles to a height between 50.0 and 64.0 cm which ensured that the upper plane was well covered with the particles. The lower and higher

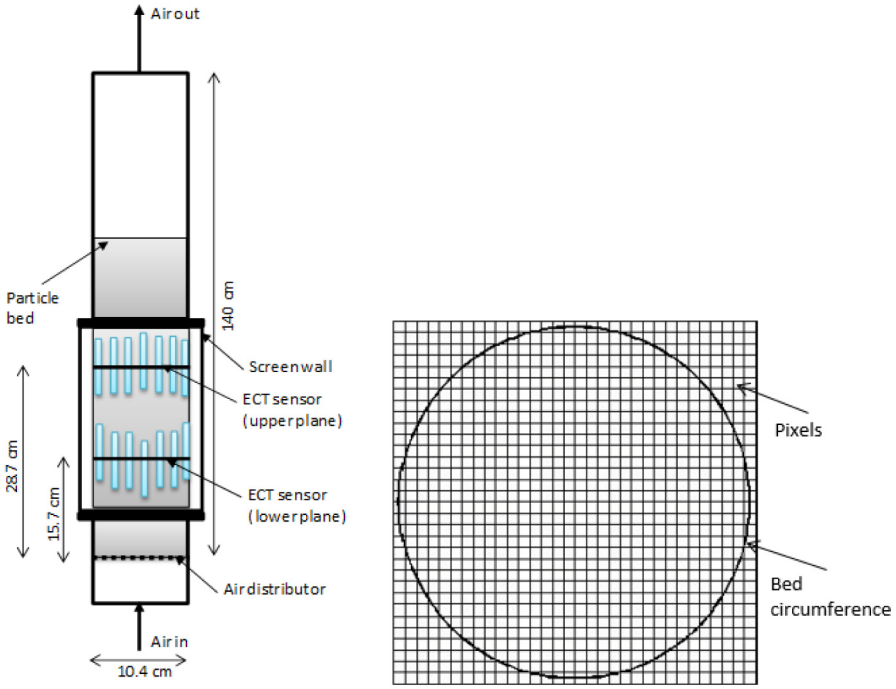

Fig. 1. (a) Schematic illustration of a cold fluidized bed where two plane ECT sensors are used to measure solids fraction. (b) Cross-section of the bed divided into 812 pixels.

Table 1
Bed properties with the associated range of superficial air velocity.

Materials	Material density [kg/m^3]	Particle size [μm]	Mean particle diameter [μm]	Solids fraction in fixed state [-]	Sphericity [-]	Superficial air velocity [m/s]
Glass	2500	100–550	261	0.62	0.96	0.039–0.334
Glass	2500	100–550	188	0.63	0.96	0.010–0.275
Lime stone	2837	150–450	293	0.51	0.84	0.039–0.373

permittivity values defining the range of the measurement are normalized into values 0 and 1, respectively. The normalized relative permittivity ε_r [-] is a measure of volume fraction of solids in the bed. The volume fraction of particles ε_s [-] at any point in the plane is obtained from $\varepsilon_s = \varepsilon_{s0}\varepsilon_r$. The observed value of the fixed bed solids fraction ε_{s0} is given in Table 1.

After the sensor calibration, the air supply line was opened and the superficial air velocity was gradually increased until the full range was covered. For each air velocity, the images of solids distribution at each plane of the ECT sensors were recorded for 60 s. The image data were captured at a frame frequency of 100 Hz, giving 6000 frames over the 60 s. The recorded image data were exported for analysis in MATLAB. To reduce the experimental random error, five different measurements were taken at interval of 2 min for each air velocity. These five data sets were analysed separately, and their average was taken.

3.2. Measurement of solids fraction fluctuation

At a given gas velocity, the solids fraction fluctuation is measured by computing the standard deviation of the plane-average solids fraction over the measurement periods. For each pixel in a given plane, the solids fraction is measured with the ECT sensor as described in 3.1, and then stored in a matrix **A**(i,j,k). The indices, "i" and "j" locate each pixel in a 32 × 32 plane; see Fig. 1b, while the index "k" is the time frame at which the pixel value is obtained. The plane-average solids fraction, ε_{sk} at a given frame is then obtained from

$$\varepsilon_{sk} = \frac{1}{n}\sum_{i}^{32}\sum_{j}^{32} A(\mathrm{i},\mathrm{j},\mathrm{k})$$

Over the entire frames, the time average solids fraction, ε_s at each plane is computed from

$$\varepsilon_s = \frac{1}{N}\sum_{k=1}^{N}\varepsilon_{sk}$$

The standard deviation σ_p of the solids fraction in each plane at a given gas velocity is then computed from

$$\sigma_p = \sqrt{\frac{1}{N-1}\sum_{k=1}^{N}(\varepsilon_{sk}-\varepsilon_s)^2}$$

Here, $n = 812$ is the number of pixels within each plane and $N = 6000$ is the number of frames taken. The subscript "p" denotes upper or lower plane.

4. Results and discussion

First, to determine the minimum fluidization velocity, pressure measurements for the beds of limestone and glass particles with mean size 261 μm were recorded in a separate cold fluidized bed fitted with pressure sensors; see [37] for detailed description of the experimental setup. The results are shown in Fig. 2. The minimum fluidization velocities of limestone and glass particles are 0.157 m/s and 0.095 m/s, respectively.

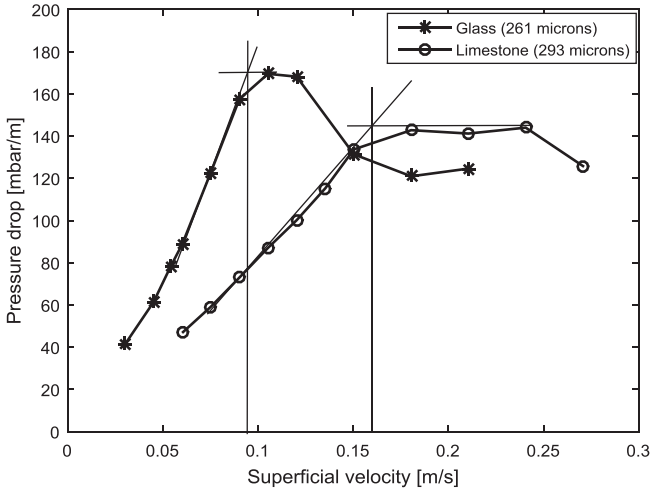

Fig. 2. Pressure drop as a function of the superficial air velocity in beds of lime stone particles (mean diameter 293 μm) and glass particles (mean diameter 261 μm), used to determine the particle minimum fluidization velocity.

Fig. 3 shows the behaviour of the 261 μm glass particles over time at different velocities. The initial bed height was 64.0 cm. The results show that as the air velocity is increased the bed moved from the static state (Fig. 3a) through the bubble regime (Fig. 3b and c) to the slow-rising bubble (or slug) regime (Fig. 3d). Figs. 4 and 5 show that the 188 μm glass particles and limestone particles respectively have the same type of behaviour, but the transitions occur at different velocities. A bubble region in this work is regarded as where the solids fraction is 0.2 or less as indicated in the colorbars.

The superficial air velocity at the onset of each regime can be obtained by analysing the standard deviation of the solids fraction for the range of the superficial gas velocities used. Plots of the standard deviations against the superficial air velocities in both planes are shown in Fig. 6 for the 261 μm glass particles, Fig. 7 for the 188 μm glass particles and Fig. 8 for the limestone particles. The standard error bars are also shown in each of the plots to indicate how the solids fraction fluctuations measured in the five different measurements taken at each air velocity, spread around the mean value reported in this study. As the standard error for each data point is very small, the mean value of the solids fraction fluctuation used in the further analysis, is reliable. The difference in the upper and lower planes standard deviation ($\sigma_{upper} - \sigma_{lower}$) are also shown in the respective figures.

As shown in Figs. 6–8, the solids fraction fluctuations increase rapidly from 0 (zero) due to bubble passage and increase in bubble rise velocity as the gas velocity increases. With increasing gas velocity, the bubbles grow rapidly and increase in size, resulting in the increase in the solids fraction fluctuation. After a certain velocity, the rate of increase in the fluctuations decreases when the bubble approaches a stable size. This region of decreasing rate

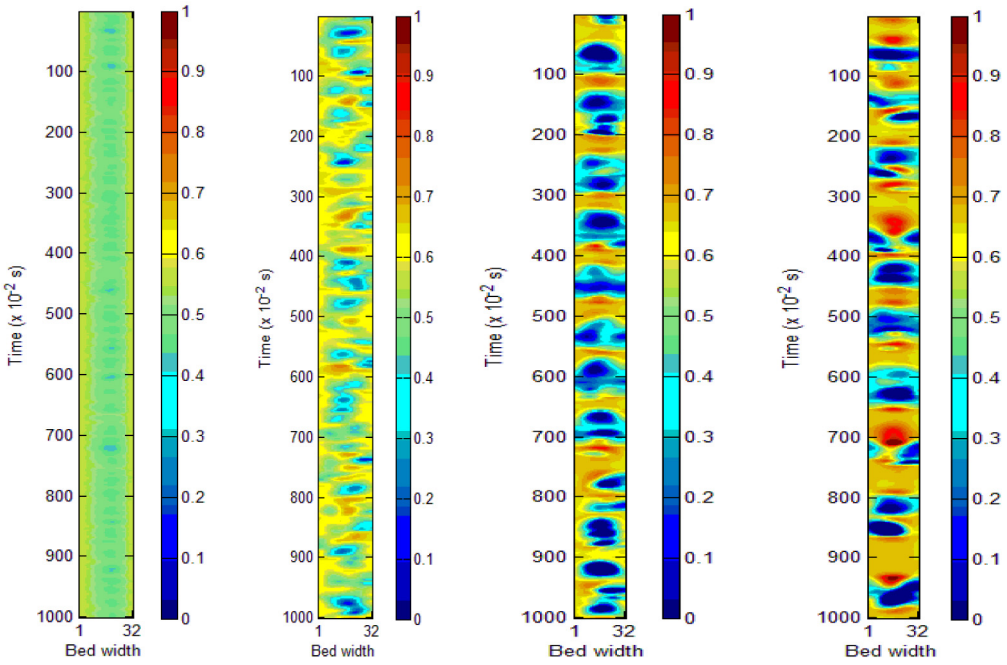

Fig. 3. Images from the upper plane ECT sensor stacked in time for the first – 10 s of the flow in a bed of glass particles (mean diameter 261 μm) at different superficial air velocities (a) 0.088 m/s, no sign of bubble in the plane. (b) 0.098 m/s, bubbles emerge in the plane. (c) 0.137 m/s, bubbles coalesce and become larger in the plane. (d) 0.157 m/s, the frequency of bubble rise decreases as the bubbles become even larger. Bed height is 64.0 cm; time axis increases from top to bottom.

of solids fraction fluctuation in the bed marks the slugging regime. In Fig. 6, for example, the solids fraction fluctuation begins to increase above zero at a velocity of about 0.088 m/s which corresponds to the onset of fluidization shown in Fig. 3a. As there is no sign of bubble in Fig. 3a, it means that the bed was not bubbling at the minimum fluidization velocity. The behaviour shown in Fig. 3 indicates that the velocity at onset of bubbling lies between 0.088 and 0.098 m/s. Similarly, Figs. 7 and 8 show that the beds of 188 μm glass and limestone particles begin to bubble when solids fraction fluctuation are significantly above zero in the upper plane. This shows that there could be factors other than bubble formation and passage responsible for the fluctuations in the fluidized bed. According to Bi [5], this may be due to self-excited oscillation of fluidized particles near the gas distributor.

As there is no clear demarcation between the particulate and bubbling regimes, it is difficult to obtain the minimum bubbling velocity from Figs. 6–8. The onset of bubbling in this study is obtained where a significant bubble is first observed in the upper plane, and these are virtually detected as shown in Figs. 3–5. With further increase in gas velocity, the solids fraction fluctuations in both planes increase. Within a certain range of gas velocity, the increase in the solids fraction fluctuation is almost linear in the upper plane and exponential in the lower plane. When the bubble reaches a stable size (such as that in the slugging) at a higher gas velocity, the rate of increase in the solids fraction fluctuation decreases and then remains constant with further increase in the gas velocity. This can be seen from Figs. 3 and 6. Because $\frac{h_0}{D_b}$ = 6.15 (>2), the decrease in the rate of solids fraction fluctuation indicates a transition from bubbling to slugging. As the change in the rate of increase in the solids fraction fluctuation is gradual especially in the lower plane, it is difficult to determine the exact gas velocity at the onset of slugging from any of the planes.

The patterns of the curve of solids fraction fluctuation σ_{upper} in the upper plane and that σ_{lower} in the lower plane show that even when the rate of increase in σ_{upper} value decreases, the rate of increase in σ_{lower} value still increases. Considering the curve presenting the difference in the standard deviations ("Difference in fluctuation") in each of the Figs. 6, 7 and 8, it can be seen that this curve increases from zero as the gas velocity is raised above the minimum fluidization velocity. The difference in fluctuation $\sigma_{upper} - \sigma_{lower}$ measures the relative change in the rate of increase in the solids fraction fluctuations between the upper and lower planes. The $\sigma_{upper} - \sigma_{lower}$ curve peaks at a certain velocity, where the rate of increase in solids fraction fluctuation in the upper plane equals that in the lower plane. For velocities below the velocity at the peak, the rate of increase in the solids fraction fluctuation in the upper plane is higher than that in the lower plane, indicating that the bed is bubbling. Beyond the peak velocity, the rate of increase in the solids fraction fluctuation in the lower plane is higher than that in the upper plane, indicating that the bed is slugging. The gas velocity at the peak corresponds to the minimum slugging velocity. Because of the uncertainties in identifying the exact point the $\sigma_{upper} - \sigma_{lower}$ curve peaks, this method may be difficult to use in obtaining the onset of slugging velocity.

Fig. 9 shows the rates of increase in the solids fraction fluctuation obtained in both planes for the bed of 261 μm glass particles. The increase in the solids fraction fluctuation rate is obtained from the ratio $\frac{\Delta\sigma}{\Delta U_0}$ [s/m], where the operator Δ indicates a change and U_0 is the superficial gas velocity [m/s]. It can be seen that the $\frac{\Delta\sigma}{\Delta U_0}$ curve

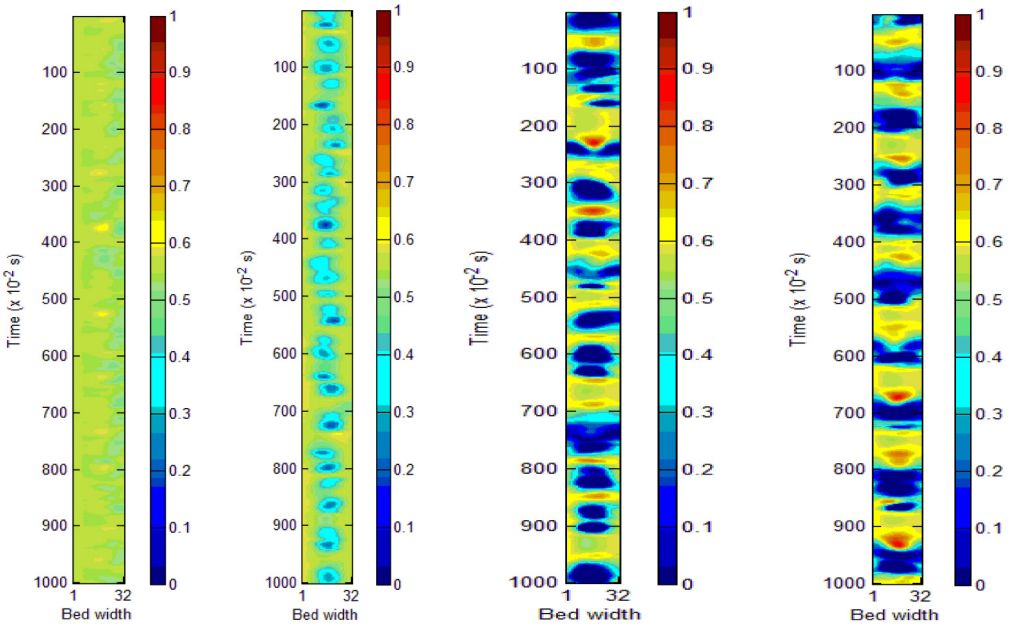

Fig. 4. Images from the upper plane ECT sensor stacked in time for the first – 10 s of the flow in a bed of glass particles (mean diameter 188 μm) at different superficial air velocities (a) 0.039 m/s, no sign of bubble in the plane. (b) 0.049 m/s, bubbles emerge in the plane. (c) 0.128 m/s, bubbles coalesce and become larger in the plane. (d) 0.157 m/s, slugs rise in the plane. Bed height is 52.0 cm; time axis increases from top to bottom.

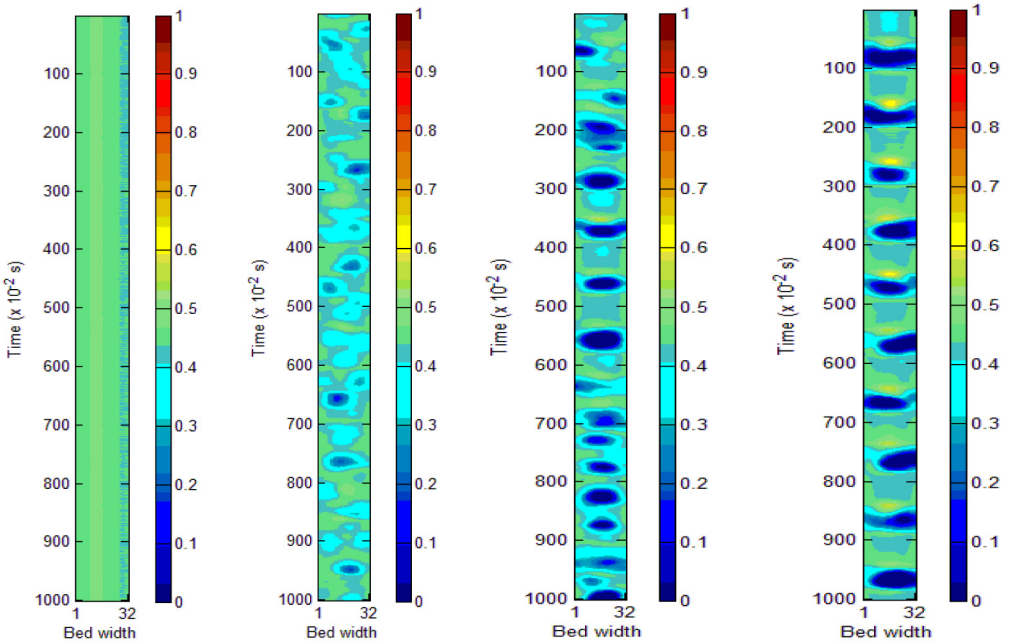

Fig. 5. Images from the upper plane ECT sensor stacked in time for the first – 10 s of the flow in a bed of limestone particles (mean diameter 293 μm) at different superficial air velocities (a) 0.137 m/s, no sign of bubble in the plane. (b) 0.157 m/s, bubbles emerge in the plane. (c) 0.216 m/s, bubbles coalesce and become larger in the plane. (d) 0.235 m/s, the frequency of bubble rise decreases as the bubbles become even larger. Bed height is 52.0 cm; time axis increases from top to bottom.

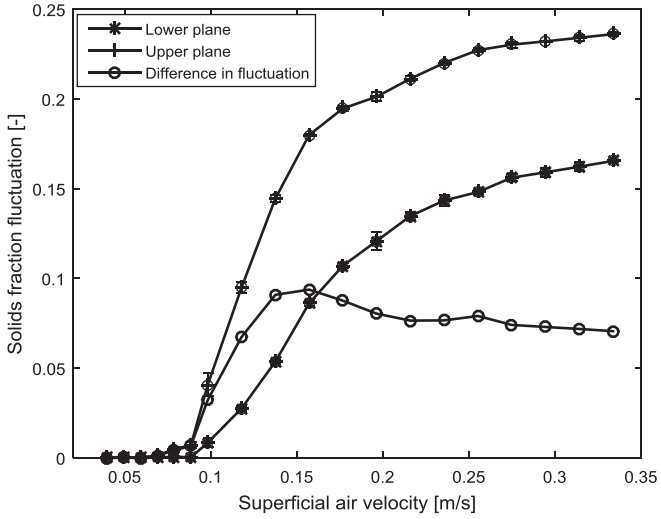

Fig. 6. Solids fraction fluctuation as a function of superficial air velocity in a bed of glass particles (mean diameter 261 μm), showing values for the upper plane, lower plane and their difference.

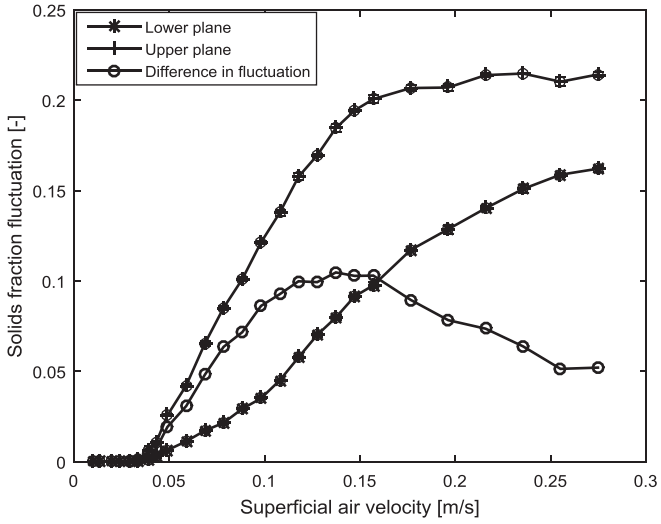

Fig. 7. Solids fraction fluctuation as a function of superficial air velocity in a bed of glass particles (mean diameter 188 μm), showing values for the upper plane, lower plane and their difference.

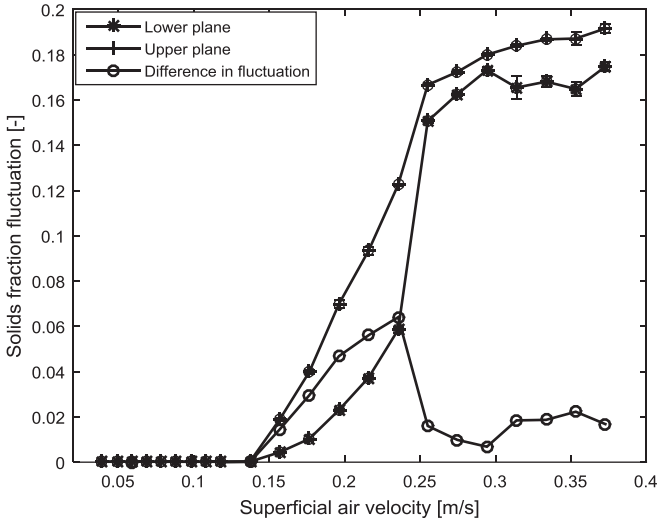

Fig. 8. Solids fraction fluctuation as a function of superficial air velocity in a bed of limestone particles (mean diameter 293 μm), showing values for the upper plane, lower plane and their difference.

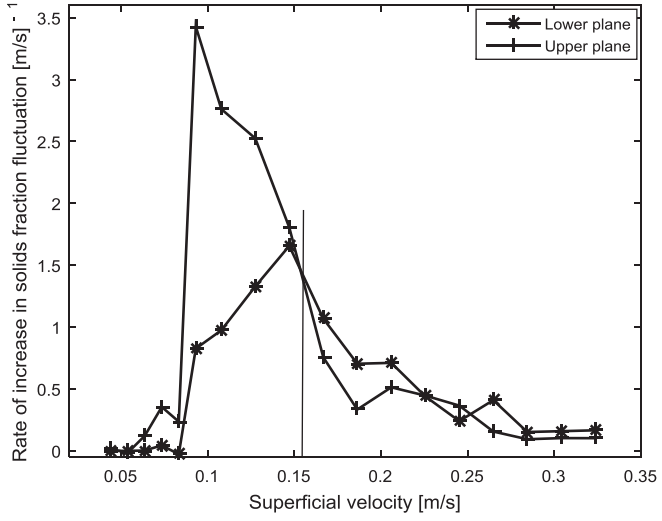

Fig. 9. Rate of solids fraction fluctuation increase as a function of superficial air velocity in a bed of glass particles (mean diameter 261 μm). The vertical line through the point of intersection of the two curves indicates the onset of slugging.

for the upper plane begins to decrease after a velocity of about 0.1 m/s while $\frac{\Delta\sigma}{\Delta U_0}$ curve for the lower plane is still increasing. This gas velocity is below the minimum slugging velocity, thus the bed will still be in bubbling zone. Beyond the point of intersection of both curves, the $\frac{\Delta\sigma}{\Delta U_0}$ values decrease in both planes towards a stable value. The decrease in $\frac{\Delta\sigma}{\Delta U_0}$ values in both planes indicates that the bed is slugging. Similar behaviour are also observed for all the particles studied in this work. The intersection of the $\frac{\Delta\sigma}{\Delta U_0}$ curves indicates the onset of slugging, which can be obtained at that point. This method for identifying the minimum slugging velocity depends on the values of velocity plotted against $\frac{\Delta\sigma}{\Delta U_0}$ values. If the lower value U_{01} in the change $\Delta U_0 = U_{02} - U_{01}$ is used, the corresponding minimum slugging velocity will be lower. A more accurate result is obtained when $\frac{\Delta\sigma}{\Delta U_0}$ is plotted against the average velocity $\frac{1}{2}(U_{02} + U_{01})$.

It should be noted that this approach of finding the onset of slugging is possible because of the sufficient gap between the two planes. As observed during the experiments, the upper part of the bed showed high bubbling activities and signs of slugging earlier than the lower part. This is probably because the location of the upper plane $\frac{L_u}{D_b}$ = 2.76 is greater than 2 (precondition for slugging) while that of the lower plane $\frac{L_l}{D_b}$ = 1.51 is less than 2.

In addition, the results show that the bed of the 261 μm glass particles and that of the 188 μm glass particles show similar flow behaviour. Transitions from fixed state to fluidized state and from bubbling to slugging as shown in Figs. 6 and 7 are smooth, and the bubbles rise closer to the centre than to the wall of the beds, as shown in Figs. 3 and 4. This similarity in behaviour of the particles is due to the same material properties and the same range of particle sizes contained in the different beds, although with different distributions. The flow behaviour of limestone particles is, however, a bit different. Fig. 8 shows that the transitions from one regime to another in the bed of limestone particles are sharp. This can be seen at the onset of fluidization (solids fraction fluctuations suddenly increase above 0) and prior to the onset of slugging

where the $(\sigma_{upper} - \sigma_{lower})$ curve has a pointed peak. Fig. 5 shows that bubbles rise closer to the wall than to the centre.

4.1. Minimum fluidization velocities and fluidization index

The observed minimum fluidization velocities obtained from analysis of the ECT image data are compared with those computed using the drag models given in Eq. (2) and Eq. (4). The particle shape factors used in these computations, i.e. the sphericity (φ_s) values given in Table 1, were derived by fitting Eq. (3) to the experimental data in Fig. 2 for limestone and for the 261 μm glass particles. Since the 188 μm glass particles contain the same range of particles sizes as the 261 μm glass particles, both mixtures are assumed to have the same average particle shape factor.

Fig. 10 compares the experimental minimum fluidization velocities with the computed values. The minimum fluidization velocity is plotted against the particle Archimedes number, expressed as $Ar = \frac{d_s^3 \rho_g (\rho_s - \rho_g) g}{\mu_g^2}$, which compares the net weight of a particle with the internal viscous force due to fluid flow. The result shows that the minimum fluidization velocity increases with the Archimedes number. The upper plot in Fig. 10 shows U_{mf} computed based on the estimated bed void fraction at minimum fluidization conditions using Eqs. (7) and (8). The results show that the inaccuracy in computing the minimum fluidization velocity from both drag models increases as the Archimedes number increases, although the drag model based on Gilbiaro et al. in general gives a better result and is quite close to the experimental data when $Ar <$ 1500. Comparing with the computations using the void fraction obtained in the experiments (as given in Table 1), the lower plot shows that the Gidaspow model gives a better estimation. Fig. 10 shows that the computed U_{mf} are lower than the experimental values with the use of estimated ε_{mf} and higher with the use of experimental values of ε_{mf}. This shows that the value of ε_{mf} that will give a better estimation lies between the estimated and the experimental values. More so, as U_{mf} depends on the effective diameter of the particles, which depends on the particle shape, adjustment of the values of φ_s may improve the estimation.

Variations of the excess velocity to the onset of bubbling, $U_{mb} - U_{mf}$ and that of the fluidization index $\frac{U_{mb}}{U_{mf}}$ with the Archimedes numbers are shown in Fig. 11. From the results, it can be seen that the excess velocity to the onset of bubbling is invariant with the particle size. This explains that most resistance to gas flow is encountered before the minimum fluidization condition, which solely depends on the particle size and density. Once bubbles begin to rise, the particle properties have less influence on the overall behaviour of the bed. The fluidization index, which decreases towards a unity as the Archimedes number increases, measures the degree to which a bed can be expanded uniformly before bubbling. This shows that with an increase in the particles size, the bed may begin to bubble without actually being expanded beyond the height at the minimum fluidization.

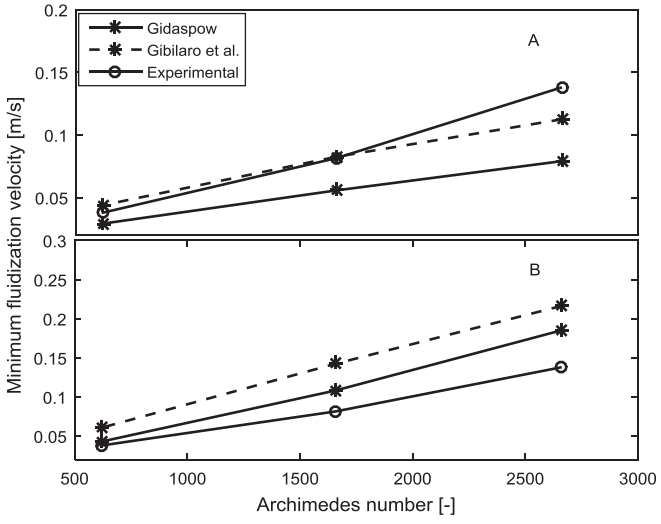

Fig. 10. Minimum fluidization velocity as a function of Archimedes number, comparing the experimental data with the computed values based on two different drag models (Gidaspow and Gilbiaro et al.), applying the estimated void fraction (upper plot, A) and the measured void fraction (lower plot, B) at minimum fluidization conditions.

4.2. Superficial gas velocities at onset of slugging

As described above, the gas velocity at the onset of slugging is obtained at a point where the curve of the rate of increase in the solids fraction fluctuation at the upper plane intersects with that at the lower plane, which may occur at the peak or immediately after the peak of the $(\sigma_{upper} - \sigma_{lower})$ curve. Fig. 12 compares the experimental data with those computed from Eq. (11) at different initial bed heights. The bed height at minimum fluidization conditions used in the computation is obtained from the mass balance, which yields $h_{mf} = \frac{\varepsilon_{s0} h_0}{1 - \varepsilon_{mf}}$. The standard error bars shown in Fig. 12 indicate that the error in determining the onset of slugging by analysing the average of the five measurements (solids fraction) taken at each gas velocity is small. For the three different particles at the three different bed heights, Fig. 12 shows that the experimental data are in good agreement with the computed values. Both results show that the minimum slugging velocity increases with an increase in the particle size. Eq. (11) suggests that U_{ms} decreases with the bed height up to $h_{mf} = 60 D_b^{0.175}$, after which it increases. The value of $60 D_b^{0.175}$ defines the bed height at minimum fluidization conditions for a stable slug flow. As the computed U_{ms} for each particle decreases with the bed height, it follows that the three bed heights are below the height $60 D_b^{0.175}$ (= 90.4 cm) for a stable slug.

Fig. 12 also shows that the variations of computed U_{ms} with h_0 are almost linear, and the lines for the different particles are parallel. However, the experimental results show some degree of scatter which increases with increase in the particle size. This shows that the dependency of minimum slugging velocity on the initial bed height decreases when the particle size increases.

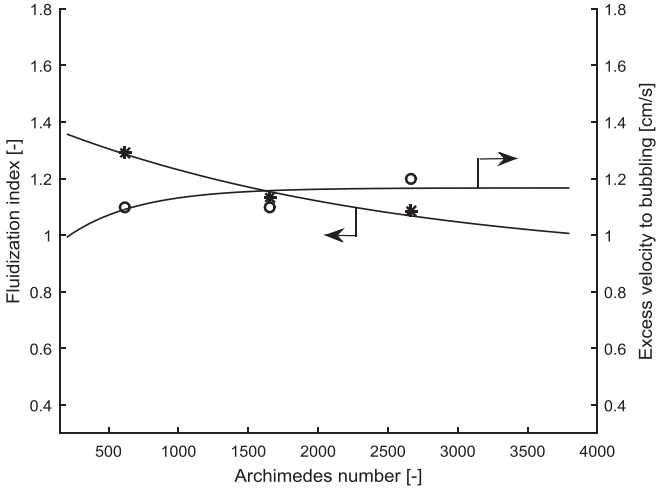

Fig. 11. Influence of particle size on the onset of bubbling, showing excess velocity, $U_{mb} - U_{mf}$ and fluidization index, $\frac{U_{mb}}{U_{mf}}$ as functions of particle Archimedes number. Lines are the data fittings.

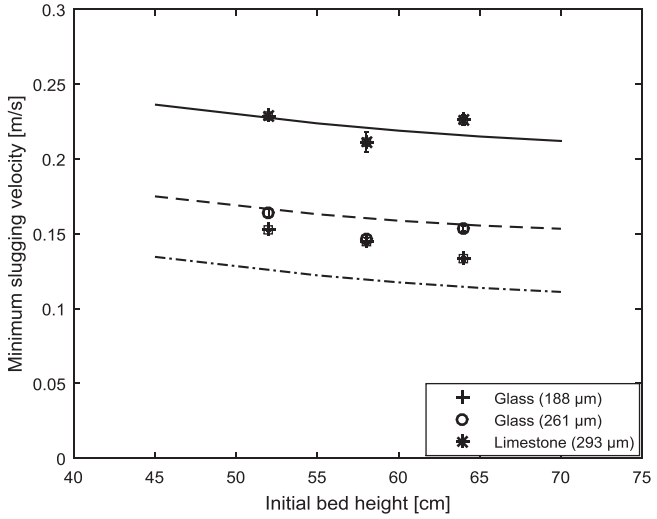

Fig. 12. Minimum superficial gas velocity for slugging as a function of bed height. Lines are the computed values from Eq. (11).

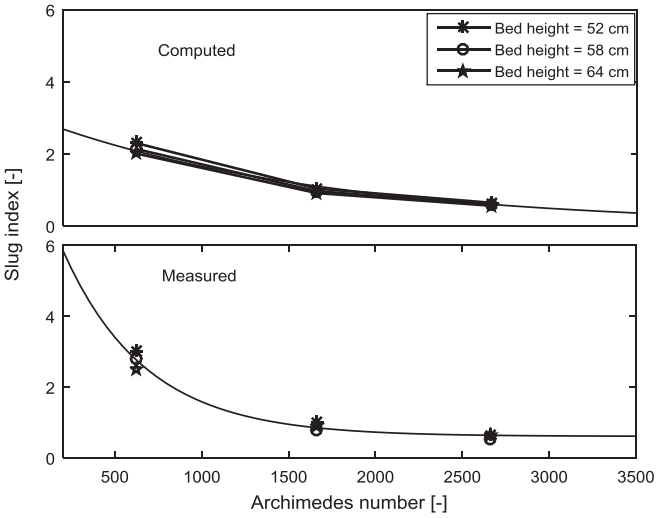

Fig. 13. Slug index, $\frac{U_{ms}-U_{mf}}{U_{mf}}$ as a function of Archimedes number, comparing the computed values (top plot) with the experimental data (bottom plot) at different bed heights. Lines are the data fittings.

The ease of bed slugging can be evaluated from the ratio $\frac{U_{ms}-U_{mf}}{U_{mf}}$, referred to as the slug index. A lower value of the slug index indicates that the bed can easily slug. Fig. 13 compares the computed slug index values with the experimental values at different Archimedes numbers. Both plots show that $\frac{U_{ms}-U_{mf}}{U_{mf}}$ decreases rapidly in the lower range of *Ar* and decreases slightly in the upper range.

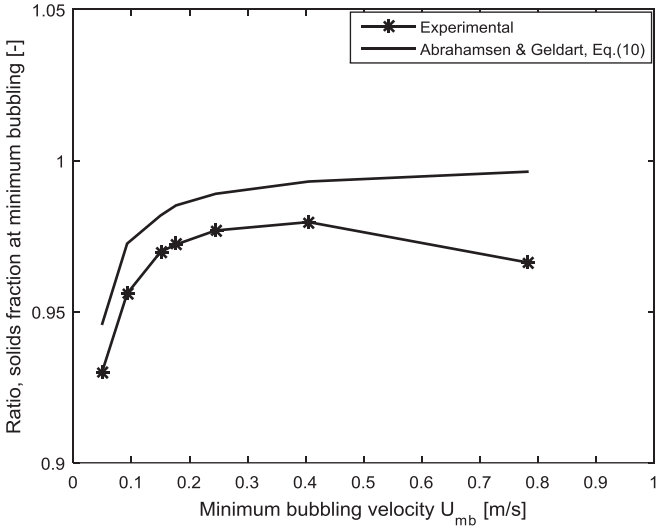

Fig. 14. Bed average solids fraction, $\frac{1-\varepsilon_{mb}}{1-\varepsilon_{mf}}$ at minimum bubbling condition as a function of minimum bubbling velocity, comparing the computed values with the experimental data.

The decrease in the value of the slug index with the Archimedes number shows that a bed of larger particles has a greater tendency to slug than a bed of smaller particles. It can also be seen that the slug index slightly depends on the bed height, and its dependency on the bed height decreases with an increasing Archimedes number. The curve fitting the experimental data suggests that the slug index approaches a stable value (in this case about 0.61) when *Ar* is very large, whereas the fitting of the computed $\frac{U_{ms}-U_{mf}}{U_{mf}}$ values shows that the stable slug index value is about 0.0016.

4.3. Average bed void fraction at onset of bubbling and slugging

At a given gas velocity, the average void fraction, $\varepsilon = 1 - \frac{1}{2}(\varepsilon_{s1} + \varepsilon_{s2})$ is computed for all the particles. The range of particles and bed properties considered in this study are given in Table 2.

Fig. 14 shows the variation of the measured void fraction with the minimum bubbling velocity, U_{mb}. The results show that the measured average solids fraction ratios $\frac{1-\varepsilon_{mb}}{1-\varepsilon_{mf}}$ are in good agreement with the computed values from Eq. (10). As can be seen, the solids fraction ratio increases rapidly at the lower values of U_{mb} and then slightly tends towards a constant value at the higher values of U_{mb}.

Fig. 15 shows how the bed average solids fraction $\frac{1-\varepsilon_{ms}}{1-\varepsilon_{mf}}$ at the onset of slugging varies with the slugging velocity $\frac{U_{ms}}{U_{mf}}$. Since the slug velocity ratio $\frac{U_{ms}}{U_{mf}}$ increases with a decrease in particle size, the result shows that $\frac{1-\varepsilon_{ms}}{1-\varepsilon_{mf}}$ decreases as the particle size increases. The lower value of $\frac{1-\varepsilon_{ms}}{1-\varepsilon_{mf}}$ indicates a relatively higher void at the

Table 2
Properties of fluidized beds at different regimes.

Materials	Mean size [μm]	Density [kg/m^3]	ε_{mf} [-]	ε_{mb} [-]	ε_{ms} [-]	U_{mf} [cm/s]	U_{mb} [cm/s]	U_{ms} [cm/s]
Glass	188	2500	0.430	0.450	0.526	3.80	4.90	14.50
Glass	261	2500	0.450	0.474	0.536	8.15	9.25	14.69
Limestone	293	2837	0.530	0.544	0.620	13.80	15.0	21.16
Sand	483	2650	0.460	0.475	0.565	16.50	17.66	25.82
Glass	624	2500	0.488	0.493	0.570	23.20	24.50	33.80
Limestone	697	2837	0.607	0.616	0.683	39.24	40.50	48.22
Molecular sieve	2170	1300	0.472	0.490	0.607	76.85	78.15	91.57

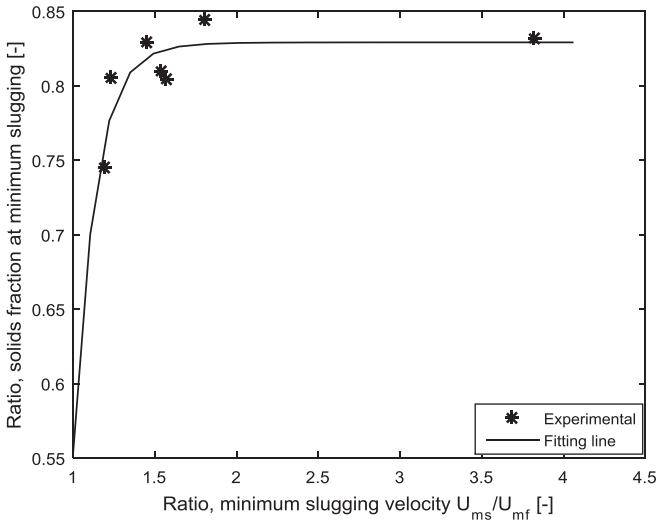

Fig. 15. Bed average solids fraction, $\frac{1-\varepsilon_{ms}}{1-\varepsilon_{mf}}$ at minimum slugging condition as a function of minimum slugging velocity ratio $\frac{U_{ms}}{U_{mf}}$.

onset of slugging compared with that at the minimum fluidization condition. The associated smaller values with larger particles follow the fact that bubbles grow faster and larger in the bed of larger particles. At the onset of slugging, bubble could even be as large as the bed diameter, leading to large void in the bed.

As can be seen, the experimental data can be fitted to a curve over the range of particle size and density considered. The curve fitting the measured solids fraction ratio at the minimum slugging condition is given in Eq. (13). This equation can be used to predict the average value of bed void fraction ε_{ms} at the minimum slugging condition.

$$\frac{1-\varepsilon_{ms}}{1-\varepsilon_{mf}} = \left[1.206 + 0.604\left(\frac{U_{ms}}{U_{mf}}\right)^{-10}\right]^{-1} \quad (13)$$

5. Conclusions

In this study, a method is developed for determining the onsets of bubbling and slugging in a fluidized bed using a dual-plane electrical capacitance tomography (ECT) sensor. The method involves analysis of the bed behaviour at different superficial gas velocities based on the standard deviation of the solids fraction fluctuation in each plane of the sensor.

The minimum fluidization velocity is obtained where the solids fraction fluctuation begins to increase from zero. The onset of bubbling is determined when a significant bubble is first observed at the upper plane of the bed. The onset of slugging is characterized by the peak of the difference in the solids fraction fluctuation between the upper and lower planes, and is determined at the point closest to the peak where the rates of increase in the solids fraction fluctuations are the same in both planes.

The accuracy of the computed minimum fluidization velocity based on the Gidaspow [27] and the Gilbilaro et al. [29] drag models depends on the values of the particle shape factor and the bed void fraction at minimum fluidization conditions. The required value of the void fraction for accurate results was then found to lie between the measured value and the estimated value based on the Wen and Yu empirical expressions. With an increase in the particle size, the fluidization index decreases while the excess velocity to the onset of bubbling appears relatively the same. Both the particle size and the bed height influence the transition from bubbling to slugging. The larger the particle size is, the greater is the particle tendency to slug. The dependency of minimum slugging velocity on the bed height decreases with increase in the particle size. The ratio of the average solids fraction at the onset of slugging to that at onset of fluidization appears to be constant for small particles, but decreases with an increase in the particle size for larger particles. Based on the experimental data obtained over a wide range of particle size 180–2200 μm, a correlation was developed for prediction of average bed void fraction at the onset of slugging.

Furthermore, the three different particle samples primarily considered in this study show that the method developed in this paper for determining the onset of slugging in a fluidized bed is consistent with different material properties (sphericity, density and size distributions). Fitting of the experimental data suggests that a set of empirical correlations as a function of the Archimedes number can be obtained for estimating the velocities at the onset of fluidization (minimum fluidization velocity), at the onset of bubbling and at the onset of slugging, but this will require more experimental data in a future work.

Funding sources

This research did not receive any specific grant from funding agencies in the public, commercial, or not-for-profit sectors.

Appendix A. Supplementary data

Supplementary data associated with this article can be found, in the online version, at http://dx.doi.org/10.1016/j.cej.2017.07.098.

References

[1] C. Alberto, S. Felipe, S.C.S. Rocha, Time series analysis of pressure fluctuation in gas-solid fluidized beds, Braz. J. Chem. Eng. 21 (2004) 497–507.
[2] B. Du, W. Warsito, L.-S. Fan, ECT studies of gas-solid fluidized beds of different diameters, Ind. Eng. Chem. Res. 44 (2005) 5020–5030.
[3] R.K. Padhi, Y.K. Mohanty, G.K. Roy, B. Sarangi, Hydrodynamic studies of gas solid fluidization in non- cylindrical conduits for spherical and non-spherical particles – a review, Int. J. Sci. Res. Publ. 3 (2014) 1–8.
[4] D. Kunii, O. Levenspiel, Fluidization Engineering, second ed., Butterworth – Heinemann, Washington Street, USA, 1991.
[5] X. Bi, Flow Regime Transitions in Gas-Solid Fluidization and Transport, PhD thesis, Department of Chemical Engineering, the University of British Columbia, 1994.
[6] P.W.K. Kehoe, J.F. Davidson, Continuously slugging fluidized beds, chemeca '70, Inst. Chem. Eng. Symp. Ser. 33 (1970) 97–116.
[7] J. Baeyens, D. Geldart, An investigation into slugging fluidized beds, Chem. Eng. Sci. 29 (1974) 255–265.
[8] R. Cliff, J.R. Grace, M.E. Weber, Bubbles, Drops and Particles, Academic Press, New York, 1978.
[9] J.T. William, E.P. Owen, Slugging in fluidized beds, Ind. Eng. Chem., Fundam. 16 (1977) 242–247.
[10] R. Roy, J.F. Davidson, V.G. Tuponogov, The velocity of sound in fluidized beds, Chem. Eng. Sci. 45 (1990) 3233–3245.
[11] J.R. Grace, Agricola aground: characterization and interpretation of fluidization phenomena, AIChE Symp. Ser. 88 (1992) 1–16.
[12] C. Rautenbach, R.F. Mudde, X. Yang, M.C. Melaaen, B.M. Halvorsen, A comparative study between electrical capacitance tomography and time-resolved X-ray tomography, Flow Measur. Instrum. 30 (2013) 34–44.
[13] M. Puncochar, J. Drahos, J. Cermak, K. Selucky, Evaluation of minimum fluidization velocity in gas fluidized bed from pressure fluctuations, Chem. Eng. Commun. 35 (1985) 81–87.
[14] C.A.S. Felipe, S.C.S. Rocha, Prediction of minimum fluidization velocity of gas-solids fluidized beds by pressure fluctuation measurements – analysis of standard deviation methodology, Powder Technol. 174 (2007) 104–113.
[15] D. Wilkinson, Determination of minimum fluidization velocity by pressure fluctuation measurement, Can. J. Chem. Eng. 73 (1995) 562–565.
[16] C. Rautenbach, M.C. Melaaen, B.M. Halvorsen, Possible identification of size difference segregation using electrical capacitance tomography and statistical analysis, Eur. J. Sci. Res. 11 (2013) 351–364.
[17] Y.T. Makkawi, P.C. Wright, Fluidization regimes in a conventional fluidized bed characterized by means of electrical capacitance tomography, Chem. Eng. Sci. 57 (2002) 2411–2437.
[18] W. Kong, T. Tan, J. Baeyens, G. Flamant, H. Zhang, Bubbling and slugging of geldart group a powders in small diameter columns, Ind. Eng. Chem. Res. 56 (2017) 4136–4144.

[19] L.-P. Leu, F.-C. Tsai, Hydrodynamics of Geldart group A particles in gas-solid fluidized beds, Kor. J. Chem. Eng. 26 (2009) 513–517.
[20] D.G. Dimattia, P.R. Amyotte, F. Hamdullahpur, Slugging characteristics of group d particles in fluidized beds, Can. J. Chem. Eng. 75 (1997) 452–459.
[21] T.E. Broadhurst, H.A. Becker, Onset of fluidization and slugging in beds of uniform particles, AIChE J. 21 (1975) 238–247.
[22] T.C. Ho, N. Yutani, L.T. Fan, W.P. Walawender, The onset of slugging in gas fluidized beds with large particles, Powder Technol. 35 (1983) 249–257.
[23] I. Noordergraaf, W.A. Van Dijk, C.M. Van Den Bleek, Fluidization and slugging in large-particle systems, Powder Technol. 52 (1987) 59–68.
[24] F. Taghipour, N. Ellis, C. Wong, Experimental and computational study of gas-solid fluidized bed hydrodynamics, Chem. Eng. Sci. 60 (2005) 6857–6867.
[25] S. Benzarti, H. Mhiri, H. Bournot, Drag models for simulation gas-solid flow in the bubbling fluidized bed of FCC particles, Int. J. Chem. Mol., Nucl., Mater. Metall. Eng. 6 (2012) 111–116.
[26] P. Li, X. Lan, C. Xu, G. Wang, C. Lu, J. Gao, Drag models for simulating gas-solid flow in the turbulent fluidization of FCC particles, Particuology 7 (2009) 269–277.
[27] D. Gidaspow, Multiphase Flow and Fluidization: Continuum and Kinetics Theory Descriptions, Academic Press Inc., San Diego, California, USA, 1994.
[28] S. Ergun, Fluid flow through packed column, Chem. Eng. Progr. 48 (1952) 89–94.
[29] L.G. Gibilaro, R. Di – Felice, S.P. Waldram, Generalized friction factor and drag coefficient for fluid-particle interaction, Chem. Eng. Sci. 40 (1985) 1817–1823.
[30] C.Y. Wen, Y.H. Yu, A generalized method for predicting the minimum fluidization velocity, AIChE J. 12 (1966) 610–612.
[31] D. Geldart, Types of gas fluidization, Powder Technol. 7 (1973) 185–195.
[32] D. Geldart, A.R. Abrahamsen, Homogeneous fluidization of fine powders using various gases and pressures, Powder Technol. 19 (1978) 133–136.
[33] H.I. de Lasa (Ed.), Chemical Reactor Design and Technology:- Overview of New Development of Energy and Petroleum Reactor Technologies Projection for the 90's, Martinus Nijhoff Publishers, 1986.
[34] W.C. Yang (Ed.), Handbook of Fluidization and Fluid-Particle Systems, Marcel Dekker, Inc., 2003.
[35] D. Geldart, Chapter 4, Gas Fluidization Technology, first ed., John Wiley & Sons, Ltd., 1986, pp. 53–97.
[36] Process Tomography, Electrical Capacitance Tomography System. Operating Manual Volume 1: Fundamentals of ECT, Process Tomography Ltd., 2009.
[37] R.K. Thapa, B.M. Halvorsen, Study of Flow Behaviour in Bubbling Fluidized Bed Biomass Gasification Reactor using CFD Simulation. in: Proceedings of the 14th International Conference on Fluidization – from Fundamentals to Products, Eds. ECI Symposium Series, Volume, 2013.

Article 2 (A2)

Simulation of bubbling fluidized bed using a one-dimensional model based on the Euler-Euler method, 9th EUROSIM Congress on Modelling and Simulation

By

Cornelius Agu, Marianne Eikeland, Lars Tokheim and Britt Moldestad

Presented in the

EUROSIM 2016, and 57th SIMS Conference on Simulation and Modelling, SIMS 2016, Oulu, Finland, 12 – 16 September, 2016

Simulation of Bubbling Fluidized Bed using a One-Dimensional Model Based on the Euler-Euler Method

Cornelius Agu* Marianne Eikeland Lars Tokheim Britt Moldestad

Department of Process, Energy and Environmental Technology
University College of Southeast Norway, Norway, {Cornelius.e.agu, Marianne.Eikeland, Lars.A.Tokheim, britt.moldestad}@usn.no

Abstract

The behaviour of a fluidized bed can be modeled based on the Euler-Euler approach. This method has been fully utilized in both three-dimensional (3D) and two-dimensional (2D) systems for obtaining, for example, the axial and radial distribution of fluidized bed properties. However, the bed property such as void fraction distribution along the flow direction can be of great interest for a design purpose. To save computational cost, an appropriate one-dimensional (1D) model can be used to obtain the average bed property along the vertical axis of a fluidized bed. In this paper, a 1D model based on the Euler-Euler method is presented. The results show that the model can be used to describe the behaviour of a fluidized bed. With a reasonable accuracy, the results also show that the 1D model can predict the minimum fluidization velocity and the superficial gas velocity at the onset of slugging regime.

Keywords: Euler-Euler, bubbling, void fraction, fluidized bed, flow regime

1 Introduction

The fluidized bed has wide industrial applications. Such applications include circulation of catalyst particles in a chemical reactor, pneumatic transport of particles and gasification of coal/biomass. In fluidized bed reactors, there is a good mixing of solids and fluid, and this enhances heat and mass transfer rates between the fluid and the particles.

For the purpose of design and prediction of hydrodynamic behaviour of fluid-particle systems, several empirical and semi-empirical models have been developed. Moreover, the computational fluid dynamics has also been applied in such a multi-phase system. As in a single-phase system, the mass, momentum and energy transfers also govern the motions of fluid and particles in the bed. The interface momentum transfer between the phases influences the behaviour of the system. When a fluid flows through a bed of particles, the drag force acts continuously against the weight of the bed. At a certain fluid velocity, the bed begins to float in the fluid stream. This velocity is generalized as the minimum fluidization velocity. Previous studies have shown that at this fluid velocity, the interphase drag force corresponds to the net weight of the bed. This concept is used in deriving models for estimating the minimum fluidization velocity from the drag models (Kunnii and Levenspiel, 1991). Due to complexities arising from particle-particle interactions and particle-wall interactions, it has been proven difficult to establish accurate fluid-particle interphase drag models to predict accurately the behaviour of fluidized beds. However, a number of drag models can be found in the literature (Taghipour et al, 2005; Beuzarti and Bournot, 2012; Li et al, 2009).

Beyond the onset of bed fluidization, and with increasing superficial gas velocity, the agitation of particles in the bed increases. Different phase transitions can be observed when a bed is fluidized. As the fluid velocity increases, a fluidized bed passes through the bubbling regime, the turbulent regime, fast fluidization and the pneumatic conveying regime (Kunnii and Levenspiel, 1991).

In this study, the focus is on modelling a bubbling fluidized bed. A number of models have been developed for such a regime. Davidson and Harrison (1965) developed a simple two-phase model based on a mass balance and experimental observations. The underlying assumption in this model is that two distinct phases, – bubble and emulsion exist throughout the bed. A more advanced model based on physics of mass, momentum and energy conservations have also been developed. Two widely used approaches to this model development are those based on the Euler-Euler and the Euler-Lagrange methods (Crowe et al, 2012). Depending on the fluid-particle drag model and the numerical method employed, the two- and three-dimensional (2D and 3D) versions of these models have been proven successful in predicting the behaviour of fluid-particle multiphase systems. One major drawback is that the 2D and 3D models are highly computational time demanding.

There is a limited number of studies based on a 1D model. Solsvik et al (2015) used a 1D model in a methane reforming studies, and Silva (2012) presented a non-conservative version of the model for simulating

the bubbling bed behaviour of a biomass gasification process.

In this paper, the goal is to develop a detailed one-dimensional model that predicts well the behaviour of a fluidized bed with less computational time. A 1D model based on the Euler-Euler approach is used to study the behaviour of glass bead particles in a bubbling bed. The simulated results are compared with experimental data obtained from a cold fluidized bed, and with the simulation results based on a three dimensional model. The simulated superficial gas velocity at the onset of slugging is compared with the result obtained from the correlation (Geldart, 1986).

2 Computational Model

2.1 Governing Equations

The governing equations for the motions of fluid and particles in a fluidized bed are developed based on the Euler approach, and are given in (1) – (5). In the following, the subscripts "s" and "g" denote solid and gas. u and v are the respective gas and particle velocities, g is the acceleration due to gravity, β_d is the momentum transfer coefficient, and P, ε and ρ are the pressure, volume fraction and density, respectively. f is the wall frictional factor.

2.1.1 Continuity Equations

$$\frac{\partial}{\partial t}\left(\varepsilon_g\rho_g\right) + \frac{\partial}{\partial z}\left(\varepsilon_g\rho_g u\right) = 0 \tag{1}$$

$$\frac{\partial}{\partial t}\left(\varepsilon_s\rho_s\right) + \frac{\partial}{\partial z}\left(\varepsilon_s\rho_s v\right) = 0 \tag{2}$$

$$\varepsilon_g + \varepsilon_s = 1 \tag{3}$$

2.1.2 Momentum Equations

$$\frac{\partial}{\partial t}\left(\varepsilon_g\rho_g u\right) + \frac{\partial}{\partial z}\left(\varepsilon_g\rho_g u.u\right) = \frac{\partial}{\partial z}\left(\mu_{eg}\frac{\partial u}{\partial z}\right) - \varepsilon_g\frac{\partial P_g}{\partial z} - \frac{2f_g\varepsilon_g\rho_g u|u|}{D_h} - \varepsilon_g\rho_g g + \beta_d(v - u) \tag{4}$$

$$\frac{\partial}{\partial t}\left(\varepsilon_s\rho_s v\right) + \frac{\partial}{\partial z}\left(\varepsilon_s\rho_s v.v\right) = \frac{\partial}{\partial z}\left(\mu_{es}\frac{\partial v}{\partial z}\right) - \varepsilon_s\frac{\partial P_g}{\partial z} - \frac{2f_s\varepsilon_s\rho_s v|v|}{D_h} - \varepsilon_s\rho_s g - \frac{\partial P_s}{\partial z} + \beta_d(u - v) \tag{5}$$

Here, $D_h = 4A/P_{wet}$ is the bed hydraulic diameter, where A is the bed cross-sectional area and P_{wet} is the wetted perimeter of the bed. $\mu_{es} = 2\mu - \lambda$ is the phase equivalent dynamic viscosity. The solid pressure and solid stress due to collisions are based on the kinetic theory of granular flow. The constitutive equations of the model (1) – (5) are given in (6) - (10).

2.1.3 Constitutive Equations

- Gas phase (Gidaspow, 1994)

$$f_g = \begin{cases} 16Re_g^{-1} ; & Re_g \le 2300 \\ 0.0791Re_g^{-0.25} ; & Re_g > 2300 \end{cases} \tag{6}$$
$$Re_g = \varepsilon_g\rho_g uD/\mu_g$$

- Solid phase (Gidaspow, 1994; Lathowers and Bellan, 2000)

$$f_s = 0.048|v|^{-1.22} \tag{7}$$

$$P_s = K_1\varepsilon_s^2\theta \tag{8}$$

$$\lambda_s = K_2\varepsilon_s\sqrt{\theta} \tag{9}$$

$$\mu_s = K_3\varepsilon_s\sqrt{\theta} \tag{10}$$

where

$K_1 = 2(1 + e)\rho_s g_0$,

$K_2 = \frac{4d_p\varepsilon_s\rho_s g_0(1 + e)}{3\sqrt{\pi}} - \frac{2}{3}K_3$,

$K_3 = d_p\rho_s/2\left[\frac{\sqrt{\pi}}{3(3 - e)}\left\{1 + 0.4\varepsilon_s g_0(1 + e)(3e - 1)\right\} + \frac{8\varepsilon_s g_0(1 + e)}{5\sqrt{\pi}}\right]$,

$g_0 = \frac{3}{2}\left[1 - \left(\frac{\varepsilon_s}{\varepsilon_{maxP}}\right)^{1/3}\right]^{-1}$,

$\theta = \left[\frac{\left(\sqrt{(K_1\varepsilon_s)^2 + 4K_4\varepsilon_s(K_2 + 2K_3)} - K_1\varepsilon_s\right)}{2K_4\varepsilon_s}\frac{\partial v}{\partial z}\right]^2$,

$K_4 = 12\rho_s g_0(1 - e^2)/(d_p\sqrt{\pi})$.

Here, θ is the granular temperature, g_0 is the radial distribution function, e is the coefficient of restitution and d_p is the single particle diameter. ε_{maxP} is the solid fraction at maximum packing with a value of about 0.7406. μ and λ are shear and bulk viscosity, respectively.

2.2 Drag Model

There are number of drag models that can be found in literature. In this paper, the model proposed by Gidaspow (1994) is used.

$$\beta_d = \begin{cases} \beta_{dErg} ; & \varepsilon_g \le 0.8 \\ \beta_{dWY} ; & \varepsilon_g > 0.8 \end{cases} \tag{11}$$

Here, β_{dErg} and β_{dErg} are given by (12) and (13), respectively.

$$\beta_{dErg} = 150\frac{\varepsilon_s^2\mu_g}{\varepsilon_g(\emptyset_s d_p)^2} + 1.75\frac{\varepsilon_s\rho_g|u - v|}{\emptyset_s d_p} \tag{12}$$

$$\beta_{dWY} = \frac{3}{4}C_d\frac{\varepsilon_s\varepsilon_g\rho_g}{\emptyset_s d_p}|u - v|\varepsilon_g^{-2.65} \tag{13}$$

where

$$C_d = \begin{cases} \frac{24}{Re_p}\left(1 + 0.15Re_p^{0.687}\right); & Re_p<1000 \\ 0.44; & Re_p\geq 1000 \end{cases},$$

$$Re_p = \frac{\varepsilon_g \rho_g |u - v|}{\mu_g} d_p.$$

C_d is the drag coefficient and Re_p is the particle Reynolds number. $\emptyset_s$ is the single particle sphericity. To avoid discontinuity in using the above drag model, a weighting function proposed by Lathowers and Bellan (2000) is used.

$$\beta_d = (1 - \omega_d)\beta_{dErg} + \omega_d \beta_{dWY} \quad (14)$$

$$\omega_d = \frac{1}{\pi}\tan^{-1}\left(150*1.75\left(0.2 - \left(1 - \varepsilon_g\right)\right)\right) + 0.5 \quad (15)$$

2.3 Void Fraction Equation

Another crucial issue is the prediction of void fraction ε_g along the bed. It is obvious that neither (1) nor (2) can predict the void if used alone. This is due to the dependency of void fraction on the relative velocity between the solid particles and the fluid. In the computer code MFIX, the solid volume fraction is obtained based on a guess-and-correction method (Syamlal, 1998). Effective application of this method requires a known function of solid pressure with the solid volume fraction.

With the assumption that both solid particles and fluid have a constant density over the bed, the void fraction equation is established based on (1) and (2) (Gidaspow, 1994). However, due to changes of fluid pressure in the bed, there could be slight changes in the fluid density, which may influence the bed behaviour. In this paper, a new version of the void equation developed based on the continuity equations for gas and solid phases, is introduced. The new void equation, described below, partially accounts for the effect of fluid density variation.

$$\alpha_v \frac{\partial \varepsilon_g}{\partial t} + v_m \frac{\partial \varepsilon_g}{\partial z} = \varepsilon_s \varepsilon_g \rho_{rg} \frac{\partial v_r}{\partial z} \quad (16)$$

Here, $v_r = v - u$ is the relative velocity between the solid particles and the fluid. v_m and α_v are mixture mass velocity and relative volume fraction, respectively, and are expressed as

$$\alpha_v = \varepsilon_g \rho_{rg} + \varepsilon_s, \quad (17)$$

$$v_m = \varepsilon_g \rho_{rg} v + \varepsilon_s u. \quad (18)$$

where, $\rho_{rg} = \rho_g/\rho_{ref}$ is the reduced gas density. The gas density is obtained, assuming the ideal gas behaviour, $\rho_g = \frac{P_g}{RT}$.

2.4 Minimum Fluidization Velocity

The onset of fluidization occurs at a certain velocity where the net weight of the bed balances the drag force between the fluid and the bulk of particles in the bed. The minimum fluidization velocity, U_{mf} can be obtained from

$$U_{mf} = \frac{\mu_g}{\rho_g d_p} Re_{p.mf}. \quad (19)$$

The particle Reynolds number at minimum fluidization condition $Re_{p.mf}$ is based on the Ergun's bed pressure drop model (Ergun, 1952),

$$150\frac{(1 - \varepsilon_{mf})}{\varepsilon_{mf}^3 \emptyset_s^2} Re_{p.mf} + 1.75\frac{1}{\varepsilon_{mf}^3 \emptyset_s} Re_{p.mf}^2 = Ar, \quad (20)$$

where Ar is the Archimedes number, expressed as

$$Ar = \frac{d_p^3 \rho_g (\rho_s - \rho_g) g}{\mu_g^2}. \quad (21)$$

Here, ε_{mf} is the bed void fraction at the minimum fluidization condition. U_{mf} and ε_{mf} are bed properties, and either of them must be known for the other to be calculated from (19) – (21). A number of empirical correlations for ε_{mf} are available (Kunnii and Levenspiel, 1991), but this paper uses the correlation proposed by Wen and Yu (1966).

$$\frac{1}{\emptyset_s \varepsilon_{mf}^3} \approx 14 \quad (22)$$

3 Experimental setup

The experimental setup consists of a vertical cylindrical column of height 1.4 m and base diameter 0.084 m. The rig is fitted with ten pressure sensors, measuring the fluid pressure in the column up to the height of about 1.0 m. Compressed air at ambient temperature is used as the fluidizing medium. The bottom of the column is fitted with a porous plate. The porous plate ensures even distribution of air within the bed.

Thapa and Halvorsen (2013) conducted experiments with this cold fluidized bed rig using glass beads particles (particle size 350 μm) at a bed height of 0.32 m (see Figure 1). The experimental data used in this paper are those reported in Thapa and Halvorsen (2013).

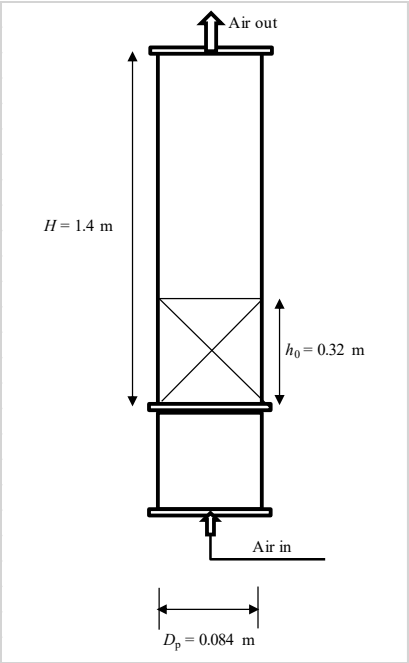

Figure 1. Physical Dimension of the fluidized bed column.

4 Simulations

The solution of the model described in Section 2 for the fluid-particle system is based on the finite volume method with staggered grids. The models are discretized in space using the first order upwind scheme, and in time based on the implicit method. The SIMPLE algorithm is used for the pressure-velocity coupling. The entire codes for the system are implemented and run in MATLAB. The properties of fluid and particles used in the computation are summarized in Table 1.

4.1 Fluidized bed regimes

In addition to simulating a bubbling fluidized bed, the transitions between different regimes for a fluidized bed are simulated using the 1D model. The flow transition from one regime to another depends on a number of factors. These include the bed particle size, the size distribution, the superficial gas velocity and the relative size between the bed height and the bed diameter. For a bed with Geldart B particles, the particle size and size distribution do not influence slugging in the bed (Baeyens and Geldart, 1974). As given in Yang (2003), slugging will occur if $\frac{h_0}{D_h} > 2$. The minimum gas velocity for the onset of slugging can be obtained from (23) (Geldart, 1986) as used in Xie et al (2008).

$$U_{ms} = U_{mf} + 0.0016(60D_t^{0.175} - h_{mf})^2 + 0.07(gD_t)^{0.5} \quad (23)$$

Here, all the length units are expressed in (cm), and h_{mf} is the bed height at minimum fluidization condition.

4.2 Initial and Boundary Conditions

Initially, the fluid pressure distribution is assumed hydrostatic, and the fluid velocity is considered uniform throughout the column, as described in Table 2. The inlet fluid pressure is assumed fixed, and it corresponds to the total weight of particles in the bed. Since the focus is on a bubbling bed, the outlet solid volume fraction is fixed to zero, while the fluid pressure at exit is taken to be atmospheric. The inlet boundary value for the solid volume fraction is dynamic, and then obtained appropriately from the void propagation equation.

5 Results and Discussion

Thapa and Halvorsen (2013) used the experimental rig described above to study the fluid-particle behaviour in a bed with particles having an average diameter of 350 μm. The pressure drop values across the bed were recorded for different superficial gas velocities (0.05 – 0.40 m/s). The minimum fluidization velocity obtained by plotting the pressure drops against the superficial gas velocity, is about 0.15 m/s. This result shows that the theoretical minimum fluidization velocity specified in Table 1 for the bed, is about 14% lower than the experimental value.

Table 1. Parameters for model computations.

Parameters	Values	Units
Particle diameter, d_p	350	μm
Particle sphericity, $\emptyset_s$	1.0	-
Particle density, ρ_s	2500	kg/m^3
Gas density, ρ_g	1.186	kg/m^3
Gas viscosity, μ_g	1.78x10^{-5}	Pa.s
Gas constant, R	0.287	kJ/(kg-K)
Gas temperature, T	25	^{0}C
Gas reference pressure, P_{ref}	1.0	bar
Initial bed height, h_0	0.32	m
Initial solid volume fraction, ε_0	0.52	-
Minimum fluidization velocity (19), U_{mf}	0.129	m/s
Bed height at minimum fluidization, h_{mf}	0.32	m
Superficial gas velocity, U_0	0.05 – 0.40	m/s
Maximum solid volume fraction, ε_{smax}	0.63	-
Restitution coefficient, e	0.90	-
Simulation time step	0.001	s
No of cells	125	-

Table 2. Initial and boundary conditions.

Initial Conditions	$0 \le z \le h_0$ $p_g(0, z) = \varepsilon_0 \rho_s g(h_0 - z)$ $\varepsilon_s(0, z) = \varepsilon_0$ $h_0 < z \le H$ $P_g(0, z) = 0$ $\varepsilon_s(0, z) = 0$ $0 \le z \le H$ $u(0, z) = U_0/\varepsilon_g$ $v(0, z) = 0$
Inlet Boundary	$u(t, 0) = U_0$ $v(t, 0) = 0$ $p_g(t, 0) = \varepsilon_0 \rho_s g h_0$
Outlet Boundary	$p_g(t, H) = 0$ $\varepsilon_s(t, H) = 0$

Figure 2 compares the simulated fluid pressure with the experimental data. The simulated results are obtained from the 1D model presented here and a 3D model reported by Thapa and Halvorsen (2013). As can be seen, the simulated data agree well with the experimental results at a height of 0.13 m above the distributor. At this height, the predictions from the 1D-model are better compared with the predictions from the 3D models. At the height of 0.23 m, the 1D model results also agree very well with the results from the 3D model.

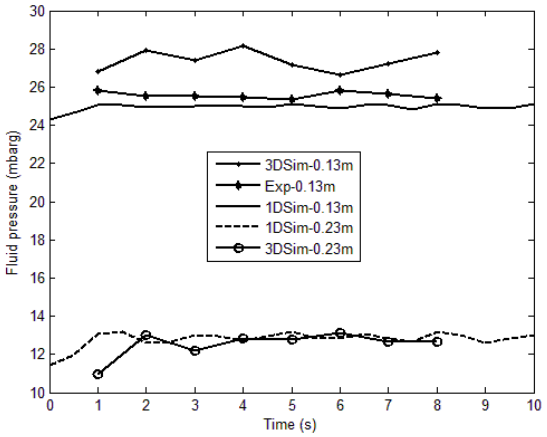

Figure 2. Evolution of fluid pressure at superficial gas velocity 0.18 m/s.

Figure 3 shows the time-averaged velocities of the fluid and particles for two different superficial gas velocities, 0.18 m/s and 0.32 m/s. From these results, it can be seen that the fluid velocity at the exit of the column is slightly higher than the velocities at the inlet. This variation in the fluid velocity along the bed axis is probably due to changes in the fluid density along the bed height. The figure also shows that fluid velocities within the bed are higher than the inlet velocities, which could be due to lower flow area available for the gas as particles occupy space within this region. The variation of particle velocity within the bed at different gas velocities conforms to the solid movement pattern described by Kunii and Levenspiel (1991). Figure 4 gives the instantaneous solid volume fractions for the respective velocities after 5, 10 and 20 s. These results show that the movement of particles in the fluidized bed are more vigorous with higher superficial gas velocity.

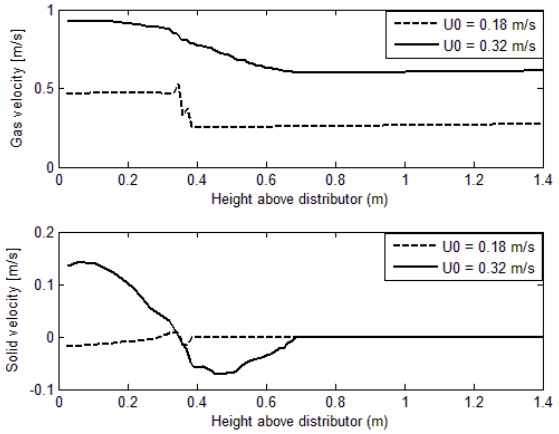

Figure 3. Time-averaged velocity profiles for fluid (upper plot) and particles (lower plot).

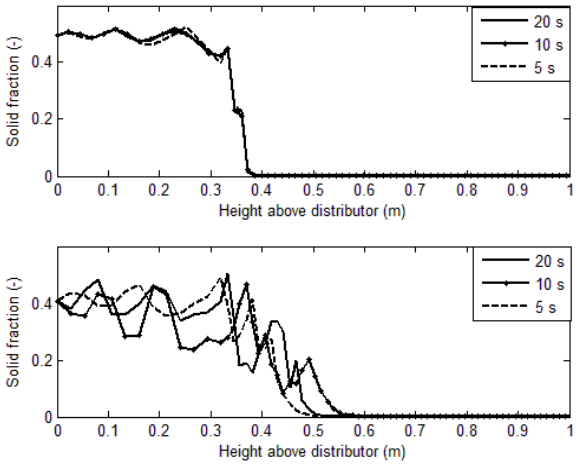

Figure 4. Instantaneous profile of solid fraction with superficial velocities 0.18 m/s (upper plot) and 0.32 m/s (lower plot).

The variation of average void fraction with superficial gas velocity within the dense region is shown in Figure 5. The average void fraction is obtained up to the height of 0.32 m above the distributor. The figure shows that the void fraction increases with increasing superficial gas velocity. It can also be seen that the bed transits into different regimes within different ranges of the superficial gas velocity.

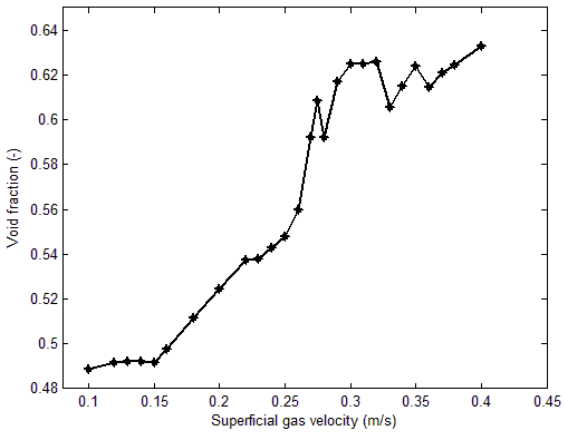

Figure 5. Variation of average bed void fraction with superficial velocity.

Four different flow regimes can be distinguished from Figure 5. Below 0.14 m/s, the bed's void fraction is about 0.49. Within this region, the bed behaves like a fixed bed with all the particles retained within the dense bed. The abrupt increase in the void fraction after 0.14 m/s indicates that the bed is fluidized. As expected for a Geldart B solid, the bed will begin to bubble when the velocity is above 0.14 m/s. Between 0.14 m/s and 0.22 m/s, the void fraction increases linearly. Beyond 0.22 m/s, it increases exponentially with an increase in the gas velocity up to 0.27 m/s. Within this velocity, the bed is more agitated with fast-rising bubbles. From (23), the minimum gas velocity for the onset of slugging is about 0.26 m/s. Since $\frac{h_0}{D_h} = 3.81\ (> 2)$, there is possibility of slug flow in the bed when the superficial gas velocity is above 0.26 m/s. From Figure 5, it can be seen that the void fraction flattens out with a superficial gas velocity beyond 0.27 m/s. More so, the variation of void fraction above 0.27 m/s fluctuates as the gas velocity increases, which shows that the bed is slugging. Thus, the velocity 0.27 m/s is the gas velocity at onset of slugging based on this simulation. The fluctuation of the bed void fraction as the velocity increases could be because in a slug flow the bed does not have a clear defined height over which the averaging is taken. In comparison, similar phase changes have been experimentally observed in Sundaresan (2003) with beds of fine particles that can readily agglomerate. With the simulated minimum fluidization velocity being 0.14 m/s, compared with the experimental value of 0.15 m/s, and with the simulated gas velocity being 0.27 m/s compared with the theoretical value of 0.26 m/s at onset of slugging, it can be concluded that the 1D model predicts the bed flow behaviour reasonably well.

Figure 6 shows the profiles of solid volume fraction at velocities 0.08, 0.20, 0.25 and 0.32 m/s, hence comparing the different flow regimes shown in Figure 5. The result shows that within the bubbling regime, the bed height expands by about 0.04 m (representing 12.5%) above the height at the minimum fluidization. The decrease in the solids fraction as the gas velocity increases is accompanied with a small fraction of particles in the freeboard. This keeps the mass of particles in the column balanced. In the solid region (fixed bed), the bed height is reduced below the settling bed height (about 0.32 m, accompanied with an increase in solid fraction), owing to the fact that the bed is closely packed towards the maximum packing solid fraction of about 0.63 used in the simulation. The figure shows that in the slugging regime, the bed expands unevenly with some particles flowing into the freeboard up to a height of 0.6 m. This shows that the bed height is not clearly defined within the slugging region, as can also be seen from Figure 7.

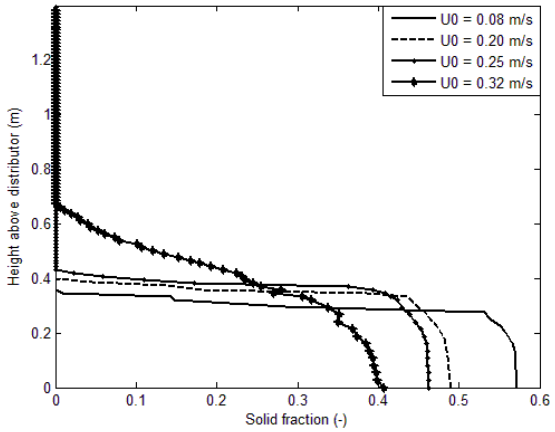

Figure 6. Simulated profile of solid fraction at different bed flow regimes.

Figure 7 shows the profile of solid fraction for some velocities within the slugging regime. Within the height interval 0.2 – 0.4 m, the solid fractions at velocity 0.32 m/s are lower than the corresponding solid fractions at velocity 0.36 m/s. This explains why the void fraction fluctuates with increasing superficial gas velocity within the slugging regime as given in Figure 5. Figure 7 also shows that the average solids volume fraction for the same range of velocities within the slugging regime is almost the same.

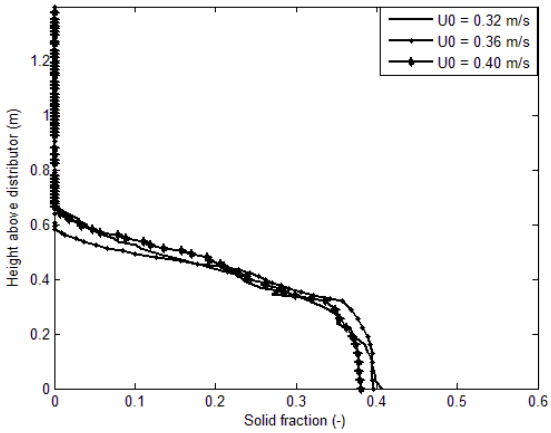

Figure 7. Simulated profile of solid fraction at different velocities within slugging regime.

6 Conclusions

This paper presents a detailed one-dimensional model based on the Euler-Euler approach for predicting hydrodynamics of a bubbling fluidized bed. The solution algorithm includes a void propagation equation that accounts for the effect of fluid density variations. The method developed here is computational efficient, taking only 10 minutes computer time for simulation of a 20 s flow in the bed, against several hours required in a 3D model computation.

Qualitatively, the results show that the 1D model predicts the different regimes of a fluidized bed. The simulated minimum fluidization velocity agrees well with the experimental data, and the value of gas velocity at the onset of slugging compares well with the value obtained from the empirical expression proposed by Geldart (1986).

Further work will include full validation of the 1D model against a 3D model results and analysis of sensitivity of the model to different parameters.

References

J. Baeyens and D. Geldart. An Investigation into Slugging Fluidized Beds. *Chemical Engineering Science*, 29: 255 – 265, 1974.

H. M. Benzarti and H. Bournot. Drag Models for Simulation Gas-Solid Flow in the Bubbling Fluidized Bed of FCC Particles. *International Journal of Chemical, Molecular, Nuclear, Materials and Metallurgical Engineering*, 6 (1), 2012.

C. T. Crowe, J. D. Schwarzkopf, M. Sommerfeld, and Y. Tsuji. *Multiphase Flows with Droplets and Particles*, 2nd ed., Taylor & Francis Group, Boca Raton London, New York, USA, 2012.

J. F. Davidson and D. Harrison. *Fluidized Particles*, Cambridge University Press, New York, 1965.

S. Ergun. Fluid Flow through Packed Column. *Chemical Engineering Progress*, 48: 89 – 94, 1952.

D. Geldart (Ed.). *Gas Fluidization Technology*, 1st ed., John Wiley & Sons, Ltd., pp. 53 – 97, Chap. 4, 1986.

D. Gidaspow. *Multiphase Flow and Fluidization*: Continuum and Kinetics Theory Descriptions, Academic Press Inc., San Diego, California, USA, 1994.

D. Kunii and O. Levenspiel. *Fluidization Engineering*, 2nd ed Butterworth – Heinemann, Washington Street, USA, 1991.

D. Lathowers and J. Bellan. Modeling of Dense Gas-Solid Reactive Mixtures Applied to Biomass Pyrolysis in a Fluidized Bed. In *Proceedings of the 2000 US, DOE Hydrogen Program Review*, NREL/CP-570-28890, USA, 2000.

P. Li, X. Lan, C. Xu, G. Wang, C. Lu and J.Gao. Drag Models for Simulating Gas-Solid Flow in the Turbulent Fluidization of FCC Particles. *Particuology*, 7: 269 – 277, 2009.

J.D. Silva. Numerical Modelling of the Fluid Dynamics in a Bubbling Fluidized Bed Biomass Gasifier. *Journal of Petroleum and Gas Engineering,* 3 (3): 35 – 40, 2012.

J. Solsvik, Z. Chao, and H. A. Jakobsen. Modeling and Simulation of Bubbling Fluidized Bed Reactors using a Dynamic One-dimensional Two-Fluid Model: The Sorption-Enhanced Steam-Methane Reforming Process. *Advances in Engineering Software,* 80: 156 – 173, 2015.

S. Sundaresan. Instabilities in Fluidized Beds. *Annual Review of Fluid Mechanics*, 35: 63 – 88, 2003.

M. Syamlal. *MFIX Documentation Numerical Technique*. Report, Department of Energy, Federal Energy Technology Center, DOE/MC 31346-5824, USA, 1998.

F. Taghipour, N. Ellis, and C. Wong. Experimental and Computational Study of Gas-Solid Fluidized Bed Hydrodynamics. *Chemical Engineering Science*, 60: 6857 – 6867, 2005.

R.K. Thapa and B.M. Halvorsen. Study of Flow Behaviour in Bubbling Fluidized Bed Biomass Gasification Reactor using CFD Simulation. In *Proceedings of the 14th International Conference on Fluidization – from Fundamentals to Products*, Eds. ECI Symposium Series, Volume, 2013.

C.Y. Wen and Y.H. Yu. A Generalized Method for Predicting the Minimum Fluidization Velocity. *AIChE J.*, 12: 610 – 612, 1966.

N. Xie, F. Battaglia, and S. Pannala. Effects of Using Two– Versus Three-Dimensional Computational Modeling of Fluidized Beds: Part I, Hydrodynamics. *Powder Technology*, 182: 1 – 13, 2008.

W.C. Yang (Ed.). *Handbook of Fluidization and Fluid-Particle Systems,* Marcel Dekker, Inc., 2003.

Article 3 (A3)

Measurement of bubble properties in a fluidized bed using electrical capacitance tomography

By

Cornelius Agu, Lars-André Tokheim and Britt Halvorsen

Presented in the

12th International Conference on Fluidized Bed Technology, Krakow, Poland, 23 – 26 May, 2017

MEASUREMENT OF BUBBLE PROPERTIES IN A FLUIDIZED BED USING ELECTRICAL CAPACITANCE TOMOGRAPHY

Cornelius Agu*, Lars-André Tokheim, Britt Halvorsen

Department of Process, Energy and Environmental Technology, University College of Southeast Norway, 3918 Porsgrunn, Norway

*Email: *cornelius.e.agu@usn.no*

Abstract – The behaviour of a bubbling fluidized bed can be measured by analyzing appropriate bubble properties. With knowledge of the solids fraction distribution across the bed at any instance, a number of bubble properties can be determined. This study discusses how bubble properties can be obtained using a dual-plane Electrical Capacitance Tomography (ECT). ECT is a non-intrusive sensor consisting of a number of electrodes that measure the distribution of relative permittivity between two phases (for example, solid and gas). Based on the analysis of image data obtained at each plane of the ECT, the criteria for adequate mixing of solids in the bed are established. Since not all bubbles that pass a given plane in the bed may influence its mixing activities, a condition is established for identifying significant bubbles that pass over a plane. For illustration purposes, the flow behaviour of a bed of glass beads with particle size distribution 100-600 μm, is studied and analyzed.

Keywords: Bubble Properties; Fluidized Bed; ECT Sensors; Solid Mixing, Bubbling.

INTRODUCTION

Application of fluidized beds in processes involving chemical reactions requires knowledge about how gas-solids mixing can effectively be achieved. Several techniques have been employed in ascertaining the mixing effect of bubbling beds. Most of the techniques use probes such as pressure and temperature sensors to measure the quality of the fluidized beds (Saxena and Tanjore, 1993; Lin and Wey, 2004). Studies have shown that size, orientation and growth of bubbles are among bubble properties that measure the degree of gas-solids mixing. Bubbles influence the mixing because they carry solid particles in their wakes as they rise up the bed, and the larger a bubble is the larger its wake becomes (Kunii and Levenspiel, 1991). Measurement of pressure fluctuation gives a qualitative indication of passage of bubbles, but not their magnitudes. Recent research on fluidization put focus on the use of tomographs such as X-ray (Bieberle et al., 2010), γ-ray transmission (Werther, 1999) and Electrical Capacitance Tomography (ECT) (Makkawi and Wright, 2004).

In this paper, the use of ECT to measure bubbling fluidized bed properties is described, and results from applying this method are discussed. ECT is a non-intrusive sensor that measures the distribution of relative permittivity between two phases (for example, solid and gas) (Process Tomography, 2009). In addition to its potential to characterize bubble size, shape and 3D orientation, ECT is fast, cheap and flexible to use (Chandrasekera et al., 2015). In fluidized beds, the relative permittivity measurement is directly related to the volume fraction of solids within a section of the bed. Fig. 1 gives the structure of a typical ECT setup with 12 electrodes. To prevent external interferences, the sensor is covered with an outer screen and a guard electrode (Zainal-Mokhtar and Mohamad-Saleh, 2013). The outer screen eliminates the variation in the stray capacitance to earth while the guard electrode protects the sensor from external noise.

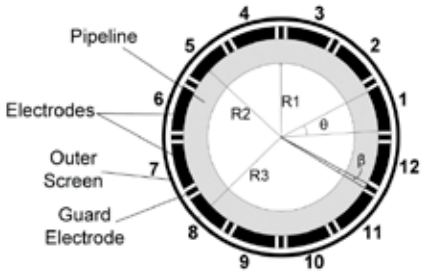

Fig. 1: Structure of an ECT sensor with 12 electrodes. R1 is the inner pipe wall radius, R2 the outer pipe wall radius and R3 the screen wall radius. θ is the electrode angular size and β is the gap within which the guard electrode is 2.5° (Zainal-Mokhtar and Mohamad-Saleh, 2013; Mohamad-Saleh, 2001).

The aim of this paper is to describe how ECT tomographs can be analyzed for determining bubble properties. Such properties include bubble size and shape, bubble frequency, bubble growth and bubble spread. These properties are used to assess the behaviour of fluidized beds at different superficial gas velocities and particle sizes. Particularly in chemical reactions, bubble or gas spread across a bed measures the effectiveness of gas-solids mixing in the reactor (Kunii and Levenspiel, 1991), which is vital for reactor design.

This study is performed using a cold fluidized bed with dual plane ECT sensors. The image data obtained in each plane are processed and analyzed in MATLAB to obtain various bubble properties. In the remaining sections of this paper the bubble properties are described, the experimental techniques adopted for their measurements are explained, and the experimental results are presented and discussed.

BUBBLE PROPERTIES

ECT measures the distribution of relative permittivity between solids and gas in a bubbling bed at a given plane. These permittivity data are used to determine a number of bubble properties, which measure the performance of bubbling beds. The bubble properties include bubble fraction, bubble size, bubble frequency, bubble spread and bubble growth rate. The use of a dual-plane ECT sensor system to measure the solids fraction distribution in a fluidized bed makes it possible to determine the bubble rise velocity when the time it takes a bubble to move between the two planes is known. However, due to frequent coalescence and splitting of bubbles as they move from one plane to another, it is difficult to trace a single bubble (Rautenbach et al., 2011), thus difficult to determine the bubble rise velocity.

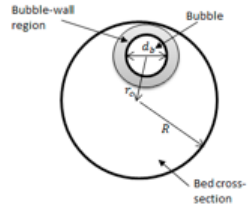

Fig. 2: Illustration of bubble and bubble-wall interaction regions in a bubbling bed.

Bubble diameter

The bubble diameter, d_b in Fig. 2, is the diameter of an equivalent sphere having its projected area the same as the bubble and may be expressed as

$$d_b = \sqrt{\frac{4A_b}{\pi}}, \tag{1}$$

where A_b is the projected area of the bubble. The shape of a bubble can be compared with that of a sphere. The diameter of the sphere d_{bs} is obtained by averaging the lengths of the major and minor axes of an ellipse that has the same normalized second central moments as the bubble (The MathWorks, 1997). The bubble shape factor, φ_b is thus expressed as

$$\varphi_b = \frac{A_b}{A_s}, \tag{2}$$

where $A_s = \frac{1}{4}\pi d_{bs}^2$ is the projected area of the sphere.

Bubble fraction

The bubble fraction describes the fraction of the bed occupied by a bubble at a given instant of time, and it can be expressed as

$$\delta_f = \frac{a_b}{A_t}, \tag{3}$$

where δ_f is the bubble fraction, $a_b(t)$ is the instantaneous projected area of the bubble and A_t is the cross-sectional area of the bed.

Bubble spread

The bubble spread measures the fraction of a region bounded by the wall where the bubbling activities can be felt. The spread could be dynamic as bubbles frequently change orientation (alternately moving towards the wall and towards the center in the bed). The relative frequency of bubble passage near the wall and near the

center of the bed measures the quality of gas-solids mixing in the bed. In this paper, quantities termed bubble location, bubble boundary factor and near-wall to near-center bubble frequency ratio are introduced to quantify the bubble spread.

The factor describing the location of a bubble at any plane is expressed as

$$\delta_l = \frac{(R-r_c)^2}{R^2}, \tag{4}$$

where R is the radius of the plane and r_c is the distance between the center of the bubble and the the center of the plane where the bubble lies as illustrated in Fig. 2. The δ_l value only gives an indication of bubble location relative to the wall of the bed. The location factor lies within $[\delta_l, 1]$. When $\delta_l = \delta_f$, the bubble has contact with the wall, and when $\delta_l = 1$, the bubble lies at the center of the bed plane.

Within the spread region, the ratio of the area surrounding the bubble up to the wall (shaded portion in Fig. 2) to the area of the bubble is termed bubble boundary factor δ_b.

$$\delta_b = \frac{\delta_l}{\delta_f} - 1; \quad \delta_b \in (-1, \infty). \tag{5}$$

In addition to location, the boundary factor indicates relative size of bubbles in a plane. Since $\delta_l > 0$, $\delta_b \to -1$ means that the bubble is very large and $\delta_b \to \infty$ means that the bubble is very small. The value $\delta_b = 0$ indicates that the bubble has a point contact with the wall while $\delta_b < 0$ means that the bubble lies along the wall.

For the purpose of analysis, the bubble properties are usually time-averaged in every plane. For this reason, only the significant bubbles are considered. Since δ_b relates the bubble size to its location from the wall, a value of boundary factor can be used to set a condition for recognizing a significant bubble. In this work, a bubble that has a boundary factor less than 8 is considered significant. The threshold value $\delta_b = 8$ is obtained by assuming that the shortest distance between such a significant bubble and the wall is 3 times its radius.

When there are more than one significant bubbles in a plane, the average distance of the bubbles from the center of the plane can be obtained by taking the second moment of area of all the bubbles about the center:

$$r_c = \left(\frac{\sum(\delta_{fi} r_{ci}^2)}{\sum \delta_{fi}}\right)^{1/2}, \tag{6}$$

where δ_{fi} and r_{ci} are the individual bubble fraction and center distance, respectively.

Bubble spread frequency

Two different bubble spread frequencies are described here: near-wall bubbling frequency and near-center bubbling frequency

The near-wall bubbling frequency, f_w, -is the number of times significant bubbles in the plane moves radially towards the wall of the bed per unit time, while the near-center bubbling frequency, f_c, -describes the number of times significant bubbles in the plane moves toward the center of the plane.

$$f_w = \left[\frac{1}{t_{w,inter}}\right]_{\delta_b \le 0} \tag{7}$$

$$f_c = \left[\frac{1}{t_{c,inter}}\right]_{\delta_b > 0}. \tag{8}$$

The relative value between f_w and f_c indicates the extent of mixing of solid particles in the plane. If $\frac{f_w}{f_c} < 0$, the spread of gas within the plane are more around the center than near the wall, and conversely.

Bubbling frequency

The bubbling frequency is defined as the number of times at least one significant bubble passes through a given plane of a bed in a unit time.

$$f_b = \frac{1}{T_b}, \tag{9}$$

where T_b is the time taken for complete passage of a bubble in the plane. T_b can be obtained as the average period of bubble cycle in the plane (see Fig. 3), as described in Eq. (10).

$$T_b = \frac{1}{n}\sum T_{bi}. \quad (10)$$

Here, n is the number of bubbles that pass through the plane over a period of time and T_{bi} is the individual bubbling period. Higher bubbling frequency indicates a high possibility of gas-solids mixing provided the bubble is large enough to give adequate gas spread in the plane.

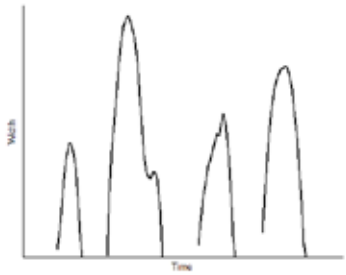

Fig. 3: Variation of projected width of a bubble with time over a plane. Bubbling period is proportional to bubble diameter.

The efficiency of gas-solids mixing due to bubbles can be measured by the volume of bubbles swept in a given time. The rate at which a bubble volume passes over a unit area of a plane (also referred to as bubble flow rate per unit area), can be expressed as

$$v_r = \frac{v_b}{T_b A_t}, \quad (11)$$

where v_r is the bubble flow rate per unit area and v_b is the volume of a bubble. Assuming a spherical bubble, Eq. (11) can be simplified, yielding

$$v_r = \frac{2}{3} f_b \delta_f d_b. \quad (12)$$

A very low value of v_r indicates less possibility of gas-solids mixing due to insufficient gas spread, while a very high value of v_r indicates a poor gas retention time as most of the gas is carried away from the bed by the bubble. With knowledge about the values of v_r, an optimum operating velocity in a bubbling fluidized bed can be established.

EXPERIMENTAL

The setup used in this work consists of a cylindrical column of diameter 10.4 cm and height 1.4 m. The bottom of the column is fitted with a porous plate and an air supply hose. The porous plate ensures even distribution of air in the bed. The measuring equipment is a dual-plane ECT sensor as shown in Fig. 4. The sensors are located at two different positions, 15.7 cm and 28.7 cm above the distributor. Each sensor consists of 12 electrodes, uniformly distributed around the plane circumference. The cross-section of each sensor is divided into 32x32 square pixels, of which 812 lie within the bed. Each pixel holds a normalized permittivity with intensity lying between 0 and 1. When the sensors are energized by the applied voltage, the capacitance between each pair of electrodes is measured and converted into permittivity values according to the relationship $C = SP$ (Process Tomography, 2009). Here, C is an M x 1 capacitance matrix with M = 66 (number of inter-electrode pairs), P is an N x 1 relative permittivity matrix with N = 1024 (number of pixels) and S is an M x N sensor sensitivity matrix. The relative permittivity is evaluated based on the Linear Back Projection algorithm available in the ECT software.

The experiment was performed with glass bead particles of size range 100 – 600 μm having the Sauter mean diameter of 261 μm and minimum fluidization velocity of 0.09 m/s. The fluidizing fluid is compressed air at ambient temperature and superficial velocity of 0.18 m/s ($2U_{mf}$), where U_{mf} is the minimum fluidization velocity. In the experiment, the ECT sensors were first calibrated for the lower permittivity value when the column was empty, and then for the higher permittivity value by filling up with glass particles to a height of 64.0 cm giving the bed aspect ratio $h_0/D = 6.2$. The lower and higher permittivity values defining the range of the equipment are normalized into values 0 and 1, respectively. The normalized relative permittivity ε_r is a measure of volume fraction of solids in the bed. The volume fraction of particles at any point in the plane is

obtained from $\varepsilon = \varepsilon_0 \varepsilon_r$, where ε_0 is the volume fraction of the solid particles in a fixed state. The observed value of ε_0 in this experiment is 0.62.

After the sensor calibration, the bed was fluidized at a superficial air velocity of 0.25 m/s for 2 min, and thereafter the air supply was cut off. This action was to ensure that the particles in the bed were evenly mixed. At a superficial air velocity of 0.18 m/s, the images for solids distribution at each position of the ECT sensors were recorded for 60 s. The image data were captured at a frame frequency of 100 Hz, giving 6000 frames over the 60 s. The recorded image data were exported for analysis in MATLAB and to determine the bubble properties.

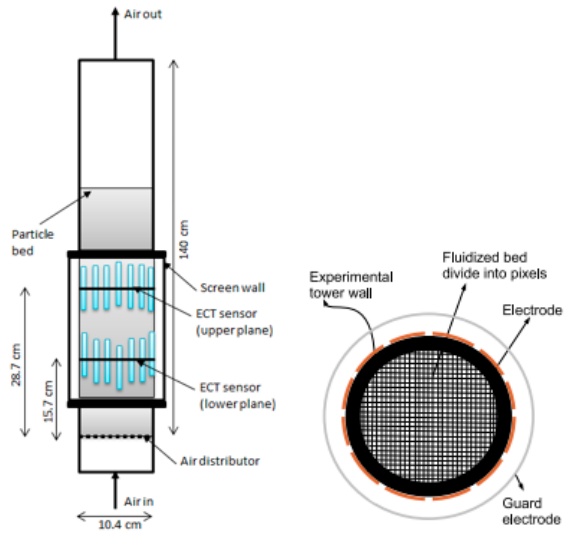

(a) (b)

Fig. 4: (a) Schematic illustration of a cold fluidized bed where two plane ECT sensors are used to measure solids fraction. (b) Cross-section of an ECT sensor divided into 812 pixels.

BUBBLE REGION

A dense fluidized bed is divided into two regions – an emulsion region (of high solids concentration) and a bubble region (of low solids concentration) (Kunii and Levenspiel, 1991). So far, no definite value has been assigned to the bubble-emulsion threshold that marks the boundary of a bubble region. This is because different beds have different bubble rise characteristics due to particle nature and size distribution; also, different equipment units produce different results (Rautenbach et al., 2013).

Different researchers use different values of solids fraction at the bubble threshold. Gidaspow (1994) describes the bubble region as where the solids fraction is less than 0.2. In the work of Rautenbach et al. (2013), the bubble threshold is obtained by trial such that the ECT data are used to estimate the known diameter of a ping-pong ball falling through the bed. Fig. 5 shows the distribution of solids fraction in the bed recorded in the first-30 s at the lower and upper planes of the ECT sensors. In these figures, the blue regions within the bed cross section are evidence that there are bubble passages over the time interval, and as can be seen these regions lie within the solids fraction [0, 0.2]. Hence, bubbles in this paper are defined as regions where the solids fraction is not more than 0.2.

Having identified the bubble threshold, properties such as bubble size (measured by the number of pixels occupied by the bubble) and bubble orientation (measured by the centroid of the bubble) are determined using the image region property toolbox in MATLAB. The actual projected area of a bubble within a plane at any instant is obtained from $A_b = A_t \left(\frac{N_b}{N_{pix}}\right)$, where N_b is the number of pixels occupied by the bubble and $N_{pix} = 812$ is the total number of pixels within the plane.

RESULTS AND DISCUSSION

The information acquired from each of the ECT sensors over 60 s of airflow was analyzed in MATLAB. The results of the experiment and the analysis are shown in Figs. 6 – 7 and Table 1.

Fig. 6(a and b) show the bubble regions in the bed at the 9th s, where the region in white represents the bubble. The bubble shape is compared with that of a sphere represented by the circles.

The time series of the largest bubble that passed each of the planes over 60 s are shown in Fig. 7. The vertical axes represent the projected bubble fraction, while the horizontal axes give the frame time in seconds. These results show that there were a higher number of bubble passages in the lower plane than in the upper plane within a time interval. From the variation of the bubble fraction, it shows that bubbles grow into a more stable size (larger bubble fraction) as they rise in the bed, leading to the more pulsating bubbling recorded at the upper plane.

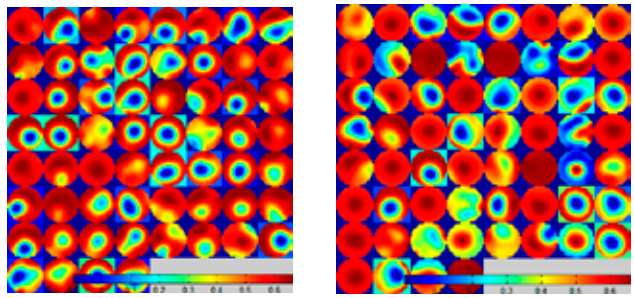

(a) (b)

Fig. 5: Map of solids fraction distribution for the first-30 s taken at 0.5 s interval: (a) lower plane (b) upper plane. Time of sampling increases from left to right and from top to bottom. The superficial air velocity was 0.18 m/s.

(a) (b)

Fig. 6: Behaviour of the fluidized bed in the (a) lower plane and (b) upper plane, at 900th frame showing the region occupied by the actual bubble (white) and region defined by the whole-spherical bubble (bounded by a red circle).

Table 1 shows the time-averaged values of various bubble properties calculated from the solids fraction distribution captured with each of the ECT sensors over 60 s. As shown in Table 1, there are more bubbles rising in the lower plane (frequency 5.97 s^{-1}) than in the upper plane (frequency 3.66 s^{-1}) in a unit time. The difference in the bubbling frequency is associated with different bubble sizes between the two planes: a smaller average bubble diameter 5.04 cm at the lower plane and a larger average bubble diameter 8.00 cm at the upper plane. The bubble size increases due to bubble coalescence and pressure drop along the bed. The smaller bubbles take less time than the larger bubbles to pass over a plane, as shown in Fig. 3, leading to a higher number of bubble passages at the lower plane in a given time. The fraction of the bed cross sectional area occupied by most of the bubbles in each time interval is 19.6% in the lower plane and 43.2% in the upper plane.

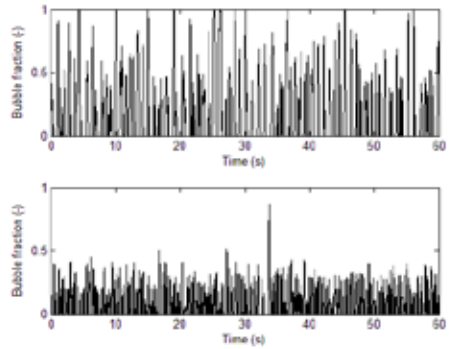

Fig. 7: Projected bubble fraction of the largest bubble as a function of time. Upper plot (upper plane); Lower plot (lower plane).

Table 1: Results: Bubble properties obtained from ECT image data analysis.

Symbols	Lower plane	Upper plane	Units
$\bar{d}_b$	5.04	8.00	cm
$d_{b,max}$	7.85	10.40	cm
φ	0.96	0.79	-
δ_f	0.196	0.432	-
f_b	5.97	3.66	s^{-1}
f_w/f_c	0.055	0.693	-
v_r	3.57	7.14	cm/s

The maximum attainable bubble diameter within 60 s is 7.85 cm at the lower plane and 10.40 cm at the upper plane (the same as the bed diameter). Though there was no fully developed slug in the entire bed, the maximum attainable bubble size at the upper plane indicates a slug flow and with further increase in the superficial gas velocity, the slug will expand to the lower part of the bed (see Fig. 8). The shape factors of 0.96 and 0.79 at the lower and upper planes, respectively, show that a bubble gets less spherical as it grows in size.

The ratio of near-wall bubbling frequency to near-center bubbling frequency in the two planes are less than unity and quite different (0.055 for the lower plane and 0.693 for the upper plane). These values suggest that most of the bubble activities in the lower plane occur near the center of the plane. At the upper plane, the difference in activity is less pronounced - the bubble activity near the center is about twice as high as near the wall. The bubble flow rate per unit area of the bed suggests that the upper plane holds less amount of gas than the lower plane in a unit time. The average of the flow rate across the bed is 5.36 cm/s per unit area.

CONCLUSION

The behaviour of a bubbling fluidized bed was studied by analyzing the bubble properties determined from the measurement of solids fraction distribution using a dual-plane ECT sensor system. With the bubble threshold defined as a region with solids fraction less than 0.2, bubble properties such as size, shape, spread frequency, bubbling frequency and bubble flow rate were determined using the image region property toolbox in MATLAB.

From the bubble spread frequency, it is possible to determine where the bubble activities are concentrated. Knowledge about this aids the design of chemical reactors, for example, for proper heat distribution.

In further works, determination of bubble rise velocity from the ECT image data will be considered. Future work will also be extended to analysis of bubbling bed behaviour from the solids fraction measurement and validation of bubble properties at different superficial gas velocities and bed materials.

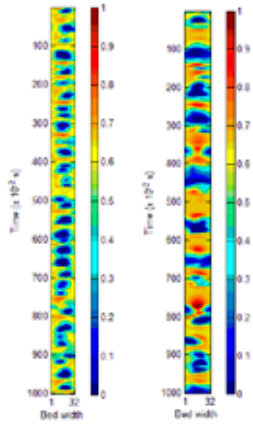

(a) (b)

Fig. 8: Images from the ECT sensors stacked in time for the first-10 s of the flow. Time axis increases from top to bottom. (a) Lower plane: Bubble size is large but less than the bed diameter. (b) Upper plane: Bubble size grows to the size of bed diameter, indicating slugging.

REFERENCES

Bieberle M., Schleicher E., Fischer F., Koch D., Menz H.-J., Mayer H.-G., et al. 2010. Dual-Plane Ultrafast Limited-Angle Electron Beam X-ray Tomography. Flow Measurement and Instrumentation 21(3): 233 – 239.

Chandrasekera T.C, Li Y., Moody D., Schnellmann M.A., Dennis J.S., Holland D.J. 2015. Measurement of Bubble Sizes in Fluidized Beds Using Electrical Capacitance Tomography. Chemical Engineering Science 126: 679 – 687.

Gidaspow D. 1994. Multiphase Flow and Fluidization: Continuum and Kinetics Theory Descriptions, Academic Press Inc., San Diego, California, USA.

Kunii D., Levenspiel O. 1991. Fluidization Engineering, 2nd ed., Butterworth – Heinemann, Washington Street, USA.

Lin C., Wey M.Y. 2004. Statistical and Power Spectral Analysis of Quality of Fluidization for Different Particle Size Distributions at High Temperature. Advanced Powder Technology 15(1): 79 – 96.

Makkawi Y., Wright P. 2004. Electrical Capacitance Tomography for Conventional Fluidized Bed Measurements – Remarks on the Measuring Techniques. Powder Technology, 148: 142 – 157.

Mohamad-Saleh J., Hoyle B.S., Podd F.J.W., Spink D.M. 2001. Direct Process Estimation from Tomography Data Using Artificial Neural Systems. Journal of Electronic Imaging 10(3): 646 – 652.

Process Tomography 2009. Electrical Capacitance Tomography System. Operating Manual Volume 1. Fundamentals of ECT, Process Tomography Ltd.

Rautenbach C., Melaaen M.C., Halvorsen B.M. 2011. Investigating the Influence of Fines in Fluidized Bed Reactors Using 3D ECT Images. In: Mammoli A.A. and Brebbia C.A., editors. Computational Methods in Multiphase Flow VI, Wessex Institute of Technology, WIT – Press, Ashurst Lodge, Ashurst, Southampton SO40 7AA, UK, p141 – 151.

Rautenbach C., Mudde R.F., Yang X., Melaaen M.C., Halvorsen B.M. 2013. A Comparative Study between Electrical Capacitance Tomography and Time-Resolved X-ray Tomography. Flow Measurement and Instrumentation 30: 34 – 44.

Saxena S., Rao N., Tanjore V. 1993. Diagnostic Procedures for Establishing the Quality of Fluidization of Gas-Solid Systems. Experimental Thermal and Fluid Science 3: 56 – 73.

The MathWorks. 1997. Image Processing Toolbox for Use with MATLAB. User's Guide Version 2, The MathWorks Inc.

Werther J. 1999. Measurement Techniques in Fluidized Beds. Powder Technology 102: 15 – 36.

Zainal-Mokhtar K., Mohamad-Saleh J. 2013. An Oil Fraction Neural Sensor Development Using Electrical Capacitance Tomography Sensor Data. Sensors 13(9): 11385 – 11406.

Article 4 (A4)

Investigation of Bubbling Behavior in Deep Fluidized Beds at Different Gas Velocities using Electrical Capacitance Tomography

By

Cornelius E. Agu, Ambrose Ugwu, Christoph Pfeifer, Marianne Eikeland, Lars-Andre Tokheim, Britt M.E. Moldestad

Published in

Industrial & Engineering Chemistry Research 58 (2019) 2084 – 2098

I&EC research
Industrial & Engineering Chemistry Research

Article

Cite This: Ind. Eng. Chem. Res. 2019, 58, 2084−2098

pubs.acs.org/IECR

Investigation of Bubbling Behavior in Deep Fluidized Beds at Different Gas Velocities using Electrical Capacitance Tomography

Cornelius E. Agu,*[,†] Ambrose Ugwu,[‡] Christoph Pfeifer,[§] Marianne Eikeland,[†] Lars-Andre Tokheim,[†] and Britt M. E. Moldestad[†]

[†]Department of Process, Energy and Environmental Technology, University College of Southeast Norway, 3918 Porsgrunn, Norway
[‡]Department of Energy and Process Engineering, Norwegian University of Science and Technology, 7491 Trondheim, Norway
[§]Department of Material Sciences and Process Engineering, University of Natural Resources and Life Sciences, 1190 Vienna, Austria

ABSTRACT: Deep bubbling fluidized beds have some advantages that make them attractive for industrial applications. Using different powders, this paper investigates the bubbling behavior in deep beds. The results show that bubbles grow faster in the bed of angular/rough particles than in that of round/smooth particles and that the rate of bubble growth increases with increase in the particle size. With an increase in the bed height, the changes in the bubble diameter and solids distribution decrease within the bubbling regime but may vary within the slugging regime due to the chaotic behavior of slug flows. The bubble frequency increases with an increase in the gas velocity only when the bubble diameter is below a certain threshold value; for larger bubbles, the bubble frequency is lower. The maximum bubble frequency indicates the onset of slugging. Correlations for predicting the maximum bubble/slugging frequency averaged over the bed height and the corresponding bubble diameter are proposed.

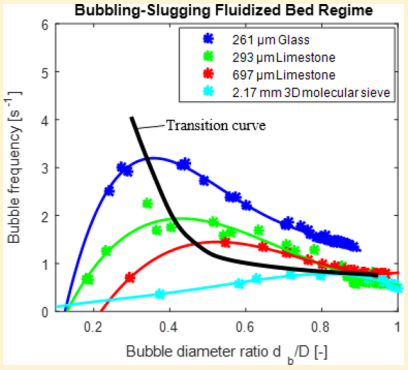

1. INTRODUCTION

The application of bubbling fluidized beds covers a wide range of bed aspect ratios (ratio of bed height to bed diameter), but several studies have been focused mainly on beds with aspect ratios slightly above unity, usually within the range of 1−2. This is possibly because the behavior in freely bubbling beds with such aspect ratios can be analyzed using simple theories and physics such as the two-phase theory proposed by Toomey and Johnstone.[1] Studies have also shown that in such shallow beds bubbles do not grow into slugs but instead transit into the turbulent fluidization regime as the gas velocity increases. Bubbles can develop into slugs when the bed height is larger than twice the bed diameter.[2] Baeyens and Geldart[3] proposed models that describe the maximum bed height below which a freely bubbling behavior is guaranteed and the bed height above which the slug flow can be stable as given in eqs 1 and 2, respectively, where h_0 [cm] is the height of the bed in fixed state and D [cm] is the bed diameter.

$$\frac{h_0}{D} = 60D^{-0.175} \tag{1}$$

$$\frac{h_0}{D} = \frac{(1 - 2.51D^{-0.8})}{0.13D^{0.47}} \tag{2}$$

When the aspect ratio is greater than 2, the bed is usually described as a deep bed. With the same bed diameter, an increase in the aspect ratio results in an increase in the pressure drop over the bed. For the application of fluidized beds in chemical reactors, the basic requirement is to provide adequate heat for reactions, particularly in thermochemical processes, and to increase the reactant contact time and surface area while ensuring uniform temperature and material distribution. Provided that the bed is in the bubbling regime, a proper heat and material distribution within the bed can be achieved. With increasing bed pressure drop, the gas residence time increases. In addition, due to flow of well-established bubbles, the circulation of solids at increasing gas velocity is more vigorous in a deep bed than in a shallow bed.[4] However, the advantage of using a deep bed especially in laboratory and pilot scales is limited to the critical gas velocity above which slugs begin to appear in the bed. In most fluidized bed applications, slugging is avoided as a mode of contact due to the possibility of gas escaping with the slugs. The slugs usually separate gas from the solid particles in the bed, reducing the contact area and time for the reacting species.

The aim of this study is to investigate the behavior of bubble flow through a deep bed at different gas velocities and bed heights. Few studies are available on the chosen topic,[5] although there are numbers of related studies. In a computational study, Wang et al.[6] investigated the effect of non-spherical particles on the bubbling behavior in a bed of aspect ratio 12 and concluded that bubbles move with higher degree of fluctuation compared with those in a bed of spherical particles. Using CFD computations, Verma et al.[7] found that bubble size increases only within a certain range of different

Received: October 10, 2018
Revised: January 8, 2019
Accepted: January 11, 2019
Published: January 11, 2019

DOI: 10.1021/acs.iecr.8b05013
Ind. Eng. Chem. Res. 2019, 58, 2084−2098

bed diameters and then remains constant. An increase in a bed diameter at a constant bed height indicates a decrease in the aspect ratio. The study[7] was focused mainly on shallow beds where the highest bed aspect ratio investigated was 2.0. In a similar study using ultrafast electron beam X-ray tomography in beds with aspect ratio limited to 2.0, Verma et al.[8] concluded that there is no significant difference in the bubble characteristics with changes in the bed aspect ratio. Laverman et al.[9] investigated the effect of bed aspect ratio and bed diameter in a freely bubbling bed using a 2-D particle image velocimetry, and their results show that bubble sizes hardly depend on the bed height within the experimental error but are affected by the bed diameter. In addition, the slug flow behaviors in deep fluidized beds have also been investigated in different studies.[10,11] In a bed of diameter 76.2 mm and height 40.0 cm containing 1.5 mm spherical iron oxide particles, Wang et al.[10] showed that at lower gas velocities bubbles flow freely but at higher gas velocities above the minimum slugging velocity the bed slugs. The slug rise velocity increases with an increase in the gas velocity but at nearly the same frequency of 1 Hz. A similar value for the limiting slug frequency was also observed in Cho et al.,[11] where polyethylene particles of size 603 μm were fluidized in a bed of diameter 7.0 cm and aspect ratio 5.3. The setup used in Cho et al.[11] was designed to simulate the dimensional similarity of a commercial fluidized bed reactor, indicating that the behavior observed in their study can be scaled up to a larger bed.

As there have not been many experimental works on the behavior of a deep fluidized bed at increasing gas velocity, this study focuses on the measurement and analysis of bubble behavior at different gas velocities. The analysis is based on the radial distribution of the solids fraction and on the bubble properties such as bubble size and bubble frequency, which are among the parameters that give an indication about the behavior of fluidized beds.[4] Although slugging behavior is peculiar to small and pilot-scale fluidized bed reactors, Raghuraman and Potter[12] showed that it can also be expected in some large scale reactors depending on the bed aspect ratio. Therefore, for in-depth characterization of behavior in deep beds, a small-scale fluidized bed column is used in this study. In the experimental setup, the bubble properties are determined by analysis of the solids fraction obtained with a dual-plane electrical capacitance tomography (ECT) at ambient temperature and pressure. ECT is used to measure the relative permittivity between two nonconducting phases, and being a nonintrusive sensor, it does not interrupt the flow or bed it measures. Previous studies[13,14] confirmed that this measurement technique provides bubble diameters that compare well with bubble sizes obtained with other techniques. In the subsequent sections, the experimental procedure is presented. The results, which include effects of bed height, material, and particle size on bubble properties and solids distribution, are discussed.

2. PREDICTION OF BUBBLE PROPERTIES

Several models described in the literature can predict bubble properties, including the bubble size and bubble rise velocity. For this study, the bubble diameter and bubble frequency are considered the most relevant. There are only a few correlations[15,16] available for the bubble frequency. The bubble diameter can be predicted using a number of different correlations.[17−20] However, the review of Karimipour and Pugsley[21] showed that the models given by Choi et al.[17] and Mori and Wen[18] give the best results for Geldart B solids.[22] The Choi et al. model is described as follows:

$$(U_0 - U_{mf})[d_b - d_{b0c} - 1.132h] + 0.474g^{0.5}(d_b^{1.5} - d_{b0c}^{1.5}) = 0 \quad (3)$$

where, d_b [cm] is the bubble diameter at a position h [cm] from the bottom of the bed, U_0 [cm/s] is the superficial gas velocity, U_{mf} [cm/s] is the particle minimum fluidization velocity, and g [cm/s^2] is the acceleration due to gravity. The initial bubble diameter d_{b0c} [cm] is obtained from

$$d_{b0c} = \frac{1.63}{g^{0.2}}[A_0(U_0 - U_{mf})]^{0.4} \quad (4)$$

where A_0 is the catchment area [cm^2] defined as the area of a distributor plate per hole. For a porous plate, $A_0 \approx 0.56$ cm^2 as described in Darton et al.[19]

The bubble diameter based on Mori and Wen[18] can be obtained from eqs 5 and 6.

$$d_b = 0.652[A(U_0 - U_{mf})]^{0.4} - (0.652[A(U_0 - U_{mf})]^{0.4} - d_{b0m})\exp\left(-0.3\frac{h}{D}\right) \quad (5)$$

$$d_{b0m} = 0.00376(U_0 - U_{mf})^2 \quad (6)$$

Again, d_b, h, and D are in [cm], U_0 and U_{mf} are in [cm/s], and $A = \frac{1}{4}\pi D^2$ is the bed cross sectional area. Here, d_{b0m} is the initial bubble size near the surface of a porous plate distributor.

3. EXPERIMENTAL PROCEDURES

3.1. Experimental Setup. The experimental setup is similar to that described in Agu et al.[23] As shown in Figure 1, the setup consists of a cylindrical column with a 10.4 cm

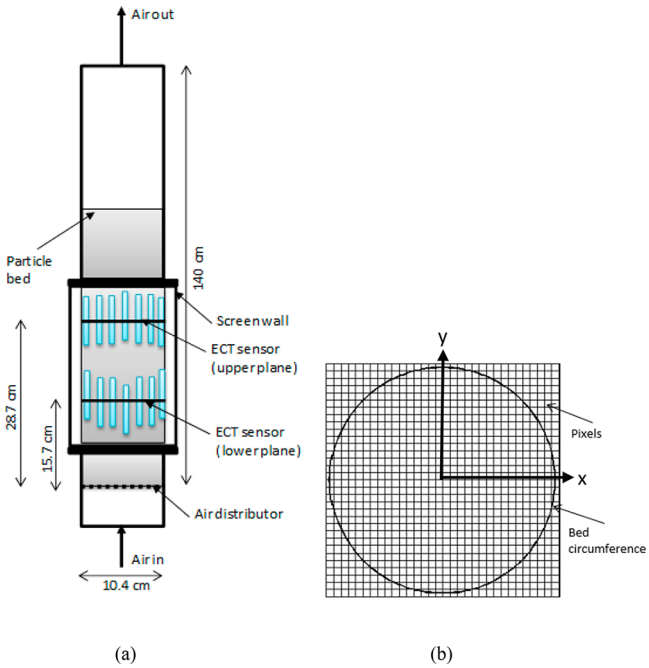

Figure 1. (a) Cold fluidized bed using dual-plane ECT sensors for measurement of solids fraction distribution. (b) Cross section of the bed divided into 32 by 32 pixels in the x and y directions, respectively.

DOI: 10.1021/acs.iecr.8b05013
Ind. Eng. Chem. Res. 2019, 58, 2084−2098

internal diameter and 1.4 m height. The column is fitted with a porous plate distributor and twin-plane ECT sensors located at 15.7 and 28.7 cm from the distributor. The porous plate is made of highly porous sintered stainless steel material and has a diameter of 10.8 cm, thickness of 3 mm, and a porosity of 40%, corresponding to a flow area of 36.6 cm^2. Figure 2 shows

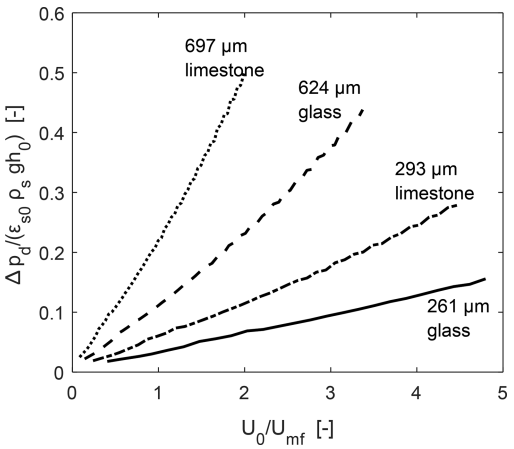

Figure 2. Ratio of pressure drop across a porous plate to pressure drop over different beds. Δp_d is the pressure drop across the distributor, and $\varepsilon_{s0}\ \rho_s\ gh_0$ is the mean bed pressure drop.

the pressure drop across the distributor plate at different gas velocities compared with the pressure drop in the bed of different particles. Each of the ECT sensors consists of 12 electrodes, uniformly distributed around the plane circumference on the outer wall of the bed column. The sensors are shielded against external field effects. The cross section of each sensor is divided into 32 × 32 square pixels, of which 812 pixels lie within the bed as shown in Figure 1(b). Each pixel holds a normalized relative permittivity between 0 and 1, denoting the gas and solids concentrations, respectively. The ECT sensors were calibrated prior to use for a given powder. To minimize the signal-to-noise level, the solid particles forming the bed were uniformly filled across the measurement planes during the calibration. In operation, ECT measures the capacitance value between every pair of electrodes around the bed. The maximum rate at which the ECT sensors acquire information from the bed is 100 frames per second. The Linear Back Projection reconstruction algorithm[24] is applied to obtain the distribution of relative permittivity of the dense material from the ECT data.

In this study, different powders were investigated. The powders include limestone particles with two different mean particle sizes, glass particles with three different particle sizes, and sand and molecular sieve particles. The Z10-02 molecular sieve manufactured and supplied by Zeochem AG is used for gas adsorption. Including this powder increases the range of particle sizes covered in this study. Table 1 shows the particle properties of all the powders, where ρ_s is the particle density obtained with a gas pycnometer and d_s is the mean particle size obtained from the sieve analysis. The solids fraction ε_{s0} at a fixed state was obtained from $\varepsilon_{s0} = m/(\rho_s A h_0)$, where m is the mass of solids charged into the bed. The round (spherical) particles are also smooth in texture, while the angular (nonspherical) particles are rough in texture. As can also be seen in Table 1, these different particle types belong to a wide range of solid classes (Geldart[22] classification) ranging from small Geldart B to large Geldart D solids. The chosen range of particle sizes is widely applied in fluidized bed reactors. For example, the size of particles in the Geldart BD or D group is used in fluidized bed combustors to minimize particle entrainment, while in biomass gasifiers particle size in the B group is often used due to lower the gas velocity involved. To demonstrate the effect of bed height on the bed behavior, the three powders with smaller particle sizes were used since for larger particles the minimum slugging velocity is less dependent on the bed height,[3] indicating that the effect of bed height on bubble size may be insignificant for larger particles. For each of the three smaller powders, the bed heights applied were 52, 58, and 64 cm, and for the other powders, the bed height was in the range of 40−60 cm. The corresponding aspect ratios for all the bed heights lie between 3.9 and 6.2, which are within the range of 1.6−8.7 calculated from eqs 1 and 2 for flow of unstable slugs in the bed.

The experiments were carried out using compressed air supplied through a root blower. The maximum flow rate and pressure drop across the air blower are 120 m^3/h and 0.15 bar(g) at the ambient temperature, respectively. The air velocity was varied at an increasing step within the range given in Table 2. For each powder, Table 2 also shows the minimum fluidization velocity and the minimum slugging velocity obtained in this study by the method described in Agu et

Table 2. Gas Velocities Investigated with Minimum Velocities at Flow Regimes

Materials	Mean particle diameter [μm]	Minimum fluidization velocity [cm/s]	Minimum Excess velocity at slugging [cm/s]	Superficial air velocity [cm/s]
Glass	188	3.80	10.7	1.0−27.5
Glass	261	8.15	6.54	3.9−33.4
Glass	624	23.20	10.60	15.7−53
Limestone	293	13.80	7.36	3.9−37.3
Limestone	697	39.24	9.76	35−76.5
Sand	483	16.50	9.32	11.8−43
Molecular sieve	2170	76.85	14.72	68.6−102

Table 1. Bed Materials Investigated with Their Properties

Materials	Size range [μm]	Solid class	Shape	ρ_s [kg/m^3]	d_s [μm]	ε_{s0} [-]
Glass	100−550	B	round	2500	188	0.63
Glass	100−550	B	round	2500	261	0.62
Glass	450−900	BD	round	2500	624	0.62
Limestone	150−450	B	angular	2837	293	0.51
Limestone	450−1100	BD	angular	2837	697	0.48
Sand	300−700	B	angular	2650	483	0.55
Molecular sieve	1600−2600	D	round	1300	2170	0.62

DOI: 10.1021/acs.iecr.8b05013
Ind. Eng. Chem. Res. 2019, 58, 2084−2098

al.[23] At a given air velocity, the images of the solids distribution at the measurement planes were captured and recorded for 60 s at a frequency of 100 Hz, the same as the maximum rate of measurements with the ECT sensors. The recorded image data were exported for analysis in MATLAB.

As described in Agu et al.,[25] Figure 3 shows the distribution of solids fraction obtained in the bed of 261 μm glass particles

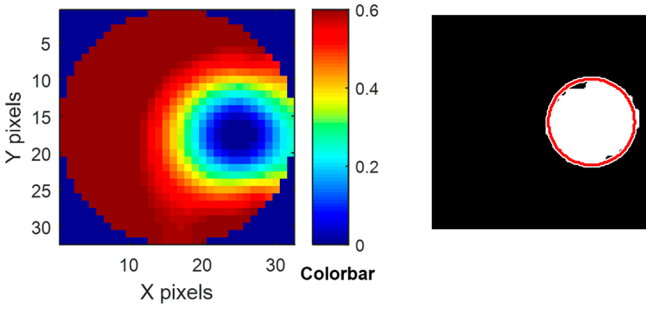

(a) (b)

Figure 3. Behavior in the lower plane of the bed of 261 μm glass particles. (a) Distribution of solids volume fraction as indicated by the numbers in the color bar. (b) Actual bubble region (white) and approximately spherical bubble (region bounded by a red circle).

at a 35th s of 0.147 m/s airflow. The higher values on the figure color bar indicate higher solid concentrations. In the regions where the solid concentration approaches zero, bubbles can be observed. As bubbles have been found to contain a certain amount of solids,[4] any region bounded by the solids fraction between 0 and 0.2 is considered as a bubble in this study. Using this bubble-solid threshold, different bubbles are identified. The sensitivity of bubble properties to a change in the threshold value decreases with increasing gas velocity and particle sphericity. Within the bubbling regime, a change in the cutoff solids fraction to a value within 0.15−0.25 (corresponding to ±25% change) results in a change in the bubble diameter within 5% to 7% for the round particles and 6% to 10% for the angular particles. Despite the bubble-solid threshold value, analysis of the image data reveals that only a single bubble can be mostly observed in each plane at every gas velocity as shown in Figure 3. This is probably due to the small size of the bed diameter, which may enhance the lateral bubble coalescence and due to the location of the ECT sensors (15.7 and 28.7 cm) before which the number of rising bubbles must have been reduced due to axial coalescence. However, the activities of a single bubble can be traced easily, making the data analysis less cumbersome. For every bubble identified in this analysis, its properties are calculated using the "image processing toolbox" in MATLAB. The number of pixels occupied by a bubble at any given time is obtained and mapped into the actual bubble projected area based on $A_b = A\left(\frac{N_b}{N_{pix}}\right)$, where N_b is the number of pixels occupied by the bubble and N_{pix} = 812 is the total number of pixels within the plane. The changes in the values of A_b with time are used to obtain the bubble frequency as described in the next section.

Figure 4 shows the sketch of a typical profile of the projected bubble area at a given plane that can be observed during the bubble passage. As can be seen, the projected area gradually increases from zero, reaching a peak value and then gradually

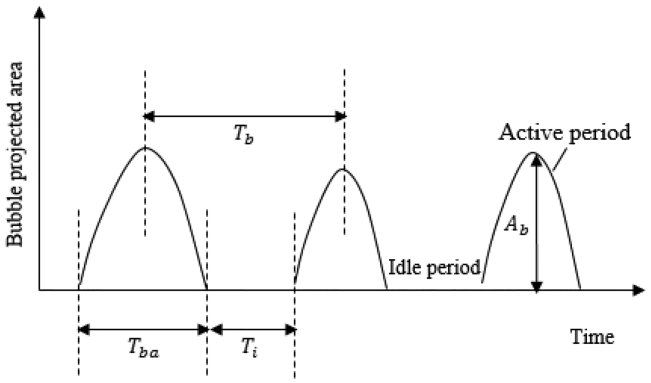

Figure 4. Sketch of the time evolution of the bubble projected area typical for a bubbling fluidized bed, where T_{ba} is the average active bubble period, T_i the average idle period, T_b total bubble period, and A_b the average bubble cross sectional area.

decreases to zero. After the observed projected area is reduced to zero, the bed becomes idle (free from bubble) until the next active period. The gradual increase and decrease in the projected area during the active period is evidence that the bubble is spherical or oval in shape. The peak of the projected area during the bed active period corresponds to the cross-sectional area at the center of the bubble.

To verify the repeatability of the experiment, five different measurements were taken at intervals of 2 min for each air velocity. These five data sets were analyzed separately, and their average was taken to reduce the random error associated with the measurements. For all the beds, the mean variation in the measurements when the experiment is repeated a number of times is less than 2.5%.

3.2. Measurement of Bubble Properties. The bubble diameter in each plane is obtained as the time-averaged diameter of an equivalent sphere having the same projected area as the bubble. As shown in Figure 4, the bubble diameter can be based on the peak projected area assuming a spherical bubble.

$$d_b = \frac{1}{n}\sum\left(\sqrt{\frac{4A_{b,i}}{\pi}}\right) \tag{7}$$

Here, n is the number of times over the measurement period when full bubble passages are observed in the plane, and $A_{b,i}$ is the peak of the projected areas observed in the plane at each bubble passage.

As the bubble activity in each plane is cyclic, Figure 4 shows that it is possible to record the time at which a bubble arrives at a plane and the time at which the next bubble arrives at the same plane. The time interval between the arrivals of two successive bubbles is referred to as the bubble period. For the single bubble observed at every gas velocity, the inverse of the bubble period T_b is described as the bubble frequency, f_b.

$$f_b = \frac{1}{T_b} \tag{8}$$

4. RESULTS AND DISCUSSION

The four different materials considered in this study have different properties that can influence the behavior of a fluidized bed. For example, in addition to the difference in their densities, limestone particles are cohesive and irregular in

DOI: 10.1021/acs.iecr.8b05013
Ind. Eng. Chem. Res. 2019, 58, 2084−2098

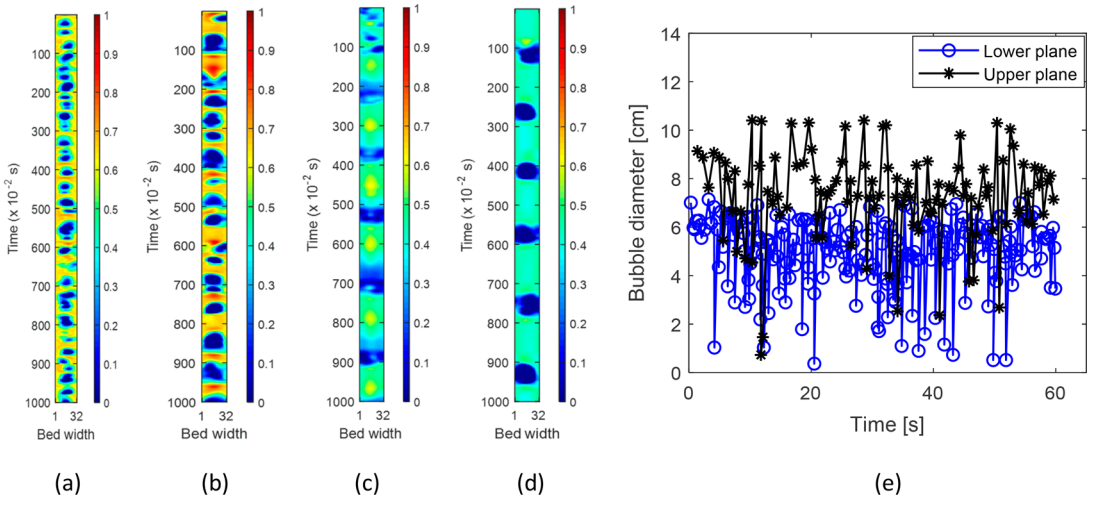

Figure 5. Images for the first 10 s of the flow in beds of 261 μm glass at 0.177 m/s [(a) lower plane and (b) upper plane] and 293 μm limestone at 0.235 m/s [(c) lower plane and (d) upper plane], where the horizontal axis is the position on a line through the bed cross section. Solids fraction increases with the color scale value. (e) Temporal variation of bubble diameter in the lower and upper planes of the glass particles. Bed aspect ratio: 5.6.

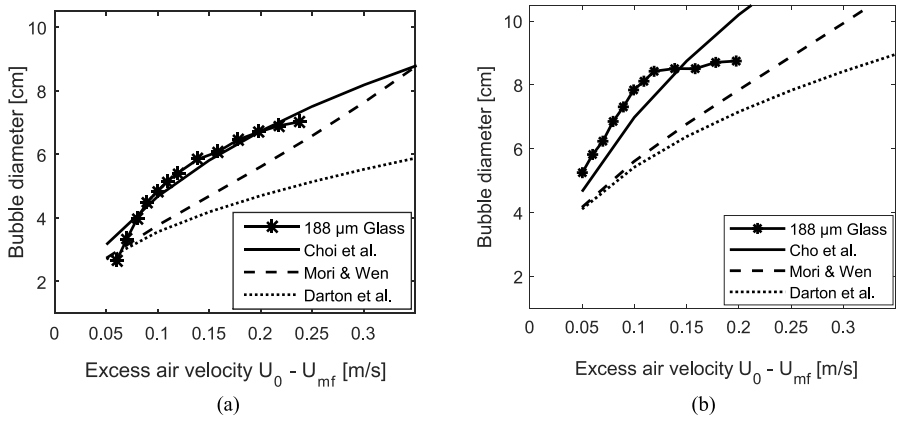

Figure 6. Bubble diameters measured in the bed of 188 μm glass particles compared with the values computed from different correlations: (a) lower plane and (b) upper plane. Bed height = 52 cm.

shape, whereas glass particles are noncohesive and regular in shape. Of all these materials, limestone and glass are the two extremes. Sand particles are rough but not as cohesive as limestone particles, while the molecular sieve particles are smooth and spherical in shape but porous unlike the glass particles. These properties are explored in this study to investigate their effects on the bubbling behavior. Figure 5 compares the bubble behavior in the bed of 293 μm limestone with that in the bed of 261 μm glass particles at about the same excess gas velocity $U_0 - U_{mf}$, 0.097 and 0.095 m/s, respectively. For the bed of glass particles, bubbles rise more frequently in the lower plane (15.7 cm above the distributor), but as they coalesce in the axial direction while moving up to the upper plane at 28.7 cm above the distributor, the rise frequency decreases. This behavior is typical of particles of good fluidity.[4] For the bed of limestone particles, a different behavior can be observed in the two different planes. The bubble frequency in the two planes is almost the same after 1 s. In the lower plane, bubbles spread across the bed and coalesce to form a flat face bubble similar to those at high velocity in Geldart D solid beds. However, Figure 5(d) shows that as the bubbles rise up the bed, splitting and coalescence result in a round face bubble that sticks to the wall, a behavior peculiar to fine rough particles at high gas velocity.[9] In addition to the particle properties, this nonuniform bubbling behavior over the bed of limestone particles may also be attributed to segregation, where the larger particles move down and the smaller particles move up the bed due to bubble passage. Moreover, since the gas velocity $U_0 - U_{mf}$ is higher than that at the minimum slugging condition as shown in Table 2, there are flows of slugs in both beds, though at this moderate gas velocity, the flows of slugs is not continuous as can be seen in Figure 5(e). When slugs flow, the bubble diameter is close to the bed diameter. Between two successive slugs, the bed bubbles freely. There is no slug flow in the lower plane, but the impact of the flow of slugs in the upper plane can still be seen in the planes below. The complete passage of slugs leads to a sudden drop in the bubble diameter at both planes due to escape of gas which results in a temporal higher concentration of solids in the bed.

4.1. Measured versus Predicted Bubble Diameter. Most correlations available in the literature provide bubble volume-equivalent diameter, which has been considered as the true bubble diameter. In this study, the method for measuring the bubble diameter using 2D ECT data is based on the maximum projected bubble area during each bubble passage

DOI: 10.1021/acs.iecr.8b05013
Ind. Eng. Chem. Res. 2019, 58, 2084−2098

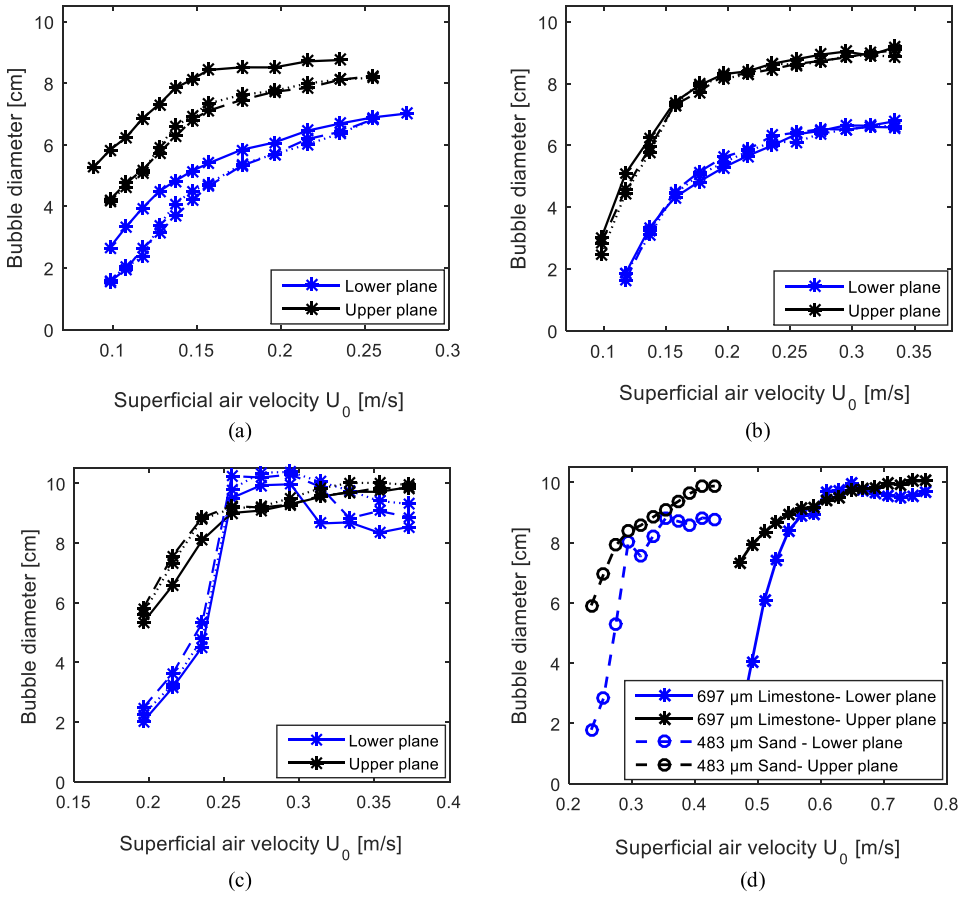

Figure 7. Bubble diameter against superficial gas velocity for (a) 188 μm glass particles, (b) 261 μm glass particles, and (c) 293 μm limestone particles at different aspect ratios h_0/D. Lines: solid, h_0/D = 5; dashed, h_0/D = 5.6; and dotted, h_0/D = 6.2, and for (d) 697 μm limestone and 483 μm particles comparing their behavior with that of 293 μm limestone particles.

assuming a spherical bubble. However, a more realistic bubble size based on ECT measurements can also be obtained by integrating the product of the projected bubble area and bubble velocity with respect to time. The average bubble velocity over a bed height can be calculated from the time it takes a bubble to pass from one plane to another. This method, however, may be limited by the spacing between the measurement planes. As observed in this study, bubbles become larger before reaching the upper plane due to coalescence, especially in the bubbling regime, making it difficult to determine the time it takes a bubble to pass through the two planes by any technique such as the cross-correlation technique. With the use of ECVT (electrical capacitance volume tomography), the bubble volume-equivalent diameter has been obtained by different researchers,[26] with some indications that the measured bubble diameter can be larger than the bed diameter, showing that bubbles are nonspherical in shape when they are large due to wall effects. Figure 6 compares the bubble diameter measured in this study with those obtained from the correlations given by Choi et al.,[17] Mori and Wen,[18] and Darton et al.[19] For the same value of $U_0 - U_{mf}$, the results show that the bubble diameter is larger in the upper plane. The bubble diameter increases with an increase in the excess air velocity except when the bubble (slug) size approaches the bed diameter as can be seen in the upper plane. On average, the trend of the experimental data is the same as those obtained from the three different bubble diameter models. The predictions given by Choi et al. agree well with the bubble diameter measured in the lower plane over the entire range of excess velocity and with that obtained in the upper plane up to the excess velocity of 0.15 m/s. Over the range of velocities shown, the two other models underpredict the experimental data in both planes, but the predictions given by the Mori and Wen correlation are better than those obtained from the Darton et al. model. Moreover, none of the correlations predict the behavior in the slugging regime, where the excess gas velocity is greater than that corresponding to the minimum slugging velocity as given in Table 2. This is probably because these models are developed for a freely bubbling bed. Although the Choi et al.[17] model still predicts the bubble diameter with a good accuracy even in the slugging regime where $U_0 - U_{mf} > 0.107$ m/s, particularly in the lower plane it should be noted that the slug flow is not continuous, and it starts from the upper part of the bed as shown in Figure 5(e). The extent to which the flow of slugs covers the bed height depends on the gas velocity and particles. For this smaller particle size, 188 μm, the lower plane bubbles freely at all gas velocities in the range shown in Figure 6 due to low bubble growth rate. At the upper plane, the bed slugs but not continuous. Since the bubble diameter presented in this study is the time-averaged value as given in eq 7, the bubble diameter depends on the most frequent value recorded between the bubbling and slugging regimes over the measurement period. Increasing the gas velocity increases the chances of slug flow over time. However, this behavior is peculiar to fine and smooth particles. For rough (angular) or large particles, the

DOI: 10.1021/acs.iecr.8b05013
Ind. Eng. Chem. Res. 2019, 58, 2084−2098

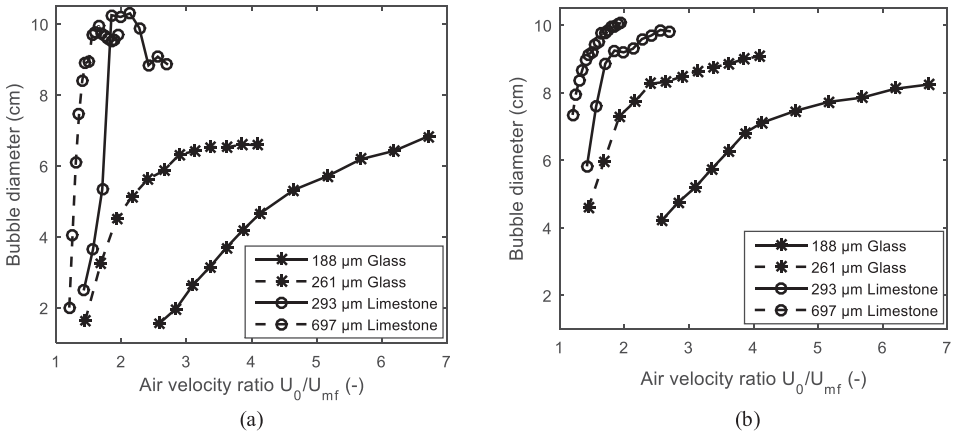

Figure 8. Variation of bubble diameter with the gas velocity ratio, showing the influence of particle sizes on bubble growth: (a) lower plane and (b) upper plane. Bed height = 58 cm.

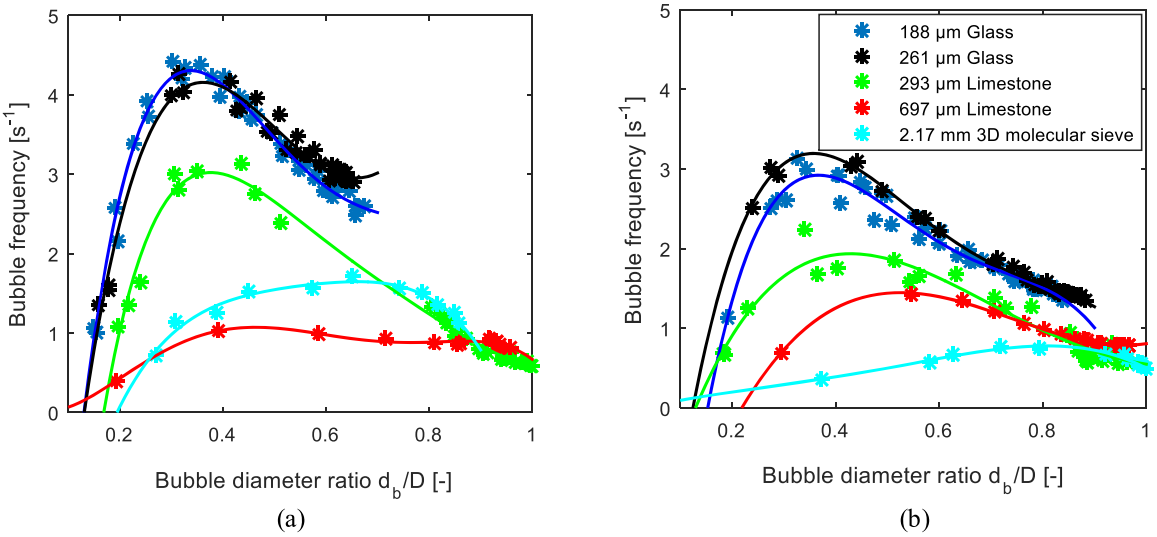

Figure 9. Bubble frequency curve based on bubble diameter, showing the minimum slugging condition at the peak of the curve: (a) lower plane and (b) upper plane.

occurrence of slugs over time and along the bed axis dominates, leading to a larger bubble diameter than that predicted by the Choi et al. model as can be seen in the subsequent sections. The bed of 188 μm glass particles at an initial height of 52 cm is used in this demonstration since it provides results, which are in closest agreement with at least one of the bubble diameter correlations in the literature.

4.2. Effect of Bed Height on Bubble Diameter. The variation of bubble diameter with initial bed height is shown in Figure 7 for the three different powders with smaller particle sizes. As can be seen, changes in the bed height have no significant effect on the bubble diameter for the bed of 261 μm glass particles. Between the higher bed heights h_0/D = 5.6 and 6.2, the respective bubble diameters are also the same for the beds of 188 μm glass and 293 μm limestone particles. However, when the bed height is reduced to h_0/D = 5, the corresponding bubble diameter significantly increases for the bed of 188 μm glass and slightly decreases for the bed of 293 μm limestone particles. This effect is more significant in the upper plane for both powders but seems to decrease at increasing gas velocity. Within the bubbling regime, $U_0 < U_{ms}$, the results in general show that for $h_0/D > 5$ the increase in the bed height has a negligible effect on the bubbling behavior. However, at a higher gas velocity, the behavior may be different due to the chaotic behavior of slug flows, especially in the bed of angular particles as shown in Figure 7(c). Figure 7(c) also suggests that when $U_0 > U_{ms}$, the occurrence of slugs dominates in both planes. Within the gas velocity 0.25−0.3 m/s, the predominant flat face slugs, which spread across the bed diameter, flow in the lower plane, while wall slugs rise over the upper plane, resulting in the difference in the bubble diameter seen in this figure. At a higher gas velocity, the wall slugs become dominant in both planes. The wall slugs are smaller than the flat slugs, and as they flow up the bed, coalescence takes place. This behavior can also be seen in the bed of 697 μm limestone particles and to some extent in the bed of sand particles as shown in Figure 7(d). The 624 μm glass and the molecular sieve particles have similar behavior as those of the two smaller glass particles due to the similarities in their shapes and texture.

4.3. Effect of Particle Size on Bubble Diameter. As shown in Figure 5, bubble behavior can be influenced by the particle properties. Based on the two glass powders with smaller particle sizes and the two limestone powders described in Table 1, the influence of material and particle size on bubble diameter can be seen when the bubble diameter is plotted

DOI: 10.1021/acs.iecr.8b05013
Ind. Eng. Chem. Res. 2019, 58, 2084−2098

against the gas velocity ratio U_0/U_{mf} as presented in Figure 8. The value of U_0/U_{mf} measures the degree of bed expansion due to flow of gas at velocity above that required for minimum fluidization as can be seen in eq 9, where $\Delta e = (H_f - H_{mf})/H_{mf}$ is the degree of bed expansion and ε_{mf} is the bed voidage at the minimum fluidization condition. Equation 9 can be derived assuming that the gas residence time and mass of solid particles remain the same at any given gas velocity.

$$\Delta e = \varepsilon_{mf}\left(\frac{U_0}{U_{mf}} - 1\right) \tag{9}$$

Figure 8 shows that the bubble diameter increases with an increase in the gas velocity ratio U_0/U_{mf}, but the rate of this increase varies between the two materials. Bubbles grow faster in the beds of limestone particles than in those of glass particles. This low resistance to bubble growth in the bed of limestone particles can be attributed to higher bed porosity due to low particle sphericity. As given in Table 1, all the angular (nonspherical) particles have a lower solids volume fraction compared to the round (spherical) glass and molecular sieve particles. The lower initial solids fraction indicates that the bed is more porous and will offer a lower resistance to gas and bubble flows. The rate of increase in the bubble size with U_0/U_{mf} also increases with the particle size in both planes. This behavior may also be attributed to the variation in the resistance to gas flow between the different particle sizes. As the particle size increases, the number of particles per unit volume of the bed decreases, resulting in a lower flow resistance. The higher bubble growth rate indicates that slugs can form easily in the fluidized beds of larger particle sizes. For the limestone particles where the bubble diameter is already closer to the bed diameter in both planes at a higher gas velocity, $U_0/U_{mf} > U_{ms}/U_{mf}$, any section above the upper plane will have the same bubble diameter as close as the bed diameter.

4.4. Effect of Particle Size on Bubble Frequency. Figure 9 shows the bubble frequency against the bubble diameter normalized with the bed diameter. For the particles 188 μm glass, 261 μm glass, and 293 μm limestone, the plots include the data from the three different initial bed heights: 52, 58, and 64 cm. As can be seen, the bubble frequency increases with an increase in d_b/D when the bubble diameter ratio is below a certain value $(d_b/D)_M$. At a value of $(d_b/D)_M$, the bubble frequency is maximum. Beyond $(d_b/D)_M$, the bubble frequency decreases with an increase in the bubble diameter. Since bubble diameter increases as gas velocity is increased, this implies that the bubble frequency increases with an increase in the gas velocity until a peak value and thereafter decreases with a further increase in the gas velocity. The bubble frequency increases due to a higher rate of increase in the bubble rise velocity as the gas velocity increases.[27] At higher gas velocities, when the bubble size approaches that for slugs to flow in the bed, the rate of bubble rise velocity becomes lower. This thus increases the time at which bubbles are observed at a given plane, thereby decreasing the bubble frequency. The peak frequency decreases with an increase in the particle size and from the lower to the upper plane, a behavior which has been similarly observed in the previous studies.[26,28] Since the bubble frequency decreases continuously after the peak value, it shows that the local peak frequency denotes the point of local incipient slugging.

The corresponding value of $(d_b/D)_M$ in each plane defines the local minimum bubble size at which a slug begins to flow in the bed. As shown in the figures, $(d_b/D)_M$ increases along the vertical axis of the bed and with increasing particle size. The bubble diameter at the peak frequency is larger in the upper plane due to bubble coalescence. For the powders shown, $(d_b/D)_M$ is in the range of 0.34−0.7 in the lower plane and 0.38−0.8 in the upper plane. Since the peak bubble frequency corresponds to the point at the local onset of slugging, these results show that slugs will be observed in most beds when the ratio of the bubble diameter to the bed diameter is within 0.34−0.8. The results also agree with the findings of Werther.[29] In a 10 cm bed of fine particles with mean diameter 83 μm, Werther[29] observed that slugs begin to flow when $d_b/D \approx 0.33$, and at this minimum slugging condition, the bubble velocity is at its maximum value. However, as the value of $(d_b/D)_M$ depends on the vertical position in the bed, a wider range of bubble diameters at the peak frequency can also be obtained in the fluidized beds. Figure 9 also shows that for the large or angular particles, the bubble/slug frequency reduces to a value closer to or less than 1.0 s^{-1} when the bubble diameter approaches the bed diameter as also observed in other studies.[10,11] However, for the small and smooth particles, the limiting bubble/slug frequency may be over 1.0 s^{-1} as can be seen in Figure 9(b).

4.5. Maximum Slugging Frequency. Similar to the superficial gas velocity U_{ms} at the onset of slugging, the maximum slugging frequency f_{Ms} is an important parameter that also characterizes a deep fluidized bed and is defined as the bubble frequency at which a slug will begin to flow in the bed. The maximum slugging frequency sets a boundary between the bubbling regime and the slugging regime and also offers a secondary confirmation for the onset of slugging regime. In addition, knowledge about the slugging frequency, particularly its maximum value, is important since this parameter can affect the gas−particle contacting. Moreover, as shown in Figure 10, the average bubble diameter over the bed height at the maximum frequency is lower than that characterizing the bed at the minimum slugging velocity. The normalized bubble diameter at the minimum slugging velocity is also the arithmetic mean of the bubble diameters measured

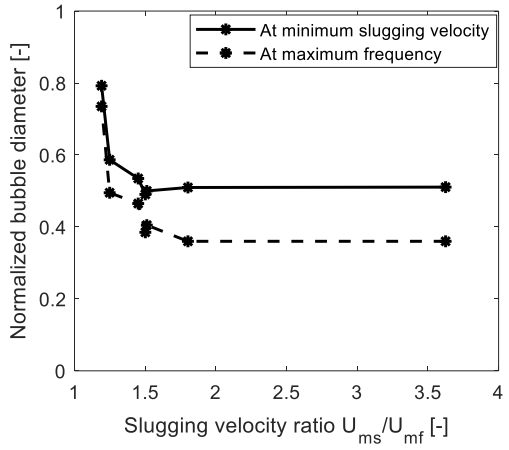

Figure 10. Comparison between bubble diameter at the maximum frequency and that at the minimum slugging velocity for the beds of the glass, limestone, and molecular sieve particles given in Table 1. The bubble diameter for each of the three smaller particles is also averaged over the three different initial bed heights.

DOI: 10.1021/acs.iecr.8b05013
Ind. Eng. Chem. Res. 2019, 58, 2084−2098

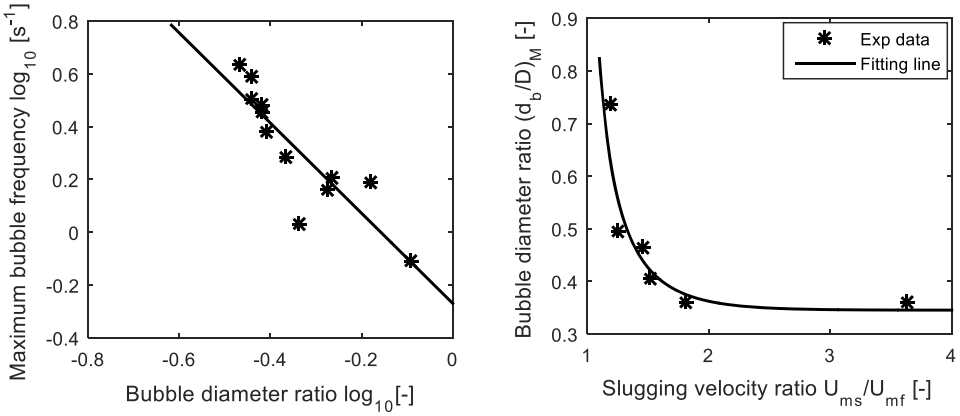

(a) (b)

Figure 11. (a) Maximum bubble frequency versus the bubble diameter at this maximum bubble frequency. (b) Bubble diameter at maximum frequency versus minimum slugging velocity ratio for f_{Ms} model development.

from both planes at the minimum slugging velocity since the two measurement planes lie approximately within the middle of the bed for most of the aspect ratios of 4−5.6 covered. This result therefore shows that operating a fluidized bed at the maximum bubble frequency will prevent slugging in a large portion of the bed while achieving higher gas velocity.

From the previous studies,[30−32] different correlations for predicting slugging frequency within the slugging regime are provided. However, there are no such correlations found for the maximum slugging frequency. Based on the analysis of results in this study, a correlation for the maximum slugging frequency can be proposed. It should also be noted that the maximum slugging frequency corresponds to the maximum bubble frequency before the bed begins to slug.

Figure 11(a) shows the plot of $\log_{10}(f_{Ms})$ against the corresponding bubble diameter ratio $\log_{10}(d_b/D)_M$ for the different powders given in Table 1 including glass, limestone, and the molecular sieve particles. The data in the figure also include those obtained from both planes. The result shows that the maximum slugging frequency decreases with the corresponding bubble diameter. As the dependence of bubble frequency on bubble diameter is independent of the bed material,[25] these data can be fitted to a straight line on the log scale with a regression coefficient (R-square) of 0.77. The linear relationship between the maximum slugging frequency and the corresponding bubble diameter can be represented by eq 10.

$$f_{Ms} = k\left(\frac{d_b}{D}\right)_M^{-1.792} \tag{10}$$

where $k = 0.537\ s^{-1}$.

As the local value of $(d_b/D)_M$ is not known, prediction of the local maximum slugging frequency using eq 10 may be difficult. However, using the average of the values of $(d_b/D)_M$ from both planes, an approximate value for the maximum slugging frequency can be obtained. Figure 11(b) shows the plot of average value of $(d_b/D)_M$ against the gas velocity ratio U_{ms}/U_{mf} at the onset of slugging. The bubble diameter decreases with an increasing value of U_{ms}/U_{mf}. The data in the figure can be fitted with a function described by eq 11.

$$(d_b/D)_M = \left(2.90 - 36.66\exp\left(-2.80\frac{U_{ms}}{U_{mf}}\right)\right)^{-1} \tag{11}$$

Combining eqs 10 and 11, the maximum slugging frequency f_{Ms} (s^{-1}) averaged over the bed height can then be expressed as

$$f_{Ms} = 0.537\left(2.90 - 36.66\exp\left(-2.80\frac{U_{ms}}{U_{mf}}\right)\right)^{1.792} \tag{12}$$

Figure 12 compares the prediction of the proposed model for maximum slugging frequency with the experimental data.

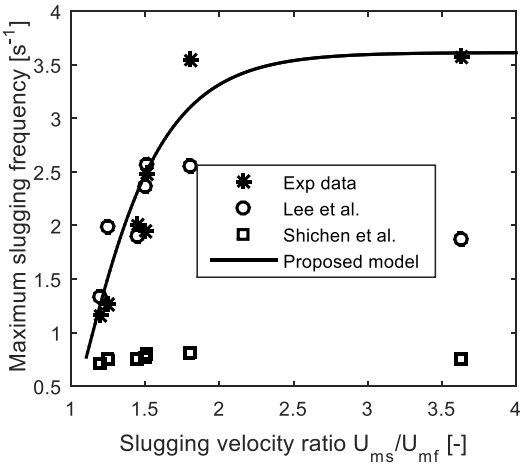

Figure 12. Prediction of maximum slugging frequency using the proposed model compared with results from models in the literature.

The predictions using the correlations given by Lee et al.[30] and Shichen et al.[31] are also shown. The computation of f_{Ms} using the Lee et al. and Shichen et al. correlations are obtained at the superficial gas velocity corresponding to the gas velocity U_{ms} at the onset of slugging. As can be seen, the proposed model, eq 12, predicts the experimental data with reasonable accuracy over a wide range of U_{ms}/U_{mf}. The prediction based on the Lee et al. correlation also agrees with the experimental data for $U_{ms}/U_{mf} < 1.75$. The accuracy of the Lee et al. model in the lower range of U_{ms}/U_{mf} may be due to the range of particle sizes of 450−3000 μm on which the development of the model

DOI: 10.1021/acs.iecr.8b05013
Ind. Eng. Chem. Res. 2019, 58, 2084−2098

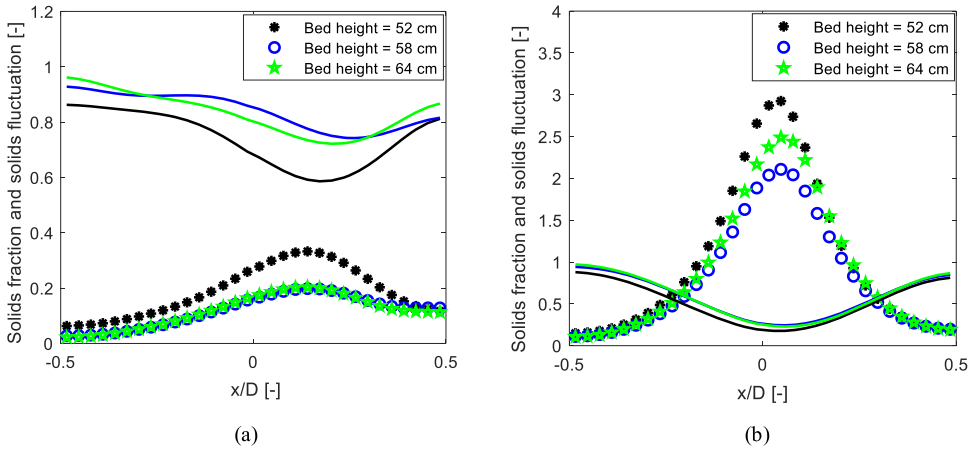

Figure 13. Radial distribution of normalized solids fraction and relative solid fluctuations at the lower planes for the beds of 188 μm glass particles: (a) $U_0 - U_{mf}$ = 0.060m/s. (b) $U_0 - U_{ms}$ = 0.029m/s. Lines: normalized solids fraction. Data points: relative solids fraction fluctuation.

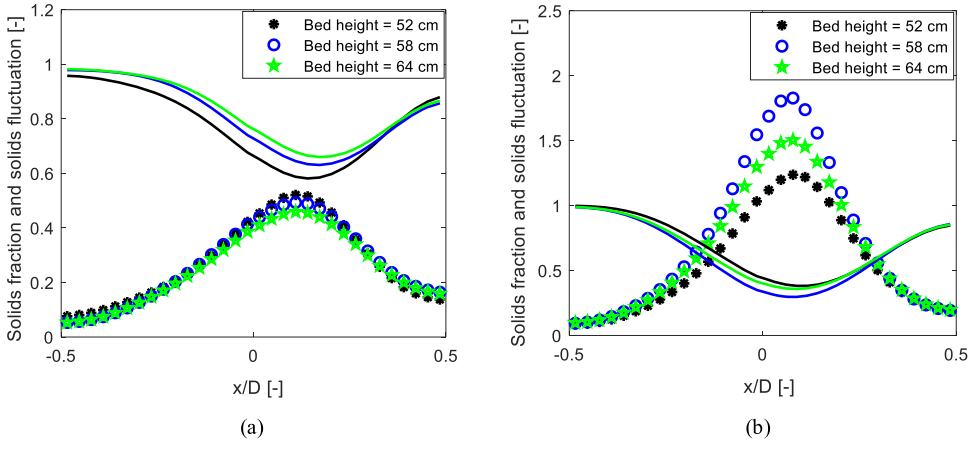

Figure 14. Radial distribution of normalized solids fraction and relative solid fluctuations at the lower planes for the beds of 261 μm glass particles: (a) $U_0 - U_{mf}$ = 0.056m/s and (b) $U_0 - U_{ms}$ = 0.030m/s. Lines: normalized solids fraction. Data points: relative solids fraction fluctuation.

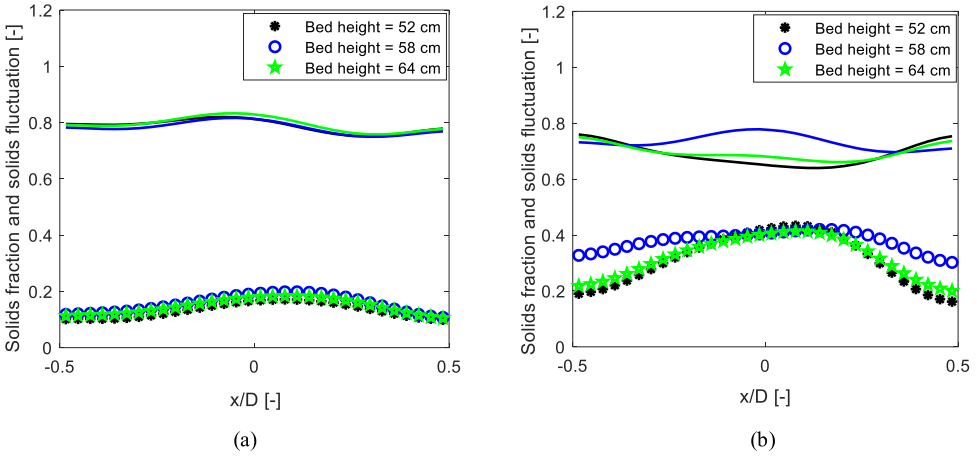

Figure 15. Radial distribution of normalized solids fraction and relative solid fluctuations at the lower planes for the beds of 293 μm limestone particles: (a) $U_0 - U_{mf}$ = 0.058m/s and (b) $U_0 - U_{ms}$ = 0.027m/s. Lines: normalized solids fraction. Data points: relative solids fraction fluctuation.

was based. The Shichen et al. correlation underpredicts the experimental data including those of 697 μm limestone and 624 μm glass particles even though the model was developed based on a particle size of 650 μm. The model might have been developed for a fully developed slug where the slugging frequency approaches 1.0 s^{-1} or less depending on the particles as can be seen in Figure 9, accounting for the inaccuracy in predicting the maximum slugging frequency. Based on these results, the model proposed in this paper can therefore be applied to obtain the maximum bubbling/slugging frequency over a wide range of particle size. Moreover, since the minimum slugging velocity, U_{ms}/U_{mf}, depends on the bed aspect ratio,[3,25] the models given by eqs 11 and 12 can also be

DOI: 10.1021/acs.iecr.8b05013
Ind. Eng. Chem. Res. 2019, 58, 2084−2098

applied in beds of different diameters and heights to a large extent.

4.6. Solids Movement and Distribution of Solids Fraction. In a deep fluidized bed, the higher-pressure drop across the bed may influence the axial bubble distribution. Contrary to shallow beds that are characterized by an even distribution of bubbles, deep beds may be separated into regions of top bubbling zones and regions of bottom quiescent zones. Where a portion of a bed is not bubbling, the solids movement, and thus the required gas−solids mixing in that region, will be jeopardized. The distribution of solids gives an indication of particle mixing in a fluidized bed. Due to bubble formation and passage, the solids are set into oscillate about a fixed position. The degree of movement of solids in the bed at a given gas velocity can be measured by the fluctuations of the solids fraction. The standard deviation of the solids fraction over the measurement period can be used to predict the solids fluctuations in the bed at a given gas velocity. For a given pixel, the standard deviation can be obtained from $\sigma_q = \sqrt{\frac{1}{n-1}\sum(\varepsilon_{sq} - \varepsilon_s)^2}$, where, ε_{sq} is the solids fraction at the pixel $q(i,j)$, and $\varepsilon_s = \frac{1}{n}\sum\varepsilon_{sq}$ is the time average of the solids fraction at that pixel. The indices "i" and "j" locate the pixel in the 32 × 32 plane (Figure 1(b)).

Figures 13, 14, and 15 show the distributions of normalized solids fraction and relative solids fraction fluctuation as a function of the static bed height at the lower plane across the x axis. The normalized solids fraction is obtained from $\varepsilon_{sn} = \varepsilon_s/\varepsilon_{s0}$, while the relative solids fraction fluctuation is computed as $\sigma_{qr} = \sigma_q/\varepsilon_s$, where ε_{s0} is the solids fraction at the fixed state. The value of ε_{sn} ranges from 0 to 1, and it measures the relative permittivity of the solid material. When $\varepsilon_{sn} = 1$, the section of the bed is completely filled with the solid material, but when $\varepsilon_{sn} = 0$, it is completely filled with air. A value in between 0 and 1 means that the bed section is occupied by solids and air. The relative solids fluctuation is used to scale up the effect of gas interactions on the solid particles since $0 < \varepsilon_s \leq 1$, making it easier to compare different bed behavior. The value of σ_{qr} can be less or greater than 1 depending on how severe the gas−solids interaction is. In Figures 13−15, the plots with lines denote the normalized solids fraction, while the data points with the same color represent the corresponding relative solids fraction fluctuation. For each of the beds, two different values of excess velocities are used to compare the effect of particle properties on gas−solids mixing in both bubbling and slugging regimes. For the bubbling regime, the excess velocity above the minimum fluidization velocity $U_0 - U_{mf}$ is kept approximately the same, whereas for the slugging regime the excess velocity above the minimum slugging velocity $U_0 - U_{ms}$ is also approximately the same. The results show that most of the particle movements occur near the center of the beds. The central peak and gradual drop of the solids fluctuations in each bed indicate that particles move upward near the central axis and downward near the walls of the bed in the form of a vortex ring as described in Kunii and Levenspiel[4] for beds of larger diameters. However, there is a significant difference in the bed behavior between the two different materials, glass and limestone particles, at the two different velocities.

For the glass particles, the normalized solids fraction is close to unity near the walls and below unity around the central region, showing that most of the up-flowing gas follows the central axis of the bed. As the bubble rises along the central axis, it pushes the particles by its sides toward the wall and those in its front forward, enhancing gas passage. The emulsion gas tends to follow the region around the central axis due to less resistance to the flow, resulting in the lower solids fraction in this region. When the bubble erupts or coalesces with another bubble, the solids fall back along the sides of the trailing bubble toward the walls. However, as the value of the solids fraction within the central region is below that at the walls, it indicates that only a fraction of the solids carried upward falls back to the plane. This results in an uneven expansion of the bed and slight fluctuations of the solids observed around the wall region. With an increase in the gas velocity, this effect is severe. The region bounded by the central solid movement becomes narrower, increasing the quiescent wall regions. The peak value of the solids fluctuation is high due to passage of slugs. As shown in Figure 5, the passage of the round-nose (axial) slugs increases the wall region due to continuous raining and compression of solids at the sides of the slugs.

For the bed of limestone particles, the distribution of the solids fraction is almost uniform across the bed diameter at the lower gas velocity with the value of ε_{sn} significantly lower than 1.0. This shows that the up-flowing gas is in contact with most of the particles and that the bed expands almost uniformly across the bed cross section. Since the gas distribution is better, the distribution of the solids fraction fluctuation shows that the spread of bubbles is also better than that in the beds of the glass particles. The wider distribution of gas in the limestone bed may be attributed to higher bed porosity due to the nonspherical nature of the particles. At the higher gas velocity, the bed slugs. However, since the rate of occurrence of the flat-face slugs as shown in Figure 5(c) is lower than that of the axial slug shown in Figure 5(b), the fluctuation of the solids fraction in the limestone bed is low compared to that of glass particles at the same excess gas velocity. Figure 15 also shows that as gas velocity is increased, the region bounded by the upward moving particles becomes wider, while the wall region becomes narrower. At this higher gas velocity, the solids fraction distribution is also almost uniform although slightly lower due to an increase in the bed expansion. From these results, it therefore shows that the quality of deep bed fluidization in terms of gas−particles contacting is better in the bed of limestone particles than in that of glass particles.

Moreover, in the bubbling regime, the results clearly show that the effect of bed height on the distributions of solids fraction and solids fluctuation decreases with increasing bed height and with increasing particle size. However, in the slugging regime, the behavior is chaotic. For example, with a bed height 58 cm, the peaks of the solids fluctuation compared to those for the other two heights is the least in the bed of 188 μm glass particles but the greatest in the bed of the larger glass particles. In the bed of limestone particles, the peak values are the same for all the bed heights, but the solids fluctuations spread more evenly at the bed height 58 cm compared to the other heights.

In addition, Figures 13− 15 show that the peak of solids fluctuation is closer to the right wall but shifts toward the central axis as the gas velocity increases. With increasing particle size at the same excess gas velocity, the peak of the fluctuations also moves closer to the central axis due to wider gas distribution. This asymmetric behavior, where the peak of solids fluctuation always lies at the right of the bed central axis, was also observed when the experiments were repeated at the

DOI: 10.1021/acs.iecr.8b05013
Ind. Eng. Chem. Res. 2019, 58, 2084−2098

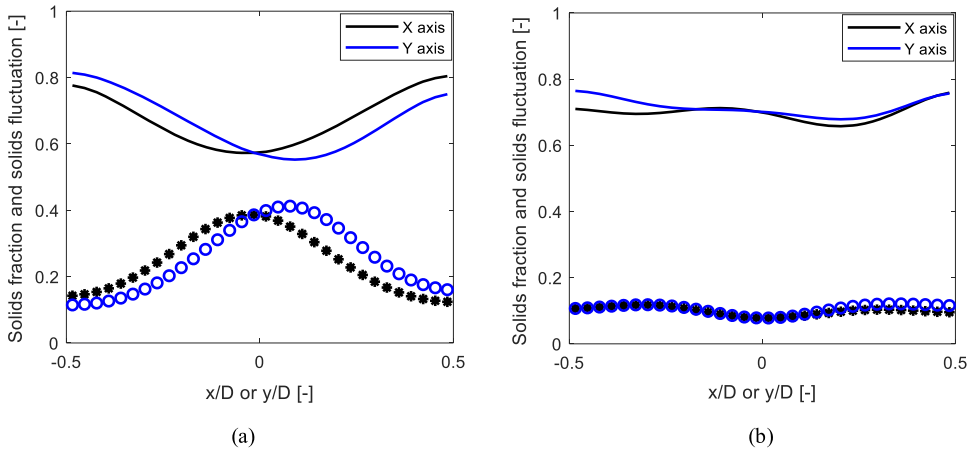

Figure 16. Radial distribution of normalized solids fraction and relative solid fluctuations at the lower planes for the beds of (a) 624 μm glass particles, $U_0 - U_{ms}$ = 0.033m/s, and (b) 697 μm limestone particles, $U_0 - U_{ms}$ = 0.028m/s. Lines: solids fraction. Data points: relative solid fluctuation.

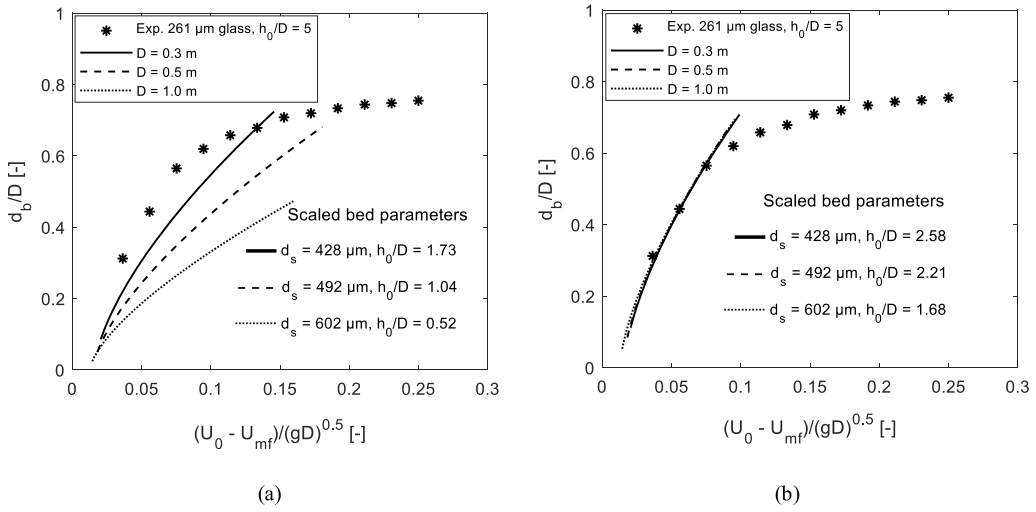

Figure 17. Normalized bubble diameter averaged over a bed height comparing the bubbling behavior in the experimental smaller bed diameter with those in different scaled beds of larger diameters (a) with the same bed height of 52 cm in both experimental and scaled beds and (b) with correctly adjusted bed height for the scaled beds. Scaling laws based on Horio et al.;[34] experimental data and bubble diameter model are as given in Agu et al.[25]

same conditions, indicating a maldistribution of the gas velocity across the bed cross section.

However, the position of the peak of solids fluctuation with respect to the central axis differs between these particles in the *y*-axis (not shown), although the profile of the solids fluctuation as well as the solids fraction is the same as in the *x*-axis. For the higher gas velocity in the *y*-axis, the peak lies at the central axis for the 261 μm glass particles, at the right of the central axis for the 188 μm glass particles, and at the left of the central axis for the limestone particles. When the gas velocity is further increased, the turning points of the solids fraction and fluctuation lie at the central axis in both *x*- and *y*-axes for all the particles, indicating an even distribution of gas/bubbles across the bed. The variation in the orientation of the solids fraction and fluctuation between the *x*- and *y*-axes can be seen clearly in Figure 16 for the beds of 624 μm glass and 697 μm limestone particles at $U_0 - U_{ms} \approx 0.03$m/s. The results also show that the peak of the solids fluctuation lies at different positions between the *x*- and *y*-axes for the glass particles but at the same position in both *x*- and *y*-axes for the limestone particles.

Since the position of the peak of solids fluctuations in either the *x*- or *y*-axis depends on both particle size and gas velocity, the distribution of bubbles in the bed might have also been influenced by the distributor plate. As can be seen in Figure 2, the ratio of the distributor pressure to the bed pressure drop is very low for smaller particles and high for larger particles at the same gas velocity ratio. Increasing the gas velocity increases the distributor pressure drop. With a sufficiently high pressure drop across the distributor, a large number of pores on the plate are active to give a better gas distribution.[4] The maldistribution of the gas velocity from the distributor plate, particularly in the bed of smaller particle sizes, can be minimized by adding a packed bed or porous medium in the plenum below the distributor plate. It should be noted that in this study the distributor pressure drop was kept low to be able to operate all the beds within the range of gas velocities covered since the maximum pressure drop across the air blower is 0.15 bar(g).

4.7. Modeling and Scale-Up. From the results obtained in this study, different correlations for different bubble

DOI: 10.1021/acs.iecr.8b05013
Ind. Eng. Chem. Res. 2019, 58, 2084−2098

properties have been proposed.[25,27] In Agu et al.,[27] models for the bubble velocity, bubble frequency, and bed expansion were presented, while the models for the bubble volumetric flux and bubble diameter averaged over the bed height were proposed in Agu et al.[25] The bubble frequency and bubble diameter models are as given in eqs 13 and 14, respectively.

$$f_b = \left(0.52\left(\frac{d_b}{D}\right)^{1.48} + \gamma u_b^{\beta} d_b\right)^{-1} \tag{13}$$

$$\bar{d}_b/D = 0.848\left(\frac{U_0}{D}\right)^{0.66}\left(1 - c\left(\frac{U_0}{U_{mf}}\right)^{a-1}\right)^{0.66} \tag{14}$$

where u_b is the bubble velocity. All the model parameters γ, β, a, and c depend on whether the bed is in bubbling or slugging regime. While γ and β depend on the particle class, a and c depend on the particle and fluid properties as described in the respective literature. These two models can accurately predict the results presented in this study for different gas velocities, particle sizes, and flow regimes.

As shown in previous sections, different particle types behave differently in the 10.4 cm diameter bed used in this study at their respective initial bed heights. In a larger bed diameter, the behavior shown by the same particles may differ due to higher degrees of freedom in both particle and bubble flows. To obtain a similarity in the behavior shown by any of the powders, a correctly scaled bed of another particle type is required. There are several scaling laws in the literature[33] for achieving a similarity in the fluidized bed behavior between smaller and larger diameter beds. For simplicity, the dimensionless group described in eq 15 as proposed by Horio et al.[34] for attaining a similarity in a bubbling bed is used for a demonstration.

$$\frac{U_0 - U_{mf}}{\sqrt{gD}}, \frac{U_{mf}}{\sqrt{gD}}, \frac{\rho_g}{\rho_s} \tag{15}$$

For the 261 μm glass particles in the bed of dimeter 10.4 cm and initial height 52 cm, for example, Figure 17 shows the behavior when the bed is scaled to larger bed diameters, 30, 50, and 100 cm, using the scaling dimensionless group given in eq 15. The experimental data are the normalized bubble diameter $\bar{d}_b/D$ averaged over the bed height at different gas velocities. The values of $\bar{d}_b/D$ for the scaled beds are determined from eq 14. For the same particle density and air properties, the particle diameter in the scaled bed is obtained by back calculation from the Wen and Yu[35] correlation proposed for predicting the minimum fluidization velocity of a known fluid and particle properties. When the bed height is 52 cm, giving the aspect ratios h_0/D = 1.73, 1.04, and 0.52 for the respective bed diameters, Figure 17(a) shows that there is no similarity between the scaled and the experimental beds. The bubble diameter decreases with decreasing bed aspect ratio, reflecting a characteristic behavior of shallow beds. To match the normalized bubble diameter from the scaled bed to that of the experimental bed, the bed aspect ratio has to be increased as shown in Figure 17(b). The new bed aspect ratio is given as h_{0*}/D_*, where h_{0*} = 52 cm and D_* is a characteristics scaling bed diameter obtained by fitting eq 14 for a given scaled particle properties to the experimental data from the small scale bed. It should also be noted that the similarity attained is only within the bubbling regime as can be seen in Figure 17(b). To achieve a similar behavior in the slugging regime, a different set of scaling dimensionless groups may be applied.

From these results, it therefore shows that the bubbling bed behavior observed in this study can be scaled up using appropriate scaling laws in addition to eq 14.

5. CONCLUSIONS

In this paper, a number of experiments were carried out to deepen the understanding of influence of particle properties and bed height on the behavior of deep bubbling fluidized beds. The powders including limestone, glass, sand, and molecular sieve particles with mean particle sizes in the range of 180−2200 μm were investigated. The bed height was varied between 50 and 65 cm in a 10.4 cm diameter cylindrical bed. The bubble properties were obtained at two different positions in the bed using the information acquired by a dual-plane ECT sensor.

The results show that particle properties influence the bubbling behavior and that the effect of bed height depends on the particle size. The findings of this study are summarized as follows:

- Bubbles grow faster in the bed of limestone particles than in that of glass particles, possibly due to variation in their shapes that influences the bed porosity.
- The rate of bubble growth increases with increasing particle size, basically due to low resistance to gas flow in the bed of larger particles.
- Bubble frequency increases with gas velocity only when the bubble diameter is below a threshold value. At the threshold bubble diameter, the bubble frequency is maximum, and above the threshold value, the bubble frequency decreases with increasing gas velocity.
- The bubble diameter at the maximum bubble frequency increases with increasing particle size.
- When the bubble diameter reaches a value at which the bubble frequency is maximum, the bed begins to slug.
- For rough particles, the slug type can change from flat slugs to wall slugs depending on the gas velocity and axial position in the bed.
- The limiting slug frequency is closer to or less than 1.0 s^{-1} for large or rough particles but may be higher for small and smooth particles.
- Correlations for predicting average maximum bubble frequency and the corresponding bubble diameter are proposed.
- Gas−solid contacting is more effective at higher gas velocity in the bed of limestone particles than in that of glass particles.
- The effect of bed height decreases with increasing aspect ratio within the bubbling regime but may vary within the slugging regime due to the chaotic behavior of slug flows.

With the findings in this paper, understanding of bubbling behavior in deep fluidized beds is enhanced for efficient operations and designs of such systems. The effect of different particle size distributions and gas distributors on deep bed behavior will be considered in further studies.

AUTHOR INFORMATION

Corresponding Author

*E-mail: cornelius.e.agu@usn.no.

DOI: 10.1021/acs.iecr.8b05013
Ind. Eng. Chem. Res. 2019, 58, 2084−2098

ORCID

Cornelius E. Agu: 0000-0002-5339-9794
Christoph Pfeifer: 0000-0002-7747-9297

Funding

This research did not receive any specific grant from funding agencies in the public, commercial, or not-for-profit sectors.

Notes

The authors declare no competing financial interest.

NOMENCLATURE SYMBOLS

A [m^2] = cross-sectional area
D [m] = bed diameter
D_* [m] = characteristic scaled bed diameter
d [m] = diameter
f_b [1/s] = bubble frequency
g [m/s^2] = acceleration due to gravity
H [m] = total bed height
h [m] = vertical position in the bed
h_{0*} [m] = initial bed height for this small bed diameter of 10.4 cm
n [-] = number
T [s] = period
U,u [m/s] = velocity

GREEK LETTERS

ε_s [-] = solids fraction
ρ [kg/m^3] = density
σ [-] = solids fraction standard deviation

SUBSCRIPTS

b = bubble
ba = active bubble
f = fluidized
i = idle/index
M = maximum
mf = minimum fluidization
q = pixel
s = slug/solid
0 = initial/bottom reference

REFERENCES

(1) Toomey, R. D.; Johnstone, H. F. Gaseous fluidization of solid particles. *Chem. Eng. Prog.* **1952**, *48*, 220.
(2) Grace, J. R. Contacting modes and behaviour classification of gas-solid and other two-phase suspensions. *Can. J. Chem. Eng.* **1986**, *64*, 353.
(3) Baeyens, J.; Geldart, D. An investigation into slugging fluidized beds. *Chem. Eng. Sci.* **1974**, *29*, 255.
(4) Kunii, D.; Levenspiel, O. *Fluidization Engineering*, second ed.; Butterworth−Heinemann: Oxford, U.K., 1991.
(5) Gupta, C. K.; Sathiyamoorthy, D. *Fluid Bed Technology in Materials Processing*, first ed.; CRC Press: Boca Raton, FL, 1999.
(6) Wang, T.; He, Y.; Tang, T.; Zhao, Y. Numerical investigation of particle behaviour in a bubbling fluidized bed with non-spherical particles using discrete hard sphere method. *Powder Technol.* **2016**, *301*, 927.
(7) Verma, V.; Padding, J. T.; Deen, N. G.; Kuipers, J. A. M. Effect of bed size on hydrodynamics in 3-D gas-solid fluidized beds. *AIChE J.* **2015**, *61*, 1492.
(8) Verma, V.; Padding, J. T.; Deen, N. G.; Kuipers, J. A. M.; Barthel, F.; Bieberle, M.; Wagner, M.; Hampel, U. Bubble dynamics a in 3-D gas-solid fluidized bed using ultrafast electron beam X-ray tomography and two-fluid model. *AIChE J.* **2014**, *60*, 1632.
(9) Laverman, J. A.; Roghair, I.; Annaland, M. V. S.; Kuipers, H. Investigation into the hydrodynamics of gas-solid fluidized beds using particle image velocimetry coupled with digital image analysis. *Can. J. Chem. Eng.* **2008**, *86*, 523.
(10) Wang, D.; Xu, M.; Marashdeh, Q.; Straiton, B.; Tong, A.; Fan, L.-S. Electrical capacitance volume tomography for characterization of gas-solid slugging fluidization with Geldart group D particles under high temperatures. *Ind. Eng. Chem. Res.* **2018**, *57*, 2687.
(11) Cho, H.; Han, G.; Ahn, G. Characteristics of slug flow in a fluidized bed of polyethylene particles. *Korean J. Chem. Eng.* **2002**, *19*, 183.
(12) Raghuraman, J.; Potter, O. E. Modeling the Slugging Fluidized Bed Reactor. In *Chemical Reaction Engineering − Houston*; Vern, W.; Weekman, Jr.; Dan, L., Eds.; ACS Symposium Series *65*, 1978; pp 400−410.
(13) van Ommen, J. R.; Mudde, R. F. Measuring the gas-solids distribution in fluidized beds − A review. *Int. J. Chem. React. Eng.* **2008**, *6*, 1.
(14) Rautenbach, C.; Mudde, R. F.; Yang, X.; Melaaen, M. C.; Halvorsen, B. M. A comparative study between electrical capacitance tomography and time-resolved X-ray tomography. *Flow Meas. Instrum.* **2013**, *30*, 34.
(15) Nguyen, X. T.; Leung, L. S. A note on bubble formation at an orifice in a fluidized bed. *Chem. Eng. Sci.* **1972**, *27*, 1748.
(16) Verloop, J.; Heertjes, P. M. Periodic pressure-fluctuations in fluidized-beds. *Chem. Eng. Sci.* **1974**, *29*, 1035.
(17) Choi, J. H.; Son, J. E.; Kim, S. D. Bubble size and frequency in gas fluidized beds. *J. Chem. Eng. Jpn.* **1988**, *21*, 171.
(18) Mori, S.; Wen, C. Y. Estimation of bubble diameter in gaseous fluidized beds. *AIChE J.* **1975**, *21*, 109.
(19) Darton, R. C.; La Naueza, R. D.; Davidson, J. F.; Harrison, D. Bubble growth due to coalescence in fluidized beds. *Trans. Inst. Chem. Eng.* **1977**, *55*, 274.
(20) Cai, P.; Schiavetti, M.; De Michele, G. D.; Grazzini, G. C.; Miccio, M. Quantitative estimation of bubble size in PFBC. *Powder Technol.* **1994**, *80*, 99.
(21) Karimipour, S.; Pugsley, T. A critical evaluation of literature correlations for predicting bubble size and velocity in gas-solid fluidized beds - A review. *Powder Technol.* **2011**, *205*, 1.
(22) Geldart, D. Types of gas fluidization. *Powder Technol.* **1973**, *7*, 285.
(23) Agu, C. E.; Tokheim, L.-A.; Eikeland, M.; Moldestad, B. M.E. Determination of onset of bubbling and slugging in a fluidized bed using a dual-plane electrical capacitance tomography system. *Chem. Eng. J.* **2017**, *328*, 997.
(24) *Electrical Capacitance Tomography System. Operating Manual Vol. 1: Fundamentals of ECT*; Process Tomography Ltd., 2009.
(25) Agu, C. E.; Pfeifer, C.; Eikeland, M.; Tokheim, L.-A.; Moldestad, B. M.E. Models for predicting average bubble diameter and volumetric bubble flux in deep fluidized beds. *Ind. Eng. Chem. Res.* **2018**, *57*, 2658.
(26) Weber, J. M.; Mei, J. S. Bubbling fluidized bed characterization using electrical capacitance volume tomography (ECVT). *Powder Technol.* **2013**, *242*, 40.
(27) Agu, C. E.; Tokheim, L.-A.; Eikeland, M.; Moldestad, B. M.E. Improved models for predicting bubble velocity, bubble frequency and bed expansion in a bubbling fluidized bed. *Chem. Eng. Res. Des.* **2019**, *141*, 361.
(28) Lu, Y.; Huang, J.; Zheng, P. A CFD-DEM study of bubble dynamics in fluidized bed using flood fill method. *Chem. Eng. J.* **2015**, *274*, 123.
(29) Werther, J. Bubble Growth in Large Diameter Fluidized Beds. In *Fluidization Technology*; Keairns, D. L., Eds.; Hemisphere Publishing Corporation: Washington, DC, 1976; pp 216−235.
(30) Lee, S. H.; Lee, D. H.; Kim, S. D. Slug characteristics of polymer particles in a gas-solid fluidized bed. *Korean J. Chem. Eng.* **2002**, *19*, 351.

DOI: 10.1021/acs.iecr.8b05013
Ind. Eng. Chem. Res. 2019, 58, 2084−2098

(31) Shichen, C.; Heling, Z.; Feichen, J. A Study of Hydrodynamics Behaviour of the Slugging Fluidized Bed. In *Fluidization*; Kwauk, M. K.; Kunii, D., Eds.; Elsevier: Amsterdam, 1985; pp 75−85.
(32) Noordergraaf, I. W.; VanDijk, A.; Van Den Bleek, C. M. Fluidization and slugging in large-particle systems. *Powder Technol.* **1987**, *52*, 59.
(33) Rudisuli, M.; Schildhauer, T. J.; Biollaz, S. M. A.; van-Ommen, J. R. Scale-up of bubbling fluidized bed reactors − A review. *Powder Technol.* **2012**, *217*, 21.
(34) Horio, M.; Nonaka, A.; Sawa, I.; Muchi, Y. A new similarity rule for fluidized bed scale-up. *AIChE J.* **1986**, *32*, 1466.
(35) Wen, C. Y.; Yu, Y. H. A Generalized Method for Predicting the Minimum Fluidization Velocity. *AIChE J.* **1966**, *12*, 610.

DOI: 10.1021/acs.iecr.8b05013
Ind. Eng. Chem. Res. 2019, 58, 2084−2098

Article 5 (A5)

Models for predicting average bubble diameter and volumetric bubble flux in deep fluidized beds

By

Cornelius E. Agu, Christoph Pfeifer, Marianne Eikeland, Lars-Andre Tokheim and Britt M.E. Moldestad

Published in

Industrial & Engineering Chemistry Research 57 (2018) 2658 – 2669

I&EC research
Industrial & Engineering Chemistry Research

Article

Cite This: Ind. Eng. Chem. Res. 2018, 57, 2658−2669

pubs.acs.org/IECR

Models for Predicting Average Bubble Diameter and Volumetric Bubble Flux in Deep Fluidized Beds

Cornelius E. Agu,*[,†] Christoph Pfeifer,[‡] Marianne Eikeland,[†] Lars-Andre Tokheim,[†] and Britt M. E. Moldestad[†]

[†]Department of Process, Energy, and Environmental Technology, University College of Southeast Norway, 3918 Porsgrunn, Norway
[‡]Department of Material Sciences and Process Engineering, University of Natural Resources and Life Sciences, 1190 Vienna, Austria

ABSTRACT: The average bubble diameter and volumetric bubble flux give indications about the overall bed expansion in a fluidized bed. As these properties depend on the particle properties and fluidized bed regime, their accurate predictions have been a challenge. A new set of models for predicting the average bubble properties within the bubbling and slugging regimes in a deep fluidized bed is proposed, where bubble flux is modeled by $G = U_0 - c\left(\frac{U_0}{U_{mf}}\right)^a U_{mf}$, bubble diameter is modeled by $\bar{d}_b = 0.848G^{0.66}D^{0.34}$ and transition velocity is modeled by $\frac{U_{bs}}{U_{mf}} = 1 + 2.33U_{mf}^{-0.027}(\varphi^{0.35}c_t^{a_t} - 1)\left(\frac{h_0}{D}\right)^{-0.588}$. The models are developed using the information obtained from an experimental setup equipped with a dual-plane electrical capacitance tomography and a porous distributor plate. Although they are empirical, the proposed models are based on the two-phase theory used in describing the bubble flow in a fluidized bed. These models have been validated, and the results show that they can be used to predict the behavior in different regimes at different gas velocities.

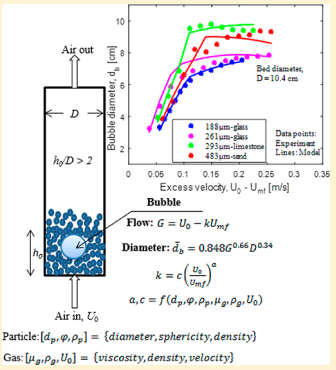

1. INTRODUCTION

Due to numerous advantages, fluidized bed technologies have wide industrial applications. To ensure sufficient residence time for the reacting gases, a fluidized bed reactor can be operated in bubbling or nonbubbling regime. Nonbubbling fluidization is also regarded as particulate fluidization, and it is often desired when high gas residence time is required. In the bubbling fluidized bed, there is higher transfer of heat and mass due to a higher degree of solid movement, but this is at the expense of gas residence time. Particle size is among the factors that influence the fluidized bed regimes. For Geldart A particles,[1] a fluidized bed passes through the particulate regime before it begins to bubble when the gas velocity is further increased, whereas for Geldart B particles, which can be fluidized easily, bubbles appear in the bed as soon as the minimum fluidization velocity is exceeded. Mandal et al.[2] show that a bed of Geldart B particles can exhibit nonbubbling fluidized bed behavior at higher gas velocity when it is formed within the interstitial void space of large and stationary particles. Similar to internals such as vertical tubes and baffles, the large particles serve as bubble breakers, preventing rise and flow of bubbles in the binary beds. In this study, the focus is on the bubbling fluidized beds often applied in small-scale reactors. Designing a bubbling fluidized bed reactor, especially in the preliminary stage, may require a knowledge about the average bed properties. For a given gas velocity, the average bubble diameter and volumetric bubble flux are important parameters that give an indication of bed expansion.

Several correlations[3−6] found in the literature provide the bubble diameter at any position along the axis of the bed. For a given superficial gas velocity above the minimum fluidization velocity, these correlations give the same bubble diameter independent of the particle characteristics. This may probably be because most of these models are developed based on the two-phase theory proposed by Toomey and Johnstone.[7] According to the two-phase theory, the gas velocity in excess of the minimum fluidization velocity constitutes the bubble flow in the bed. On the basis of this assumption, different beds of particles have the same volumetric bubble flux at the same excess gas velocity independent of the particle properties. However, studies of Hilligardt and Werther[8] and Grace and Cliff[9] showed that the actual volumetric bubble flux is lower than that given by the two-phase theory. These findings indicate that many of the existing bubble diameter models may not be appropriate for all systems. Moreover, the bubble diameter and volumetric bubble flux at the same excess gas velocity have been observed to vary between different types of particles. Several factors, which include particle shape and size distribution, can be responsible for this deviation.

Accurate prediction of bubble diameter in deep fluidized beds has also been a challenge for most of the available models because they are developed for freely bubbling beds. For a deep bed where there is a possibility of slug flow, none of these models has been found to predict the behavior in the slugging regime. Even though they are developed for freely bubbling

Received: October 22, 2017
Revised: January 30, 2018
Accepted: February 1, 2018
Published: February 1, 2018

DOI: 10.1021/acs.iecr.7b04370
Ind. Eng. Chem. Res. 2018, 57, 2658−2669

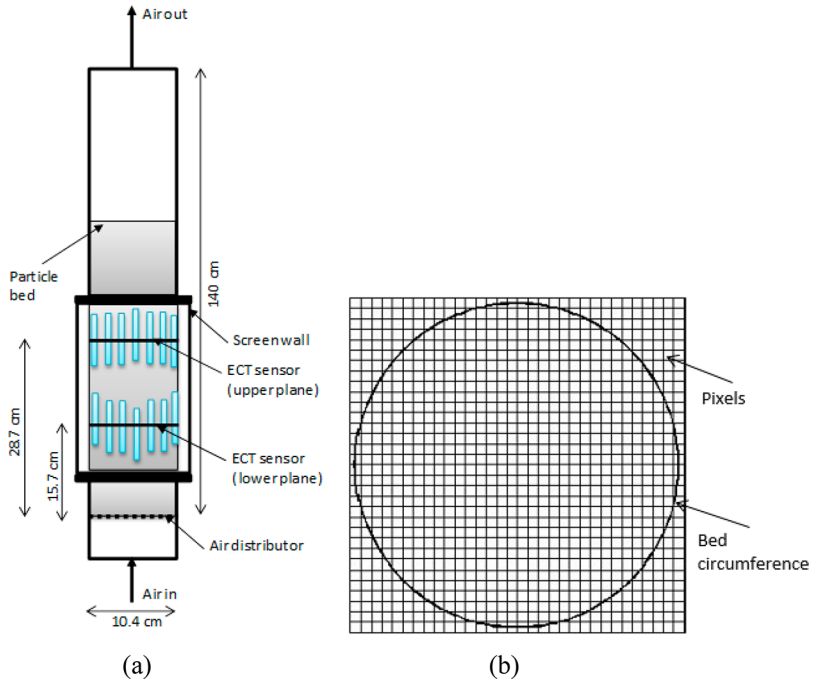

Figure 1. (a) Physical view of a cold fluidized bed with dual-plane ECT sensors for measurement of the solids fraction distribution. (b) Cross section of the bed divided into 812 pixels.

beds, the predictabilities of these different models also differ from one system to another. Karimipour and Pugsley[10] reported that bubble diameters in the beds of Geldart B particles can be best predicted using the models developed by Choi et al.[3] and Mori and Wen,[4] while for Geldart A and D particles, the correlation of Cai et al.[11] is best suited. As most of these correlations are either fully empirical or semiempirical, the measurement techniques used to acquire the experimental data for their developments may also influence their accuracies. Although the use of photographic techniques (video imaging) in two-dimensional (2D) beds provides adequate information about the bubble growth, bubble shape and bubble spatial distribution,[12] this information may not be applicable for three-dimensional (3D) beds. Most of the techniques used for 3D systems do not measure the bubble diameter directly. Depending on the technique, the information acquired during the bubble passage is analyzed to obtain the relevant bubble properties such as bubble holdup, bubble size, and bubble rise velocity. Since these properties are inter-related, measurement of any one of them is often used to determine the other properties.[12] X- and γ-ray absorption techniques are widely applied to obtain properties of a single rising bubble.[5,13,14] For beds with a large diameter, these methods fail to provide accurate bubble properties due to difficulties to identify a particular bubble in the presence of large number of different bubbles. Different types of probes are also employed to measure the bubble properties.[3,5,15−18] The needle capacitance probes are extensively used[5,15] despite their low signal-to-noise ratio. In general, the techniques based on the use of conductivity, inductance, and capacitance probes provide information about the local bubble size, but to obtain the average bubble diameter at any cross-section of the bed requires a considerable effort.[12] Being intrusive devices, probes also have the capacities to change the hydrodynamics of their surroundings, thus acquiring false results. Viswanathan and Rao[12] obtained the bubble holdup from pressure measurements, and provided an iterative procedure for determining the bubble diameter by back-calculations using the relevant correlations relating the bubble rise velocity, bubble holdup, and bubble diameter.

The aim of this study is to develop a set of models for obtaining the average bubble volumetric flux and bubble diameter in deep fluidized beds. Farshi et al.[19] highlighted four different ways to compute the average bubble diameter, which is also called the effective diameter. Each of these methods depends on the total bed height, and the simplest of them is by finding the bubble diameter at the middle of the bed. Due to variety of concepts involved, these different methods may give different results. This paper presents models that are independent of the total bed height for obtaining the average bubble diameter and average volumetric bubble flux. The models are based on the analysis of information obtained from an experimental setup equipped with a dual-plane electrical capacitance tomography (ECT). Being a noninvasive technique, a number of researchers[20−22] have used ECT in their studies to characterize bubbling fluidized beds. ECT sensors provide adequate information about the solids fraction distribution, which can be analyzed to obtain different bubble properties at a given plane in a fluidized bed. In this study, sets of ECT data are acquired and analyzed with different MATLAB codes. From the data analysis, relevant bubble properties are found, which are then used to develop the models for determining the gas velocity at transition between bubbling and slugging regime, the average bubble volumetric flux and the average bubble diameter at different gas velocity. The experimental method used for the data acquisition is presented in the following section, while the details for the proposed model development are given in the subsequent sections.

2. DATA ACQUISITION

2.1. Experimental Setup. In this paper, the experimental setup used to acquire the necessary data consists of a cylindrical

DOI: 10.1021/acs.iecr.7b04370
Ind. Eng. Chem. Res. 2018, 57, 2658−2669

Table 1. Properties of Different Particles Investigated in This Work

materials	mean particle diameter [μm]	density [kg/m^3]	Geldart group	sphericity [-]	fixed bed solids fraction [-]	minimum fluidization velocity [cm/s]
glass beads	188	2500	B	1.0	0.63	4.00
glass beads	261	2500	B	1.0	0.62	8.15
limestone	293	2837	B	0.65	0.51	14.00
sand	483	2650	B	0.72	0.55	17.5
glass	624	2500	B/D	1.0	0.62	23.30
limestone	697	2837	D	0.65	0.49	39.24
molecular sieve	2170	1300	D	1.0	0.6	76.85

column of 104 mm internal diameter equipped with a dual-plane ECT sensor as shown in Figure 1. The sensors are located at two different positions: 15.7 and 28.7 cm above the gas distributor. Each sensor consists of 12 electrodes, uniformly distributed around the measurement plane. The cross-section of each sensor is divided into 32 × 32 square pixels, of which 812 pixels lie within the bed as shown in Figure 1b. Each pixel holds a normalized relative permittivity between 0 and 1. The normalized relative permittivity ϵ_r is a measure of volume fraction of solids in the bed. The volume fraction of particles ϵ_s at any point in the plane is obtained from $\epsilon_s = \epsilon_{s0}\epsilon_r$, where ϵ_{s0} is the fixed bed solids fraction. More detail about this setup can be found in Agu et al.[23]

The experiments were conducted using seven different types of particles. The properties and Geldart classification of these particles are given in Table 1. The minimum fluidization velocity of these different particles were obtained from this setup. The particle densities for the different powders were measured with a gas pycnometer and the particle sizes were obtained from the sieve analysis. The average sphericity of the particles is difficult to measure, although the approximate value can be obtained by fitting experimental pressure drop data to a pressure drop model[24] such as Carman−Kozeny[25] and Ergun[26] equations. However, the value of sphericity obtained from this method may differ from one pressure drop equation to another. For the purpose of model development, the sphericity values given in Table 1 correspond to the average of those listed in the literature for the same materials. The initial bed height in each of the experiments lied between 40 and 65 cm. For the Geldart B glass and limestone particles, the experiments were performed with three different initial bed heights, 52, 58, and 64 cm, to obtain the influence of bed height on the fluidized bed behavior.

In the experiments, dry compressed air was used. The air velocity above the minimum fluidization velocity for the different types of particles was varied in the range of 0.05−0.40 m/s. For each air velocity, the images of the solids distribution at the measurement planes were captured. The image data were recorded for 60 s at a frequency of 100 Hz. Figure 2 is an example of the solids fraction distribution obtained during the experiments. The higher values on the figure color bar indicate higher solid concentrations. The flow of bubbles can be observed in the regions where the solid concentration approaches zero. Considering that bubbles contain some amount of solids,[24] any region bounded by the solids fraction between 0 and 0.2 is regarded as a bubble in this work. On the basis of this bubble−solid threshold, different bubbles are identified. The bubble properties are calculated using the "image processing toolbox" in MATLAB. The number of pixels occupied by a bubble at any given time is obtained and mapped into the actual bubble projected area using $A_b = A\left(\frac{N_b}{N_{pix}}\right)$,

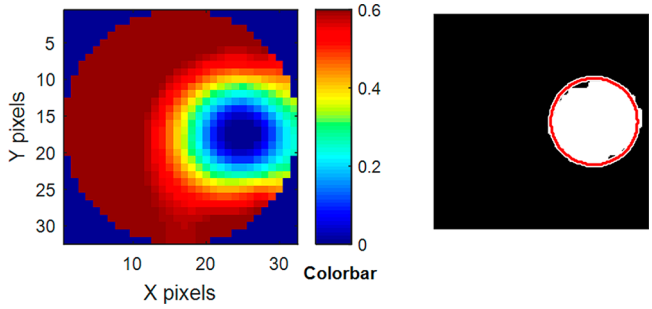

Figure 2. Fluidized bed behavior obtained at the ECT lower plane for the 261 μm glass particles. (a) Distribution of solids where numbers in the color bar give the solids volume fraction. (b) Region occupied by the actual bubble (white) and region defined by approximately spherical bubble (bounded by a red circle).

where A is the cross-sectional area of the bed, N_b is the number of pixels occupied by the bubble, and N_{pix} = 812 is the total number of pixels within the plane. The changes in the values of A_b with time are used to obtain other properties such as bubble frequency and bubble volumetric flow rate as described in the following section.

2.2. Measurement of Bubble Properties. Analysis of the experimental data shows that the passage of bubbles through a given plane is in a regular periodic manner. Figure 3 is the

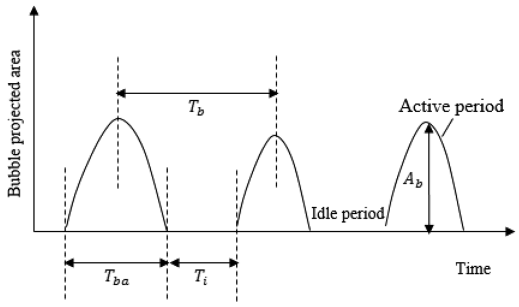

Figure 3. Evolution of bubble-projected area, showing the active and idle periods in a deep bed. Symbols: T_{ba} average active bubble period, T_i average idle period, T_b total bubble period, and A_b average bubble cross-sectional area.

variation of bubble-projected area with time, which is typical for all the beds studied in this work. The projected area increases from zero to a peak value and then decreases to zero as the bubble passes through a given plane. This variation indicates that bubble shape is either spherical or oval. When a bubble first arrives a plane, its projected area is zero. The bubble projected area decreases to zero from a peak value immediately the bubble leaves the plane. The peak of the projected area represents the bubble cross-sectional area through its center.

DOI: 10.1021/acs.iecr.7b04370
Ind. Eng. Chem. Res. 2018, 57, 2658−2669

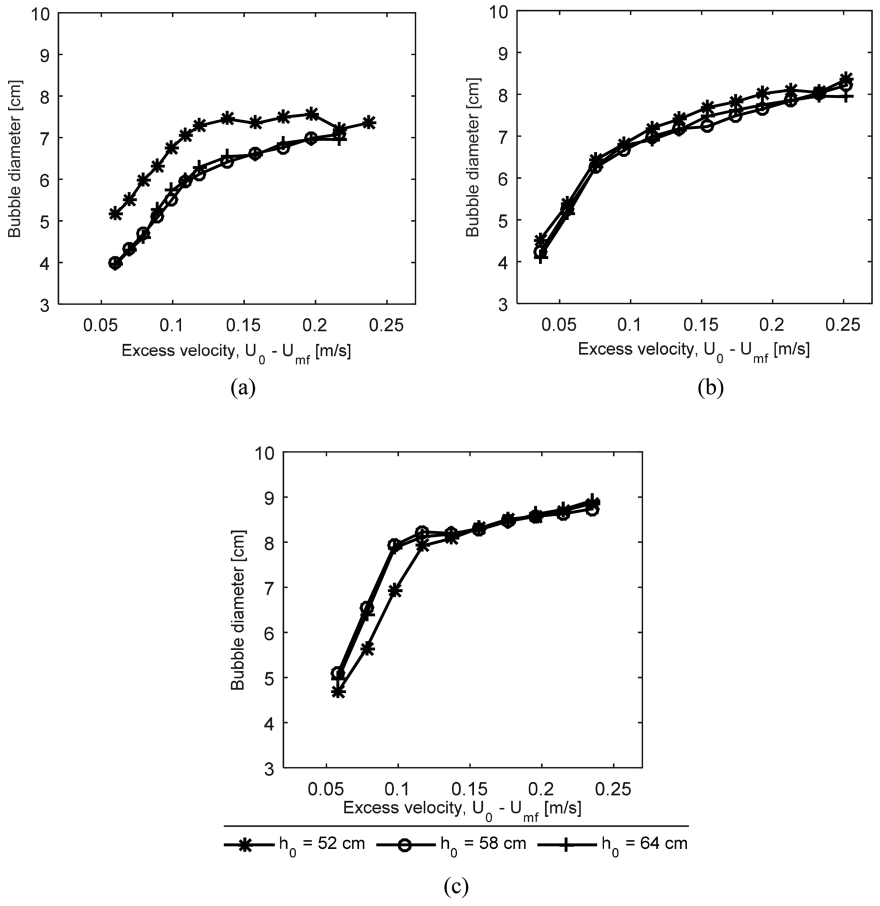

Figure 4. Effect of bed height on the bubble diameters measured at 28.7 cm above the distributor: (a) 188 μm glass particles, (b) 261 μm glass particles, and (c) 293 μm limestone particles.

The time interval between when the bubble arrives and when it completely leaves the plane is described as the active bubble period.

The bubble diameter can be best determined from the bubble equivalent volume.[27] In this study, the 2D ECT sensors employed only provide information about the bubble cross-sectional area and none for the bubble height, making it difficult to measure the bubble volume directly. Assuming a spherical bubble, an approximate bubble size can be obtained from the peak of the projected areas. The time-average bubble diameter can therefore be described by

$$d_b = \frac{1}{n}\sum\left(\sqrt{\frac{4A_{b,i}}{\pi}}\right) \tag{1}$$

where n is the number of peaks of the projected areas recorded over the measurement period and $A_{b,i}$ is the peak of the projected areas during the individual bubble passage. The active bubble frequency f_{ba} is obtained as the reciprocal of the active bubble period:

$$f_{ba} = \frac{1}{T_{ba}} \tag{2}$$

$$T_{ba} = \frac{1}{n}\sum T_{bai} \tag{3}$$

Here T_{ba} is the time-average of the individual active bubble periods, T_{bai}. It should be noted that the concept of active bubble period and frequency are introduced in this work, and that the true bubble period T_b is represented by the sum of the active and idle periods as shown in Figure 3. The true bubble frequency is lower than the active bubble frequency since $T_b > T_{ba}$.

The volumetric bubble flux G is measured by considering the volume of bubble that passes through an observer plane of unit area in a unit time. Considering that the active bubble period is the time for complete bubble passage as shown in Figure 3, the volumetric bubble flux can be expressed as

$$G = \frac{v_b}{AT_{ba}} \tag{4}$$

where v_b is the volume of bubble that passes through a given plane within the time period T_{ba}. For spherical bubbles, $v_b = \frac{\pi}{6}d_b^3$, and eq 4 can be rewritten as

$$G = \frac{\pi}{6A}f_{ba}d_b^3 \tag{5}$$

3. MODEL DEVELOPMENT, RESULTS, AND DISCUSSION

As stated earlier, the proposed models for predicting the average bubble volumetric flux and bubble diameter are independent of initial bed height within the bubbling and slugging regime. This statement is first discussed here.

Figure 4 shows the bubble diameters measured at 28.7 cm above the distributor in different beds of particles: 188 μm glass particles, 261 μm glass particles, and 293 μm limestone

DOI: 10.1021/acs.iecr.7b04370
Ind. Eng. Chem. Res. 2018, 57, 2658−2669

particles. For the beds of 261 μm glass particles, the bubble diameter is independent of the initial bed height at the same gas velocity. For the 293 μm limestone and 188 μm glass particles beds, there are also no differences in the corresponding bubble diameters when the initial bed height is increased from 58 to 64 cm. However, for the height of 52 cm, the bed of 188 μm glass particles shows a significant increase in bubble diameters while that of 293 μm limestone particles shows a decrease in bubble diameters compared with the values recorded at the bed height of 58 cm, although this effect seems to decrease with increasing gas velocity. These results show that the bubble diameter is independent of bed height when the bed height is relatively high. Therefore, the models developed in this section are to be applied in deep beds with large aspect ratios (bed height to bed diameter ratio).

3.1. Model for Average Volumetric Bubble Flux. According to Grace and Clift,[9] the volumetric bubble flux can be expressed as

$$G = U_0 - kU_{mf} \tag{6}$$

Equation 6 is a form of modified two-phase theory describing the bubble flow rate in a fluidized bed, where the parameter k accounts for deviation of the theoretical bubble flow rate from the actual bubble volumetric flow rate. The value of k may vary depending on the superficial gas velocity, bed properties and vertical position in the bed.[28] In a freely bubbling beds, Choi et al.[29] obtained a correlation between the value of k and the gas velocity ratio as given in eq 7, where a and c are constant with values of 0.62 and 1.0, respectively.

$$k = c\left(\frac{U_0}{U_{mf}}\right)^a \tag{7}$$

In the present work, values of k are obtained and analyzed. From the measured volumetric bubble flux, $k = \frac{(U_0 - G)}{U_{mf}}$ can be determined. Figure 5 shows the average values of k against the gas velocity ratios $\frac{U_0}{U_{mf}}$ for four different beds: 483 μm sand, 293 μm limestone, 261 μm glass, and 188 μm glass. In each bed, the trend of variation in k changes as the bed transits from bubbling to slugging regime with increasing gas velocity. The data in the two different regimes can be fitted with separate straight lines as shown in the figure. The extension of the fitting lines beyond the data points is arbitrary. For example, at the vertical intercept where $\frac{U_0}{U_{mf}} = 1$, slugs are never observed. The value of $\frac{U_0}{U_{mf}} = 1$ gives the minimum possible velocity for a bubble to flow, and depending on the particle size, a bubble may or may not exist at this velocity. However, since the lines are used to describe the behavior in the different regimes, the vertical intercepts as well as the line slopes are essential. Also, as shown in Figure 5, the relative standard error for each of the fitting lines is small, indicating that the data points can be well described by the linear functions.

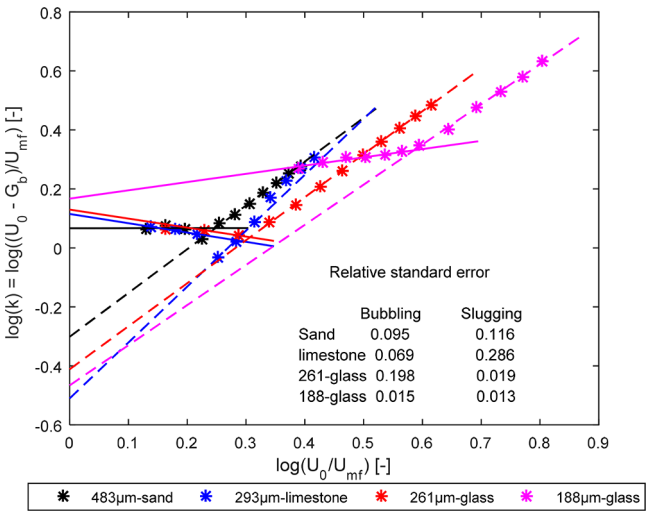

Figure 5. Variation of $k = (U_0 - G)/U_{mf}$ with gas velocity ratio U_0/U_{mf}. Solid lines, bubbling regime; dashed lines, slugging regime.

The slope of each line increases as the flow regime changes from bubbling to slugging. In the bubbling regime, the intercept on the vertical axis is closer to zero for the larger particles, but increases as the particle size decreases. This variation is as expected since smaller particles require significantly higher values of $\frac{U_0}{U_{mf}}$ for the bubble to rise in the beds. In addition, the line slopes in this regime differ between the different beds. The slope decreases between 188 μm glass and limestone and increases thereafter toward the sand particles. This behavior can be attributed to the variation in size and shape between these particles. However, in the slugging regime, sand and glass particles have almost the same line slopes, which differ significantly from that of limestone particles.

On the basis of these linear relationships shown in Figure 5, the expression $k = c\left(\frac{U_0}{U_{mf}}\right)^a$ can be used to describe the behavior in both bubbling and slugging regimes, where a and c are the line slope and the line intercept, respectively. As described above, the values of a and c depend on the particle size, shape, and fluidization regime. Further analysis of these behavior (Figure 5) provides different expressions for values of a and c as given in Table 2. For the slugging regime, the correlations are based on the beds of 188 μm glass, 293 μm limestone, sand, 697 μm limestone, and the 3D molecular sieves particles. The correlations for the bubbling regime are based on the glass particles (188 and 261 μm), the sand particles and two of the Geldart D particles (697 μm limestone and 2.17 mm molecular sieve particles).

Table 2. Correlations for the Proposed Model Parameters a and c

parameters	expressions	validity
	Bubbling Regime	
a	$\varphi^{1.5}(4.168 - 1.389\log(Ar))$	$\log(Ar) < 3.5$
	$\varphi^{1.5}(0.329 - 1.156 \times 10^3\, Ar^{-0.9})$	$\log(Ar) \geq 3.5$
c	$(1.321 + 8.161 \times 10^4\, Ar^{-1.04})^{0.083}$	$\log(Ar) > 0$
	Slugging Regime	
a	$0.725 + 0.230\log(Ar)$	$\log(Ar) < 3.9$
	$1.184 + 8.962 \times 10^4\, Ar^{-1.35}$	$\log(Ar) \geq 3.9$
c	$0.042 + 0.108\log(Ar)$	$\log(Ar) < 4.0$
	$(0.978 - 1.964 \times 10^2\, Ar^{-0.8})^{4.88}$	$\log(Ar) \geq 4.0$

Table 2 shows that the expressions for a and c vary between the bubbling and slugging regimes and that these parameters depend on the particle Archimedes number, $Ar = d_p^3\rho_g(\rho_p - \rho_g)g/\mu_g^2$, where d_p is the particle diameter, φ is the particle sphericity, ρ_p is the particle density, and g is the acceleration

DOI: 10.1021/acs.iecr.7b04370
Ind. Eng. Chem. Res. 2018, 57, 2658−2669

due to gravity. ρ_g and μ_g are the gas density and dynamic viscosity, respectively.

3.1.1. Validation of the Proposed Model for Volumetric Bubble Flux. Using the expressions for the parameters a and c as given in Table 2, the average volumetric bubble flux in deep fluidized beds can be obtained from

$$G = U_0 - c\left(\frac{U_0}{U_{mf}}\right)^a U_{mf} \tag{8}$$

Figure 6 compares the average volumetric bubble flux obtained from eq 8 with the experimental data. As shown in the figure,

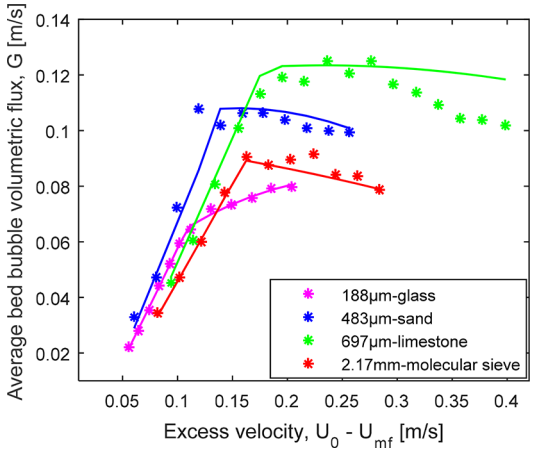

Figure 6. Computed average volumetric bubble flux based on $G = U_0 - c\left(\frac{U_0}{U_{mf}}\right)^a U_{mf}$ (lines) compared with the experimental data (stars) used in the model development.

these results are for the particles used in developing the models in Table 2. Quantitatively, it can be seen that the model results are in good agreement with the experimental data. The transition from bubbling to slugging regimes are well-captured, and the trends of the bubble flux in both regimes correspond with those of the experiments. Figure 7 shows the computed average volumetric bubble flux against the gas excess velocity

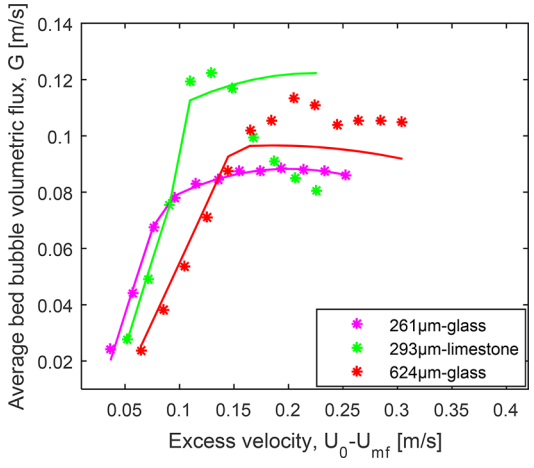

Figure 7. Computed results (lines) based on the proposed model $G = U_0 - c\left(\frac{U_0}{U_{mf}}\right)^a U_{mf}$ compared with the experimental data (stars) from different beds.

for other sets of particles also studied in this work. It can be seen that the model prediction is also in good agreement with the experimental data within the given range of gas velocities.

3.2. Model for Gas Velocity at Bubble to Slug Transition. To apply the models in Table 2 successfully at any given gas velocity, a model at the boundary between the bubbling and slugging regimes is required. Different bubble−slug transition models are available in the literature.[30−33] The transition models provide the velocity at the onset of slugging. Among the available models, the Baeyens and Geldart[30] model is commonly used.

$$U_{ms} = U_{mf} + 0.16(1.3D^{0.175} - h_{mf})^2 + 0.07(gD)^{0.5} \tag{9}$$

.

The Baeyens and Geldart[30] correlation (eq 9) shows that the minimum gas velocity required for a slug to flow in a fluidized bed depends on the particle minimum fluidization velocity, the bed height, and the bed diameter, but the excess velocity $U_{ms}-U_{mf}$ is independent of the fluid and particle properties except where h_{mf} changes with these properties. In this section, a model where $U_{ms}-U_{mf}$ is fully dependent on fluid and particle properties is developed.

As shown in Figure 5, the transition from bubbling to slugging regime occurs at the point of intersection between the two different regime lines. At the intersection, the values of k from the two regimes are the same:

$$c_b\left(\frac{U_{ms}}{U_{mf}}\right)^{a_b} = c_s\left(\frac{U_{ms}}{U_{mf}}\right)^{a_s} \tag{10}$$

Here, a_b and a_s are the corresponding values of a in the bubbling and slugging regimes, c_b and c_s are the respective values of c, and U_{ms} is the superficial gas velocity at the transition. With the values of a and c known in the respective regime, eq 10 can be simplified:

$$\frac{U_{ms}}{U_{mf}} = c_t^{a_t} \tag{11}$$

where $c_t = c_b/c_s$ and $a_t = 1/(a_s - a_b)$.

Figure 8 compares the transition velocity ratios computed from eq 11 with those obtained in the experiment for the different powders. For the spherical particles, the results show that the computed data agree very well with the experimental data. The results differ significantly when the particles are nonspherical. This indicates that at the onset of slugging

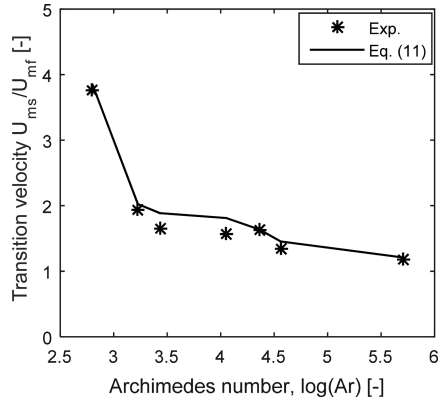

Figure 8. Computed values of gas velocity ratio at the transition from bubbling to slugging regime for different particles using eq 11.

DOI: 10.1021/acs.iecr.7b04370
Ind. Eng. Chem. Res. 2018, 57, 2658−2669

regime, particle shape plays a significant role. In Dimattia et al.,[34] the minimum slugging velocity is also reported to depend on the particle sphericity. Therefore, eq 11 can be modified to account for the influence of particle sphericity at the transition.

By introducing a factor of $\varphi^{0.35}$ in eq 11, the errors associated with the computed values of $\frac{U_{ms}}{U_{mf}}$ for the nonspherical particles are minimized.

$$\frac{U_{ms}}{U_{mf}} = \varphi^{0.35} c_t^{a_t} \tag{12}$$

Contrary to the Baeyens and Geldart model, the results from eq 12 are independent of the bed height and bed diameter. This shows that the transition velocity described by this model can be accurate when the bed is relatively deep, that is, where $\frac{h_0}{D} \geq 4$. To be able to utilize eq 12 in beds with smaller aspect ratios, some modifications are needed.

Agu et al.[23] show that the onset of slugging depends on the bed height especially in the bed of smaller particles, and as given by eq 9, this in general should depend on both h_0 and D. Figure 9 shows the ratio, $\frac{U_{ms}/U_{mf} - 1}{(\varphi^{0.35} c_t^{a_t} - 1)U_{mf}}$, computed against the

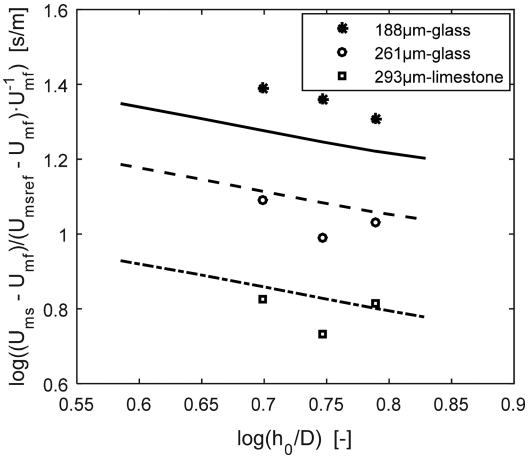

Figure 9. Variation of normalized gas velocity at slugging with bed height. Data points: experiment; lines: Baeyens and Geldart model, eq 9.

bed aspect ratio $\frac{h_0}{D}$ for the different beds: 188 μm glass, 261 μm glass, and 293 μm limestone particles. For the bed of 188 μm glass particles, the experimental data show a continuous decrease in the value of $\frac{U_{ms}/U_{mf} - 1}{(\varphi^{0.35} c_t^{a_t} - 1)U_{mf}}$ with an increase in $\frac{h_0}{D}$, but for the two larger particle beds, some degrees of scatter can be observed. However, the results from the Baeyens and Geldart model suggests that the variation of this normalized slug velocity ratio with $\frac{h_0}{D}$ is linear with a constant slope when $\frac{h_0}{D} < 6.5$ for all the beds. On the basis of this linearity, the following relationship can be derived:

$$\frac{U_{ms}/U_{mf} - 1}{(\varphi^{0.35} c_t^{a_t} - 1)U_{mf}} = \beta \left(\frac{h_0}{D}\right)^{\alpha} \tag{13}$$

Here, α is the slope of the line, taken to be constant for all the beds, and β is the intercept on the vertical axis, which decreases with increasing particle size as can be seen in Figure 9.

Figure 10 shows that the three sets of the experimental data can be fitted with different straight lines of the same slope. It

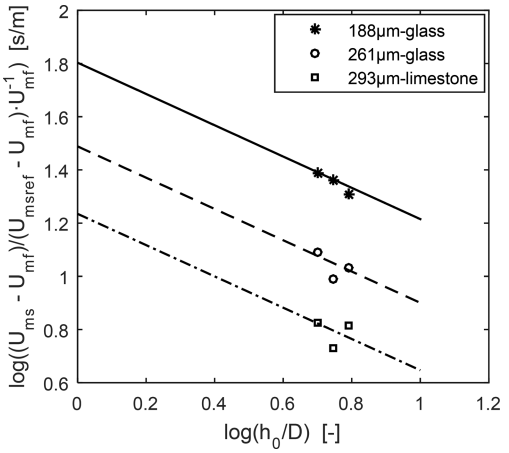

Figure 10. Normalized minimum gas velocity for slugging fitted with constant slope lines.

can be seen clearly that as the particle size increases, the degree of data scatter increases. Dimattia et al.[34] also reported a similar scatter variation. The scatter variation indicates that the dependency of the minimum slugging velocity on the bed height may be insignificant when the particle size is large. The slope of each line in Figure 10 is $\alpha = -0.588$. The value of the intercept β is found to depend on the particle minimum fluidization velocity by the expression $\beta = \gamma U_{mf}^{\theta}$, where $\gamma = 2.33$ and $\theta = -1.027$. From these results, the onset of slugging velocity can be obtained as a function of bed aspect ratio as described by eq 14.

$$\frac{U_{ms}}{U_{mf}} = 1 + 2.33 U_{mf}^{-0.027} (\varphi^{0.35} c_t^{a_t} - 1)\left(\frac{h_0}{D}\right)^{-0.588}; \; 1.5 < \frac{h_0}{D} < 7.2 \tag{14}$$

The coefficient $U_{mf}^{-0.027}$ in eq 14 accounts for the bed expansion above the height at fixed state during the transition. The bed height expansion is also accounted for in the Baeyens and Geldart model by replacing h_0 with h_{mf}. Note that in both eqs 9 and 14, U_{mf} is measured in m/s. Equations 14 and 9 agree very well within the aspect ratio range of 1.5−7.2, and this is taken as the range of validity of this model until further verification is obtained.

3.2.1. Validation of Proposed Model for Onset of Slugging Regime. Equation 14 shows that both U_{ms} and $U_{ms} - U_{mf}$ depend on the fluid and particle properties. This makes the model more robust to predict the onset of slugging velocity in different systems with varying operating conditions, including temperature and pressure. However, reliability of this model also depends on its performance when compared with results from other setups or correlations.

Figure 11 compares the minimum slugging velocity computed from eq 14 with those obtained in the experiments reported by Singh and Roy.[35] The values based on the Baeyens and Geldart model are also shown for comparison. The bed height at minimum fluidization condition, $h_{mf} = \frac{\varepsilon_{s0} h_0}{1 - \varepsilon_{mf}}$, used in eq 9 is based on the average bed height $h_0 = 55$ cm characterizing the present work. The values of solids fraction ε_{s0} in fixed state are given in Singh and Roy[36] for the same set of particles. The void fractions at minimum fluidization ε_{mf} are

DOI: 10.1021/acs.iecr.7b04370
Ind. Eng. Chem. Res. 2018, 57, 2658−2669

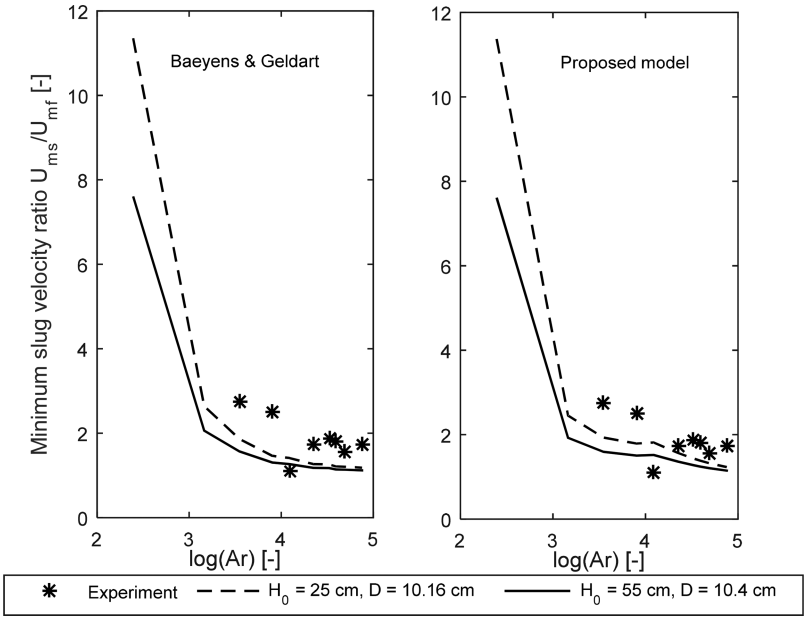

Figure 11. Computed minimum gas velocity for slug flow at different bed heights and bed diameters.

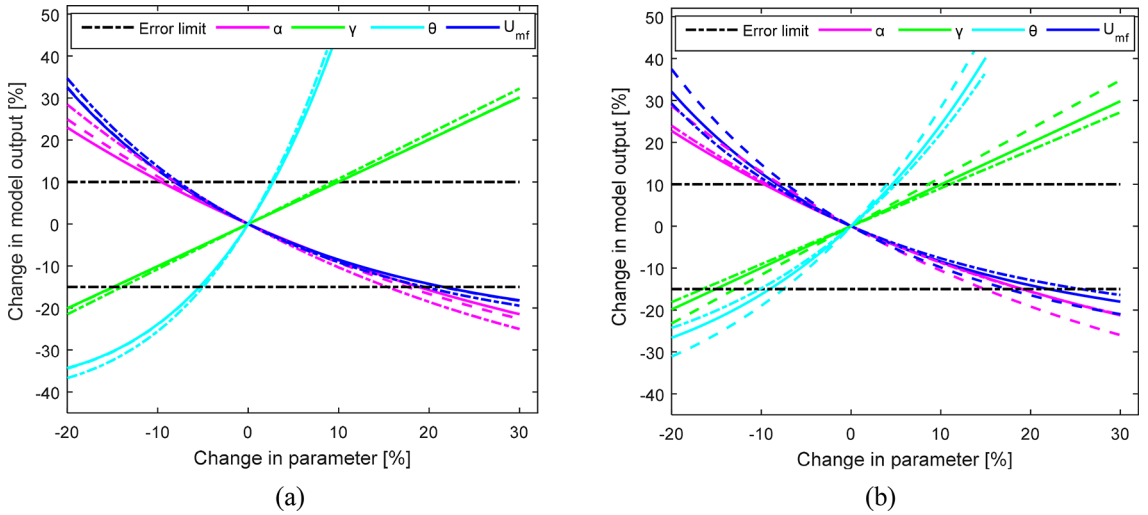

Figure 12. Response of the model $R = \gamma U_{mf}^{\theta}\left(\frac{h_0}{D}\right)^{\alpha}$ for changes in the model parameters at different bed heights. (a) 188 μm glass particles (b) 293 μm limestone particles. Colored lines: $\frac{h_0}{D}$ = 5.0 (solid), $\frac{h_0}{D}$ = 5.6 (dashed), and $\frac{h_0}{D}$ = 6.2 (dotted).

obtained according to Wen and Yu[37] based on a sphericity of 0.70 for all the powders. As shown in Figure 11, the proposed model, eq 14 agrees very well with the Baeyens and Geldart model, and the results from both models are in good agreement with the experimental data.

With a different bed height, h_0 = 25 cm, and the bed diameter D = 10.16 cm reported in Singh and Roy,[35] eqs 9 and 14 also agree very well with each other. Compared with eq 9, the proposed model responds very well to the variations in the bed height to bed diameter ratio. The results from both models also show that the effect of bed height is insignificant when increasing the particle size.

3.2.2. Sensitivity of the Model, Equation 14, to the Fitting Parameters α, γ, θ, and U_{mf}. Although the results presented in Figure 11 show that the proposed bubble-slug transition model can predict the onset of slugging regime with good accuracy, the model validity depends on the particle size due to uncertainty in U_{mf} measurement. In Figure 10, the slopes of the actual lines that can fit separately the data from the three different sets of particles differ from the average value, −0.588 used in the proposed model. The actual intercept of each line also differs from that given by the correlation $\beta = 2.33U_{mf}^{-1.027}$ following the deviation in the corresponding line slope. Due to these deviations, the maximum error associated with the right-hand side of eq 13, $R = \gamma U_{mf}^{\theta}\left(\frac{h_0}{D}\right)^{\alpha}$, lies between −15 and +10% for all the bed heights. It should be noted that changes in the model parameters α, γ, θ, and U_{mf} from their base values may cause a significant change in the model maximum error. On the basis of this, it will be interesting to check the model sensitivity to these parameters within a possible range of changes.

Figure 12 shows how the model responds to small changes in any of the four parameters. These results show that the model

DOI: 10.1021/acs.iecr.7b04370
Ind. Eng. Chem. Res. 2018, 57, 2658−2669

sensitivity is not affected by changes in the bed aspect ratio for changes in any of the parameters within ±10%. For the changes in the parameters α, γ, and U_{mf}, the sensitivity is independent of the bed particles within the ±10% changes. Any slight increase in the parameter θ from the nominal value results in a rapid increase in the model output, although this effect seems to decrease with an increase in the particle size. Hence, due to this high sensitivity, the nominal value $\theta = -1.027$, should be maintained in the model.

As can be seen, a change in α within ±15% has the same effect on the model output as the same change in U_{mf}. Within ±10%, a change in γ has the same magnitude, but the opposite effect as an equal change in α or U_{mf}. This means that any change applied to α should be applied to γ to minimize the model error. Since U_{mf} is also a variable in the model, it follows that the value of γ can be varied from the base value according to the uncertainty in measurement or estimation of U_{mf}.

3.3. Model for Average Bubble Diameter. As shown in Figure 3, the active bubble frequency depends on the bubble size. As the bubble size increases, the time taken by the bubble to pass through a given plane increases. Figure 13 shows how the bubble frequency changes with the bubble diameter. The plotted data are obtained from nine different beds of three different types of particles, 188 μm glass, 261 μm glass, and 293 μm limestone, with three different bed heights, 52, 58, and 64 cm. The plot includes all the data obtained from both planes (15.7 and 28.7 cm above the distributor) for each bed. The result indicates that the relationship between the bubble frequency and the bubble diameter is independent of bed height and can be described by a curve with the following function:

$$f_{ba} = 1.927\left(\frac{D}{d_b}\right)^{1.48} \tag{15}$$

Equation 15 shows that when the bubble diameter is as large as the bed diameter, the active bubble frequency is reduced to 1.93 s^{-1}.

With eq 15, the volumetric bubble flux described by eq 5 can be written as

$$G = 0.321\frac{\pi}{A}\left(\frac{D}{d_b}\right)^{1.48} d_b^3 \tag{16}$$

Substituting $\frac{\pi}{4}D^2$ for A, eq 16 can be simplified to

$$G = m\left(\frac{d_b}{D}\right)^{1.52} D \tag{17}$$

where m is a constant with a value of 1.285 s^{-1}. Keeping the units of d_b and D the same, the unit of G is thus m/s, cm/s, or mm/s depending on what unit assigned to the bed diameter, D.

The results from eq 17 are compared with the experimental data as shown in Figure 14. The average bubble diameters used in these results are those obtained from the experiments with the different types of particles. As can be seen in Figure 14a, the model predicts the behavior in the different beds with a reasonable accuracy. For the beds of particles shown in Figure 14b, the model accuracies are as good as those obtained from the three beds used in the model development, particularly in the bubbling regime. Moreover, the results show that the model

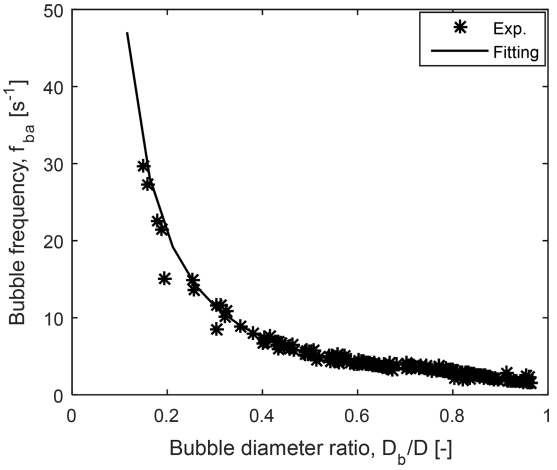

Figure 13. Relationship between the active bubbling frequency and bubble diameter.

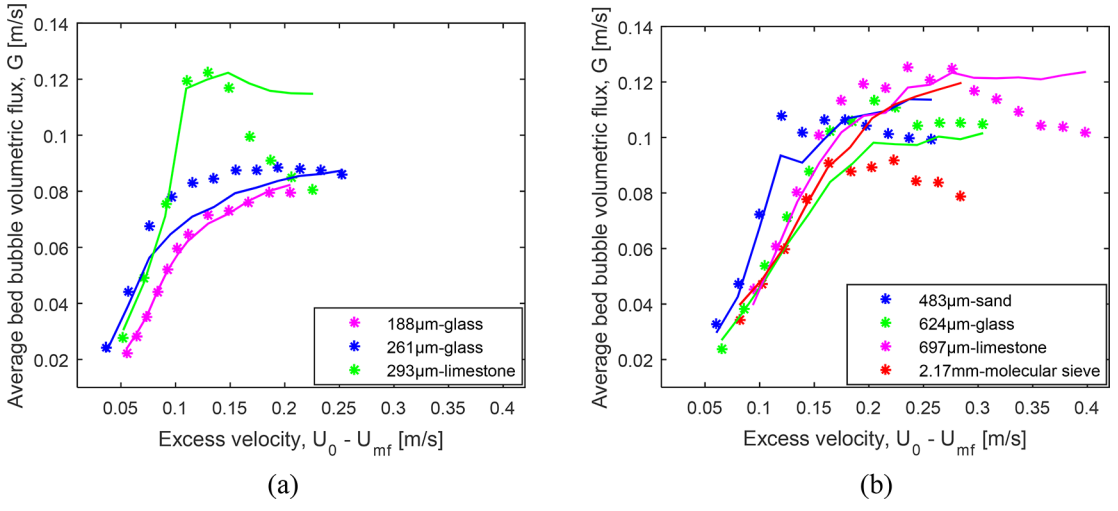

Figure 14. Computed average volumetric bubble flux based on $G = m\left(\frac{d_b}{D}\right)^{1.52} D$ (a) Comparison with data used in the model development. (b) Comparison with data from other different beds.

DOI: 10.1021/acs.iecr.7b04370
Ind. Eng. Chem. Res. 2018, 57, 2658−2669

predicts well the similar behavior observed in the different beds of the same material.

Since the results from both models, eqs 8 and 17, agree very well with the experimental data, a combination of these models can be used to obtain the average bubble diameter in deep fluidized beds at different gas velocities. Assuming that all the bubbles passing over a given bed at a given gas velocity is represented by a single bubble with average diameter $\bar{d}_b$, a combination of eqs 8 and 17 gives

$$U_0 - c\left(\frac{U_0}{U_{mf}}\right)^a U_{mf} = 1.285\left(\frac{\bar{d}_b}{D}\right)^{1.52} D \tag{18}$$

Recasting eq 18, the model for average bubble diameter is given by

$$\bar{d}_b = 0.848\left(U_0 - c\left(\frac{U_0}{U_{mf}}\right)^a U_{mf}\right)^{0.66} D^{0.34} \tag{19}$$

3.3.1. Validation of the Proposed Model for Average Bubble Diameter. For a given gas velocity, the average bubble diameter in a deep fluidized bed can be predicted using eq 19. The unit of gas velocity in this empirical model must be in "per second" and must correspond to any unit assigned to the bed diameter.

To validate this model, the computed average bubble diameters for different beds of particles are compared with the experimental data as shown in Figure 15. These results are

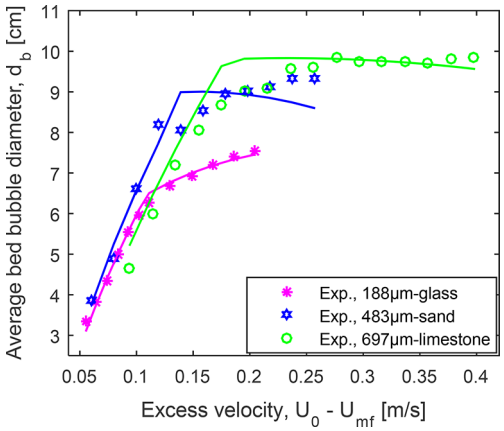

Figure 15. Computed average bubble diameter based on the proposed model $\bar{d}_b = 0.848\left(U_0 - c\left(\frac{U_0}{U_{mf}}\right)^a U_{mf}\right)^{0.66} D^{0.34}$ compared with the experimental data used in the model development.

based on the set of particles used in formulating the model. The results show that a strong agreement exists between the model and the experimental data within the range of gas velocities shown.

Further validation of this model for average bubble diameter is obtained by comparing its results with those from the existing models. In this case, the models proposed by Choi et al.[3] and Mori and Wen[4] are considered since both models are widely applied in predicting the bubble diameters. The Choi et al. and Mori and Wen models are as described in eqs 20 and 21, respectively.

$$(U_0 - U_{mf})[d_b - d_{b0} - 1.132h] + 0.474g^{0.5}(d_b^{1.5} - d_{b0}^{1.5}) = 0$$

$$d_{b0} = \frac{1.63}{g^{0.2}}[A_c(U_0 - U_{mf})]^{0.4} \tag{20}$$

$$d_b = 0.652[A(U_0 - U_{mf})]^{0.4} - (0.652[A(U_0 - U_{mf})]^{0.4} - d_{b0})\exp\left(-0.3\frac{h}{D}\right)$$

$$d_{b0} = 0.00376(U_0 - U_{mf})^2 \tag{21}$$

Here, h [cm] is a vertical position in the fluidized bed, A_c [cm^2] is the catchment area described in Darton et al.,[5] g is in [cm/s^2], and U_0 and U_{mf} are in [cm/s]. The bed average bubble diameters based on these models, eqs 20 and 21, are obtained by integration taken between the two measurement planes, 15.7 and 28.7 cm above the gas distributor.

The results from these three models, the present work, the Choi et al.[3] model, and the Mori and Wen[4] models, are shown in Figure 16 for three different beds of particles. The figure

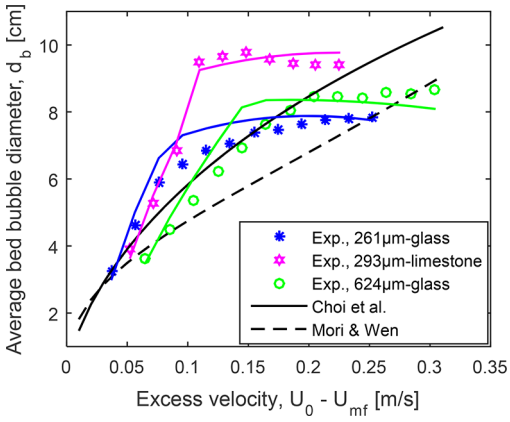

Figure 16. Predictability of the proposed model $\bar{d}_b = 0.848\left(U_0 - c\left(\frac{U_0}{U_{mf}}\right)^a U_{mf}\right)^{0.66} D^{0.34}$ compared with those of existing models eqs 20 and 21.

shows that the bubble diameters computed with the present model agree very well with the experimental data in all the beds. Each of the Choi et al. and Mori and Wen models predicts the same bubble diameter in the different beds at the same excess gas velocity, $U_0 - U_{mf}$. Within the range of the excess gas velocities shown, the results from the Choi et al. model are closer to the experimental data if averaged compared with those from the Mori and Wen model. While neither Choi et al. nor Mori and Wen model predicts the behavior in the slugging regime, the present model reasonably predicts this behavior. This ability to predict the bubble diameters in different regimes of the deep fluidized beds makes the present model superior to these two other models previously described in the literature.

4. SUMMARY OF THE PROPOSED MODELS

The models developed in this paper for predicting the average volumetric bubble flux, the average bubble diameter, and gas velocity of transition from the bubbling to the slugging are summarized in Table 3. The main assumption of these models is that within the bubbling or the slugging regime the average

DOI: 10.1021/acs.iecr.7b04370
Ind. Eng. Chem. Res. 2018, 57, 2658−2669

Table 3. Proposed Models for Average Bubble Flux, Bubble Diameter, and Bubble to Slug Transition Velocity

fluidized bed parameter	model
volumetric bubble flux	$G = U_0 - c\left(\frac{U_0}{U_{mf}}\right)^a U_{mf}$
bubble diameter	$\overline{d}_b = 0.848\left(U_0 - c\left(\frac{U_0}{U_{mf}}\right)^a U_{mf}\right)^{0.66} D^{0.34}$
gas velocity at bubble to slug transition	$\frac{U_{ms}}{U_{mf}} = 1 + 2.33U_{mf}^{-0.027}(\varphi^{0.35}c_t^{a_t} - 1)\left(\frac{h_0}{D}\right)^{-0.588}$

volumetric bubble flux and bubble diameter are independent of the initial bed height, h_0. However, the expressions for the transition velocity indicates that the bed height is an important parameter for determining the regime of operation.

The dependency of the model parameters a and c on the particle and fluid properties makes it possible for the model to predict unique bubble diameter in fluidized beds of different particles with the same excess gas velocity, $U_0 - U_{mf}$. It should be noted that the expressions for G and $\overline{d}_b$ are discontinuous over the entire range of gas velocity $1 < \frac{U_{bs}}{U_{mf}} < \frac{U_0}{U_{mf}}$. The discontinuity over this velocity range is due to the expressions for a and c that are different in the two different regimes. However, within each of the regimes, $1 < \frac{U_0}{U_{mf}} < \frac{U_{bs}}{U_{mf}}$ and $\frac{U_0}{U_{mf}} > \frac{U_{bs}}{U_{mf}}$, the expressions for G and $\overline{d}_b$ are continuous and differentiable.

5. CONCLUSIONS

A fluidized bed can be operated in bubbling or nonbubbling regime depending on the Geldart class of the bed particles. For a bubbling fluidized bed, the bubble properties also depend on the particle properties and fluidized bed regime (freely bubbling or slugging), making their accurate predictions a challenge. This paper presents a set of new models for predicting the average volumetric bubble flux, average bubble diameter and gas velocity at the transition between bubbling and slugging regimes in deep fluidized beds:

Bubble flux:

$$G = U_0 - c\left(\frac{U_0}{U_{mf}}\right)^a U_{mf}$$

Bubble diameter:

$$\overline{d}_b = 0.848G^{0.66}D^{0.34}$$

Transition velocity:

$$\frac{U_{bs}}{U_{mf}} = 1 + 2.33U_{mf}^{-0.027}(\varphi^{0.35}c_t^{a_t} - 1)\left(\frac{h_0}{D}\right)^{-0.588}$$

The model parameters a, c, a_t, and c_t depend on the fluid and particle properties, and their correlations with these properties are also presented in this paper. In the slugging regime where $\frac{U_0}{U_{mf}} > \frac{U_{bs}}{U_{mf}}$, the same models are applied but with different correlations for the parameters a and c.

These models are developed based on the analysis of data obtained from a cylindrical setup equipped with a dual-plane electrical capacitance tomography. Although the models are empirical, they are also based on the two-phase theory used in describing the bubble flow in fluidized beds.

These models have been tested with different types of particles having mean diameters in the range of 130−2200 μm, and their results are consistent with different experimental data. The models capture the behavior in different regimes of deep fluidized beds at increasing gas velocity. The dependency of the model for average bubble diameter on the bed diameter increases its applicability for design purposes. However, these models require further validation with experimental data based on different measurement techniques as well as bed height to diameter ratio less than 4.

AUTHOR INFORMATION

Corresponding Author

*E-mail: cornelius.e.agu@usn.no.

ORCID

Cornelius E. Agu: 0000-0002-5339-9794

Notes

The authors declare no competing financial interest.

NOMENCLATURE

A	bed cross-sectional area, m^2
Ar	dimensionless particle Archimedes number
a	dimensionless fitting index
c	dimensionless fitting coefficient
D	bed diameter, m
d	diameter, m
$\overline{d}$	average diameter, m
f	frequency, s^{-1}
G	volumetric bubble flux, m/s
g	acceleration due to gravity, m/s^2
gas	
h	vertical position in the bed, m
h_0	initial bed height, m
i	index
k	dimensionless two-phase bubble flow deviation coefficient
log	logarithm function to base 10
m	dimensionless model coefficient
N, n	numbers
R	right-hand-side of a model
T	period, s
U	superficial gas velocity, m/s
v	volume, m^3

Greek Symbols

α	dimensionless fitting index
β	fitting coefficient, s/m
ε	dimensionless void fraction
ε_s	dimensionless solids fraction
θ	dimensionless fitting index
ρ	density, kg/m^3
φ	dimensionless particle sphericity
μ	dynamic viscosity, Pa·s
γ	fitting coefficient, (m/s) θ^{-1}

Subscripts

b	bubble
ba	active bubble
bs	bubble to slug transition
g	acceleration due to gravity, m/s^2
gas	
p	particle
s	solid
t	transition

DOI: 10.1021/acs.iecr.7b04370
Ind. Eng. Chem. Res. 2018, 57, 2658−2669

0 (zero) initial state or entry position

REFERENCES

(1) Geldart, D. Types of Gas Fluidization. *Powder Technol.* **1973**, *7*, 285.
(2) Mandal, D.; Vinjamur, M.; Sathiyamoorthy, D. Hydrodynamics of Beds of Small Particles in the Voids of Coarse Particles. *Powder Technol.* **2013**, *235*, 256.
(3) Choi, J. H.; Son, J. E.; Kim, S. D. Bubble Size and Frequency in Gas Fluidized Beds. *J. Chem. Eng. Jpn.* **1988**, *21*, 171.
(4) Mori, S.; Wen, C. Y. Estimation of Bubble Diameter in Gaseous Fluidized Beds. *AIChE J.* **1975**, *21*, 109.
(5) Darton, R. C.; La Naueza, R. D.; Davidson, J. F.; Harrison, D. Bubble Growth due to Coalescence in Fluidized Beds. *Trans. Inst. Chem. Eng.* **1977**, *55*, 274.
(6) Cranfield, R. R.; Geldart, D. Large Particle Fluidization. *Chem. Eng. Sci.* **1974**, *29*, 935.
(7) Toomey, R. D.; Johnstone, H. F. Gaseous Fluidization of Solid Particles. *Chem. Eng. Prog.* **1952**, *48*, 220.
(8) Hilligardt, K.; Werther, J. Local Bubble Gas Hold-up and Expansion of Gas/solid Fluidized Beds. *Ger. Chem. Eng.* **1986**, *9*, 215.
(9) Grace, J. R.; Clift, R. On the Two-phase Theory of Fluidization. *Chem. Eng. Sci.* **1974**, *29*, 327.
(10) Karimipour, S.; Pugsley, T. A Critical Evaluation of Literature Correlations for Predicting Bubble Size and Velocity in Gas-solid Fluidized Beds - A review. *Powder Technol.* **2011**, *205*, 1.
(11) Cai, P.; Schiavetti, M.; De Michele, G.; Grazzini, G. C.; Miccio, M. Quantitative Estimation of Bubble Size in PFBC. *Powder Technol.* **1994**, *80*, 99.
(12) Viswanathan, K.; Rao, D. S. Measurement of Bubble Size in Fluidized Beds. *Ind. Eng. Chem. Process Des. Dev.* **1984**, *23*, 573.
(13) Rowe, P. N. Prediction of Bubble Size in a Gas Fluidized Bed. *Chem. Eng. Sci.* **1976**, *31*, 285.
(14) Rowe, P. N.; Everett, D. J. Fluidized Bed Bubbles Viewed by X-rays. *Trans. Inst. Chem. Eng.* **1972**, *50*, 42.
(15) Werther, J. Effect of Gas Distributor on the Hydrodynamics of Gas Fluidized Beds. *Ger. Chem. Eng.* **1978**, *1*, 66.
(16) Davidson, J. F.; Harrison, D. *Fluidized Particles*; Cambridge University Press: London, 1963.
(17) Yasui, G.; Johanson, L. N. Characteristics of Gas Pockets in Fluidized Beds. *AIChE J.* **1958**, *4*, 445.
(18) Burgess, J. M.; Calderbank, P. H. The Measurement of Bubble Properties in Two-phase Dispersions-III: Bubble Properties in a Freely Bubbling Fluidized-bed. *Chem. Eng. Sci.* **1975**, *30*, 1511.
(19) Farshi, A.; Javaherizadeh, H.; Hamzavi-Abedi, M. A. An Investigation of the Effect of Bubble Diameter on the Performance of Gas-solid Fluidized Bed Reactor and Two-phase Modelling of Bubbling Fluidized Bed Reactor in Melamine Production. *Pet. Coal* **2008**, *50*, 11.
(20) Chandrasekera, T. C.; Li, Y.; Moody, D.; Schnellmann, M. A.; Dennis, J. S.; Holland, D. J. Measurement of Bubble Size in Fluidized Beds Using Electrical Capacitance Tomography. *Chem. Eng. Sci.* **2015**, *126*, 679.
(21) Wang, H.; Yang, W.; Dyakowski, T.; Liu, S. Study of Bubbling and Slugging Fluidized Beds by Simulation and ECT. *AIChE J.* **2006**, *52*, 3078.
(22) Makkawi, Y. T.; Wright, P. C. Electrical Capacitance Tomography for Conventional Fluidized Bed Measurements- Remarks on the Measuring Technique. *Powder Technol.* **2004**, *148*, 142.
(23) Agu, C. E.; Tokheim, L.-A.; Eikeland, M.; Moldestad, B. M. E. Determination of Onset of Bubbling and Slugging in a Fluidized Bed Using a Dual-plane Electrical Capacitance Tomography System. *Chem. Eng. J.* **2017**, *328*, 997.
(24) Kunii, D.; Levenspiel, O. *Fluidization Engineering*, 2nd ed.; Butterworth-Heinemann: Boston, MA, 1991.
(25) Carman, P. C. Fluid Flow through Granular Beds. *Trans. Inst. Chem. Eng.* **1937**, *15*, 150.
(26) Ergun, S. Fluid Flow through Packed Column. *Chem. Eng. Prog.* **1952**, *48*, 89.
(27) Verma, V.; Padding, J. T.; Deen, N. G.; Kuipers, J. A. M. Effect of Bed Size on Hydrodynamics in 3-D Gas-solid Fluidized Beds. *AIChE J.* **2015**, *61*, 1492.
(28) Yang, W. C. *Handbook of Fluidization and Fluid-Particle Systems*; Marcel Dekker, Inc.: New York, 2003.
(29) Choi, J. H.; Son, J. E.; Kim, S. D. Generalized Model for Bubble Size and Frequency in Gas-fluidized Beds. *Ind. Eng. Chem. Res.* **1998**, *37*, 2559.
(30) Baeyens, J.; Geldart, D. An Investigation into Slugging Fluidized Beds. *Chem. Eng. Sci.* **1974**, *29*, 255.
(31) Shaul, S.; Rabinovich, E.; Kalman, H. Generalized Flow Regime Diagram of Fluidized Beds Based on the Height to Bed Diameter Ratio. *Powder Technol.* **2012**, *228*, 264.
(32) Ho, T. C.; Yutani, N.; Fan, L. T.; Walawender, W. P. The Onset of Slugging in Gas Fluidized Beds with Large Particles. *Powder Technol.* **1983**, *35*, 249.
(33) Broadhurst, T. E.; Becker, H. A. Onset of Fluidization and Slugging in Beds of Uniform Particles. *AIChE J.* **1975**, *21*, 238.
(34) Dimattia, D. G.; Amyotte, P. R.; Hamdullahpur, F. Slugging Characteristics of Group D Particles in Fluidized Beds. *Can. J. Chem. Eng.* **1997**, *75*, 452.
(35) Singh, R. K.; Roy, G. K. Prediction of Minimum Slugging Velocity, Bubbling Bed Index and Range of Bubbling Fluidization in Cylindrical and Non-cylindrical Gas-solid Fluidized Beds. *Indian J. Chem. Technol.* **2008**, *15*, 85.
(36) Singh, R. K.; Roy, G. K. Prediction of Minimum Bubbling Velocity, Fluidization Index and Range of Particulate Fluidization for Gas-solid Fluidization in Cylindrical and Non-cylindrical Beds. Powder. *Powder Technol.* **2005**, *159*, 168.
(37) Wen, C. Y.; Yu, Y. H. A Generalized Method for Predicting the Minimum Fluidization Velocity. *AIChE J.* **1966**, *12*, 610.

DOI: 10.1021/acs.iecr.7b04370
Ind. Eng. Chem. Res. 2018, 57, 2658−2669

Article 6 (A6)

Improved models for predicting bubble velocity, bubble frequency and bed expansion in a bubbling fluidized

By

Cornelius Emeka Agu, Lars-Andre Tokheim, Marianne Eikeland and Britt M.E. Moldestad

Published In

Chemical Engineering Research and Design 141 (2019) 361 - 371

Contents lists available at ScienceDirect

Chemical Engineering Research and Design

journal homepage: www.elsevier.com/locate/cherd

Improved models for predicting bubble velocity, bubble frequency and bed expansion in a bubbling fluidized bed

Cornelius Emeka Agu, Lars-Andre Tokheim, Marianne Eikeland, Britt M.E. Moldestad*

Department of Process, Energy and Environmental Technology, University of South-Eastern Norway, 3918 Porsgrunn, Norway

ARTICLE INFO

Article history:
Received 21 July 2018
Received in revised form 5 October 2018
Accepted 2 November 2018
Available online 17 November 2018

Keywords:
Bubble velocity
Bed expansion
Bubble frequency
Fluidized bed
Slug rise velocity

ABSTRACT

An efficient design and operational control of a fluidized bed reactor relies on accurate prediction of bubble properties. This paper employs measurement of bed void fraction in determining the bubble velocity in a given bed. An analytical model is developed for bubble rise velocity, which shows that the rise velocity of a single bubble is proportional to the rate of change of the bubble-projected area. Based on the model for bubble rise velocity, a correlation for bubble velocity is obtained as given by $u_b = \varphi_N\left(U_0 - U_{mf}\right) + 12.51\varphi_D\left(U_0 - U_{mf}\right)^{0.362} d_b{}^{0.52}$. Bubble frequency is also modelled and presented as $f_b = \left(0.52\left(\frac{d_b}{D}\right)^{1.48} + mu_b^n d_b\right)^{-1}$, and bed expansion due to bubble flow in a larger particle bed ($Ar \geq 400$) is modelled by $\Delta e = \left[1 - 0.0873\left(U_0 - U_{mf}\right)^{-0.362}\left(\frac{U_0}{D}\right)^{0.66}\left(1 - \gamma\left(\frac{U_0}{U_{mf}}\right)^{\beta-1}\right)^{0.66}\right]^{-1} -$ 1. The three models have been validated against experimental data and the results show that the bubble velocity model has a better prediction accuracy than the existing models for Geldart B and D particles with prediction errors of 15.5% and 12.0%, respectively. The results also show that the proposed bed expansion model predicts better than the existing models in the literature.

1. Introduction

In bubbling fluidized bed reactors, the diameter and rise velocity of bubbles can be used to obtain the bed expansion, which helps in determining the reactor effective volume and residence time. In addition to reactor design, the bubble properties at a given gas velocity are also used to characterize bubbling behaviour in fluidized beds. This paper is aimed at presenting a set of models that can be used to predict bubble velocity and bubble frequency in a fluidized bed for a wide range of particle and bed properties, and also a model for predicting the overall bed expansion in a bubbling fluidized bed regime.

There are different correlations for predicting bubble velocity in the literature (Karimipour and Pugsley, 2011) but their prediction accuracies vary from one system to another. However, no available literature clearly presents a model for obtaining the bubble frequency. In the slugging regime, few correlations are available (Lee et al., 2002; Noordergraaf et al., 1987). The available models for the slug frequency are correlations assuming a fully developed slug where the slug size is closer to the bed diameter. The slug frequency models may also be limited to a large particle (or rough small particle) bed since bubbles in such a bed can easily grow to the size of the bed diameter (Kunii and Levenspiel, 1991). For a bed of small spherical particles, a slug may have a fully

* *Corresponding author.*
E-mail addresses: cornelius.e.agu@usn.no (C.E. Agu), Lars.A.Tokheim@usn.no (L.-A. Tokheim), Marianne.Eikeland@usn.no (M. Eikeland), britt.moldestad@usn.no (B.M.E. Moldestad).
https://doi.org/10.1016/j.cherd.2018.11.002

Nomenclature

A	Cross sectional area, m^2
Ar	Dimensionless particle Archimedes number
a	Instantaneous cross-sectional area, m^2
D	Bed diameter, m
d	Diameter, m
$\overline{d}$	Average diameter, m
Δe	Dimensionless bed expansion
f	Frequency, s^{-1}
G	Volumetric bubble flux, m/s
g	Acceleration due to gravity, m/s^2
h	Vertical position in the bed from distributor, m
H	Total bed height, m
k	Dimensionless model coefficient
k_1	Dimensionless slug flux correction coefficient
k_2	Dimensionless wall coefficient on slug rise
m	Dimensionless model coefficient
n	Model parameter
r	Radial position, m
t	Time, s
T	Period, s
U	Superficial gas velocity, m/s
u_b	Bubble velocity, m/s
u_{br}	Single bubble rise velocity, m/s
v	Volume, m^3
z	Axial position, m

Greek symbols

α	Dimensionless wall coefficient on bubble
β	Dimensionless model parameter
δ_b	Dimensionless bubble volume fraction
ε	Dimensionless void fraction
$\emptyset$	Dimensionless bubble flux correction coefficient
φ	Dimensionless particle sphericity
φ_D, φ_N	Model coefficients
γ	Dimensionless model parameter

Subscripts

b	Bubble
ba	Active bubble
f	Fluidized
fm	Maximum frequency
i	Idle
mf	Minimum fluidization
ms	Minimum slugging
p	Solid particle
0	Initial/inlet position

developed size far less than the bed diameter even at a very high gas velocity. The prediction of bed expansion is generally based on the two-phase theory, where it is assumed that the bed void fraction is a linear combination of bubble volume fraction and gas volume fraction in the emulsion phase of the bed (Kunii and Levenspiel, 1991). The bed expansion obtained based on this theory depends on the bubble velocity and bubble volumetric flow rate, the accurate predictions of which have been a challenge. The bubble volumetric flow rate is usually obtained based on the two-phase theory (Toomey and Johnstone, 1952), although there are other types of models (Hilligardt and Werther, 1986; Grace and Cliff, 1974) accounting for the shortcomings of this theory. Based on the form of modified two-phase theory proposed by Grace and Cliff (1974), Agu et al. (2018) proposed a model for predicting the bubble volumetric flux, which depends on the particle properties including the sphericity. However, different models (Hepbasli, 1998; Singh et al., 1999; Geldart, 2004) are also available for the bed expansion in a fluidized bed.

To characterize a fluidized bed behaviour, different measurement techniques are used. These techniques include the invasive probe technique (Werther, 1974; Choi et al., 1988) and the non-invasive tomographic technique (Wang et al., 2018; Maurer et al., 2015; Li et al., 2018; Du et al., 2005; Hulme and Kantzas, 2004). For measurement of bubble velocity, two measurement sensors separated at a fixed position are often used. The time taken by a bubble to pass from the lower to the upper sensor is obtained using a reconstruction technique such as the cross-correlation technique. One difficulty in this measurement method is identifying a single bubble as it rises across the two sensors. Near the distributor or when the gas velocity is very low, a large number of bubbles is often present, making it difficult to identify which bubble that passes the measurement sensors at a given time. Depending on the spacing between the sensors, the shape and size of the bubble may also change before reaching the upper sensor due to coalescence or splitting of the bubble. Moreover, the bubble velocity obtained using this method is an average value within a section of the bed. The minimum spacing required between two sensors to avoid signal interference makes it difficult to measure the absolute local bubble velocity. This paper employs the measurement of bubble volumetric flow rate and bubble volume fraction to determine the local bubble rise velocity. The bubble volume fraction is calculated from the two-phase theory assuming that the emulsion-phase voidage is the same as the local bed void fraction at the minimum fluidization condition. Using a two-plane ECT (electrical capacitance tomography) sensor, the local bed void fraction for a given gas velocity is measured at different locations in the bed. From the analysis of the changes in the projected area of a spherical bubble, a model for bubble rise velocity is developed. The model coefficient is obtained by fitting the analytical bubble velocity with the measured bubble velocity. In the subsequent sections, a model for predicting the bubble frequency based on the local bubble velocity is developed, and finally an expression for predicting bed expansion in the bubbling regime is developed. The results are presented and discussed.

2. Analysis of bubble flow

In a bubbling fluidized bed, bubble velocity u_b is generally given as in Eq. (1), following some modifications of the Davidson and Harrison (1963) model.

$$u_b = \emptyset\left(U_0 - U_{mf}\right) + u_{br} \tag{1}$$

$$u_{br} = \alpha\sqrt{g d_b} \tag{2}$$

Here, U_0 is the superficial gas velocity, U_{mf} is the minimum fluidization velocity of the bed material and u_{br} is the bubble rise velocity. The coefficient $\emptyset$ accounts for presence of more than one bubble and their effect on the rising of an individual bubble (Kunii and Levenspiel, 1991). The coefficient α in Eq. (2) accounts for possible wall effects on the rising of a single bubble, whereas g and d_b are the gravity constant and the bubble diameter, respectively. There are different values for α being used (Davidson and Harrison, 1963; Rowe and Partridge, 1965; Rowe and Yacono, 1976; Wallis, 1969) depending mainly on the particle size (solids classification according to Geldart (1973)). In addition to Eq. (1), other models for bubble velocity are also available (Rowe and Yacono, 1976; Dry et al., 1984). This section introduces a new model for bubble rise velocity and a model for bubble frequency.

For a single bubble rising through a fluidized bed, a typical time variation of its projected area is shown in Fig. 1(a). The bubble-projected area at a given time is shown in Fig. 1(b). Fig. 1(a) shows that when one bubble passes through a plane,

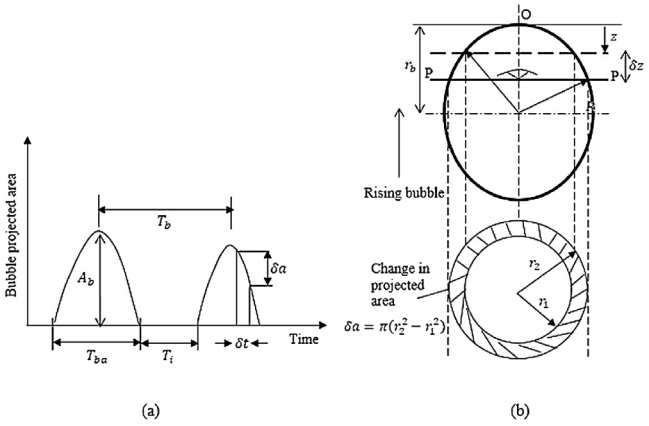

Fig. 1 – Variation of bubble-projected area (a) evolution with time (b) changes with vertical axis.

there is a time lag before another one can be observed. The time frame between when a bubble arrives and when it completely leaves a plane is described as the active period T_{ba}. The time between arrivals of two successive bubbles to the fixed plane is the bubble period, T_b, and the time at which the plane is free of bubbles is the bed idle period, T_i.

2.1. *Bubble rise velocity*

Considering an isolated wakeless spherical bubble rising through a fluidized bed, different cross-sectional areas (projected areas) can be observed at different times at the plane P-P. As shown in Fig. 1, the bubble-projected area changes from $a_1 = \pi r_1^2$ to $a_2 = \pi r_2^2$ as the bubble rises through a vertical distance δz within a time interval δt.

By geometry, the radii r_1 and r_2 can be related to the bubble radius $r_b = d_b/2$, when $z < r_b$, by

$$r_1^2 = z(2r_b - z) \tag{3}$$

$$r_2^2 = (z + \delta z)[2r_b - (z + \delta z)] \tag{4}$$

Multiplying both sides of Eqs. (3) and (4) by π and taking the difference of the resulting equations, the change in the bubble projected area $\delta a = \pi\left(r_2^2 - r_1^2\right)$ is then expressed after simplification as

$$\delta a = \pi(2r_b - 2z - \delta z)\,\delta z \tag{5}$$

Dividing Eq. (5) through by δt, the change in the value of a for a small change in time becomes

$$\frac{\delta a}{\delta t} = \pi(2r_b - 2z - \delta z)\frac{\delta z}{\delta t} \tag{6}$$

For the limit when $\delta t \to 0$, $\delta z \to 0$. Then, Eq. (6) becomes

$$\frac{da}{dt} = \pi(2r_b - 2z)\frac{dz}{dt} \tag{7}$$

In Eq. (7), the rate of change of the vertical displacement z is the bubble rise velocity, thus $u_{br} = \frac{dz}{dt}$.

$$\frac{da}{dt} = \pi(2r_b - 2z)\,u_{br} \tag{8}$$

Dividing through by the bed cross-sectional area $A = \pi D^2/4$ to normalize Eq. (8).

$$\frac{1}{A}\frac{da}{dt} = \frac{4\pi(2r_b - 2z)}{\pi D}\left(\frac{u_{br}}{D}\right)$$

$$\frac{1}{4A}\frac{da}{dt} = \left(\frac{2r_b - 2z}{D}\right)\left(\frac{u_{br}}{D}\right) \tag{9}$$

Let $k = \frac{2(r_b - z)}{D}$, then

$$u_{br} = \left(\frac{D}{4Ak}\right)\frac{da}{dt} \tag{10}$$

For a given bed, Eq. (10) shows that the bubble rise velocity is proportional to the rate of change of the projected area with time. The value of the model parameter k depends on the bubble diameter and time. Therefore, the time-averaged value of k for a given bubble will be required to obtain the velocity with which the bubble rises uniformly through a given plane in the bed. The variation of the average value of k with the flow condition can be determined from experiments. It should be noted that normalizing Eq. (8) with the bed cross sectional area makes the model constant k dimensionless. For this reason, the model in Eq. (10) can be used regardless of the bed diameter for which the k value was obtained.

Assuming that the time-variation of the bubble-projected area follows a parabolic function, $a = 4A_b\left(t/T_{ba} - (t/T_{ba})^2\right)$, it can be shown that $\left[\frac{da}{dt}\right]_{t=0} = \frac{4A_b}{T_{ba}}$ and $\left[\frac{da}{dt}\right]_{t=T_{ba}/2} = 0$. The average value of $\frac{da}{dt}$ is then

$$\frac{da}{dt} = \frac{2A_b}{T_{ba}} \tag{11}$$

where $A_b = \pi d_b^2/4$ is the bubble-projected area through its centre. The bubble properties T_{ba} and A_b can be measured in an experiment. The active bubble period strongly depends on the bubble diameter. The larger a bubble is, the longer it takes to pass through an observer plane. In Agu et al. (2018), a correlation relating $1/T_{ba}$ with the bubble diameter d_b is proposed as described in Eq. (12), where the time is measured in seconds.

$$\frac{1}{T_{ba}} = 1.927\left(\frac{d_b}{D}\right)^{-1.48} \tag{12}$$

Combining Eqs. (10), (11) and (12) yields

$$u_{br} = 1.927A_b\left(\frac{D}{2Ak}\right)\left(\frac{d_b}{D}\right)^{-1.48}$$

$$u_{br} = \frac{0.9635}{k}\left(\frac{d_b}{D}\right)^{2}\left(\frac{d_b}{D}\right)^{-1.48}D$$

$$u_{br} = \frac{0.9635}{k}\left(\frac{d_b}{D}\right)^{0.52}D \tag{13}$$

2.2. *Bubble frequency*

From Fig. 1(a), the total bubble period T_b can be expressed as

$$T_b = T_{ba} + T_i \tag{14}$$

The bubble frequency $f_b = 1/T_b$ can thus be obtained from

$$f_b = 1/(T_{ba} + T_i)$$

Table 1 – Bed materials investigated with properties.

Materials	Geldart type	Shape	ρ_p [kg/m^3]	d_p[μm]	U_{mf}[cm/s]	U_{ms}[cm/s]
Glass	B	Spherical	2500	188	3.80	14.50
Glass	B	Spherical	2500	261	8.15	14.69
Glass	B	Spherical	2500	624	23.20	33.80
Limestone	B	Angular	2837	293	13.80	21.16
Limestone	B/D	Angular	2837	697	39.24	49.00
Sand	B	Angular	2650	483	16.50	25.82
Molecular sieve	D	Spherical	1300	2170	76.85	91.57

Substituting Eq. (12) in the above equation yields

$$f_b = \left(0.52\left(\frac{d_b}{D}\right)^{1.48} + T_i\right)^{-1} \tag{15}$$

The bed idle period T_i depends on the bubble rise velocity. The faster the bubbles rise, the more active the bed is, thus the lower the idle period. Since T_i can be measured in any given bed, its relationship with the bubble velocity can be obtained from experimental data.

3. Setup and measurement procedure

The experimental setup consists of a 10.4 cm cylindrical column of height 1.4 m. The column is fitted with a porous plate and a set of two-plane ECT sensors separated at a distance of 13 cm. Here, only a brief description of the experimental setup is given. The details of this setup, the materials used and the operating conditions have previously been described in (Agu et al., 2017; Agu et al., 2018), hence will not be repeated. The method used to obtain the relevant bubble properties are also outlined in the previous studies.

The experiments were conducted at ambient conditions using air as the fluidizing gas. Six different types of particles with mean particle size in the range of 180–2200 μm were used. For each of these powders given in Table 1, the particle size, d_p was obtained from sieve analysis and particle density, ρ_p with a gas pycnometer. A bed of each particle type was formed in the fluidized bed column with initial bed height within 40–60 cm to ensure that both ECT sensors were covered by the particles. The experiment was repeated five times at each air velocity for a given bed. The image data recorded by the ECT sensors were captured at a frequency of 100 Hz for 60 s.

The ECT data provide information about the distribution of solids or void at the sensor position. The average void fraction and the standard deviation were computed as discussed in Agu et al. (2017). The standard deviation plot against the gas velocity was used to determine the minimum fluidization and slugging velocities, U_{mf} and U_{ms}, respectively. The ECT data were also analysed to identify bubbles, their properties and their behaviour over the measurement period (Agu et al., 2018; Agu et al., 2017). To verify the repeatability of the experiment, the five data sets for each gas velocity were analysed separately, and the mean variation in the measurements when the experiment is repeated was observed to be less than 2.5%. The average data from the five measurements was therefore taken to reduce random errors.

From the data analysis, it was observed that the growth of a bubble as gas velocity is increased depends on the particles. With increase in particle size, the bubble growth rate increases. In the bed of angular (rough) particles, the rate of bubble growth is higher in the lower part of the bed than in the upper section, resulting in a sharp transition from bubbling to slugging regime. Moreover, the slug flow in the bed of limestone particles changes from the flat slug type to wall slug type at a considerably high gas velocity, probably due to the cohesive nature of these particles. For the spherical (smooth) particles, the rate of bubble growth is almost uniform over the bed, and the transition from bubbling to slugging regime is smooth.

For further analysis, the bed behaviour observed in this study is classified into two types based on the bubble growth rate:

- Type A: Bed with a slow bubble growth rate and a smooth transition from bubbling to slugging regime. Slugs rise along the central axis with a full-grown size less than the bed diameter; this behaviour is typical for fine and smooth Geldart B particles.
- Type B: Bed with a rapid bubble growth rate or a sharp transition from bubbling to slugging regime. Slugs spread across the bed cross-section and attach to the wall while rising. Slugs can grow to the bed size; this behaviour is typical for large particles or rough smaller particles.

Moreover, the bubble growth rate depends on the bed height to diameter ratio. As all the beds studied are deep, it is further observed that rough particles with a mean diameter as large as 300 μm exhibit a type B behaviour. For a bed with type A behaviour, data analysis also shows that there is a retardation in the slug growth when the ratio of bubble diameter to bed diameter is between the value of $(d_b/D)_{fm}$ and 0.6. Here, $(d_b/D)_{fm}$ is the bubble diameter at which the bubble frequency is at its local maximum, and at which slugs begin to appear at the bed position. The subscript "fm" denotes maximum frequency. The value of $(d_b/D)_{fm}$ depends on the particles, and increases slightly along the bed height. The average value of $(d_b/D)_{fm}$ over a given bed is shown in Fig. 2(a) as a function of U_{ms}/U_{mf}. The figure shows that the bubble diameter at the local maximum frequency increases with decreasing U_{ms}/U_{mf}, indicating that the $(d_b/D)_{fm}$ value increase with particle size. The curve correlating the measured $(d_b/D)_{fm}$ with U_{ms}/U_{mf} value in Fig. 2(a) can be represented by Eq. (16).

$$(d_b/D)_{fm} = \left(2.90 - 36.66\exp\left(-2.80\frac{U_{ms}}{U_{mf}}\right)\right)^{-1} \tag{16}$$

Fig. 2(b) shows the variation of $1/(v_b/T_i)$ with u_b, where v_b is the bubble volume and u_b is the bubble velocity obtained as described in the subsequent sections. The figure clearly shows the behaviour of a bed due to bubble growth. The T_i/v_b value is higher for type B than for type A behaviour at the same bubble velocity, indicating that the bubble frequency is lower in the bed of larger particles than in the bed of smaller particles for the same volume of bubbles. In addition, the slopes of the

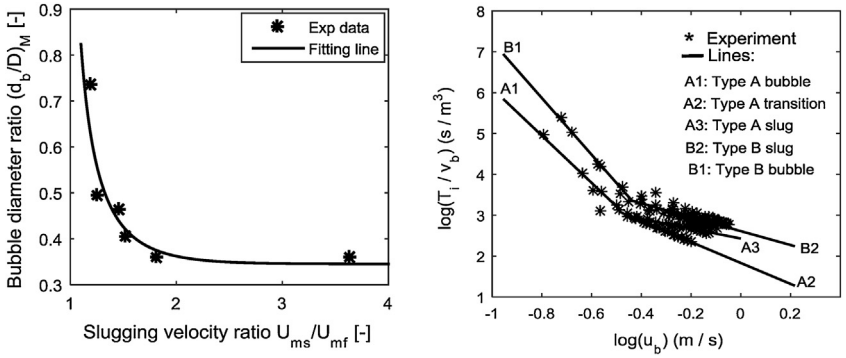

Fig. 2 – (a) Variation of bubble diameter at maximum frequency with minimum slugging velocity ratio based on the three glass, two limestone and the molecular sieve particles given in Table 1. (b) Bed idle period per unit bubble volume for two different types of behaviour in a fluidized bed; data from the three glass and the sand particles in Table 1.

trend lines for the type B behaviour are higher than the corresponding slopes in the type A beds. That is, −6.9 and −1.7 for B1 and B2, and −5.8 and −1.2 for A1 and A2, respectively. This means that the response to changes in the bubble activities is higher in the bed of larger particles than in that of smaller particles for a unit change in the flow property (gas velocity or bubble velocity). As can also be seen, three different lines are associated with the type A behaviour, and this is due to the slug growth transition as explained above.

3.1. *Measurement of bubble velocity*

The bubble velocity at the two different positions in the bed is obtained based on the mass balance, where

$$u_b = G/\delta_b \tag{17}$$

Here, G is the volumetric bubble flux obtained as in Eq. (18).

$$G = \frac{\pi}{6AT_{ba}} d_b^3 \tag{18}$$

Based on the two-phase theory, the bubble volume fraction at each of the measurement positions is calculated from the following relationship (which is also based on the mass balance) (Kunii and Levenspiel, 1991)

$$\varepsilon_f = \delta_b + (1 - \delta_b)\,\varepsilon_{mf}$$

$$\delta_b = \frac{\varepsilon_f - \varepsilon_{mf}}{1 - \varepsilon_{mf}} \tag{19}$$

Here, ε_f is the local bed void fraction and ε_{mf} is the corresponding value at the minimum fluidization condition. In Eq. (19), the void fraction in the emulsion phase is assumed the same as ε_{mf} since the particles used in this study are considered to be in the Geldart B group (Kunii and Levenspiel, 1991). It should be noted that Eq. (19) is valid only at low gas velocities. At a higher gas velocity, the void fraction in the emulsion phase is larger than ε_{mf} due to excessive bed expansion.

4. Model development and results

With measurement of relevant bubble properties, the complete models for the bubble velocity, bubble frequency and bed expansion can be derived. The accuracies of these models against experimental data are evaluated based on the mean absolute error.

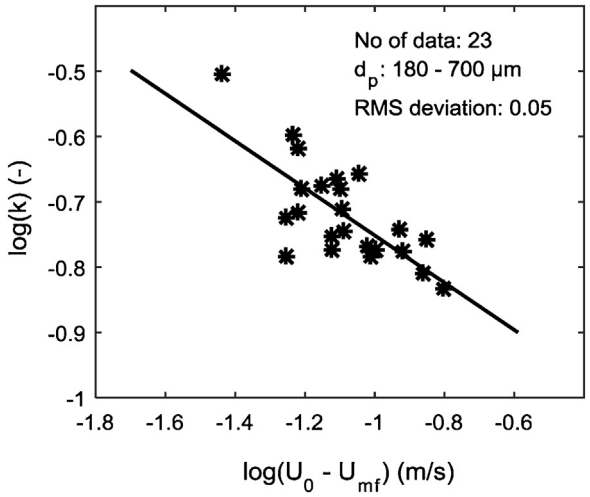

Fig. 3 – Correlation for the model parameter k in Eq. (13).

4.1. *Model for bubble rise velocity*

As the bed under this study is deep, visual observation and data analysis reveal that only a single bubble rises through the bed within the range of gas velocity investigated, thus $\emptyset = 0$ and from Eq. (1), $u_{br} = u_b$. Using the measured bubble rise velocity $u_{br,exp}$, the model parameter k in Eq. (13) can be determined from

$$k = \frac{0.9635\left(\frac{d_b}{D}\right)^{0.52} D}{u_{br,\exp}} \tag{20}$$

Fig. 3 shows the variation of k with excess gas velocity $U_0 - U_{mf}$ on the logarithmic scale. As shown in the figure, the model parameter decreases with increasing gas velocity. The line fitting the data in the figure is given by the equation

$$k = 0.077\left(U_0 - U_{mf}\right)^{-0.362} \tag{21}$$

For the correlation in Eq. (21), the gas velocity $U_0 - U_{mf}$ is in m/s. Substituting Eq. (21) into Eq. (13) yields

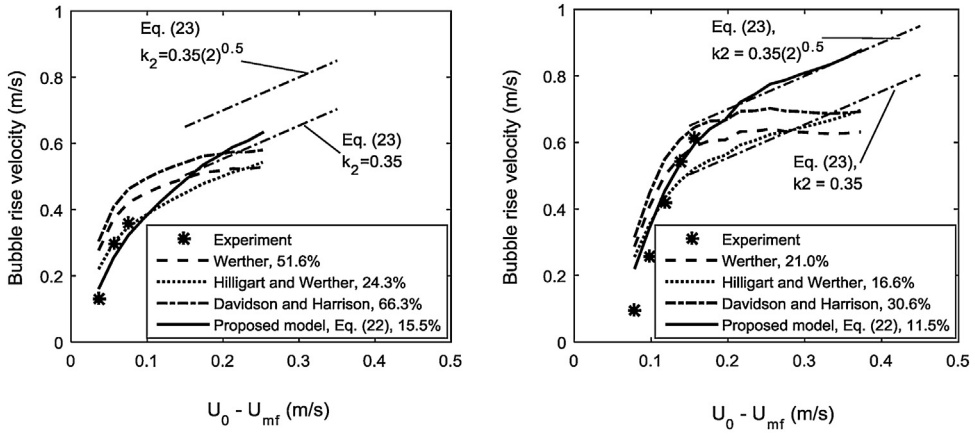

(a) (b)

Fig. 4 – Variation of bubble rise velocity with excess gas velocity predicted based on Eq. (22) compared with experimental data and other models for two different beds (a) 261 μm glass particles (b) 697 μm limestone particles.

$$u_{br} = 12.51\left(U_0 - U_{mf}\right)^{0.362}\left(\frac{d_b}{D}\right)^{0.52} D \tag{22}$$

Eq. (22) shows that bubble rise velocity increases approximately with the square root of the bubble diameter, which is in agreement with Eq. (2). The variation of u_b with $D^{0.48}$ in Eq. (22) also agrees quite well with $D^{0.4}$ in the Werther (1978) model and with $D^{0.5}$ in the Hilligardt and Werther (1986) model for Geldart B particles. With the term $\left(U_0 - U_{mf}\right)^{0.362}$, Eq. (22) can also predict an increase in the slug rise velocity with increasing gas velocity when the bubble diameter approaches a constant value. Generally, the available models for slug rise velocity, u_s are in the form

$$u_s = k_1\left(U_0 - U_{mf}\right) + k_2\sqrt{gD} \tag{23}$$

where $k_1 = 1.0$ is usually applied. The value of k_2 depends on the type of slug. For an axisymmetric slug, $k_2 = 0.35$ (Stewart and Davidson, 1967), and for a wall slug $k_2 = 0.35\sqrt{2}$ (Kehoe and Davidcon, 1970). Both types of slug can also be present in a given bed depending on the particle properties and gas velocity. The term $\left(U_0 - U_{mf}\right)^{0.362}$ also suggests that Eq. (22) is continuous and therefore can be applied for all values of $U_0 - U_{mf}$. It should be noted that the superficial gas velocity, U_0 has to be varied to achieve the same excess gas velocity, $U_0 - U_{mf}$ for different particles since U_{mf} can vary from particles to particles. Moreover, since the model is continuous over the gas velocities, it can also be applied in the transition regime between bubbling and turbulent flow/slugging provided that the bubble diameters within these regimes are used. For example, bubble breaks to a lower size at the transition to turbulent flow regime, but grows towards the bed diameter as the bed transits into slugging regime. The maximum bubble diameter at the onset of transition into turbulent flow regime can be estimated as given in Bi (1994) while the minimum bubble diameter at the transition into slugging regime can be estimated from Eq. (16).

Fig. 4 compares the bubble rise velocity predicted with the proposed model, Eq. (22) against the experimental data within the bubbling regime. The results are obtained at the position $h = 15.7$ cm above the distributor. The predictions obtained from some of the existing models are also shown including the slug rise velocity based on Eq. (23) for both values of k_2. As can be seen in both figures, Eq. (22) predicts the experimental data with a good accuracy. Both the Werther (1978) and Hilligardt and Werther (1986) models predict the bubble rise velocity with larger errors but the accuracy is better using the Hilligardt and Werther model as shown in Fig. 4. The Davidson and Harrison (1963) model over predicts the bubble rise velocity in both beds although the agreement is better for the 697 μm limestone particles. In addition, the results show that the Werther (1978) model and the Davidson and Harrison (1963) model do not predict the velocity of the rising slug when the bubble/slug diameter approaches a constant value. The Hilligardt and Werther model predicts the slug rise velocity in agreement with Eq. (23) when $k_2 = 0.35$ as can be seen in Fig. 4(b). However, in comparison with the proposed model, the Hilligardt and Werther model under predicts the slug velocity in both beds, although the model prediction is closer to the result from the 261 μm particle bed since the rising slug is of axisymmetric type. Comparing with Eq. (23), the results in Fig. 4 also show that the proposed model predicts accurately the slug rise velocity in accordance with the two different types of slug.

4.2. *Model for bubble velocity*

Although the model parameter given by Eq. (21) is obtained from a bed containing single bubbles, Eq. (22) can also be applied in a bed with more than one bubble rising across any plane in the bed. In this case, the rise velocity of each bubble can be obtained from Eq. (22), with d_b the same as the average diameter of all the bubbles present in the bed position. The bubble velocity u_b due to flow of these bubbles can then be determined by adding the flux term, $\emptyset\left(U_0 - U_{mf}\right)$ as described in Eq. (1). When the bubbles coalesce into a single bubble, this flux term can be neglected since a higher bubble diameter (equivalent to volume of all the bubbles) is then used in Eq. (22).

A comparison with published experimental data (Hilligardt and Werther, 1986; Glicksman et al., 1987) shows that the proposed model given by Eq. (22) for bubble rise velocity is sufficiently accurate for predicting the bubble velocity. For Geldart A particles, the experimental bubble velocity given by Hilligardt and Werther (1986) at different bed diameters and gas velocities can be predicted with a good accuracy when

Eq. (22) is substituted for u_{br} in Eq. (1) for which $\phi = 1$. The value of $\emptyset$ is unity in this group of particles since more than a bubble may be present due to low bubble coalescence (Kunii and Levenspiel, 1991). For the data presented in (Hilligardt and Werther, 1986) for Geldart B solids ($U_{mf} = 0.18$ m/s), Eq. (22) predicts the bubble velocity accurately with $\phi = 0$, which is similar to the case in this study for particles belonging to the same Geldart group. In a 1.2 m diameter bed of sand particles with a mean size of 1.0 mm, Glicksman et al. (1987) presented data for bubble velocity at different superficial gas velocities. Comparing the predictions from Eq. (22) with these data when $\phi = 0$, it can be observed that the model also accurately predicts the experimental data if 60% of the bed diameter in this current study is used. This reduced bed diameter also fits the model accurately to the data obtained in this study for the 2.17 mm molecular sieve particles. Based on these results, the following model is proposed for bubble velocity in a fluidized bed.

$$u_b = \varphi_N \left(U_0 - U_{mf}\right) + 12.51\varphi_D \left(U_0 - U_{mf}\right)^{0.362} d_b^{0.52} \quad (24)$$

where

$$\varphi_N = \begin{cases} 1 & \text{for Geldart A and A/B} \\ 0 & \text{for Geldart B and D} \end{cases} \quad (25)$$

$$\varphi_D = \begin{cases} D^{0.48} & \text{for type A behaviour} \\ & \text{(Geldart A and small Geldart B particles)} \\ 0.337 & \text{for type B behaviour(large Geldart B particles)} \\ 0.26 & \text{for Geldart D} \end{cases} \quad (26)$$

As demonstrated in Fig. 4, Eq. (24) can also be used to predict the slug rising velocity in a fluidized bed. For example, in a cylindrical bed of diameter 76.2 mm, the slug velocity reported in Wang et al. (2018) for spherical iron oxide particles (mean particle size 1.5 mm) can be predicted with good accuracy using Eq. (24), where $\varphi_N = 0$ and $\varphi_D = 0.26$.

For further demonstration, the predictions of the proposed model, Eq. (24) are compared with those of the existing models (Hilligardt and Werther, 1986; Davidson and Harrison, 1963; Werther, 1978) in Fig. 5. The existing models given by Davidson and Harrison (1963), Werther (1978) and Hilligardt and Werther (1986) are widely used in fluidized bed studies. The experimental data are based on those obtained in this study for Geldart B and D particles, those given in Hilligardt and Werther (1986) for Geldart A and B particles, and on those given in Glicksman et al. (1987) for D particles. Fig. 5(a) shows that the Werther model as well as the Hilligardt and Werther model have high accuracies in predicting the experimental data. The mean error associated with the model prediction for the Geldart A particle are 7.2 and 8.5%, respectively. The prediction errors based on these two models increases with increase in the gas velocity and can be over 12.0% according to the data in Fig. 5(a). The Davidson and Harrison model under predicts the experimental data with a mean error of 54.3% while the proposed model under predicts the bubble velocity with error in the range of 17–50%. Although this range of error is too high for practical application, the accuracy of Eq. (24) for Geldart A particles increases with increase in the gas velocity or bed diameter. The 17% error in this range is obtained from

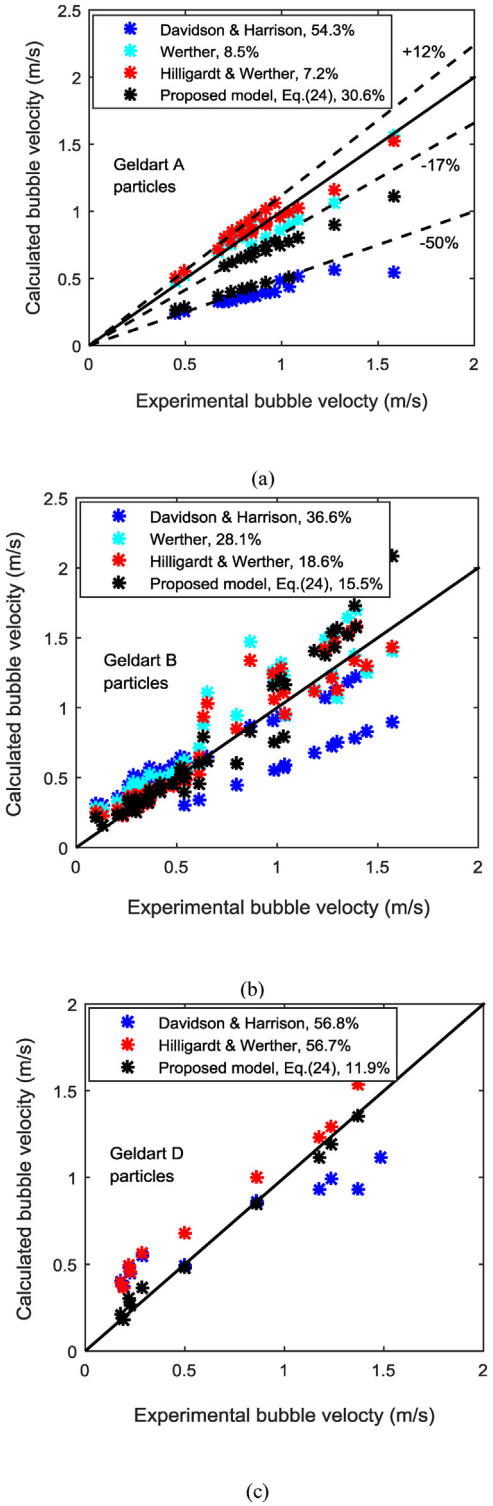

Fig. 5 – Computed bubble velocity versus experimental data for different particle groups (a) Geldart A (b) Geldart B (c) Geldart D.

those data associated with higher gas velocities and larger bed diameter while the 50% error is associated with data at lower gas velocity and smaller bed diameter. Since industrial operations based on Geldart A particles are at very high gas velocity compared to the particle minimum bubbling velocity, this shows that the proposed model will be suitable for large scale application.

Moreover, for the Geldart B and D particles, the proposed model has a better accuracy compared to the other models. The mean prediction error using Eq. (24) is 15.5% for the group

B particles. The Werther model predicts the data for the particles in the Geldart B group with an error of 28.1%. The errors for predicting the group B data using the Hilligardt and Werther model as well as the Davidson and Harrison model are 18.6 and 36.6%, respectively. For the Geldart D particles, these last two models also have a wide prediction error compared to the proposed model, which shows 12% error in predicting the experimental data. However, due to small number of data used in Fig. 5(c), the model comparison cannot be concluded in this study, and the comparison for the group A powder is not also exhaustive for the same reason. Since a large number of data set is shown for the group B powders, it can be concluded that for this group of particles, the accuracy of the proposed model is better than those of the previous models.

4.3. *Model for bubble frequency*

Bubble frequency depends on the bubble growth rate in a given bed. With reference to the rising of single bubbles in a fluidized bed, bubble frequency is defined as the number of such bubbles crossing a fixed plane per unit time. The larger the number of these bubbles, the higher is the bubble frequency. When a bubble grows to the size that slugs begin to appear, the bubble frequency decreases with further increase in the bubble size. For a given bubble diameter, a lower bubble/slug frequency indicates that the idle period of the bed is longer.

From analysis of the data given in Fig. 2, a correlation for the bed idle period T_i is obtained as given in Eq. (27).

$$T_i = m u_b^n d_b \tag{27}$$

$$\text{Bubbling regime, } \frac{d_b}{D} \le \left(\frac{d_b}{D}\right)_{fm}:$$

$$\begin{cases} m = 0.05\,; n = -3.475 \text{ for type A} \\ m = 0.05\,; n = -4.379 \text{ for type B} \end{cases}$$

$$\text{Slugging regime, } \frac{d_b}{D} > \left(\frac{d_b}{D}\right)_{fm}:$$

$$\begin{cases} m = 0.631\,; n = -1.187 \text{ for type A}, \dfrac{d_b}{D} \le 0.6 \\ m = 3.382\,; n = -0.122 \text{ for type A}, \dfrac{d_b}{D} > 0.6 \\ m = 5.277\,; n = -0.366 \text{ for type B} \end{cases}$$

Combining Eq. (27) with Eq. (15), the model for bubble frequency is therefore given by

$$f_b = \left(0.52\left(\frac{d_b}{D}\right)^{1.48} + m u_b^n d_b\right)^{-1} \tag{28}$$

The predictions from Eq. (28) at different gas velocities for two different powders are shown in Fig. 6. As can be seen, the model results agree very well with the experimental data obtained in the bed of 188 μm glass particles. For the bed of sand particles, there is also good agreement between the model predictions and the experimental data. The results in the figures show that the model also captures the trend of the bubble frequency with varying gas velocity. The local maximum frequency is well predicted in both beds. For the results presented in the previous studies (Weber and Mei, 2013; Agrawal et al., 2018), Eq. (28) can also be used to predict the bed behaviour. Eq. (28) can predict with good accuracy for example, the axial distribution of the bubble frequency including the local peak value as reported in Weber and Mei (2013) for a bed of 185 μm glass particles.

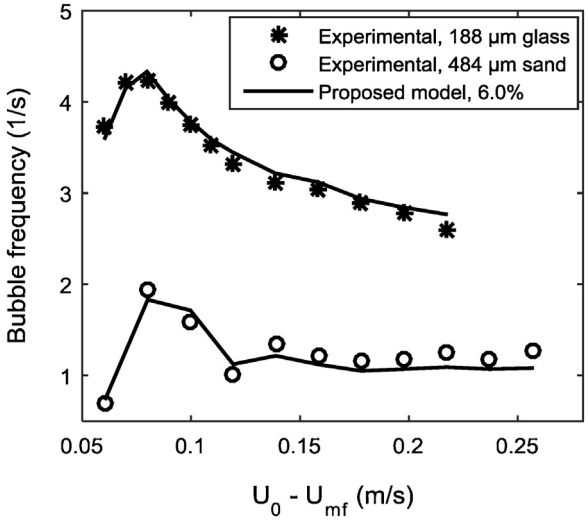

Fig. 6 – Predicted bubble frequency using Eq. (28) compared with the experimental data at different gas velocities for the bed of 188 μm glass particles and 483 μm sand particles at h = 15.7 cm.

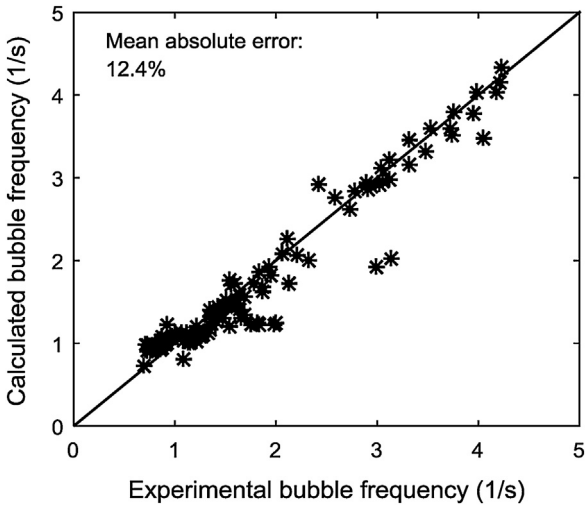

Fig. 7 – Comparison of the computed results based on Eq. (28) with experimental results, showing the model accuracy based on the particles in Table 1.

In addition, the overall prediction accuracy of Eq. (28) is shown in Fig. 7. The experimental data covers the range of powders used in this study. Similar to the results shown in Fig. 6, there is also a good agreement between the model predictions and the experimental data for the other powders. As shown in Fig. 7, the mean absolute error associated with the model prediction is 12.4%.

With these results, the proposed model for bubble frequency can be used to predict the fluidized bed behaviour in both bubbling and slugging regimes. Moreover, Eq. (28) shows that when the bubble diameter is constant, the bubble frequency increases with the gas velocity. However, such a stable bubble diameter may be difficult to attain. As observed in this study, a slug splits once it reaches a size closer to the bed diameter. When a slug splits, the smaller slug rises with a lower

velocity, thereby decreasing the slug frequency. This shows that the slug frequency may increase, decrease or remain constant when the slug diameter approaches the bed diameter depending on the net effect of slug splitting and coalescence. Hence, for accurate prediction of slug frequency using Eq. (28), measured bubble/slug diameters should be used. As an alternative, Eq. (28) can be used to predict slug size (diameter) when the trend of the slug frequency is available.

4.4. *Model for bed expansion — larger particles*

The bed expansion Δe at a fluidized state is usually defined as

$$\Delta e = \frac{H_f - H_{mf}}{H_{mf}} \tag{29}$$

where H_f is the total bed height at the fluidized state and H_{mf} is the bed height at the minimum fluidization condition. By mass balance,

$$\left(1-\varepsilon_f\right) H_f = \left(1-\varepsilon_{mf}\right) H_{mf} \tag{30}$$

Combining Eq. (29) and Eq. (30),

$$\Delta e = \frac{1-\varepsilon_{mf}}{1-\varepsilon_f} - 1 \tag{31}$$

Applying the two-phase theory, Eq. (19) can be rearranged into

$$1-\varepsilon_f = (1-\delta_b)\left(1-\varepsilon_{mf}\right) \tag{32}$$

Substituting Eq. (32) into Eq. (31), yields

$$\Delta e = \frac{1}{1-\delta_b} - 1 \tag{33}$$

From Eq. (17),

$$\delta_b = G/u_b \tag{34}$$

Combining Eq. (12) and Eq. (18),

$$G = 1.285\left(\frac{d_b}{D}\right)^{1.52} D \tag{35}$$

Substituting Eq. (22) and Eq. (35) into Eq. (34)

$$\delta_b = 0.103\left(U_0 - U_{mf}\right)^{-0.362}\left(\frac{\bar{d}_b}{D}\right) \tag{36}$$

Note that the bed expansion is over the entire bed. Hence, the bubble diameter $\bar{d}_b$ in Eq. (36) is the average value over the bed height. Substituting Eq. (36) into Eq. (33), then

$$\Delta e = \left[1 - 0.103\left(U_0 - U_{mf}\right)^{-0.362}\left(\frac{\bar{d}_b}{D}\right)\right]^{-1} - 1 \tag{37}$$

The explicit model given by Eq. (37) for bed expansion depends on the average bubble diameter over a bed, which is the only variable that can be linked to particle properties. The model is also applicable only in the bubbling regime, i.e. when $U_0 < U_{ms}$. To be able to predict a correct value for the bed expansion due to bubble flow, the average bubble diameter

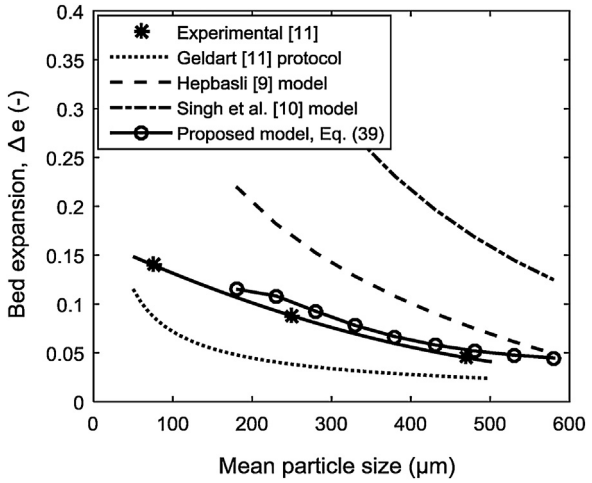

Fig. 8 – Predicted bed expansion based on different models compared with the experimental data for different sand particle sizes.

used must be dependent on the bed material properties. Most bubble diameter models available in the literature depend only on $U_0 - U_{mf}$ value, and thus provide the same results independent of the bed material. However, in (Agu et al., 2018), a model for average bubble diameter is proposed as described below.

$$\bar{d}_b/D = 0.848\left(\frac{U_0}{D}\right)^{0.66}\left(1-\gamma\left(\frac{U_0}{U_{mf}}\right)^{\beta-1}\right)^{0.66} \quad ; \quad Ar > 400 \tag{38}$$

The model parameters β and γ as described in (Agu et al., 2018) depend on the particle Archimedes number Ar and on the regime of flow. In addition, the expression for β depends on the particle sphericity φ. Using this bubble diameter model, a particle-dependent bed expansion model can be obtained.

Substituting Eq. (38) into Eq. (37) gives

$$\Delta e = \left[1 - 0.0873\left(U_0 - U_{mf}\right)^{-0.362}\left(\frac{U_0}{D}\right)^{0.66}\left(1-\gamma\left(\frac{U_0}{U_{mf}}\right)^{\beta-1}\right)^{0.66}\right]^{-1} - 1 \tag{39}$$

For complete prediction of the bed expansion using the predicted minimum fluidization velocity, the parameters, β and γ in Eq. (39) are given by

$$\beta = \varphi^{1.5}\left(0.329 - 1.156\times 10^{3} Ar^{-0.9}\right) \tag{40a}$$

$$\gamma = \left(1.321 + 8.161\times 10^{4} Ar^{-1.04}\right)^{0.083} \tag{40b}$$

The result of the proposed bed expansion model, Eq. (39) is presented in Fig. 8 for sand particles with a mean diameter in the range 180–500 μm. The figure compares the bed expansion computed by using different models with the experimental data reported in Geldart (2004). The computations are done at the conditions used in the experiment, where $U_0 - U_{mf} = 0.06$ m/s, and the bed diameter and settled bed height are 0.3 m and 0.2 m, respectively. The minimum fluidization velocity is obtained here based on the combination of the Ergun (1952) model and the Wen and Yu (1966) model. Computation of minimum slugging velocity (Agu et al., 2018) shows that each particle bed is in the bubbling regime at the given gas velocity. As can be seen in Fig. 8, all the models

predict the same trend as given by the experiment: the bed expansion decreases with increasing particle size. Quantitatively, the results from the model proposed in this paper agree very well with the experimental data. The slightly higher value of the bed expansion predicted by Eq. (39) is due to a higher average bubble diameter predicted from Eq. (38). The model for the average bubble diameter is developed from a deep bed where a bubble reaches its fully-grown size at a given gas velocity. It should be noted that the bed reported in (Geldart, 2004) is shallow ($h_0/D = 0.67$). In such a shallow bed, bubble size may be smaller than in a deep bed where $h_0/D > 2$. The deviation using the Singh et al. (1999) model is very high compared to other models. While the Hepbasli (1998) model over predicts the experimental data, the Geldart (2004) protocol under predicts the data, although the magnitude of the deviation is almost the same for both models.

Since shallow beds may contain more than one rising bubble due to lower degree of coalescence, the results in Fig. 8 show that the proposed model can also be applied for beds of multiple bubbles though a single bubble was assumed for simplicity in the development of Eq. (39). In addition to the prediction accuracy, Eq. (39) can be used at elevated temperature and pressure due to the U_0/U_{mf} term, and its dependence on the particle Archimedes number through Eq. (40). Eq. (39) also shows that the bed expansion depends on the bed diameter. Increasing the bed diameter at the same gas velocity decreases the bed expansion, which agrees with the findings in Mohanty et al. (2009).

5. Conclusion

This paper presents a set of new models for predicting local bubble velocity, local bubble frequency and overall bed expansion ratio. The three models were analytically approached by considering an isolated single bubble rising in a fluidized bed. The analysis shows that bubble rise velocity is proportional to the rate of change of bubble-projected area as it passes through a fixed plane in the bed, where the proportionality constant depends on the bed diameter and gas velocity in excess of the minimum fluidization velocity. The bed expansion model is valid in the bubbling regime and for larger particles where the particle Archimedes number is greater than 400.

The three models have been validated with experimental data obtained in this study and with some data available in the literature. The results show that the models can predict the fluidized bed properties at different gas velocities and bed diameters with good accuracy. The model for bubble velocity can predict the rise velocity of the two different types of slugs: axisymmetric and wall slugs or their mixture, accordingly. The bubble frequency model can also predict the local maximum frequency reached along the bed height or at a certain gas velocity for a given position in the bed. The dependence of the bed expansion model on the bed diameter, the fluid properties and the particle properties increases its applicability for different operating conditions, including high temperature and pressure.

Funding sources

This research did not receive any specific grant from funding agencies in the public, commercial, or not-for-profit sectors.

References

Agrawal, V., Shinde, Y.H., Shah, M.T., Utikar, R.P., Pareek, V.K., Joshi, J.B., 2018. Estimation of bubble properties in bubbling fluidized bed using ECVT measurements. Ind. Eng. Chem. Res. 57, 8319.

Agu, C.E., Tokheim, L.-A., Eikeland, M., Moldestad, B.M.E., 2017. Determination of onset of bubbling and slugging in a fluidized bed using a dual-plane electrical capacitance tomography system. Chem. Eng. J. 328, 997.

Agu, C.E., Pfeifer, C., Eikeland, M., Tokheim, L.-A., Moldestad, B.M.E., 2018. Models for predicting average bubble diameter and volumetric bubble flux in deep fluidized beds. Ind. Eng. Chem. Res. 57, 2658.

Bi, X., 1994. Flow Regime Transitions in Gas-Solid Fluidization and Transport, Thesis. The University of British Columbia, Canada.

Choi, J.H., Son, J.E., Kim, S.D., 1988. Bubble size and frequency in gas fluidized beds. J. Chem. Eng. Jpn. 21, 171.

Davidson, J.F., Harrison, D., 1963. Fluidized Particles. Cambridge University Press, London.

Dry, R.J., Judd, M.R., Shingles, T., 1984. Bubble velocities in fluidized beds of fine, dense powders. Powder Technol. 39, 69.

Du, B., Warsito, W., Fan, L.-S., 2005. ECT studies of gas–solid fluidized beds of different diameters. Ind. Eng. Chem. Res. 44, 5020.

Ergun, S., 1952. Fluid flow through packed column. Chem. Eng. Prog. 48, 89.

Geldart, D., 1973. Types of gas fluidization. Powder Technol. 7, 285.

Geldart, D., 2004. Expansion of gas fluidized beds. Ind. Eng. Chem. Res. 43, 5802.

Glicksman, L.R., Lord, W.K., Sakagami, M., 1987. Bubble properties in large-particle fluidized beds. Chem. Eng. Sci. 42, 479.

Grace, J.R., Cliff, R., 1974. On the Two-phase Theory of Fluidization. Chem. Eng. Sci. 29, 327.

Hepbasli, A., 1998. Estimation of bed expansions in a freely-bubbling three-dimensional gas-fluidized bed. Int. J. Energy Res. 22, 1365.

Hilligardt, K., Werther, J., 1986. Local bubble gas hold-up and expansion of gas/solid fluidized beds. Ger. Chem. Eng. 9, 215.

Hulme, I., Kantzas, A., 2004. Determination of bubble diameter and axial velocity for a polyethylene fluidized bed using X-ray fluoroscopy. Powder Technol. 147, 20.

Karimipour, S., Pugsley, T., 2011. A critical evaluation of literature correlations for predicting bubble size and velocity in gas-solid fluidized beds — a review. Powder Technol. 205, 1.

Kehoe P.W.K., Davidson J.F. Continuously slugging fluidized beds. CHEMECA '70, Inst. Chem. Eng. Symp. Ser. 1970, 97.

Kunii, D., Levenspiel, O., 1991. Fluidization Engineering, 2nd ed. Butterworth — Heinemann, Washington Street.

Lee, S.H., Lee, D.H., Kim, S.D., 2002. Slug characteristics of polymer particles in a gas–solid fluidized bed. Korean J. Chem. Eng. 19, 351.

Li, X., Jaworski, A.J., Mao, X., 2018. Bubble size and bubble rise velocity estimation by means of electrical capacitance tomography within gas-solids fluidized beds. Measurement 117, 226.

Maurer, S., Wagner, E.C., Schildhauer, T.J., Ommen, J.R., Biollaz, S.M.A., 2015. X-ray measurements of bubble hold-up in fluidized beds with and without vertical internals. Int. J. Multiphase Flow 74, 118.

Mohanty, Y.K., Roy, G.K., Biswal, K.C., 2009. Effect of column diameter on dynamics of gas-solid fluidized bed: a statistical approach. Indian J. Chem. Techn. 16, 17.

Noordergraaf, I.W., VanDijk, A., Van Den Bleek, C.M., 1987. Fluidization and slugging in large-particle systems. Powder Technol. 52, 59.

Rowe, P.N., Partridge, B.A., 1965. An X-ray study of bubbles in fluidized beds. Chem. Eng. Res. Des. 43, 157.

Rowe, P.N., Yacono, C.X.R., 1976. The bubbling behaviour of fine powders when fluidized. Chem. Eng. Sci. 31, 1170.
Singh, R.K., Suryanarayana, A., Roy, G.K., 1999. Prediction of bed expansion ratio for gas-solid fluidization in cylindrical and non-cylindrical beds. IE (1) J. CH. 79, 51.
Stewart, P.S.B., Davidson, J.F., 1967. Slug flow in fluidized beds. Powder Technol. 1, 61.
Toomey, R.D., Johnstone, H.F., 1952. Gaseous fluidization of solid particles. Chem. Eng. Prog. 48, 220.
Wallis, G.B., 1969. One-Dimensional Two-phase Flow. McGraw-Hill, New York.
Wang, D., Xu, M., Marashdeh, Q., Straiton, B., Tong, A., Fan, L.-S., 2018. Electrical capacitance volume tomography for characterization of gas-solid slugging fluidization with Geldart group D particles under high temperatures. Ind. Eng. Chem. Res. 57, 2687.
Weber, J.M., Mei, J.S., 2013. Bubbling fluidized bed characterization using electrical capacitance volume tomography (ECVT). Powder Technol. 241, 40.
Wen, C.Y., Yu, Y.H., 1966. A generalized method for predicting the minimum fluidization velocity. AIChE J. 12, 610.
Werther, J., 1974. Influence of the bed diameter on the hydrodynamics of gas fluidized beds. AIChE Symp. Ser. 70, 53.
Werther, J., 1978. Effect of gas distributor on the hydrodynamics of gas fluidized beds. Ger. Chem. Eng. 1, 166.

Article 7 (A7)

Behaviour of biomass particles in a bubbling fluidized bed: A comparison between wood pellets and wood chips

By

Cornelius Emeka Agu, Lars-Andre Tokheim, Christoph Pfeifer and Britt M.E. Moldestad

Published in

Chemical Engineering Journal 363 (2019) 84 – 98

Chemical Engineering Journal 363 (2019) 84–98

Contents lists available at ScienceDirect

Chemical Engineering Journal

journal homepage: www.elsevier.com/locate/cej

Behaviour of biomass particles in a bubbling fluidized bed: A comparison between wood pellets and wood chips

Cornelius Emeka Agu[a,*], Lars-Andre Tokheim[a], Christoph Pfeifer[b], Britt M.E. Moldestad[a]

[a] Department of Process, Energy and Environmental Technology, University of South-Eastern Norway, 3918 Porsgrunn, Norway
[b] Department of Material Sciences and Process Engineering, University of Natural Resources and Life Sciences, 1190 Vienna, Austria

HIGHLIGHTS

- Wood pellets segregate downwards while chips upwards at low gas velocities.
- Spreads to the walls is better with wood chips than with pellets at the same gas velocity.
- Gas velocity required to achieve good mixing increases with biomass load.
- Transition from bubbling to slugging regime gets smoother at higher biomass load.
- A mechanistic model was developed for predicting the minimum mixing gas velocity.

ARTICLE INFO

Keywords:
Segregation
Biomass
Particle mixing
Wood chips
Wood pellets

ABSTRACT

For successful operation and design of a bubbling fluidized bed reactor handling a specific biomass, in-depth knowledge about the bed behaviour is paramount. This study compares the behaviour of a bed of sand containing wood pellets with that containing wood chips at different gas velocities and biomass proportions in a cold fluidized bed of diameter, 10.4 cm. The density and volume-equivalent spherical particle diameter of the pellets are 1139 kg/m^3 and 8.96 mm, respectively while those of the wood chips are 423 kg/m^3 and 6.87 mm, respectively. The results show that at low gas velocities, wood chips segregate upwards while the pellets segregate downwards in their respective beds. The spread of biomass towards the walls is higher in the bed with wood chips than in that with wood pellets. As the biomass load increases, the bubble diameter increases and the transition from bubbling to slugging regime gets smoother, resulting in an increase in the minimum slugging velocity. The minimum gas velocity for effective solids mixing is less dependent on the bed height, but increases with increase in the biomass load and decreases with increase in the bed diameter. However, when slugs flow in the bed, the biomass layer at the bed surface plugs, preventing mixing of particles to be achieved at the desired gas velocity. A mechanistic model is developed for predicting the minimum gas velocity required to achieve an effective mixing at the surface of a segregated bed. Although this study is conducted in a cold bed, this same model is considered important for a hot bed reactor since devolatilization enhances the upward flow of biomass due to reduction of the biomass density.

1. Introduction

Application of bubbling fluidized bed for gasification or combustion of biomass requires in-depth understanding of the bed behaviour at different gas velocities. Due to the peculiar properties of biomass, for example its large size, cohesiveness and irregular shape, it is often difficult to get it fluidized at the desired operating gas velocity. However, with increase in the reactor pressure or reduction of the particle size [1], the quality of biomass fluidization can be improved. The biomass fluidization quality can also be improved by applying surface coating [2] or a noise-induced mechanism such as mechanical vibration [3] and acoustic sound [4,5]. In addition to ensuring uniform heat and mass transfer, an inert material, sand for example, can be used to achieve the fluidization of biomass at the desired operating condition. However, as sand particles are usually smaller and higher in density compared to biomass, particle segregation is often a problem in

* Corresponding author.
E-mail addresses: cornelius.e.agu@usn.no (C.E. Agu), Lars.A.Tokheim@usn.no (L.-A. Tokheim), christoph.pfeifer@boku.ac.at (C. Pfeifer), britt.moldestad@usn.no (B.M.E. Moldestad).

https://doi.org/10.1016/j.cej.2019.01.120
Received 7 November 2018; Received in revised form 16 January 2019; Accepted 21 January 2019
Available online 22 January 2019

Nomenclature

A	bed cross-sectional area, m^2
A_p	particle total surface area, m^2
D	bed diameter, m
D_b	bubble diameter, m
d	diameter, m
$d_{p,sph}$	spherical particle diameter, m
Δe	bed expansion
f_b	bubble frequency, s^{-1}
f_{wake}	bubble wake volume fraction
G	volumetric bubble flux, m/s
g	acceleration due to gravity, m/s^2
h	height, vertical position in the bed, m
H	total bed height, m
k	internal pressure coefficient
l_{max}	maximum layer thickness, m
m_p	mass of particles, kg
m, n	dimensionless model coefficient
N_{pix}	number of pixels in a bed cross section
Δp_g	gas pressure drop, Pa
s	size representative (volume, length, diameter)
U	superficial gas velocity, m/s
u_b	bubble velocity, m/s
V	volume, m^3
$\bar{V}$	bulk volume, m^3
w_i	component weight fraction
X	local mass fraction
x	biomass total mass fraction
Y	local volume fraction
y	total volume fraction

Greek symbols

α	local solids fraction
β	fluid-particle momentum transfer coefficient, N/m^3
δ_b	bubble volume fraction
ε	average bed void fraction
ε_s	average solids fraction of sand bed
ε_b	average solids fraction of biomass bed
θ_i	angle of internal friction, degree
σ	normal stress, Pa
ρ	density, kg/m^3
$\bar{\rho}_p$	particle bulk density
φ	sphericity
τ_w	wall frictional stress, Pa
μ_w	wall frictional coefficient
γ	hydrostatic pressure correction coefficient

Subscripts

b	biomass, bubble
bs	bubbling to slugging transition
f	fluidized
g	gas
i,j	indices locating a pixel
m	mixture
mf	minimum fluidization
p	particle
s	sand
0 (zero)	initial state or entry position

biomass fluidized bed reactors [6]. This study investigates the behaviour of wood-based biomass particles in fluidized beds aided by sand particles. Two different types of woody biomass: wood chips and wood pellets are investigated and their behaviour in bubbling fluidized beds are compared. Both types of biomass are widely utilized due to their availability and energy content. While the wood chips are lighter, have a wider variation in shape and a low unit cost (cost per kWh), the wood pellets have a lower moisture content and a higher energy density due to their relatively high mass density. The difference between the properties of the two different types of biomass may influence their behaviour in fluidized beds, and thus the choice of reactor design and operating conditions. It should be noted that in biomass fluidized bed reactors, different types of solid particles are present including bed material, raw biomass, ash and char particles, all with different physical properties.

A number of studies have investigated the fluidized bed behaviour in systems involving biomass mainly in cold flows. Measurement of minimum fluidization velocity of mixtures of biomass and inert bed materials at different biomass concentrations [4,7–9] is common. The minimum fluidization velocity increases with increase in the proportion of biomass in the bed. Different studies have also reported the segregation and mixing behaviour of biomass-sand mixtures at higher gas velocity using different measurement techniques. Along with the fibre optic sensors for measuring bubble properties, the most commonly used methods for the measurement of biomass distribution are the frozen bed method [10,11] and particle tracking techniques based on radioactivity [11] and magnetic fields [12]. Although the particle tracking technique requires complex analysis, it usually gives more accurate results than the frozen bed method. The accuracy of the latter depends on the biomass load in the bed [11]. Based on experimental findings, the mixing of solids is enhanced by increasing the amount of biomass in the bed [13], and the pattern of solids mixing is independent of the bed height [14]. In addition, segregation of particles in a bed increases with increase in the gas flow rate up to a certain gas velocity. Above this gas velocity, mixing of solids over the entire bed volume can be achieved [15]. Zhang et al. [15] classified the progress of a bed of a biomass-sand mixture into six stages, ranging from a well-mixed to a local-segregated state as the gas velocity is increased. Moreover, particle size, shape and densities also influence the pattern of mixing and segregation in the fluidized bed, which according to Baeyens and Geldart [16] and Yang [17] are brought about by the passage of bubbles through the bed. By using smaller or denser biomass particles, Cluet et al. [14] showed that bed homogeneity can be enhanced. When the density of the smaller particles in the mixture is higher, these particles segregate downwards at low gas velocity and upwards at high gas velocity [18]. To gain an overview of which component in a bed mixture can segregate up or down when fluidized, Di Renzo et al. [10] proposed an equilibrium model, which depends on the density and size ratios of the particles, and also on the proportion of biomass in the binary mixture.

The effects of biomass particle size and shape on the fluidized bed behaviour are reported in [8,11]. From different mixtures of biomass and 380 μm sand particles, Fotovat et al. [11] concluded that the higher the sphericity of biomass particles, the faster they rise and the slower they sink when the gas velocity is increased. The authors also showed that bubbles are more prone to break in the bed containing biomass particles with low sphericity, resulting in smaller bubbles in the bed. In addition, increasing the size and amount of biomass particles, Zhang et al. [19] showed that the probability of bubble growth in the bed mixture decreases, which leads to flow of smaller bubbles compared to that in the bed of pure sand particles.

In view of these studies, this paper is aimed at comparing the bubble-induced bed properties between a low-density ($< 500\,kg/m^3$) and high-density ($> 1000\,kg/m^3$) woody biomass in bubbling fluidized beds assisted with sand particles of density, $2650\,kg/m^3$. The pattern

and degree of segregation due to density difference between the sand and wood particles in the bed mixtures are investigated. As the required global mixing depends on the gas velocity and biomass load, this study also looks into mechanisms involved in achieving solids mixing over the biomass accumulated at the surface or at the bottom of the bed. Understanding these mechanisms can help in selecting or predicting the gas velocity required for mixing to occur over the bed height. The results presented in this study are based on measurements of solids fraction at different positions in a 10.4 cm diameter cold fluidized bed using electrical capacitance tomography (ECT) sensors. ECT measures the distribution of relative permittivity in a bed, which differs from one solid material to another. This means that the relative permittivity of a mixture of biomass and sand particles will be different from that of pure sand at the same gas velocity and bed position. Therefore, measurements of biomass distribution can be obtained by comparing the ECT data acquired from a bed mixture with those acquired from the pure sand particles under the same measurement conditions. The data from the ECT sensors are also analysed to obtain the bubble diameter, bubble frequency and volumetric bubble flux. Additionally, the segregation behaviour observed in the ECT setup is compared with that observed at different bed aspect ratios in a setup equipped with pressure sensors. In the subsequent sections, the results are presented, discussed and compared with correlations in the literature. The results obtained and described here enhance understanding of the complex fluid-particle behaviour in fluidized bed combustors and gasifiers. By using appropriate scaling laws [20] and a measured output such as the bubble to bed diameter ratio, the behaviour observed in this study can also be scaled up to larger diameter bed in a similar approach as discussed in Agu et al. [21].

2. Setup and measurement procedure

2.1. Experimental setup

Two different cold fluidized bed setups as shown in Fig. 1 were used in this study. The first of these consists of a cylindrical Perspex glass column of internal diameter 8.4 cm and height 140 cm. The column is fitted with a porous steel plate distributor of 40% flow area, and 10 different pressure sensors located along the column axis. The first sensor is located 4 cm below the gas distributor and 6.5 cm from the second sensor while the other ones are equally spaced above the distributor at 10 cm interval. Based on this setup, the minimum fluidization velocity and the corresponding void fraction of all the pure solid particles used in this study were determined.

To investigate the bubble properties in the fluidized bed of a mixture of sand and biomass particles, a setup equipped with two ECT sensors was used. The cylindrical Perspex glass column has a diameter of 10.4 cm and a height of 140 cm. The column is also equipped with a stainless steel porous plate for uniform gas distribution across the bed. The ECT sensors are located 15.7 cm and 28.7 cm above the distributor.

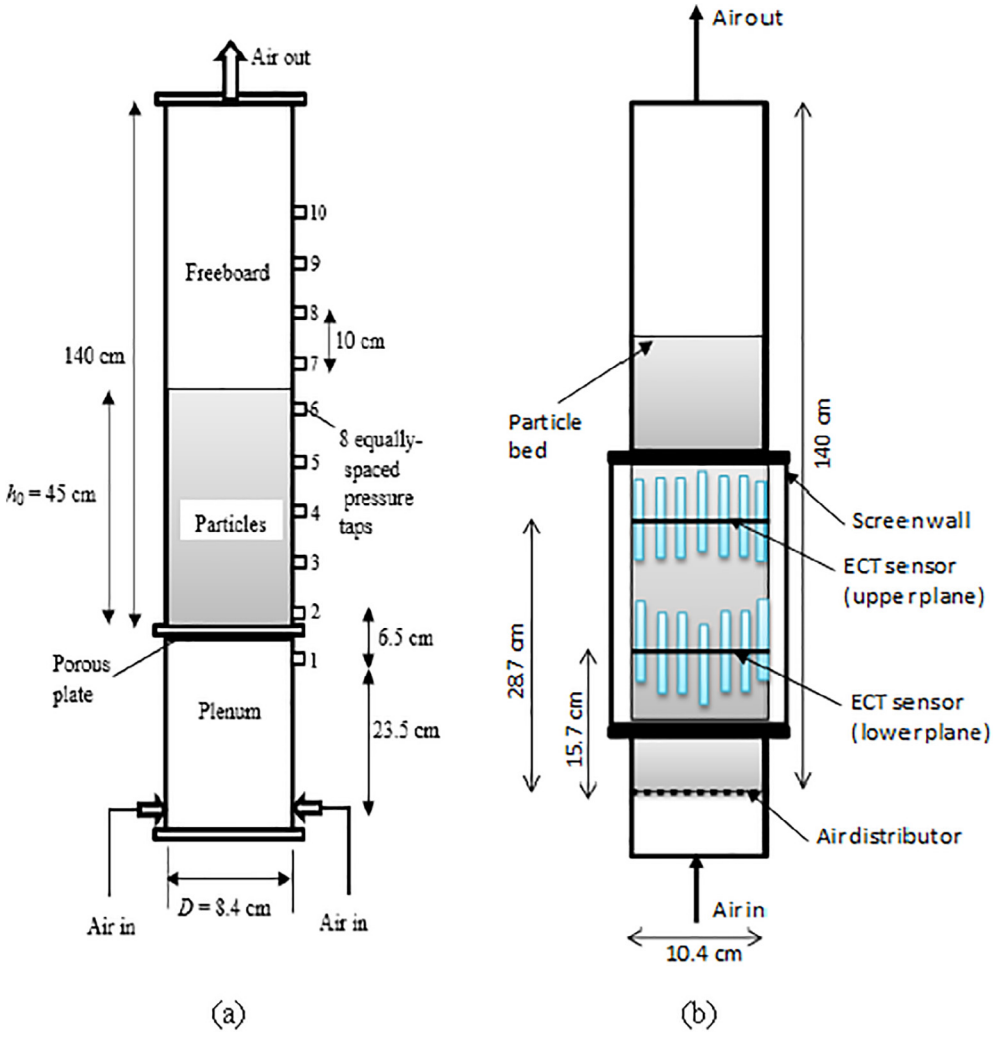

Fig. 1. Schematic illustration of a cold fluidized bed equipped with (a) pressure sensors for measurement of pressure drops (b) ECT sensors for measurement of solids fraction distribution.

The details of this setup and configuration of the ECT can be found in Agu et al. [22]. At a given gas flow rate, the ECT measures the distribution of solids fraction across a section of the bed. Similar to the pressure sensor setup, compressed air at the ambient condition was used at different velocities for all the beds investigated. For each gas velocity, the image data acquired by the ECT sensors were captured at a frequency of 100 Hz for 60 s. The bed height was also measured for each gas velocity when the flow had been established (approximately after 3 min) using a ruler attached to the column wall. The captured data were exported and analysed using MATLAB codes developed in-house. Different bubble properties including bubble diameter, bubble frequency and bubble volumetric flow rate were obtained from the analysis. During the data analysis, a bubble was considered as a region with a solids fraction below 0.2. The bubble properties were computed from the time evolution of the bubble-projected area. The variation of the projected area with time shows that for a given gas velocity above the minimum bubbling velocity, bubbles pass periodically across a measurement plane. The reciprocal of the time between arrivals of two successive bubbles to the plane gives the bubble frequency. By assuming a spherical bubble, the bubble diameter is determined from the peak of the projected area during each bubbling period. As there may be deviations in the bubble property measured at each bubble passage, the results reported in this study are the time-average values obtained over the 60 s measurement period. More information on measurement of bubble properties using this setup is given in Agu et al. [23].

2.2. Material properties and characterization

Two different types of wood-based biomass are investigated. The biomass includes cylindrical wood pellets of 6 mm diameter and wood chips with a wide variation in shape. The pellets vary in length between 5 and 30 mm. For analysis, a rectangular shape is assumed for the wood chips with variation in length, width and height in the range of 5–12 mm, 5–12 mm and 1–5 mm, respectively. The fluidized material is sand particles with a narrow size distribution (200–350 μm). The detailed properties of these materials are given in Table 1.

The void fraction of the bed is computed as

$$\varepsilon = 1 - \bar{\rho}_p/\rho_p \tag{1}$$

where $\bar{\rho}_p$ is the bulk density of the solid particles obtained as mass of the solids per unit volume of the bed, and ρ_p is the particle density. The average size, s (diameter, length, volume) of the particles in each bulk material is computed as

$$s = \frac{1}{\sum_i \left(\frac{w_i}{s_i}\right)} \tag{2}$$

where s_i is the mean value of each size range and w_i is the mass fraction of the size range in the bulk material. For the non-spherical biomass particles, the volume-equivalent spherical particle diameter, $d_{p,sph}$ is determined from:

$$d_{p,sph} = \left(\frac{6V_p}{\pi}\right)^{1/3} \tag{3}$$

where V_p is the mean volume of the particle computed from Eq. (2). With the value of $d_{p,sph}$, the effective particle diameter is obtained from $d_p = \varphi_p d_{p,sph}$. The particle sphericity, φ_p, defined as the ratio of surface area of a sphere to surface area of the particle of the same volume as the spherical particle, is given by

$$\varphi_p = \frac{6\pi^{\frac{1}{3}} V_p^{\frac{2}{3}}}{A_p} \tag{4}$$

Here, A_p is the mean particle surface area. The size of the sand particles was obtained from the sieve analysis and the average particle sphericity was obtained by fitting the Carman-Kozeny [24] equation with the pressure drop across a bed of these particles at different air velocities.

In addition, the minimum fluidization velocity of each material was obtained as the superficial gas velocity when the pressure drop across the bed is equal to the bed weight divided by the cross-sectional area of the bed. As can be seen in Table 1, the wood chips and pellets have close particle size but a wide density difference. The difference in density between the two different wood materials is key factor employed in this study. Moreover, the size variation of the two different biomass types also mimic those used in large-scale biomass gasifiers or combustors. The densities of both wood materials are lower than that of the sand particles, and as a result, segregation of sand and wood particles is expected to occur during fluidization as reported in previous studies [14,18].

2.3. Local biomass concentration

To quantify the segregation behaviour between sand and biomass particles at a given gas velocity, it is necessary to measure the distribution of biomass particles which is often present in a lesser amount. However, since no particle-tracking sensor is employed in this study, a mathematical model is needed. By comparing the volume fraction of pure sand with that of the sand-biomass mixture at the same bed position and gas velocity, it is possible to ascertain the distribution of biomass along the bed axis. For example, Fig. 2(a) compares the radial distributions of solids fraction in a bed of pure sand particles with those in a bed containing sand and 30 vol% wood pellets at different gas velocities. At the lower velocity, $U_0 = 0.06$ m/s, neither of the beds is fluidized. The higher solids fraction in the bed mixture compared to the bed of sand is due to presence of the wood particles. The relatively small amount of pellets in the bed increases the packing density of sand particles. However, at the higher gas velocity, $U_0 = 0.16$ m/s, both beds are bubbling, leading to a decrease in the solids fraction. Because biomass particles follow the path along the flow of bubbles, the concentration of biomass particles is higher near the bed axis, resulting in a stronger depression of solids fraction of the bed mixture compared to that of sand particles. It should also be noted that when a section of a bed contains nearly 100% biomass particles, the ECT sensor measures a very high relative permittivity. In this case, the solids fraction of the bed mixture becomes higher than the value at the initial state.

Assuming a linear volume combination, the time-averaged mixture solids volume fraction, $\alpha_{i,j,m}$ at a given pixel (i, j) shown in Fig. 2(b) can be expressed in terms of the corresponding pure component values as

$$\alpha_{i,j,m} = \alpha_{i,j,s} \pm \alpha_{i,j,b} \tag{5}$$

The ± sign is included since the value of $\alpha_{i,j,m}$ can be higher or lower than the solids fraction, $\alpha_{i,j,s}$, in the bed of sand particles as shown in Fig. 2(a). In relation to sand particles, the biomass solids fraction, $\alpha_{i,j,b}$ in the mixture can thus be obtained as

Table 1
Biomass and sand particle properties at fixed state.

Materials	Shape	ρ_p (kg/m^3)	$d_{p,sph}$(mm)	φ_p (−)	ε (−)	ε_{mf} (−)	U_{mf} (m/s)
Wood pellets	Cylindrical	1139	8.96	0.82	0.43	0.46	1.99
Wood chips	Rectangular	423	6.87	0.75	0.49	0.57	1.27
Sand	Angular	2650	0.293	0.86	0.42	0.46	0.079

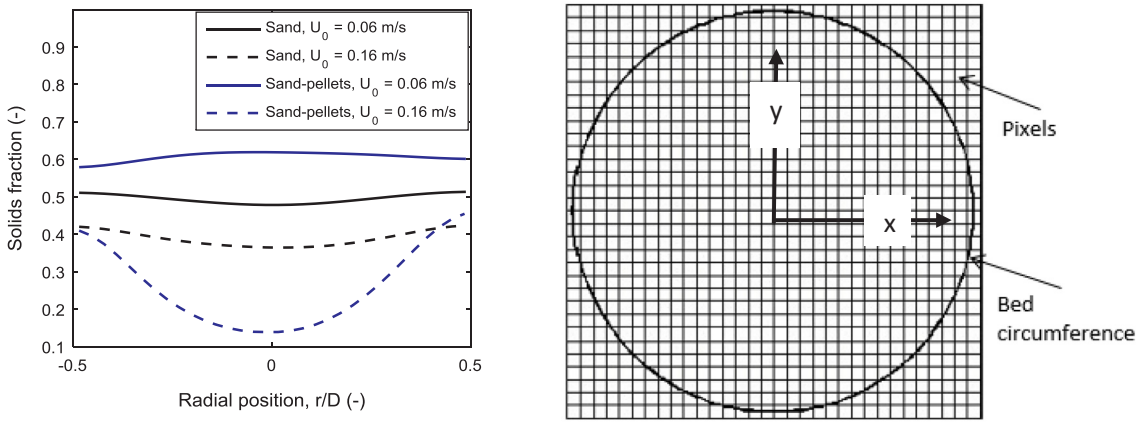

Fig. 2. (a) Radial distribution of solids fraction obtained from ECT at the lower plane for a bed with 30% wood pellets compared with that of pure sand particles; (b) Cross-section of the bed divided into 812 pixels.

Table 2
Properties of bed mixture at different biomass concentration.

Biomass volume fraction (%)	ε_m (−)		ρ_m kg/m^3		d_m (mm)	
	Pellets	Chips	Pellets	Chips	Pellets	Chips
0	0.448	0.448	2650	2650	0.252	0.252
5	0.427	0.420	2574	2539	0.265	0.265
10	0.404	0.410	2499	2427	0.279	0.279
20	0.388	0.380	2348	2205	0.312	0.311
30	0.353	0.333	2197	1982	0.355	0.352
50	0.258	0.250	1895	1537	0.487	0.481

$$\alpha_{i,j,b} = \alpha_{i,j,s} - \alpha_{i,j,m} \tag{6}$$

With $X_{i,j,b}$ the mass fraction of biomass in the mixture,

$$\alpha_{i,j,b} = X_{i,j,b} C_{i,j,m} / C_{i,j,b} \tag{7}$$

where $C_{i,j,b}$ is the mass concentration of biomass. The mixture mass concentration $C_{i,j,m}$ can be obtained from

$$C_{i,j,m} = \frac{\alpha_{i,j,m}}{\left(\frac{X_{i,j,b}}{\rho_b} + \frac{1 - X_{i,j,b}}{\rho_s}\right)} \tag{8}$$

Noting that $C_{i,j,s} = \alpha_{i,j,s}\rho_s$, it can be shown based on the mass balance that

$$\alpha_{i,j,b} = \frac{X_{i,j,b}}{1 - \frac{\alpha_{i,j,s}}{\alpha_{i,j,m}}\left[\left(\frac{\rho_s}{\rho_b} - 1\right)X_{i,j,b} + 1\right]} \tag{9}$$

From Eq. (9), $X_{i,j,b}$ can be obtained as

$$X_{i,j,b} = \frac{{\alpha_{i,j,b}}^2/\alpha_{i,j,m}}{1 + \frac{\alpha_{i,j,s}\alpha_{i,j,b}}{\alpha_{i,j,m}}\left(\frac{\rho_s}{\rho_b} - 1\right)}$$

$$X_{i,j,b} = \frac{(\alpha_{i,j,s} - \alpha_{i,j,m})^2}{\alpha_{i,j,m} + \alpha_{i,j,s}(\alpha_{i,j,s} - \alpha_{i,j,m})\left(\frac{\rho_s}{\rho_b} - 1\right)} \tag{10}$$

On volume basis, the biomass concentration at any position in the bed is therefore given by

$$Y_{i,j,b} = \frac{X_{i,j,b}}{X_{i,j,b} + \frac{\rho_b}{\rho_s}(1 - X_{i,j,b})} \tag{11}$$

The input parameters to Eq. (11) are the solids fraction of the pure sand particles, $\alpha_{i,j,s}$, measured at a position in the bed and the corresponding solids fraction of the biomass-sand mixture, $\alpha_{i,j,m}$, obtained at the same bed condition. For a given plane in the bed, the average volume fraction of biomass particles, Y_b, across the cross section of the plane can be obtained from Eq. (12), where $N_{pix} = 812$ is the total number of pixels within the bed cross section.

$$Y_b = \frac{1}{N_{pix}}\left(\sum_i \sum_j Y_{i,j,b}\right) \tag{12}$$

2.4. Experimental procedure

Five different mixture compositions were used for characterizing the fluidized bed behaviour. Table 2 shows the proportion of biomass and sand particles used in each mixture. For the individual mixture, the amount of material required to form the bed was divided into 10 portions, each containing the same proportion of sand and biomass particles as in the total mixture. The different portions of the mixture were charged into the column one after the other, and thereafter the column walls were properly shaken. This procedure helped to ensure that both different types of particles are sufficiently present at the measurement planes during the sensor calibration. The same total bed height, 50 cm at fixed state, was used for all mixtures. With this bed height, the aspect ratio, $h/D = 5$, is very high. There are two reasons for using this high aspect ratio: (1) To ensure that the upper ECT sensor located at a position 28.7 cm from the distributor is well-covered. With this, the signal to noise level can be minimized during the sensor calibration. (2) To enhance understanding of the behaviour of biomass-sand mixture across different bed aspect ratios since most of the previous studies are based on shallow beds. To verify the influence of bed height on the behaviour observed in this setup, the different mixtures of sand and biomass particles were fluidized at different gas velocities in the setup equipped with pressure sensors. As this setup is transparent over the entire bed height, the particle segregation patterns were clearly observed. Two different bed aspect ratios, 1.2 and 2.4, were used for this demonstration.

For prediction of different properties obtained in the binary mixtures at fluidized state, the average diameter, density and sphericity of the particles are based on the following expressions.

$$d_m = \left[\frac{y_b}{d_b} + \frac{(1 - y_b)}{d_s}\right]^{-1} \tag{13}$$

$$\rho_m = y_b\rho_b + (1 - y_b)\rho_s \tag{14}$$

$$\varphi_m = d_m/d_{p,sphm} \quad (15)$$

Here, y_b is the volume fraction of biomass in the mixture while the subscripts "m", "b" and "s" denote mixture, biomass and sand, respectively. Moreover, the initial void fraction of the mixture, ε_m, given in Table 2 is computed based on the mixture average density obtained from Eq. (14).

3. Results and discussion

In this section, different bed properties due to flow of bubbles are presented. The behaviour in the bed containing wood pellets is compared with that containing an equal amount of wood chips at the same gas velocity.

Fig. 3 shows the distribution of solids fraction in the upper measurement plane for the beds containing 20 vol% of biomass particles. A high value on the figure colour bar indicates a high solids fraction. Based on the threshold solids fraction of 0.2, it can be seen that a bubble contains a central region with a gas pocket (region of no solids) surrounded by a thin region of dilute phase (solids fraction less than 0.2). The size of the bubble rising in the bed with wood chips is larger than that rising in the bed with wood pellets at the same measurement plane and gas velocity. The figure also shows that the concentration of solids increases gradually away from the bubble region. Since the solids concentration is higher in the bed of pure sand particles, this indicates that in the presence of bubbles, biomass particles are located in the dilute region of the emulsion phase of the bed (the region excluding the bubbles).

3.1. Transition to fluidization and slugging regimes

For each of the biomass-sand mixtures, the minimum fluidization and slugging velocities were obtained from plots of solids fraction fluctuation against superficial air velocity, as described in Agu et al. [22]. Fig. 4 shows the measured values of U_{mf} and $U_{ms} - U_{mf}$ at different amounts of biomass in the mixture. As can be seen, the minimum fluidization velocity of the mixture with wood pellets slightly decreases with increase in biomass volume fraction up to 0.2. At higher biomass concentration, U_{mf} increases with increase in the biomass load. Since the sand particle properties are the same, the decrease in minimum fluidization velocity at increasing amount of biomass suggests that the void fraction of the bed mixture decreases. For the case of wood chips, the value of U_{mf} increases as the amount of biomass in the mixture increases due to higher void fractions of the beds. Comparing the experimental results in Fig. 4(a) with those from different correlations [4,7–9], the prediction error is as high as 40%. As illustrated, the Rao and Bheemarasetti [7] model under predicts the minimum fluidization velocity in the mixture containing up to 20% wood pellets and over predicts the fluidization velocity for higher pellets concentration. As the U_{mf} values of pure wood chips and wood pellets are almost the same, the Cheung et al. [25] model predicts approximately the same value of U_{mf} when $y_b < 0.3$ in these biomass beds.

In addition, Fig. 4(b) shows that the minimum excess slugging velocity, $U_{ms} - U_{mf}$, increases as the biomass volume fraction increases between 0 and 0.3. Although the $U_{ms} - U_{mf}$ value is slightly higher for the bed with pellets compared to that with wood chips of equal volume, the trend of the variation is the same for the two woody biomasses. The delay in the onset of slugging in the different bed mixtures suggests that bubble diameter decreases with increasing amount of biomass. No available correlations [23,26,27] applied in the beds of pure solid particles can appropriately predict the trend of $U_{ms} - U_{mf}$ shown in Fig. 4(b). However, analysis of the experimental data shows that the ratio U_{ms}/U_{mss} is independent of the biomass type as given in Eq. (16), where U_{mss} is the minimum slugging velocity of the sand particles. As shown in Fig. 4(b), Eq. (16) accurately reproduces the experimental data for the biomass loads up to 30 vol%.

$$\frac{U_{ms}}{U_{mss}} = e^{1.13 y_b} \quad (16)$$

3.2. Effect of gas velocity on biomass distribution

The distribution of biomass in a bed mixture can be obtained using different correlations [13,28]. According to Fotovat et al. [13], the biomass volume fraction along the bed axis can be predicted as follows:

$$Y_b = \frac{(1-\delta_b)(1-\varepsilon_e)}{(1-\delta_b)(1-\varepsilon_e) + f_{wake}\delta_b(1-\varepsilon_f)} Y_{be} \quad (17)$$

where the amount of biomass, Y_{be} in the emulsion phase is computed from the following equation and boundary condition (BC):

$$\frac{dY_{be}}{dh} = \frac{0.0405\delta_b(1-\varepsilon_f)A}{\varepsilon_{mf} D_b (Q_{sb} + Q_{be})} Y_{be}; \quad \text{BC:} \quad Y_{be}(h=0) = 2x_b^{1.2} U_0^{1.6} \quad (18)$$

Here, δ_b is the bubble volume fraction evaluated as the ratio of bubble volumetric flux to the bubble velocity, ε_e is the void fraction in the emulsion phase, and Q_{sb} and Q_{be} are the volumetric flow rates of sand and biomass in the bubble and emulsion phases, respectively. $A = \pi D^2/4$, where D is the bed diameter. The detailed expressions for all the necessary input to Eqs. (16 and 17) are given in [13]. For the bubble diameter, D_b, the model proposed by Darton et al. [29] is used

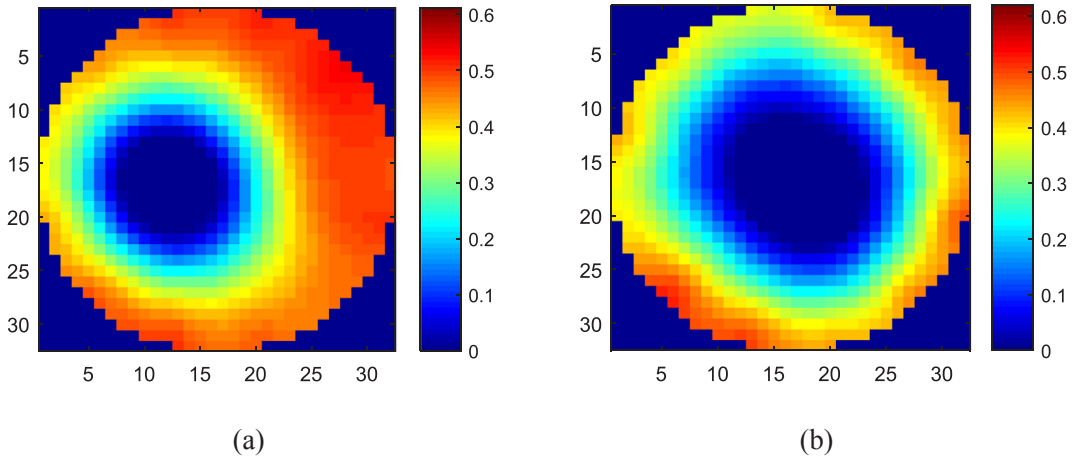

Fig. 3. Contour showing the distribution of solids fraction at $U_0 = 0.16$ m/s in a bed mixture of sand and 20% vol. of (a) wood pellets (b) wood chips; bed position = 28.7 cm above distributor. Solids fraction increases with the colour scale value (deep blue (0) = only air; deep red (0.6) = only solid; between 0 and 1 = air–solid mixture).

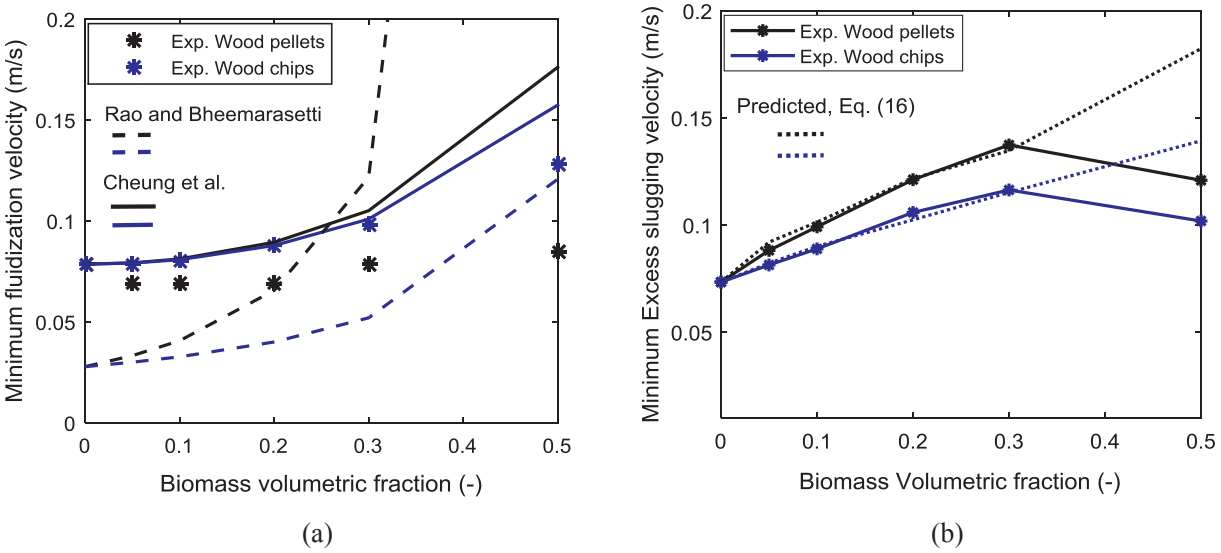

Fig. 4. Effect of biomass load on the transition velocity (a) minimum fluidization velocity (b) minimum excess slugging velocity.

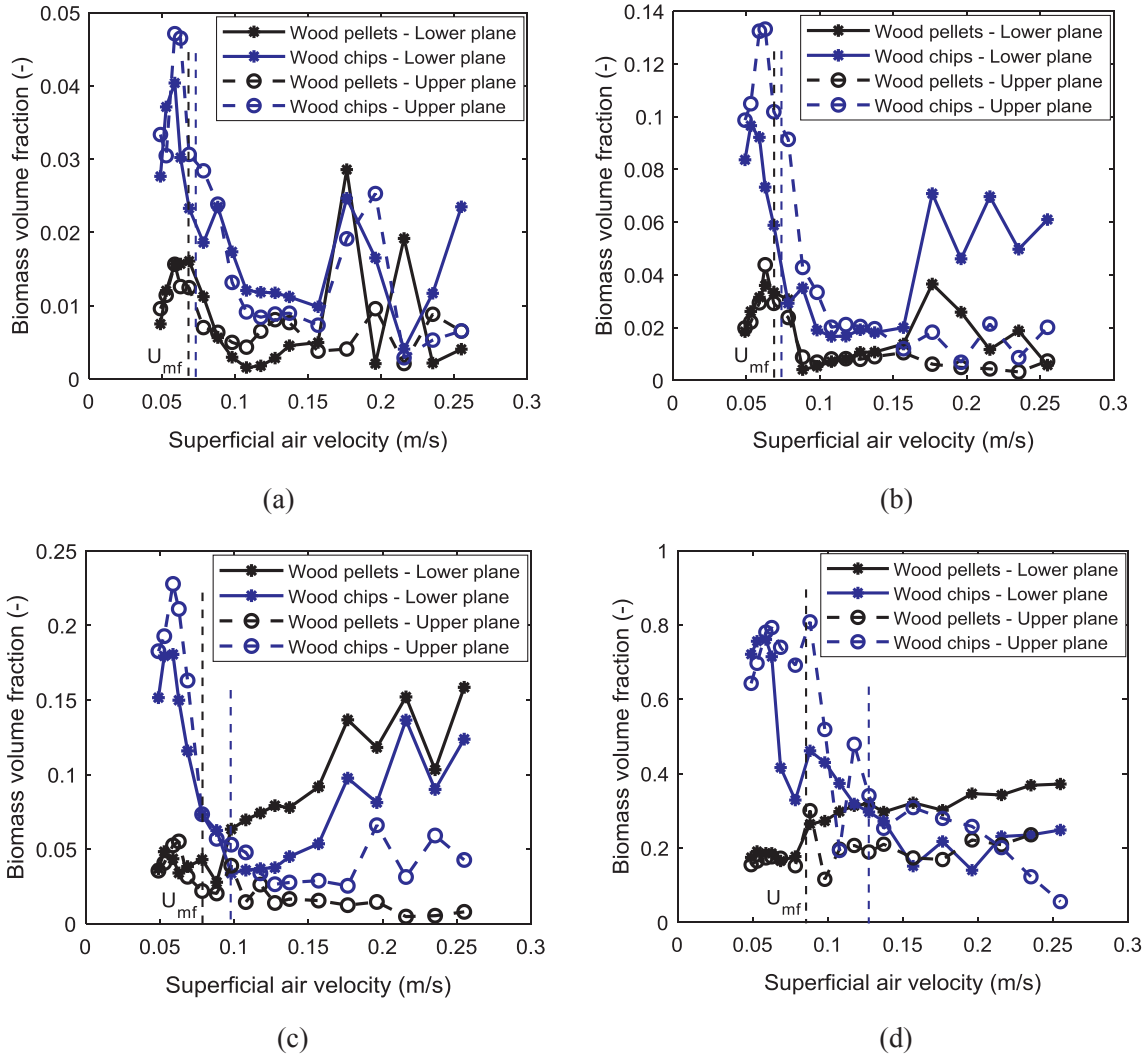

Fig. 5. Distribution of biomass particles along the bed for different amount of biomass (a) 10% (b) 20% (c) 30% (d) 50% by volume. Dotted vertical lines demarcate fixed bed from fluidized bed conditions (blue = wood chips; black = wood pellets).

while the Davidson and Harrison [30] model is applied for the bubble velocity, u_b. The results from Eq. (17) are compared with those obtained in this study based on Eq. (12).

Fig. 5 shows the variation of average concentration of biomass at different superficial air velocities computed based on Eq. (12) at both measurement planes. With increase in the gas velocity below the minimum fluidization velocity, $U_0 < U_{mf}$ (indicated by the vertical lines), the results show that the biomass concentration increases. Since the column walls were shaken to ensure that the sand particles properly fill up the void of the wood particles during calibration, a larger amount of sand particles was contained in the wood void than should be in a loosely packed state. Therefore, as air flows into the bed, sand particles flow out of the void of the wood particles, increasing the biomass concentration at the measurement planes. The higher concentration of wood chips compared to that of wood pellets at the same measurement position indicates that a larger amount of sand particles flows out in the bed with wood chips. The biomass concentration increases up to a peak value. The peak concentration attained below the bed minimum fluidization velocity increases with the amount of biomass charged into the bed. When the air velocity is slightly above that at the peak concentration, the sand particles become fluidized, leading to segregation of biomass and sand particles. The biomass particles move upwards (in the wood chips case) and downwards (in the wood pellets case), resulting in a reduction in the wood particle concentration at the measurement planes. The upward movement of wood chips at increasing gas velocity can be slightly seen in Fig. 5 since the wood concentration at the upper plane is higher than that at the lower plane when the gas velocity is increased up to the value $U_0 = U_{mf}$. For the case with pellets, Fig. 5(c and d) clearly shows that the concentration of the biomass particles increases down the bed. It should be noted that the two measurement planes are within the middle of the bed. Therefore, only a fraction of biomass in the bed is detected in each of the planes. When the entire bed is fluidized, i.e. $U_0 > U_{mf}$, further segregation occurs due to flow of gas bubbles at low gas velocity, but the rate of segregation at this stage is lower than that at the initial stage. At a higher gas velocity, the biomass particles move back into the bed due to circulation of sand particles from the top to the bottom of the bed.

The degree at which biomass sinks increases with the amount of biomass in the bed and as can be seen, this is more severe with the bed containing wood pellets due to their higher bulk density, which increases with increase in biomass load at a given plane. For example, at $y_b = 0.3$, the concentrations of pellets and chips in the lower plane increases when $U_0 > U_{mf}$, but in the upper plane, the amount of wood pellets decreases while that of wood chips increases at the increasing gas velocity. This indicates that most of the pellets are below the lower plane, and partially a good amount of wood chips is above the upper measurement plane. Similarly, this behaviour can also be observed at $y_b = 0.5$, but within the range of gas velocities shown, the wood chips are still segregated upwards. The higher concentration of biomass at the top or bottom forms a dense layer, which prevents the circulation of sand particles and thus the flow of biomass particles into the bed.

Comparing with the results from Eq. (17), the model predicts a continuous decrease in the concentration of wood chips and pellets in their respective beds at both measurement positions. At some gas velocities, $U_0 - U_{mf} < 0.1$ m/s, and biomass loads, $y_b > 0.2$, the model gives unrealistic results, i.e. $Y_b > 1$. In addition, the predicted biomass volume fractions at the measurement planes are also larger than unity when the total bed height 50 cm is used in the computation for all values of $U_0 - U_{mf}$. This implies that Eq. (17) may be suitable only for higher gas velocities, $U_0 - U_{mf} > 0.3$ m/s, and for a shallow bed, $h_0/D \leq 1.5$, since these are the conditions the authors used in the model validation.

3.3. Influence of bubble flow on biomass distribution

Fig. 6 shows the distribution of biomass particles computed from Eq. (11) across the bed for three different gas velocity ratios, U_0/U_{mfs}, where U_{mfs} is the minimum fluidization velocity of the sand particles given in Table 1, and for four different biomass fractions at both measurement planes. The value shown is the average of the concentrations at the positions in both x and y axes of the bed. As can be seen, the distribution of biomass particles depends on the gas velocity and on the amount of biomass charged into the bed. Moreover, the pattern of the distribution differs between the two different types of biomass particles.

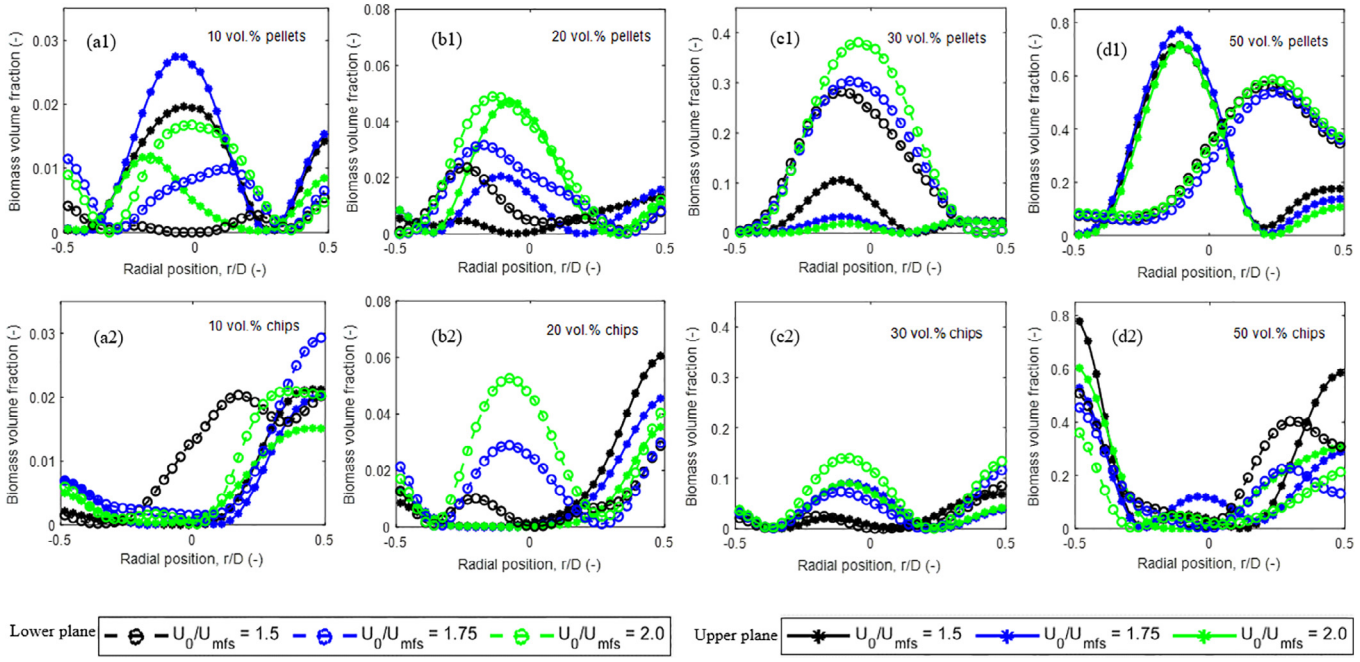

Fig. 6. Radial distribution of biomass in a bed mixture with sand particles, comparing the behaviour of wood pellets with that of wood chips at the same gas velocities and biomass loads.

3.3.1. Radial distribution of wood pellets and chips

When no bubbles flow in the bed, the biomass concentration attains a peak value at a position between the central axis and the walls. For example at $U_0/U_{mfs} = 1.5$, no bubbles flow in the lower plane of both beds shown in Fig. 6(a1 and a2). Without flow of bubbles, larger amount of sand particles near the walls flow up the bed, resulting in a higher biomass concentration at the walls than at the bed axis. With flows of bubbles, the biomass particles move round in the bed. The wood pellets tend to move towards the central axis while the chips spread to the walls at the same gas velocity due to circulation of sand particles across the segregated biomass layer formed near the bottom (for the former) and near the top (for the latter). The sand particles moving downwards along the bed walls push the wood chips into the bed, increasing the biomass concentration around the walls. In the bed of 20% wood pellets, sand particles push the biomass into the bed along the central axis as they move upwards with the rising bubbles while in that of higher biomass loads, the pellets sink along the path of bubble flows, resulting in a higher biomass concentration at the central axis. The lower concentration of biomass near the walls is due to downward flow of sand particles, and as can be seen in Fig. 6(a1–c1), the wall region with little amount of biomass particles increases from the lower to the upper plane. In addition, the spread of biomass towards the walls decreases down the bed and with an increase in the gas velocity due to increased sand particle circulation at higher gas velocities. The tendency of wood chips to move towards the bed centre increases with increasing biomass load and increasing gas velocity.

In the bed containing 50% pellets as shown in Fig. 6(d1), the lower region of the bed is not fluidized at the given gas velocities due to accumulation of the biomass and thus no flow of bubbles. At the upper plane, the biomass layer interfaces with the fluidized sand particles above. The biomass concentration is high in this plane since sand particles constantly leave the plane and no circulation through the layer below. At the walls, sand particles tend to penetrate through the biomass layer, leading to a reduced biomass concentration near the walls. In the bed with wood chips, bubbles flow in the lower plane when $U_0/U_{mfs} > 1.75$ and in the upper plane when $U_0/U_{mfs} > 1.5$. Due to these low gas velocities shown in Fig. 6(d2), the bubble-induced biomass movement is insignificant in the bed of wood chips. The higher concentration of chips at the wall region makes it difficult for sand particles to penetrate to the bottom of the bed, thus preventing rise of wood chips along the central axis.

3.3.2. Vertical distribution of wood pellets and chips

For the loads $y_b < 0.5$, the concentrations of biomass in the lower plane increase with an increase in the gas velocity as shown in Fig. 6(a–c). In Fig. 6(a1), the pellet concentration is higher in the upper plane than in the lower plane due to low bulk density of the biomass particles, which reduces the tendency of the particles to sink into the bed at this load. Increasing the gas velocity to $U_0/U_{mfs} = 2$, the higher circulation of sand pushes the biomass particles down into the bed, resulting in a higher concentration in the lower plane than in the upper plane. With $y_b = 0.2$, the wood pellets from the lower region of the bed move upwards, increasing the concentration of the biomass particles in the upper plane as the gas velocity is increased. However, in the bed with 30% wood pellets, the biomass particles are still segregating downwards even at the gas velocity, $U_0/U_{mfs} = 2$. Increasing the gas velocity increases the sinking of the biomass into the lower bed region, thereby decreasing the concentration of biomass in the upper region as can be seen in Fig. 6(c1). As the biomass particles sink, they form a thick layer, which prevents the flow of sand particles to the bottom of the bed. To breakdown the biomass layer, a higher gas velocity is required to induce a higher sand circulation effect from the surface of the bed. It should also be noted that in a gasification reactor, the extent to which pellets sink may decrease due to reduction in the biomass density as it devolatilizes.

For the bed of wood chips where $y_b < 0.5$, the biomass concentration increases in the lower plane and decreases in the upper plane due to higher degree of biomass sinking as sand circulation becomes vigorous at higher gas velocities. The distribution of wood chips along the bed axis is less symmetrical for $y_b = 0.2$ compared to that when $y_b = 0.3$, and as shown in Fig. 6(b2), little or no chips are in the upper plane near the central axis. This suggests that as bubbles grow larger and rise along the bed, they push the low concentrated biomass particles towards the walls. Moreover, it can also be seen in Fig. 6(c2) that wood chips move into the bed from the top segregated biomass layer at the same gas velocities at which the pellets are still segregating downwards. However, since the concentration of biomass up to the middle of the bed is low even at $U_0/U_{mfs} = 2$, it shows that a significant amount of wood chips is still at the bed surface.

These results therefore show that with a higher biomass load, $y_b > 0.2$, more than twice the minimum fluidization velocity of the bed material is required to overcome the segregation of the biomass particles, thereby achieving a good distribution across the bed height. This is an important point for consideration in a bubbling fluidized bed biomass gasification, which is often carried out at $U_0/U_{mfs} \approx 2$.

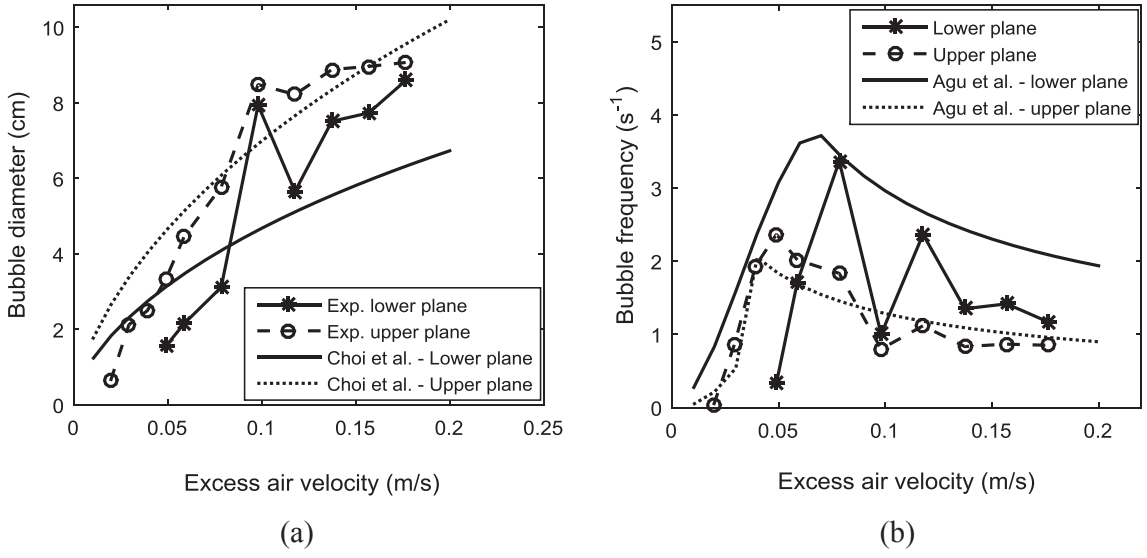

Fig. 7. Variation of (a) bubble diameter (b) bubble frequency in a bed of 293 μm sand particles.

3.4. Bubble frequency and diameter

Bubble frequency measures the rate of generation of bubbles at a given gas velocity and it depends on the bubble diameter and the rise velocity [31]. No correlation is available for prediction of bubble frequency in a binary mixture of particles. For the bed of pure sand particles, the correlation given in Agu et al. [31] is applied. Similarly, no correlation for bubble diameter is available for a mixture of biomass particles and inert particles, but a number of correlations are available [32] for pure solid particles.

Fig. 7 shows the bubble diameter and bubble frequency for the bed of 298 μm sand particles at different excess air velocities. The bubble diameter increases with increase in the value of $U_0 - U_{mf}$ and along the bed height. The rate of increase in bubble diameter with gas velocity increases at the transition between bubbling and slugging regimes $0.075\ \text{m/s} < U_0 - U_{mf} < 0.1\ \text{m/s}$, but decreases as the bed slugs. This behaviour is typical of beds containing non-spherical (angular) particles [31], which also characterizes the sand particles used in this study. Fig. 7(a) also shows that using the Choi et al. [33] model, the bubble diameter is over-predicted in the bubbling regime and under-predicted in the slugging regime, although the model fits better at the upper part of the bed.

The bubble frequency increases up to a peak value and then decreases as the gas velocity increases. The peak of the bubble frequency indicates a transition to slugging regime, and the gas velocity at which this occurs decreases along the bed height. Below the peak frequency, the change in bubble rise velocity for a unit change in gas velocity (or bubble size) is higher, resulting in an increase in the number of bubbles flowing per unit time as gas velocity is increased [31]. When the bubble size is larger than that at the maximum frequency, the frequency decreases due to the longer time it takes the bubble to pass the given plane. Fig. 7(b) also shows that the Agu et al. [31] model predicts the bed behaviour in the upper plane with a good accuracy. The bubble diameter used in this model is based on the Choi et al. [33] correlation. With the bigger and smaller bubble diameters obtained from the Choi et al. model at gas velocities below and above the peak frequency, respectively, the predicted bubble frequency is significantly higher in the lower plane.

For the mixtures of sand and wood particles, Fig. 8 shows that with an increase in the amount of biomass, the bubble diameter increases in the bubbling regime and decreases in the slugging regime. The vertical lines given in the figures demarcate the bubbling from the slugging regimes. As can be seen, the transition from bubbling to slugging gets smoother as the concentration of biomass in the bed increases. The presence of biomass within the transition region serves as a bubble breaker, preventing rising of large bubbles at high gas velocities as

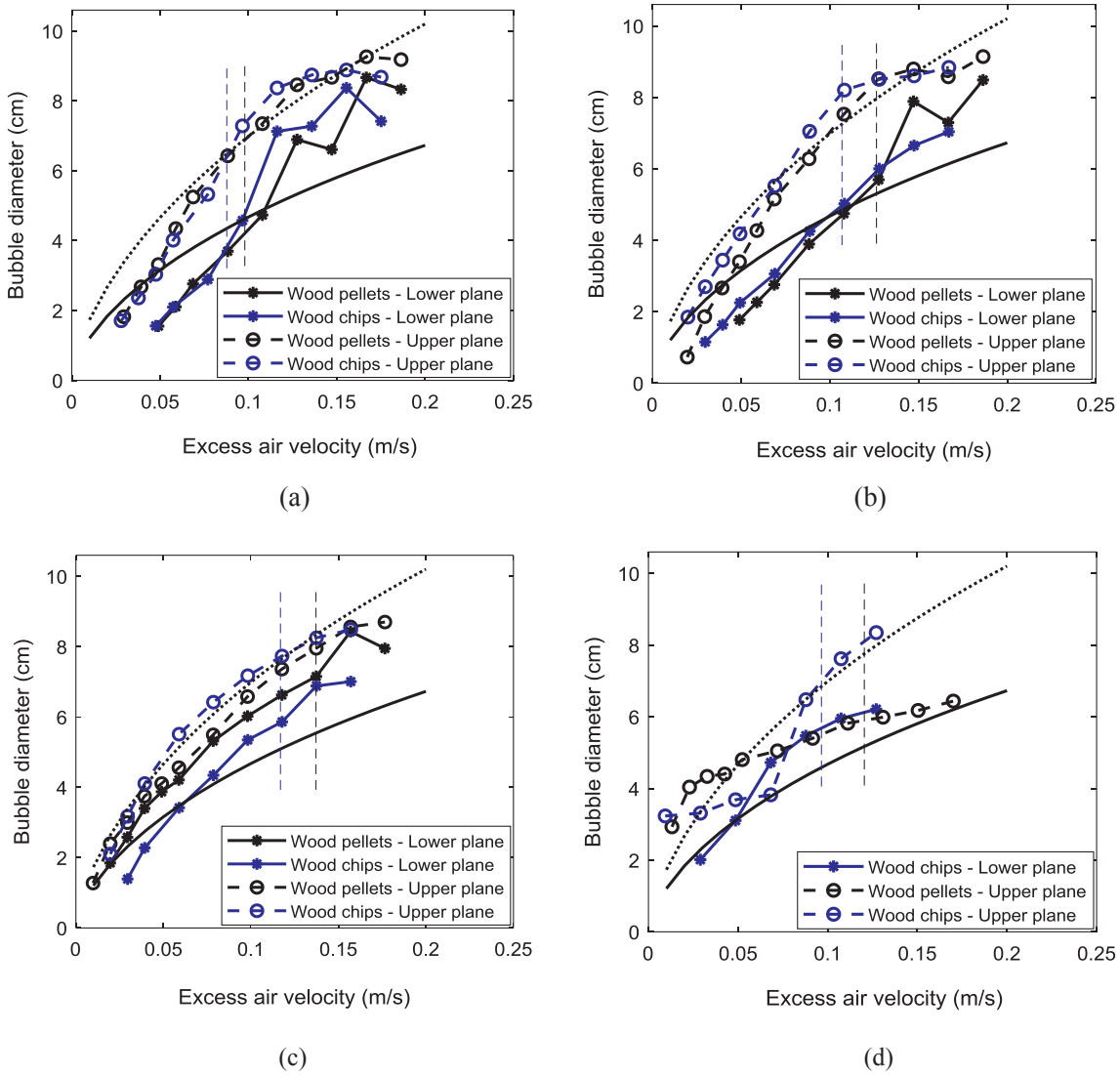

Fig. 8. Variation of bubble diameter in a bed mixture of biomass and sand particles for different amount of biomass (a) 10% (b) 20% (c) 30% (d) 50% by volume. Lines: predictions using the Choi et al. [33] model. Dotted vertical lines demarcate bubbling from slugging regimes (blue = wood chips; black = wood pellets).

similarly observed in [11,19]. This therefore explains the results shown in Fig. 4(b) where the minimum slugging velocity increases with biomass load in the bed. At lower amounts of biomass particles, the bubble diameters in both beds are approximately the same at the same measurement position. As the amount of biomass increases, the deviation in the bubble diameters between the two-biomass types increases due to increased accumulation of an un-fluidized layer of biomass. The wood chips layer prevents eruption of bubbles from the top of the bed while the pellet layer prevents fluidization of the bottom region of the bed. When the pellets volume fraction is increased to 0.5, the lower plane becomes de-fluidized due to large amount of biomass particles and thus, no bubbles rise from the bottom of the bed within the range of gas velocities shown.

Fig. 9 shows that the bubble frequency increases with increasing amounts of biomass particles and attains a peak value similar to the case of pure sand particles. The higher bubble frequency indicates that a higher number of bubbles rise through the bed mixture compared to that in the bed of pure sand particles. With a higher bubble frequency, it also suggests that the solids mixing induced by bubbles is better when the biomass load is higher. Moreover, the bubble frequency also decreases along the bed height due to bubble coalescence as similarly shown in Fig. 7(b). The gas velocity at the peak frequency decreases with the biomass load in the bed. At gas velocities above the peak frequency, the bubble frequency is higher in the bed containing wood pellets compared to that containing an equal volume of wood chips. However, for the bed with 30% pellets, the higher concentration of biomass in the lower plane reduces the rate at which bubbles rise through the lower part of the bed, resulting in a lower bubble frequency as shown in Fig. 9(a) and a larger bubble size as can be seen in Fig. 8(c) compared to those of wood chips at the same bed position.

3.5. Bed expansion

From the measured bed height at each gas velocity, the bed expansion in the fluidized state is evaluated from $\Delta e = (H_f - H_{mf})/H_{mf}$, where H_{mf} and H_f are the total bed heights from the distributor measured at the minimum fluidization velocity and at a higher gas velocity, respectively. Based on the mass balance of solids and that of gas in the bubble and emulsion phases at different gas velocities, the bed expansion, Δe can be computed from

$$\Delta e = \frac{1}{1-\delta_b} - 1 \tag{19}$$

where δ_b is the average bubble volume fraction defined as

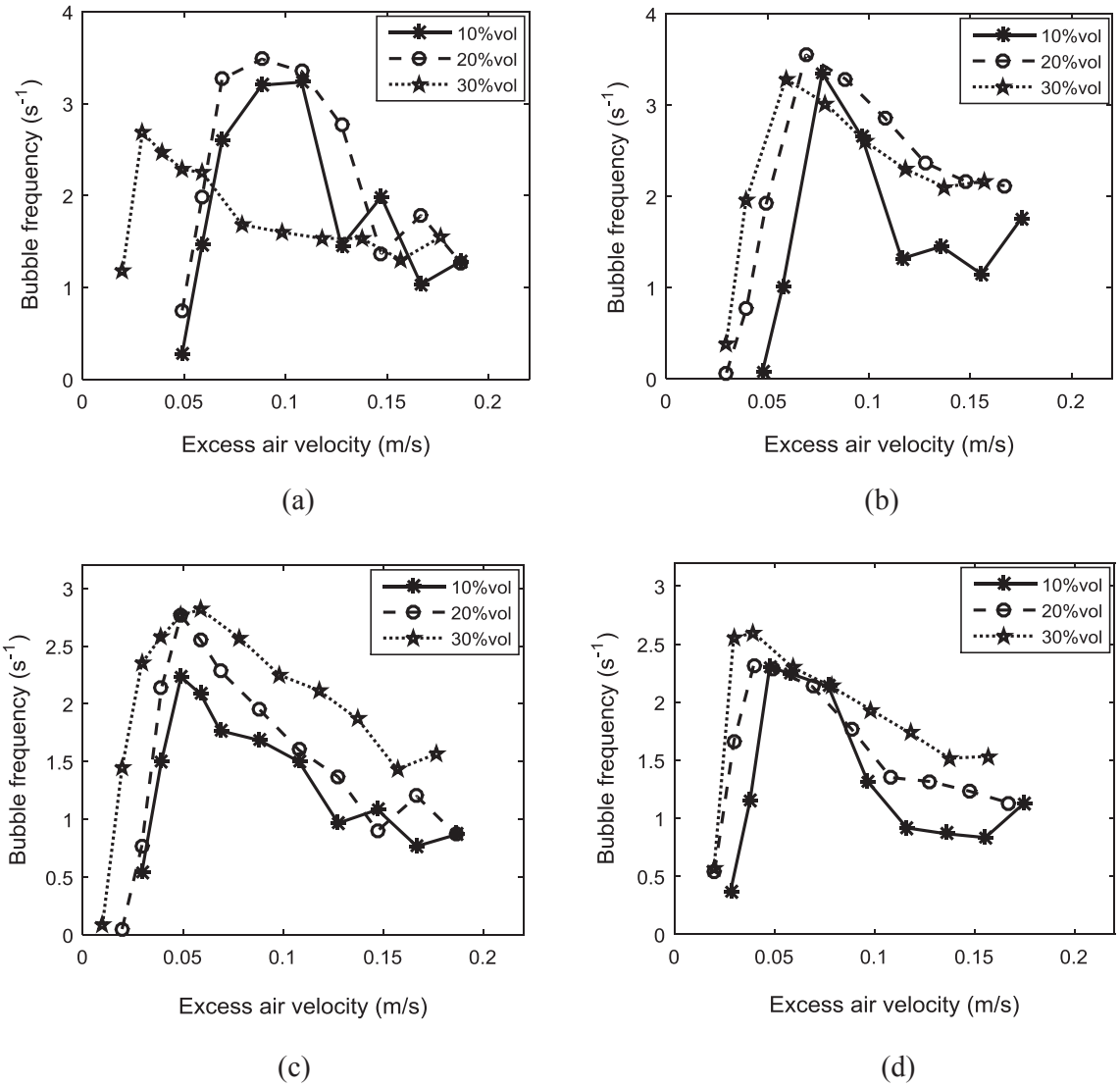

Fig. 9. Variation of bubble frequency in a bed mixture of biomass and sand particles at different measurement planes: **Lower plane** (a) wood pellets (b) wood chips. **Upper plane** (c) wood pellets (d) wood chips.

$$\delta_b = G/u_b \tag{20}$$

A value of δ_b can be obtained using the average bubble velocity, u_b predicted from the available models [30,34,35] and an expression for the bubble volumetric flux, G [23,36]. In addition to Eq. (19), Δe can also be predicted using different other correlations [37,38].

Fig. 10 shows the bed expansion measured at air velocity, $U_0/U_{mfS} = 2$ for different biomass loads. In the bed with wood pellets, the bed expansion increases with the biomass load in the range $y_b < 0.2$. For higher biomass loads, the value of Δe decreases due to decrease in the volume of bubbles rising through the bed. However, in the bed with wood chips, the total bed expansion (i.e., when the total bed height includes the un-fluidized biomass layer at the surface of the bed) increases with the biomass load up to $y_b = 0.3$ as can be seen in Fig. 10(b) (data points labelled Exp. – total). The higher bed expansion, particularly when $y_b > 0.1$ is due to higher degree of segregation in the bed with wood chips compared to that involving wood pellets. Excluding the top layer containing only the wood chip particles, the bed expansion (indicated as Exp. – fluidized) decreases with increasing amount of biomass. The rapid decrease in the value of Δe shows that the dense layer of wood chips at the top of the bed prevents rising of bubbles, thus reducing the bed expansion. In addition, Fig. 10 shows that the predicted results based on the Agu et al. [31] model agree very well with the data obtained in the beds with pellets. With exclusion of the top layer of wood chips, a good agreement with the experimental data is also obtained using the Agu et al. model. The predictions based on the bubble diameter and bubble velocity obtained from the Werther [34] correlations are lower than the experimental data although the predictions get better with increasing amount of biomass in the mixture. Conversely, at a lower biomass load ($y_b < 0.3$), the Δe prediction based on the Hepbasli [37] model gives a better result compared to that based on the Werther correlations.

3.6. Non bubbling layer – theoretical explanation

Understanding the mechanism behind the accumulation of biomass particles at either the top or bottom of the bed will help in selecting the right parameters during operation and design. For wood chips, the thickness of the top layer increases to a maximum height (observed to be within one-half of the biomass bulk volume in the total mixture) as the gas velocity is increased. While the layer is built up, the bubble eruption at the top of the bed is interrupted. When the solids fraction of the wood layer is close to the solids fraction of the pure biomass in a fixed state, walls act against the bed, preventing further rising of bubbles and penetration of sand particles to the surface of the bed. Increasing the gas velocity above that required for the maximum layer thickness, the particle impact on the layer increases. At a certain velocity, the total force exerted on the biomass layer becomes sufficiently high to overcome the wall frictional force, resulting in penetration of sand particles across the layer and induction of solids circulation at the top of the bed. This mechanism is very important for a hot bed reactor since properties of biomass change at elevated temperature.

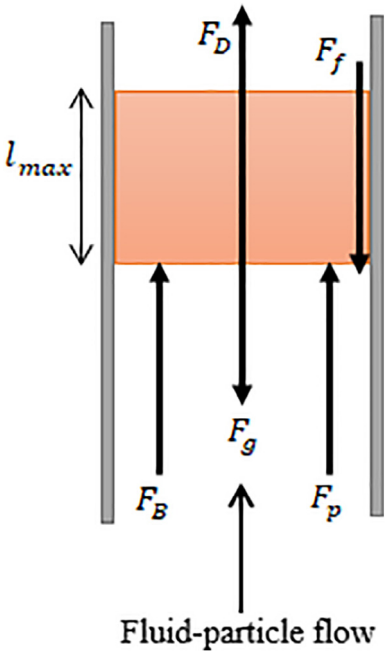

Fig. 11. Layer of biomass on the surface of a bed subjected to forces. $F_g = \varepsilon_b \rho_b g A l_{max}$, $F_f = \tau_w \pi D l_{max}$, $F_p = \varepsilon_b \Delta p_g A$, $F_B = (\rho_g + \varepsilon_s f_{wake} \rho_s) G u_b A$, $F_D = \beta A l_{max}$.

For the case of wood pellets, which segregate downwards in the cold flow, the segregation pattern may be reversed in the hot flow reactor due to devolatilization effect. Depending on the heating rate and final temperature, devolatilization can lead to a decrease in the bulk density of the particles [39]. The lower the biomass bulk density, the higher the tendency to move up the bed surface. The upward segregation of biomass in a hot fluidized bed may also be influenced by flow of bubbles

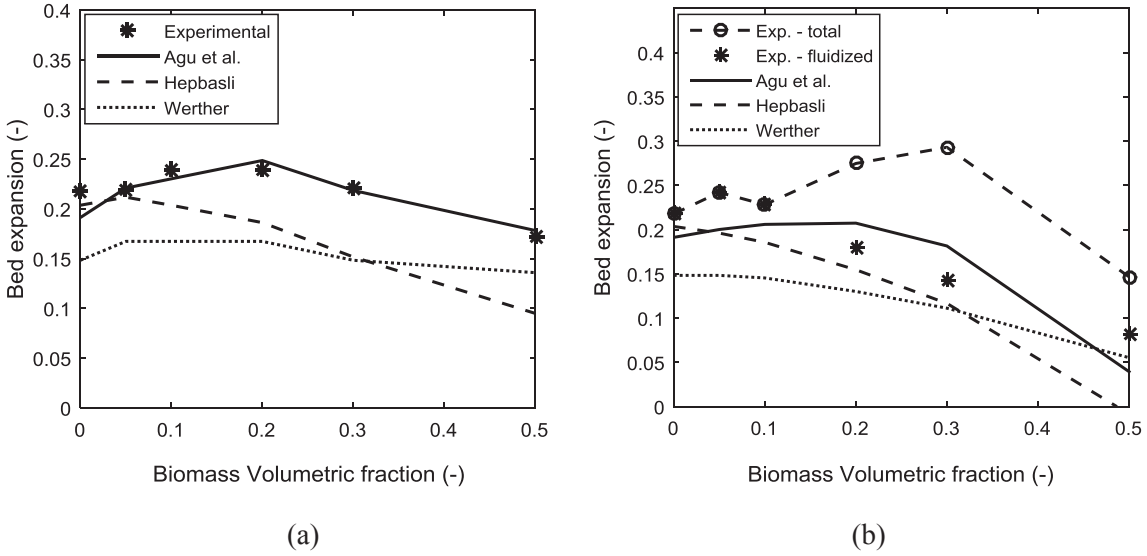

Fig. 10. Variation of bed expansion with different biomass loads at $U_0 = 2U_{mfS}$ (a) Wood pellets (b) Wood chips.

around the biomass as it devolatilizes [40], but since the devolatilization time for pellets is relatively small, the effect of volatile bubbles may be less severe [41].

From this observation, it follows that at any given gas velocity, there is a certain maximum thickness of the top layer beyond which there will be no solids circulation. In this section, a simple mathematical model is established to quantify the maximum thickness of a wood layer on the surface of a bed at a given gas velocity. Fig. 11 shows the forces acting on the biomass layer along the flow axis.

By force balance across the biomass layer,

$$\varepsilon_b \rho_b g A l_{max} + \tau_w \pi D l_{max} = \varepsilon_b \Delta p_g A + \beta A l_{max} + (\rho_g + \varepsilon_s f_{wake} \rho_s) G u_b A \tag{21}$$

where τ_w is the wall stress, ε_s is the sand solids fraction, f_{wake} is the bubble wake fraction, β is the fluid-particle momentum transfer coefficient and ε_b is the solids fraction of the biomass layer with thickness l_{max}. The expression in the right hand side is the total force transferred due to fluid pressure, gas-solid momentum exchange and impingement of bubble and sand particles carried in the wake of the bubble. The left hand side is the total resistance force due to weight of the layer and wall friction. The fluid pressure drop Δp_g across the layer can be modelled as

$$\Delta p_g = \gamma \delta_b \varepsilon_s \rho_s g l_{max} \tag{22}$$

Here, γ accounts for the effect of non-hydrostatic pressure distribution and non-uniformity of pressure across the bed cross section. For simplicity, γ can be assumed the same as the bed aspect ratio corresponding to the bed material. Thus, $\gamma = (1 - y_b)h_0/D$, where h_0 is the initial bed height. Applying Columb's law, the wall frictional stress can be obtained as $\tau_w = \mu_w \sigma$, where μ_w and σ are the coefficient of friction and the average normal stress induced on the wall due to internal stress in the wood layer, respectively. The value of σ for a given powder strongly depends on the voidage of the powder. When $\varepsilon < \varepsilon_{mf}$, the normal stress has negligible effect on the flow of the powder. For a dense powder flow, different models for σ can be found in the literature [42–44]. Based on the model given by Rankine [44], a value of σ can be predicted from

$$\sigma = \frac{1}{2} \varepsilon_b \rho_b g l_{max} k \tag{23}$$

$$k = \left(\frac{1 - sin\theta_i}{1 + sin\theta_i} \right)$$

Here, k is the pressure coefficient and θ_i is the angle of internal friction in the wood layer.

Substituting Eqs. (22 and 23) in Eq. (21), gives

$$\varepsilon_b \rho_b g A l_{max} + \frac{2}{D} \mu_w k \varepsilon_b \rho_b g {l_{max}}^2 A = \gamma \varepsilon_b \delta_b \varepsilon_s \rho_s g A l_{max} + (\rho_g + \varepsilon_s f_{wake} \rho_s) G u_b A + \beta A l_{max}$$

$$\frac{2}{D} \mu_w k {l_{max}}^2 + (1 - \gamma \frac{\rho_s}{\rho_b} \delta_b \varepsilon_s - \frac{\beta}{\varepsilon_b \rho_b g}) l_{max} = \frac{(\rho_g + \varepsilon_s f_{wake} \rho_s)}{\varepsilon_b g \rho_b} G u_b \tag{24}$$

For the application of Eq. (24), all the bubble properties are computed at the bed position near the bottom of the biomass layer, i.e. $h = (0.5 y_b + 1)h_0$. To obtain the minimum gas velocity required to achieve solids mixing at the surface of the bed, $l_{max} = 0.5 y_b h_0$ is used. The bubble diameter, bubble velocity and bubble volumetric flux can be estimated as respectively proposed by Werther [34], Davidson and Harrison [30] and Kunii and Levenspiel [36].

$$D_b = 0.853[1 + 0.272(U_0 - U_{mf})]^{1/3}(1 + 0.0684h)^{1.21}, \quad [\text{cm}] \tag{25}$$

$$u_b = U_0 - U_{mf} + 0.711(gD_b)^{0.5} \tag{26}$$

$$G = \varnothing(U_0 - U_{mf}); \ \varnothing = 0.65 \tag{27}$$

Fig. 12 illustrates the application of Eq. (24) for determining the minimum gas velocity required to achieve solid circulation at the top of a bed containing wood chips. The mean values of the frictional parameters, θ_i and μ_w used are 45° and 0.35, respectively as reported in [45], and the bubble wake fraction f_{wake} for the 293 μm sand particles is 0.24 [36]. The momentum transfer coefficient $\beta = 0$ is assumed since the size of the biomass particles is very large and the gas velocity at the operating condition is far below the minimum fluidization velocity of the wood particles. The increase in the thickness of the biomass layer as the gas velocity increases is shown in Fig. 12(a) for the bed of diameter 10.4 cm and aspect ratio of 5.0. As can be seen, the maximum thickness of the layer increases with the amount of wood particles in the bed. The minimum excess gas velocity, $U_0 - U_{mf}$, before bubbles can erupt from the bed surface also increases with biomass load. Moreover, the predicted gas velocity from Eq. (24) at the maximum thickness of the wood layer (approximated to $0.5 y_b h_0$), agrees with the experimental data. The predicted results also show that solids mixing at the top of the bed containing 5% biomass occurs when $U_0 - U_{mf} \approx 0.045$ m/s. For the mixture with 50% biomass, the predicted minimum value of $U_0 - U_{mf}$

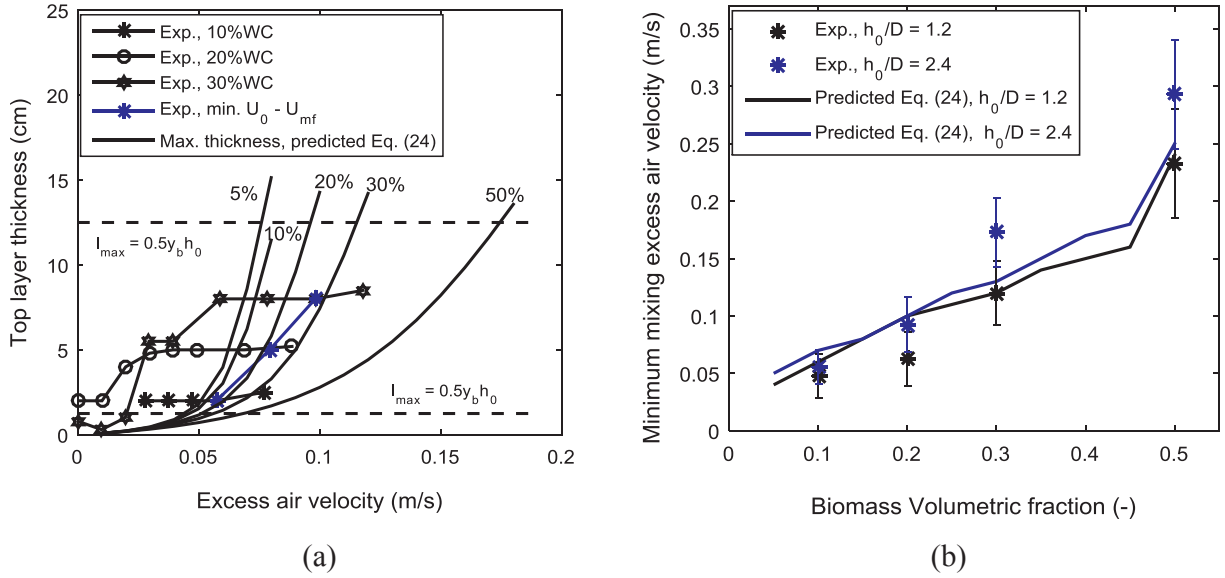

Fig. 12. (a) Variation of thickness of wood chip layer at the bed surface showing minimum gas velocity for particle mixing in the bed; $D = 10.4$ cm and $h_0/D = 5$. (b) Variation of minimum gas velocity for particle mixing with wood chips load in the bed; $D = 8.4$ cm at different aspect ratios, $h_0/D = 1.2$ and $h_0/D = 2.4$.

for the top mixing is 0.175 m/s. However, below this velocity, the bed is slugging as shown in Fig. 4, making it difficult to achieve the right mixing in this deep bed. Decreasing the bed height reduces the chances of slugs flow in a bed. The range of gas velocities required to break through the top layer and achieve a continuous mixing are shown in Fig. 12(b) for different biomass loads. The results are obtained in the bed of 8.4 cm at two different aspect ratios, $h_0/D = 1.2$ and $h_0/D = 2.4$. The error bar represents the range of gas velocity at which a complete mixing of particles was observed at the top of the bed while the data point represents the mean value of these velocities. As can be seen, the mean gas velocity increases with increase in the aspect ratio. However, the overlap in the range of velocities between the two aspect ratios shows that the bed height may have insignificant effect on the gas velocity required to achieve a continuous mixing at the surface of the bed. The figure also shows that the predicted results based on Eq. (24) agree with the experimental data within the range of observed values. The minimum values of $U_0 - U_{mf}$ predicted for different biomass concentration also vary slightly with changes in the bed aspect ratio. Comparing the results shown in Fig. 12(a and b), the excess gas velocity to achieve the solids mixing decreases with increased bed diameter, which may be due to the decrease in the wall frictional force as the bed diameter increases. From these results, it follows that Eq. (24) properly accounts for the mechanism in breaking down the top layer of biomass to achieve continuous mixing, and can be used to predict the minimum gas velocity required to achieve mixing of solid particles in binary mixtures.

4. Conclusion

This study investigated the segregation pattern and bubbling properties in cold fluidized beds containing mixtures of sand and biomass particles using measured ECT data obtained from a 10.4 cm diameter cylindrical column. The bed behaviour involving wood chips of irregular shape and low density are compared with those involving cylindrical wood pellets of higher density.

The results showed that at low gas velocity, the wood chips segregate upwards while the wood pellets segregate downwards in their respective beds. The degree of segregation increases with biomass load. The segregation behaviour at a gas velocity below the bed minimum fluidization is more severe in the case with wood chips, resulting in a steady increase in the minimum fluidization velocity compared to the case with wood pellets, which shows a negligible change in the minimum fluidization velocity up to a biomass load of 50% by volume. The maximum thickness of wood chips accumulated at the bed surface in steady state is about 50% of the height of pure biomass charged into the bed. At higher gas velocities, the biomass particles move back into the bed from the segregated layers. The gas velocity required to achieve mixing over the bed is almost independent of initial bed height, but increases with biomass load and decreases with bed diameter. By a force balance, a mechanistic model was formulated for predicting the minimum gas velocity required to achieve an effective mixing in the bed mixture.

The results also show that both the bubble diameter and bubble frequency increase within the bubbling regime as the amount of biomass increases. The transition from bubbling to slugging regime also gets smoother as the biomass load increases, resulting in an increase in the minimum slugging velocity and a decrease in the bubble diameter within the slugging regime. To successfully scale up this behaviour to a hot bed reactor, the extent to which temperature influences the distribution of biomass particles needs to be investigated.

5. Funding sources

This research did not receive any specific grant from funding agencies in the public, commercial, or not-for-profit sectors.

References

[1] X. Wu, K. Li, F. Song, X. Zhu, Fluidization behaviour of biomass particles and its improvement in a cold visualized fluidized bed, BioResources 12 (2017) 3546.
[2] Y.H. Chen, J. Yang, R.N. Dare, R. Pfeffer, Fluidization of coated group C powders, AIChE J. 54 (2008) 104.
[3] L.F. Zhang, J.T. Hou, X.T. Bi, J.R. Grace, T. Janke, C. Arato, Fluidization characteristics and changing behaviour of fly ash in vibro-fluidized bed, Powder Technol. 215 (2012) 235.
[4] C. Si, Q. Guo, Fluidization characteristics of binary mixtures of biomass and quartz sand in an acoustic fluidized bed, Ind. Eng. Chem. Res. 47 (2008) 9773.
[5] D. Escudero, T.J. Heindel, Minimum fluidization velocity in a 3D fluidized bed modified with an acoustic field, Chem. Eng. J. 231 (2013) 68.
[6] B.T. Vilches, E. Sette, H. Thunman, Behaviour of biomass particles in a large scale (2–4 MWth) bubbling bed reactor, WIT Trans. Eng. Sci. 89 (2015) 151.
[7] T.R. Rao, J.V.R. Bheemarasetti, Minimum fluidization velocities of mixtures of biomass and sands, Energy 26 (2001) 633.
[8] B. Paudel, Z.-G. Feng, Prediction of minimum fluidization velocity for binary mixtures of biomass and inert particles, Powder Technol. 237 (2013) 134.
[9] A.C. Kumoro, D.A. Nasution, A. Cifriadi, A. Purbasari, A.F. Falaah, A new correlation for the prediction of minimum fluidization of sand and irregularly shape biomass mixtures in a bubbling fluidized bed, IJAER 9 (2014) 21561.
[10] A. Di Renzo, F.P. Di Maio, R. Girimonte, V. Vivacqua, Segregation direction reversal of gas-fluidized biomass/inert mixtures – experiments based on Particle Segregation Model predictions, Chem. Eng. J. 262 (2015) 727.
[11] F. Fotovat, R. Ansart, M. Hemati, O. Simonin, J. Chaouki, Sand-assisted fluidization of large cylindrical and spherical biomass particles: Experiments and simulation, Chem. Eng. Sci. 126 (2015) 543.
[12] M. Wirsum, F. Fett, N. Iwanowa, G. Lukjanow, Particle mixing in bubbling fluidized beds of binary particle systems, Powder Technol. 120 (2001) 63.
[13] F. Fotovat, J. Chaouki, J. Bergthorson, Distribution of large biomass particles in a sand-biomass fluidized bed: Experiments and modeling, AIChE J. 60 (2014) 869.
[14] B. Cluet, G. Mauviel, Y. Rogaume, O. Authier, A. Delebarre, Segregation of wood particles in a bubbling fluidized bed, Fuel Process Technol. 133 (2015) 80.
[15] Y. Zhang, B. Jin, W. Zhong, Experimental investigation on mixing and segregation behaviour of biomass particles in fluidized bed, Chem. Eng. Process. 48 (2009) 745.
[16] J. Baeyens, D. Geldart, Solid mixing, in: G. Gelart (Ed.), Gas Fluidization Technology, New York, Willey, 1986, p. 97.
[17] S.C. Yang, Density effect on mixing and segregation processes in a vibrated binary granular mixture, Powder Technol. 164 (2006) 65.
[18] M.J.V. Goldschmidt, J.M. Link, S. Mellema, J.A.M. Kuipers, Digital image analysis measurements of bed expansion and segregation dynamics in dense gas-fluidized beds, Powder Technol. 138 (2003) 135.
[19] Y. Zhang, B. Jin, W. Zhong, B. Ren, R. Xiao, Characterization of fluidization and segregation of biomass particles by combining image processing and pressure fluctuations analysis, Int. J. Chem. React. Eng. 7 (2009) 1.
[20] M. Rudisuli, T.J. Schildhauer, S.M.A. Biollaz, van-Ommen, J.R. Scale-up of bubbling fluidized bed reactors –, A review. *Powder Technol.* 217 (2012) 21.
[21] C.E. Agu, A. Ugwu, C. Pfeifer, M. Eikeland, L.-A. Tokheim, B.M.E. Moldestad, Investigation of bubbling behaviour in deep fluidized beds at different gas velocities using electrical capacitance tomography, Ind. Eng. Chem. Res. (2019), https://doi.org/10.1021/acs.iecr.8b05013.
[22] C.E. Agu, L.-A. Tokheim, M. Eikeland, B.M.E. Moldestad, Determination of onset of bubbling and slugging in a fluidized bed using a dual-plane electrical capacitance tomography system, Chem. Eng. J. 328 (2017) 997.
[23] C.E. Agu, C. Pfeifer, M. Eikeland, L.-A. Tokheim, B.M.E. Moldestad, Models for predicting average bubble diameter and volumetric bubble flux in deep fluidized beds, Ind. Eng. Chem. Res. 57 (2018) 2658.
[24] P.C. Carman, Fluid flow through granular beds, Trans. Inst. Chem. Eng. 15 (1937) 150.
[25] L. Cheung, A.W. Nienow, P.N. Rowe, Minimum fluidization velocity of a binary mixture of different sized particles, Chem. Eng. Sci. 29 (1974) 1301.
[26] J. Baeyens, D. Geldart, An investigation into slugging fluidized beds, Chem. Eng. Sci. 29 (1974) 255.
[27] S. Shaul, E. Rabinovich, H. Kalman, Generalized flow regime diagram of fluidized beds based on the height to bed diameter ratio, Powder Technol. 228 (2012) 264.
[28] L.G. Gibilaro, P.N. Rowe, A model for a segregation gas fluidized bed, Chem. Eng. Sci. 29 (1974) 1403.
[29] R.C. Darton, R.D. La Naueza, J.F. Davidson, D. Harrison, Bubble growth due to coalescence in fluidized beds, Trans. Inst. Chem. Eng. 55 (1977) 274.
[30] J.F. Davidson, D. Harrison, Fluidized Particles, Cambridge University Press, London, 1963.
[31] C.E. Agu, L.-A. Tokheim, M. Eikeland, B.M.E. Moldestad, Improved models for predicting bubble velocity, bubble frequency and bed expansion in a bubbling fluidized bed, Accepted on Nov. 2, 2018 for publication in Chemical Engineering Research and Design.
[32] S. Karimipour, T. Pugsley, A critical evaluation of literature correlations for predicting bubble size and velocity in gas-solid fluidized beds–a review, Powder Technol. 205 (2011) 1.
[33] J.H. Choi, J.E. Son, S.D. Kim, Bubble size and frequency in gas fluidized beds, J. Chem. Eng. Jpn. 21 (1988) 171.
[34] J. Werther, Effect of gas distributor on the hydrodynamics of gas fluidized beds, Ger. Chem. Eng. 1 (1978) 166.
[35] K. Hilligardt, J. Werther, Local bubble gas hold-up and expansion of gas/solid fluidized beds, German Chem. Eng. 9 (1986) 215.

[36] D. Kunii, O. Levenspiel, Fluidization Engineering, Second ed., Butterworth – Heinemann, Washington Street, 1991.
[37] A. Hepbasli, Estimation of bed expansions in a freely-bubbling three-dimensional gas-fluidized bed, Int. J. Energy Res. 22 (1998) 1365.
[38] R.K. Singh, A. Suryanarayana, G.K. Roy, Prediction of bed expansion ratio for gas-solid fluidization in cylindrical and non-cylindrical beds, IE (1) Journal-CH. 79 (1999) 51.
[39] J. Saastamoinen, Release profile of volatiles in fluidised bed combustion of biomass, J. Fundam. Renewable Energy Appl. (2015) 5.
[40] M. Fiorentino, A. Marzocchella, P. Salatino, Segregation of fuel particles and volatile matter during devolatilization in a fluidized bed reactor – II. Experimental, Chem. Eng. Sci. 1997 (1909) 52.
[41] F. Miccio, S. Russo, N. Silvestri, Assessment of the devolatilization behaviour of fuel pellets in fluidized bed, Fuel Process Technol. 115 (2013) 122.
[42] H.A. On Janssen, the pressure of grain in silos, Proceedings of the Institution of Civil Engineers 124 (1896) 553.
[43] M.S. Ketchum, The Design of Walls, Bins and Grain Elevator, third ed., Mc Graw-Hill Book Company Inc., New York, 1919.
[44] W.J.M. Rankine, On the stability of loose earth, Phil. Trans. R. Soc. Lond. 147 (1857) 145.
[45] M.R. Wu, D.L. Schott, G. Lodewijks, Properties of solid biomass, Biomass Bioenergy 35 (2011) 2093.

Article 8 (A8)

Prediction of void fraction and minimum fluidization velocity of a binary mixture of particles: Bed material and fuel particles

By

Cornelius Emeka Agu, Christoph Pfeifer and Britt M.E. Moldestad

Published in

Powder Technology 349 (2019) 99 – 107

Powder Technology 349 (2019) 99–107

Contents lists available at ScienceDirect

Powder Technology

journal homepage: www.elsevier.com/locate/powtec

Prediction of void fraction and minimum fluidization velocity of a binary mixture of particles: Bed material and fuel particles

Cornelius Emeka Agu [a,*], Christoph Pfeifer [b], Britt M.E. Moldestad [a]

[a] Department of Process, Energy and Environmental Technology, University of South-Eastern Norway, 3918 Porsgrunn, Norway
[b] Department of Material Sciences and Process Engineering, University of Natural Resources and Life Sciences, 1190 Vienna, Austria

ARTICLE INFO

Article history:
Received 14 August 2018
Received in revised form 8 January 2019
Accepted 16 March 2019
Available online 19 March 2019

Keywords:
Binary mixture
Biomass
Void fraction
Segregation
Fluidized bed

ABSTRACT

For operational control and design of a fluidized bed reactor containing different types of solid particles, the bed void fraction and minimum fluidization velocity are vital parameters. This paper demonstrates a method for predicting the void fraction and minimum fluidization velocity of different binary mixtures of particles with improved accuracy. A new model for predicting the void fraction is presented. This model is non-linear and continuous, and it is developed by introducing a packing factor and establishing a mass balance between the solid phases in the packing environment. The results show that the model can accurately predict the void fraction of a binary mixture where the particles are well mixed, partially mixed or segregated. Using this void fraction model and the Ergun equation of pressure drop, the minimum fluidization velocity can be predicted with mean errors of 15.2% for a mixture of two inert materials and 7.0% for a mixture of biomass and inert particles.

1. Introduction

Some fluidized bed applications involve different types of solid particles. The difference in properties between these particle types may influence the bed behaviour. For example, in a bubbling fluidized bed biomass gasifier with sand as the bed material, the difference in density, size and shape between biomass and sand particles often leads to particle segregation [1]. Particle segregation in a biomass gasification reactor can also be influenced by devolatilization of the fuel particles and formation of bubbles around the particles [2,3]. For a bed of coarse particles characterized with large exploding bubbles, the quality of the fluidization can be improved by adding some amount of fine particles of the same material [4]. Due to the size difference between the fine and coarse particles, the void fraction of the mixture is lower than that of the coarse particles, resulting in flow of smaller bubbles in the fluidized bed. In addition to changes in bubbling behaviour, the difference in properties between different solid types in a bed also influences the minimum fluidization velocity of the bed. For operational control and design of a reactor containing two or more solid phases, the bed minimum fluidization velocity is a key parameter.

The minimum fluidization velocity of a bed of particles of the same size and density can be predicted using different correlations. Most of these correlations [5–7] were derived from the Ergun [8] equation but are independent of the bed void fraction. For a binary mixture of particles, similar correlations for predicting minimum fluidization velocity are also available [9–11]. Moreover, there are other models, which involve interpolations between the minimum fluidization velocities of the pure components [12,13]. Li et al. [14] and Asif [15] however, showed that the minimum fluidization velocity of a binary mixture can be predicted with a better accuracy by using a model that considers the void fraction. One major challenge in this approach is prediction of the bed void fraction at minimum fluidization condition. For a completely mixed binary system, the Westman [16] model can be used to predict the bed voidage with a good accuracy when the density difference between the solids in the mixture is very small [14]. In a bed where segregation occurs due to density difference, the Westman [16] model is inappropriate [15]. The void fraction of a completely mixed bed of two solid phases can also be predicted using other models classified as 2-parameter [17,18], compressible [19] and 3-parameter [20] models. These models are linear, and according to Chan and Kwan [21], their accuracies depend on the size ratio between the two size classes in the mixture. Moreover, each of these models comprises a set of two equations, which are solved separately to determine the mixture void fraction based on the maximum value in the solution set. The models are thus discontinuous over the entire range of mixture composition.

This study therefore presents a new model for predicting the void fraction of a binary mixture and how it can be used to improve the prediction of minimum fluidization velocity of the mixture independent of particle types. The proposed model is analytically developed based on the mass balance between two solid phases in a packing environment. In developing the model, it is assumed that the smaller particles first fill the available void without changing the volume occupied by the

* Corresponding author.
E-mail addresses: cornelius.e.agu@usn.no (C.E. Agu), christoph.pfeifer@boku.ac.at (C. Pfeifer), britt.moldestad@usn.no (B.M.E. Moldestad).

https://doi.org/10.1016/j.powtec.2019.03.027

larger particles in static conditions. The excess of these particles then occupies the space above the larger particles. On the basis that there is a limit to which solids can be packed in a given space, a packing factor is introduced. The packing factor compares the actual mass of smaller particles contained in the void of larger particles with the mass that would have occupied the maximum available void space. An expression for the packing factor is derived as a function of mass fraction of the smaller particles, the particle size ratio, and an interaction parameter between the two particle types in the mixture. The interaction parameter also depends on the size ratio as well as the density ratio between the particles. With the correlation proposed for the interaction parameter, which is obtained using some data in the literature, prediction of the mixture void fraction from the proposed model contains no adjustable parameter. For different binary mixtures, the results of the model are compared against experimental data in the literature.

2. Minimum fluidization velocity and mixture properties

Similar to pure solid components, the minimum fluidization velocity of a binary mixture of solids is generally obtained from curves of pressure drop against the superficial gas velocity. The measured minimum fluidization velocity depends on the procedure employed (i.e. whether the pressure drop is measured at increasing or decreasing gas velocity) and on the distribution of solids at the fixed bed condition [22]. The pressure drop curve at increasing gas velocity usually reviews the transition between the initial and full fluidization condition of the bed due to segregation effects. For this reason, several authors [23,24] reported the onset of full fluidization as the true minimum fluidization considering that the whole bed is capable of being fluidized beyond this gas velocity. However, for a well-mixed system, the difference between the initial and full fluidization velocities is insignificant [14]. To avoid the initial bed effect associated with increasing gas velocity procedure, the minimum fluidization velocity can be measured based on decreasing gas velocity procedure. Despite the measurement procedure, the reported minimum fluidization velocity for a given binary mixture often lies between those of the pure components of the mixture. Marzocchella et al. [23] concluded that neither of the initial and full fluidization velocities is related to the minimum fluidization velocities of the individual solids in the mixture. This means that the mixture minimum fluidization velocity is a weighted average of the pure component values [22]. This section presents the models for predicting the average minimum fluidization velocity of a binary mixture of particles and the corresponding bed void fraction. The average minimum fluidization velocity lies between the initial and full fluidization velocity, and it can be obtained from the pressure drop curve at the intersection of two extrapolation lines drawn through the fixed bed and fluidized bed conditions as noted in the literature.

2.1. Models for minimum fluidization velocity

At minimum fluidization, the required superficial gas velocity can be obtained from the force balance between the bed weight and the upward force exerted by the fluid on the particles. Using the Ergun [8] equation, the minimum fluidization velocity of a bed of mono-sized particles can be computed from

$$\frac{1.75}{\varphi_s \varepsilon_{mf}^3}\left(\frac{\rho_f U_{mf} d_s}{\mu_f}\right)^2 + \frac{150(1-\varepsilon_{mf})}{\varphi_s{}^2 \varepsilon_{mf}^3}\left(\frac{\rho_f U_{mf} d_s}{\mu_f}\right) = Ar \tag{1}$$

$$Ar = \frac{d_s^3 \rho_f \left(\rho_s - \rho_f\right) g}{\mu_f^2} \tag{2}$$

here, U_{mf} and ε_{mf} are the superficial fluid velocity and bed void fraction at minimum fluidization condition, respectively. While d_s is the particle diameter, φ_s is the particle sphericity, and ρ_f and ρ_s are the fluid and particle densities, respectively. For a binary mixture, different correlations are derived from Eq. (1) for predicting the mixture minimum fluidization velocity, where the particle diameter, density and sphericity are replaced with their equivalent average properties. Some of these correlations are given in Table 1.

As shown in Table 1, there are different expressions for the average bed properties. For the methods based on the Ergun [8] equation, it can be shown briefly that the volume-average particle density and the surface-to-volume mean diameter are appropriate.

Considering a bed containing different types of particles with d_{si}, φ_{si} and ρ_{si} the particle diameter, sphericity and density of each particle type, respectively, the total specific surface area, a of the bed can be expressed as

$$a = \sum\left(\frac{6}{\varphi_{si} d_{si}}\alpha_i\right) \tag{3}$$

giving the hydraulic diameter of the bed as

$$D_h = \frac{4\varepsilon_m}{\sum\left(\frac{6}{\varphi_{si} d_{si}}\alpha_i\right)} \tag{4}$$

where α_i is the solid volume fraction of the individual particle type and ε_m is the mean void fraction averaged over the bed height. With $1-\varepsilon_m = V_b/V$ and $\alpha_i = (V_{bi}/V_b)(V_b/V)$, it can be shown that

$$\alpha_i = \frac{\rho_{sm}}{\rho_{si}} x_i (1-\varepsilon_m) \tag{5}$$

$$\rho_{sm} = \frac{1}{\sum \frac{x_i}{\rho_{si}}} \tag{6}$$

where x_i is the mass fraction of each type of particles and ρ_{sm} is the mean density of the solid mixture. Using Eqs. (4) and (5), a modified Ergun [8] equation can be expressed as

$$\frac{\Delta p}{\Delta L} = 150\frac{\mu_f U_0 (1-\varepsilon_m)^2}{\varepsilon_m{}^3\left(\rho_{sm}\sum \frac{x_i}{\rho_{si}\varphi_{si} d_{si}}\right)^{-2}} + 1.75\frac{\rho_f U_0{}^2 (1-\varepsilon_m)}{\varepsilon_m{}^3\left(\rho_{sm}\sum \frac{x_i}{\rho_{si}\varphi_{si} d_{si}}\right)^{-1}} \tag{7}$$

Comparing Eq. (7) with the Ergun [8] equation derived for a bed of mono-sized particles, the equivalent mean particle size (Sauter mean diameter) d_{smeq} for a bed of different types of particles is given by

$$\frac{1}{d_{smeq}} = \rho_{sm}\sum \frac{x_i}{\rho_{si}\varphi_{si} d_{si}} \tag{8}$$

From the definition of particle sphericity, φ_s, as the ratio of surface area of a sphere to surface area of a particle of the same volume as the spherical particle [4], it means that d_{si} is the volume-equivalent spherical particle diameter of the individual solid in the mixture. Hence, the average volume-equivalent spherical particle diameter, d_{sm} of the mixture can be obtained as

$$\frac{1}{d_{sm}} = \rho_{sm}\sum \frac{x_i}{\rho_{si} d_{si}} \tag{9}$$

and the average mixture particle sphericity φ_{sm} as

$$\varphi_{sm} = \frac{d_{smeq}}{d_{sm}} \tag{10}$$

For a spherical particle, $\varphi_s = 1$, and if all the particles are spherical, $\varphi_{sm} = 1$. The particle sphericity can be found experimentally or computed from the particle geometry if well defined [4].

Table 1
Correlations for predicting the minimum fluidization velocity in binary mixtures.

Correlation	Application	Reference
$U_{mf} = U_{mf2}\left(\frac{U_{mf1}}{U_{mf2}}\right)^{y_1^2}$	All binary mixtures	Cheung et al. [12]
$U_{mf} = \frac{1}{\sum\left(\frac{y_i}{U_{mfi}}\right)}$	All binary mixtures	Rincon et al. [13]
$U_{mf} = \frac{d_{sm}^2(\rho_{sm}-\rho_f)g}{1650\mu_f}$; $\boldsymbol{\rho_{sm} = \sum(x_i\rho_{si})}$; $\boldsymbol{k = 20d_{s2} + 0.36}$ $d_{sm} = k^{1/2}d_{s2}\left(\frac{d_{s1}\rho_{s2}}{d_{s2}\rho_{s1}}\right)^{x_1/x_2}$	Biomass - inert mixture	Rao & Bheemarasetti [29]
$Re_{mf} = (C_1^2 + C_2Ar_m)^{1/2} - C_1$; $C_1 = 25.65(\varphi_{s1}^{0.25}\varphi_{s2}^{0.15})$ $C_2 = 0.056(\varphi_{s1}^{-0.045}\varphi_{s2}^{0.025})$ $\boldsymbol{\rho_{sm} = \sum(x_i\rho_{si})}$; $d_{sm} = d_{s1}d_{s2}\left(\frac{x_1\rho_{s2}+x_2\rho_{s1}}{x_1\rho_{s2}d_{s2}+x_2\rho_{s1}d_{s1}}\right)$	Biomass - inert mixture	Si and Guo [30]
$Re_{mf} = \{30.28^2 + [0.046(1-x_1) + 0.108x_1^{1/2}]Ar_m\}^{1/2} - 30.28$; $\rho_{sm} = \frac{1}{\sum\frac{x_i}{\rho_{si}}}$; $\frac{1}{d_{sm}} = \rho_{sm}\sum\frac{x_i}{\rho_{si}d_{si}}$	Biomass - inert mixture	Paudel and Feng [31]
$Ar_m = 914.2\varphi_{sm}^2Re_{mf} + 14.838Re_{mf}^2$; $\boldsymbol{\varphi_{sm} = \sum(x_i\varphi_{si})}$; $\boldsymbol{\rho_{sm} = \sum(x_i\rho_{si})}$; $d_{sm} = d_{s1}d_{s2}\left(\frac{x_1\rho_{s2}+x_2\rho_{s1}}{x_1\rho_{s2}d_{s2}+x_2\rho_{s1}d_{s1}}\right)$	Biomass - inert mixture	Kumoro et al. [32]

$Ar_m = \frac{d_{sm}^3\rho_f(\rho_{sm}-\rho_f)g}{\mu_f^2}$ and $Re_{mf} = \frac{\rho_f U_{mf} d_{sm}}{\mu_f}$

The mixture density and particle diameter given in Eq. (6) and Eq. (8) are described as the volume-average particle density and the surface-to-volume mean diameter, respectively. Hence, to obtain the minimum fluidization velocity of a bed of different particle types, ρ_s, d_s and φ_s in Eq. (1) are replaced with the corresponding values for the mixture.

In addition to the correlations given in Table 1, U_{mf} of a binary mixture of particles can also be obtained directly from Eq. (1) when ε_{mf} of the mixture is known. For a completely mixed binary system, the bed void fraction can be obtained from the pure component values using the Westman [16] equation.

$$\left(\frac{v-y_Sv_S}{v_L}\right)^2 + 2G\left(\frac{v-y_Sv_S}{v_L}\right)\left(\frac{v-y_S-y_Lv_L}{v_S-1}\right) + \left(\frac{v-y_S-y_Lv_L}{v_S-1}\right)^2 = 1 \quad (11)$$

here, y_S and y_L are the volumetric fraction of the smaller and larger particles, respectively, and v_S and v_L are the respective specific volume, where

$$y_j = \frac{\rho_{sm}}{\rho_{sj}}x_j; j = S, L \quad (12)$$

$$v_j = 1/\alpha_j; \varepsilon_m = 1-1/v \quad (13)$$

The parameter G can be obtained from the correlation proposed by Yu et al. [25] or Finkers and Hoffmann [26].

2.2. Model development for bed voidage

For direct application of Eq. (1) in a binary mixture of particles, this section introduces a new model for void fraction of the bed mixture.

In a given mixture of two solid phases, we define the packing factor θ as follows:

$$|\theta| = \frac{m_*}{(1-\alpha_1)\rho_{s2}V_0} \quad (14)$$

where m_* is the mass of the smaller particles occupying the interstices between the larger particles, and V_0 is the initial total volume occupied by the larger particles. The subscripts 1 and 2 denote the larger and smaller particles, respectively. The modulus $|\theta|$ indicates that θ can be negative or positive. When $\theta < 0$, the bed is contracting and when $\theta > 0$, the bed is expanding. A binary mixture of particles contracts if the bulk volume of the mixture is lower than the sum of the bulk volumes of the two particle types in the mixture. Bed expansion occurs when the volume of an initially well-mixed system increases due to particle segregation. The packing factor is a measure of packing density of a binary system. The larger the value of $|\theta|$, the lower the void fraction of the mixture.

Assuming that N_1 and N_* are the respective number of particles in the packed bed, Eq. (14) can be simplified to

$$\theta = \frac{N_*}{N_1}\frac{\alpha_1}{(1-\alpha_1)}\left(\frac{d_{s2}}{d_{s1}}\right)^3 \quad (15)$$

where

$$\frac{N_*}{N_1} \approx \frac{\alpha_*}{\alpha_1}\left(\frac{d_{s2}}{d_{s1}}\right)^{-2} \quad (16)$$

Substituting Eq. (16) into Eq. (15) and using the relation, $\alpha_i + \varepsilon_i = 1$, where ε_i is the pure component void fraction, the packing factor can be expressed as

$$\theta = \left(1-\frac{\varepsilon_1-\alpha_*}{\varepsilon_1}\right)\left(\frac{d_{s2}}{d_{s1}}\right) \quad (17)$$

when $d_{s2}/d_{s1} = 1$, $m_* = 0$. For Eq. (17) to satisfy this condition, the term $(\varepsilon_1 - \alpha_*)/\varepsilon_1$ must be a function of d_{s2}/d_{s1} in addition to the amount of smaller particles present in the mixture. Thus,

$$\theta = \left(1-\left(\frac{d_{s2}}{d_{s1}}\right)^{\beta x_2}\right)\left(\frac{d_{s2}}{d_{s1}}\right) \quad (18)$$

here, β can be described as the interaction parameter between the two solid phases. When a bed contracts during solid mixing, the value of m_* is high. On the contrary, m_* is lower when the particles segregate. To account for these effects, $\beta < 0$ for a well-mixed system and $\beta > 0$ for a segregated mixture.

Furthermore, the total mass of the bed is expressed as

$$m = (1-\varepsilon_m)\rho_{sm}(V_0 + \Delta V) \tag{19}$$

where ΔV is the total volume occupied by the smaller particles above the larger particles, and it can be obtained from

$$\Delta V = \frac{m_2 - m_*}{\alpha_2 \rho_{s2}} \tag{20}$$

here, m_2 is the total mass of the smaller particles in the bed. Substituting Eq. (20) into Eq. (19) and noting that $V_0 = m_1/(\alpha_1\rho_{s1})$,

$$\begin{aligned}(1-\varepsilon_m)\left[(\alpha_2-(1-\alpha_1)\theta)\frac{m_1}{\alpha_1\rho_{s1}}+\frac{m_2}{\rho_{s2}}\right] &= \frac{\alpha_2 m}{\rho_{sm}} \\ \varepsilon_m = 1-\frac{\alpha_2}{\rho_{sm}\left[(\alpha_2-(1-\alpha_1)\theta)\frac{x_1}{\alpha_1\rho_{s1}}+\frac{x_2}{\rho_{s2}}\right]}&\end{aligned} \tag{21}$$

Substituting Eq. (18) into Eq. (21) and replacing the subscripts 1 and 2 with the corresponding letters, yields

$$\varepsilon_m = 1-\frac{\alpha_S}{\left[\left(\alpha_S-(1-\alpha_L)\left(1-\left(\frac{d_{sS}}{d_{sL}}\right)^{\beta x_S}\right)\left(\frac{d_{sS}}{d_{sL}}\right)\right)\frac{y_L}{\alpha_L}+y_S\right]} \tag{22}$$

Eq. (22) can be used to predict the void fraction in a binary mixture of different particle types. As can be seen, the equation requires the solids/void fraction of the pure components and contains only one fitting parameter, β. The value of β depends on the relative difference between the properties of the different particle types in the mixture and on whether the bed is well mixed, partially mixed or segregated as shown in section 4. It should be noted that the value of ε_m predicted from Eq. (22) is the bed voidage averaged over the bed height which may differ from the local void fractions in the bed. Depending on the particle size ratio, d_{sS}/d_{sL}, the local void fraction can vary along the bed axis due to segregation effect [27]. For a mixture containing biomass particles, the higher the value of d_{sS}/d_{sL}, the wider the deviation of ε_m from the local void fraction at the segregated layers. The accuracy of Eq. (22) with a correctly assigned value of β is demonstrated in section 4.

3. Results and discussion

In this section, the validation of the proposed model, Eq. (22) and its application to predicting the minimum fluidization velocity of a binary mixture are demonstrated using different experimental data from the literature. Since it is often difficult to measure void fractions at minimum fluidization condition, a systematic procedure in using Eq. (22) to predict the mixture U_{mf} is also highlighted.

3.1. Bed voidage of binary particle mixtures

Fig. 1 compares the void fraction at static condition predicted using Eq. (22) against the experimental data given in Marzocchella et al. [23] for a mixture of glass particles with mean diameter 500 μm and sand particles with mean diameter 125 μm at different mixture compositions. The data obtained from Tharpa et al. [28] at fixed bed condition are also shown for a mixture of 3500 μm plastic and 709 μm zirconium oxide particles. At minimum fluidization condition, the model results are compared against the experimental data obtained from Li et al. [14] and Formisani et al. [22] for different binary mixtures: two glass powders with mean sizes (385 and 163) μm and two glass powders with mean sizes (612 and 154) μm, respectively. The particle properties in these mixtures are shown in Table 2. As can be seen, the results from Eq. (22) strongly agree with the experimental data shown in both figures. With the correlation of Yu et al. [25], the Westman [16] equation also agrees well with the experimental data at the minimum fluidization condition. For the mixtures given in Li et al. [14], the Westman [16] equation and Eq. (22) predict the same results for all values of x_1 (mass fraction of the larger particles). However, for the data obtained at fixed bed condition as shown in Fig. 1(a), the Westman [16] equation does not give good predictions.

Fig. 2 compares the accuracy of Eq. (22) with that of the Westman [16] equation against the experimental data. The experimental data include those shown in Fig. 1 and those obtained from Formisani et al. [22] for a binary mixture of two different glass particles with mean diameters 499 and 271 μm. The figure shows that Eq. (22) predicts the experimental data with a very good accuracy. The mean prediction error associated with Eq. (22) is 1.5%. The prediction error using the Westman [16] equation can be as high as ±15% due to poor prediction of the bed voidage reported in Marzocchella et al. [23] and Tharpa et al. [28] at static conditions. However, the mean errors using the Westman [13] model are 4.0% based on the Yu et al. [25] correlation and 4.1% based on the Finkers and Hoffman [26] correlation.

3.2. Correlation for β

As can be seen in Fig. 1, β varies from one system to another. The individual value of β used in the results is obtained by fitting the experimental data to the model, Eq. (22). To successfully apply Eq. (22) without experimental data, a correlation for β is required. Analysis of some literature data obtained at the minimum fluidization condition

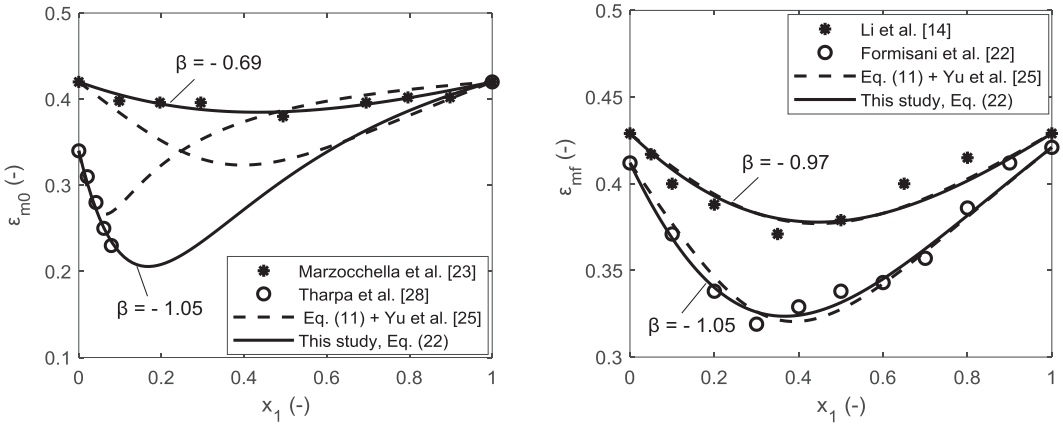

Fig. 1. Voidage variation comparing the predicted results with the experimental data obtained at (a) static bed condition (b) minimum fluidization condition.

Table 2
Properties of pairs of particles in the completely mixed binary mixtures.

Binary mixture	Particles	Shape	ρ_s (kg/m^3)	d_s (μm)	φ_s (−)	U_{mf} (m/s)	Ref.
I	Glass	Spherical	2540	500	1.0	0.225	[23]
	Sand	Spherical	2600	125	1.0	0.0212	
II	Plastic	Spherical	964	3500	1.0	0.85	[28]
	ZrO_2	Spherical	5850	709	1.0	0.67	
III	Glass	Spherical	2520	385	1.0	0.143	[14]
	Glass	Spherical	2520	163	1.0	0.025	
IV	Glass	Spherical	2480	612	1.0	0.3148	[22]
	Glass	Spherical	2480	154	1.0	0.0232	
V	Glass	Spherical	2480	499	1.0	0.2222	[22]
	Glass	Spherical	2480	271	1.0	0.0602	
VI	H. char	Spherical	1080	775	1.0	0.227	[14]
	Glass	Spherical	2520	165	1.0	0.025	

H. char = hollow char, ZrO_2 = zirconium oxide.

shows that the absolute value of β decreases with the ratio $d_{sS}\rho_{sS}/(d_{sL}\rho_{sL})$ as represented in Eq. (23).

$$\beta = 0.623\left(\frac{d_{sS}\rho_{sS}}{d_{sL}\rho_{sL}}\right)^{-0.61} \tag{23}$$

In the subsequent sections, β computed from Eq. (23) is used in Eq. (22) for prediction of the mixture void fraction.

3.3. Minimum fluidization velocity of binary mixtures

The results in Fig. 1 show that the voidage of a binary mixture can be predicted with a good accuracy from the void fractions of the pure components. Since accurate prediction of void fraction of a pure component at minimum fluidization condition is a challenge, we present a method where U_{mf} of the solid phases in a binary mixture are inputs to Eq. (22). As illustrated in Fig. 3, ε_{mf} of the pure components are computed from the respective U_{mf} values using Eq. (1). For a given mixture composition (mass fraction or volumetric fraction of the solid phases), the average particle properties and void fraction of the mixture are calculated from the relevant equations. From the values of ε_m, average density, sphericity and particle diameter of the mixture, the mixture U_{mf} is computed using Eq. (1). Due to the cohesiveness of biomass particles, the minimum fluidization velocity of a pure biomass is much higher than that predicted by Eq. (1) even when the volume equivalent spherical diameter of the particle is used. Since the sphericity of most practical biomass can be as low as 0.2, using the actual sphericity of biomass in Eq. (1) will result in a much lower value of U_{mf} for the particles. Hence, for a mixture involving biomass and inert particles, $\varphi_{si} = 1$ should be used in the proposed algorithm.

3.3.1. Mixtures of two inert materials

Fig. 4 shows the predicted values of U_{mf} based on four different models at different mass fraction of the larger particles. For each of the models, U_{mf} of the different particle types are used as inputs. As shown in Fig. 4(a), the predicted results from the different models are in good agreement with the experimental data. However, the results in Fig. 4(b) shows that a combination of Eq. (1) with the Westman [16]/Yu et al. [25] equation or with the model given by Eq. (22) shows

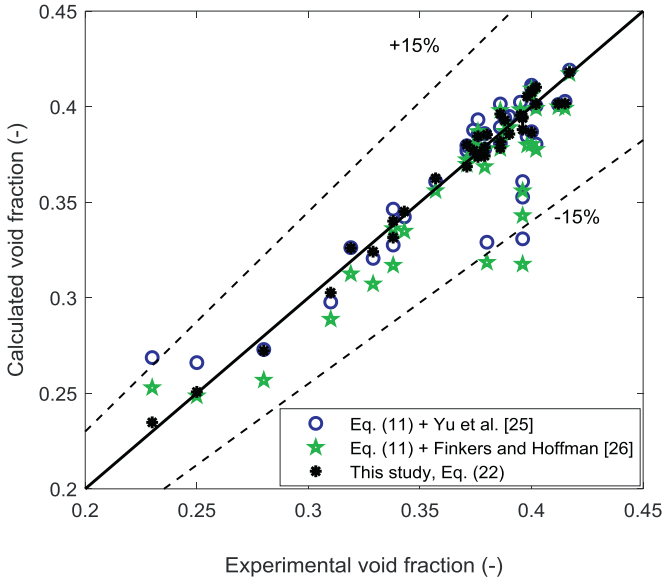

Fig. 2. Parity plot comparing the predicted void fraction with the experimental values for different beds of two inert materials.

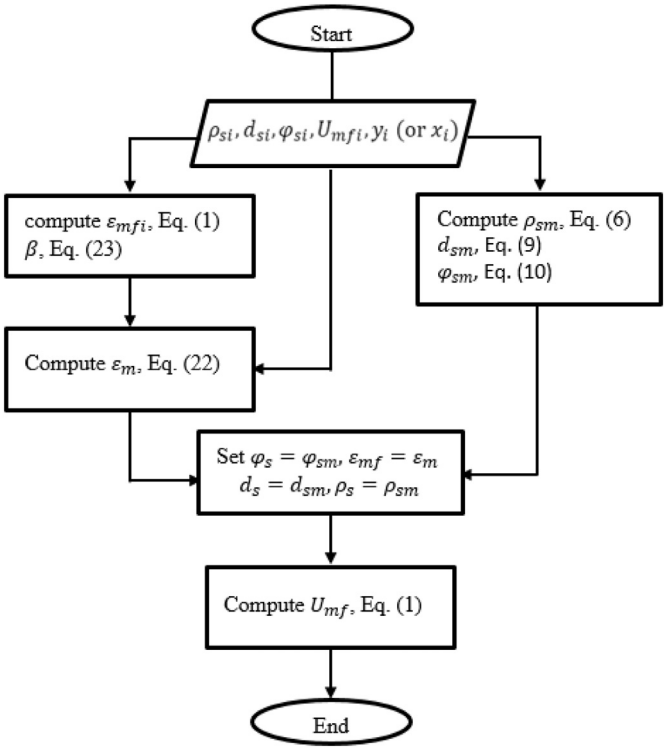

Fig. 3. Flow chart showing an algorithm for computing the minimum fluidization velocity in a bed of binary mixture of particles.

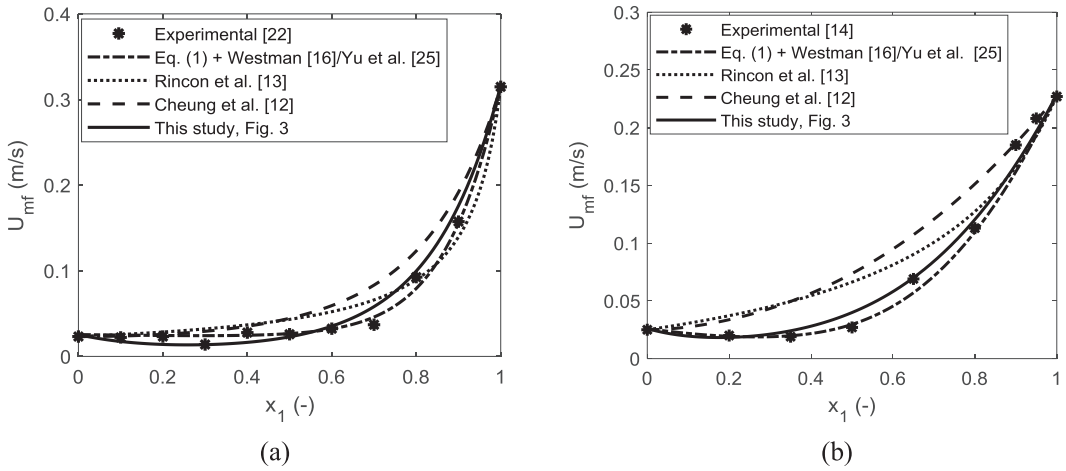

Fig. 4. Variation of minimum fluidization velocity comparing the predicted results with the experimental data for a binary mixture of particles (a) 612 /154 μm glass [22] (b) 775 μm hollow char/165 μm glass [14].

a better prediction than those given by Cheung et al. [12] and Rincon et al. [13].

Furthermore, Fig. 5 compares the calculated values of U_{mf} from these four models against the experimental data obtained from different literature [14,22,23]. The result is based on the binary mixtures (I, III, IV, V and VI) given in Table 2. By using any of the four models, Fig. 5 shows that the minimum fluidization velocity of the beds can be predicted with an error within ±35%. On average, the predictions based on the present study give the best results with mean absolute error of 15.2%, whereas those based on the Westman [16] equation with Yu et al. [25] correlation have a mean error of 15.5%. The models given by Cheung et al. [12] and Rincon et al. [13] show very high prediction errors with mean values 27.6% and 30.5%, respectively.

3.3.2. Mixtures of biomass and inert materials

Unlike the mixture of two inert materials with more or less the same particle density, a mixture of biomass and inert particles can show some degree of segregation. Hence, application of the Westman [16] equation in Eq. (1) will not be appropriate. However, this section shows that the proposed model, Eq. (22) can also be applied for prediction of minimum

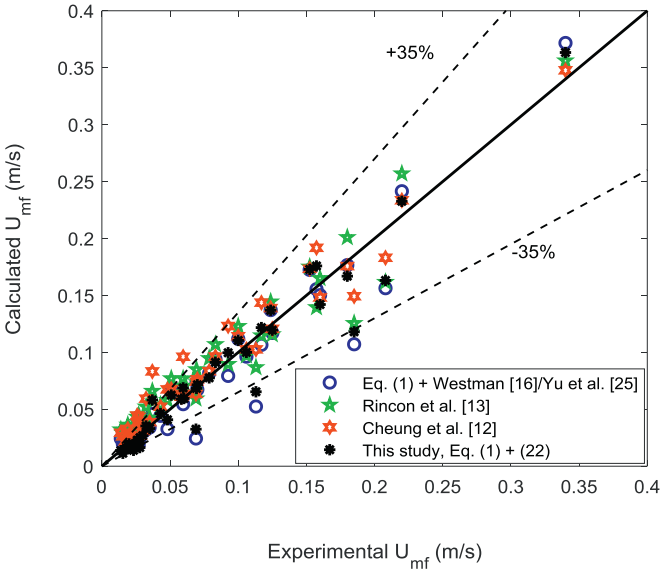

Fig. 5. Parity plot comparing the predicted minimum fluidization velocity with the experimental values for different beds of two inert materials; mixtures: I, III - VI; see Table 2.

fluidization velocity of a mixture of biomass and inert particles. To be able to predict the volume expansion in the binary mixture, a positive value of the parameter β, which can be computed from Eq. (23), is required.

Fig. 6(a) shows the void fraction computed using Eq. (22) at the minimum fluidization condition for a mixture of plastic particles with effective particle diameter 2550 μm and sand particles with particle diameter 550 μm. The plastic particles have a density of 1761 kg/m^3 and sphericity of 0.87 while the corresponding properties for the sand particles are 2664 kg/m^3 and 1.0. The experimental data are obtained from Asif [15] where water is used as the fluidizing fluid at 20 °C. With $\beta > 0$, the result shows that Eq. (22) predicts the bed voidage with a good accuracy when the mass of the plastic particles is considerably high, i.e. $x_1 > 0.4$. At a lower mass fraction, the bed is partly mixed and partly segregated. Thus, Eq. (22) with $\beta = 1.35$ (computed from Eq. (23)) over predicts the mixture voidage. However, when the value of β is reduced to - 0.38, Eq. (22) predicts the voidage with a better accuracy when $x_1 < 0.4$. This result and those presented above therefore show that with $\beta > 0$, Eq. (22) gives the voidage for a well-segregated bed. With $\beta < 0$, the model provides results where there is some degree of mixing. When $\beta < 0$ and the magnitude of β is computed from Eq. (23), Eq. (22) predicts the voidage for a well-mixed bed. For prediction of β in a bed exhibiting partial mixing behaviour, a different correlation than Eq. (23) is required. In addition, a model for predicting the mixture composition at which the bed begins to segregate is also required. In spite of the error in predicting the void fraction where the bed exhibits partial segregation, Fig. 6(b) shows that the minimum fluidization velocity of the bed can be well predicted using the combination of Eq. (1) and Eq. (22) for all values of x_1. For the result where $\beta = 1.35$ is used over the entire values of x_1, the prediction error of the proposed model is 11.3% as against 27.5% and 27.6% errors obtained from the Cheung et al. [12] and Rincon et al. [13] models, respectively. If the value $\beta = -0.38$ is used for the compositions $x_1 < 0.4$, the proposed model predicts the minimum fluidization velocity shown in Fig. 6(b) with a better accuracy and the mean prediction error is reduced to 7.5%.

As the main aim of this study is to predict with improved accuracy the minimum fluidization velocity of a biomass-inert mixture, which often exhibits segregation behaviour, the results in Fig. 6 show that this can be achieved. The properties of different mixtures of biomass and inert particles used for this demonstration are given in Table 3 and the beds as described subsequently are fluidized with air at the ambient condition. For all computations in this section, Eq. (23) is used to predict the absolute value of β.

For the mixture of 856 μm walnut shell and 241 μm sand particles, Fig. 7(a) shows the predicted values of U_{mf} compared with the

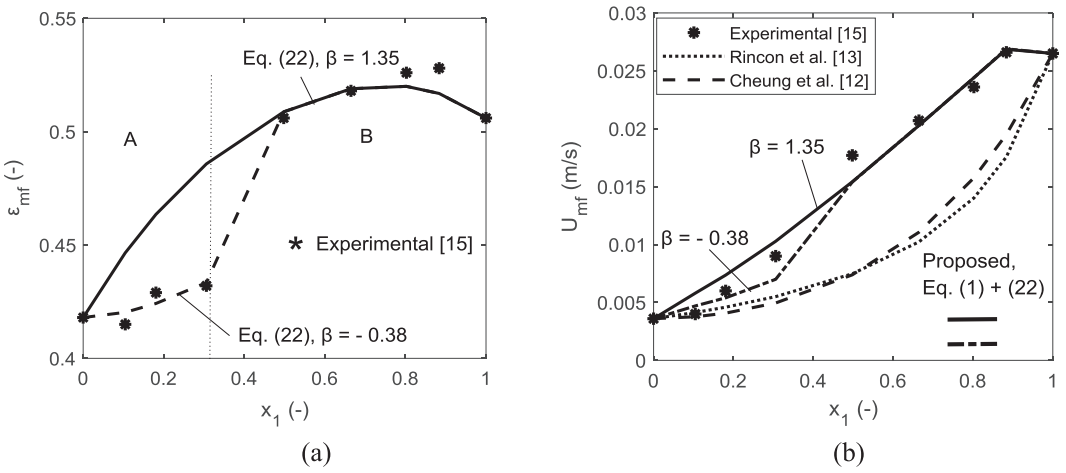

Fig. 6. (a) Variation of void fraction where A = partly mixed region and B = segregated region and (b) superficial water velocity at minimum fluidization condition, comparing the predicted results with the experimental data in a bed mixture of 2550 μm plastic and 550 μm sand particles with segregation behaviour.

experimental data. The results obtained for a mixture of 1560 μm rice husk and 350 μm sand particles are shown in Fig. 7(b). As can be seen in Fig. 7(a), the computed values of U_{mf} using the Paudel and Feng [31] model are closer to the experimental values although the model does not capture the expansion behaviour of the bed at increasing mass of biomass particles. The Kumoro et al. [32] model under predicts the bed expansion at higher values of x_1, giving a lower value of U_{mf} for the biomass mixture. The Si and Guo [30] model gives the best prediction when $x_1 \leq 0.4$ but shows the greatest prediction error at higher mass of biomass particles. However, in Fig. 7(b), the Si and Guo [30] model gives the least prediction error for biomass mass fraction within $0.3 < x_1 < 0.8$. The Kumoro et al. [32] model over predicts the U_{mf} value at a higher mass fraction of the rice husk particles even though the experimental data were used in the model development. Unlike these two latter models, which also predict the expansion and contraction behaviour of the bed, the Paudel and Feng [31] model predicts a steady increase in U_{mf} with an increase in the amount of rice husk particles. As the models given by Si and Guo [30] and Kumoro et al. [32] consider particle sphericity, these results show that particle shape plays a significant role in prediction of U_{mf}. It should be noted that inclusion of particle sphericity in these two models also means that the models indirectly consider the bed voidage since these two properties are closely related. Moreover, the results in Fig. 7 show that by using the proposed model, U_{mf} is predicted with a better accuracy in both different bed mixtures. The results given by the proposed model is based on $\beta > 0$ where β value is as given in Eq. (23). The results also show that the predicted U_{mf} using Eq. (1) and Eq. (22) gets better at increasing amount of biomass particles due to higher degree of segregation effect. Where there is some degree of bed contraction as shown in Fig. 7(a), the proposed model slightly over predicts the U_{mf} value due to the steady expansion behaviour predicted by Eq. (22) when $\beta > 0$ is used as demonstrated in Fig. 6(a).

In addition, Fig. 8 compares the prediction accuracy of the proposed model with those of the existing models for biomass-inert systems. The experimental data are based on different mixtures of biomass and inert particles given in the literature [31–33]; see Table 3. As shown in the figure, the Cheung et al. [12] model under predicts the mixture U_{mf} with an error as high as 40%. The accuracy of the Cheung et al. [12] model increases with increasing size ratio d_{s1}/d_{s2} and with increasing amount of biomass in the mixture. The high prediction errors shown by the models of Si and Guo [30], Paudel and Feng [31] and Kumoro et al. [32] are associated with the size ratio and density difference. The higher the values of d_{s1}/d_{s2} and $\rho_{s2} - \rho_{s1}$, the better the model accuracies. For $d_{s1}/d_{s2} < 3.5$, these models over predict the mixture U_{mf} with an error >40%. However, the method proposed in this study as described in Fig. 3 using Eq. (1) and Eq. (22) predicts the mixture U_{mf} with a better accuracy for all values of d_{s1}/d_{s2} and $\rho_{s2} - \rho_{s1}$. The mean prediction error using the proposed model is 7.0%, whereas those using the models of Cheung et al. [12], Si and Guo [30], Paudel and Feng [31] and Kumoro et al. [32] are 23.4%, 24.4%, 27.0% and 27.7%, respectively.

Table 3
Properties of particles in the biomass-inert mixtures.

Binary mixture	Particles	Shape	ρ_s (kg/m^3)	d_s (μm)	φ_s (−)	U_{mf} (m/s)	Ref.
VII	W. shell	Irregular	1200	856	0.78	0.553	[31]
	Sand	Spherical	2630	241	0.94	0.074	
VIII	Rice husk	Irregular	635	1560	0.18	0.642	[32]
	Sand	Spherical	2450	350	0.95	0.164	
IX	Corn cob	Irregular	1080	1040	0.71	0.608	[31]
	Sand	Spherical	2630	241	0.98	0.074	
X	M. beans	Spherical	1640	3200	1.0	1.053	[33]
	Sand	Spherical	2700	1000	1.0	0.558	
XI	M. beans	Spherical	1640	3200	1.0	1.053	[33]
	C. cinter	Spherical	1870	2800	1.0	0.918	
XII	C. stalk	Cylindrical	365	7200	0.55	1.16	[33]
	Sand	Spherical	2700	500	1.0	0.318	
XIII	C. stalk	Cylindrical	365	7200	0.55	1.16	[33]
	C. cinter	Spherical	1870	2800	1.0	0.918	

W. shell = walnut shell, M. beans = mung beans, C. cinter = CFB cinter, C. stalk = cotton stalk.

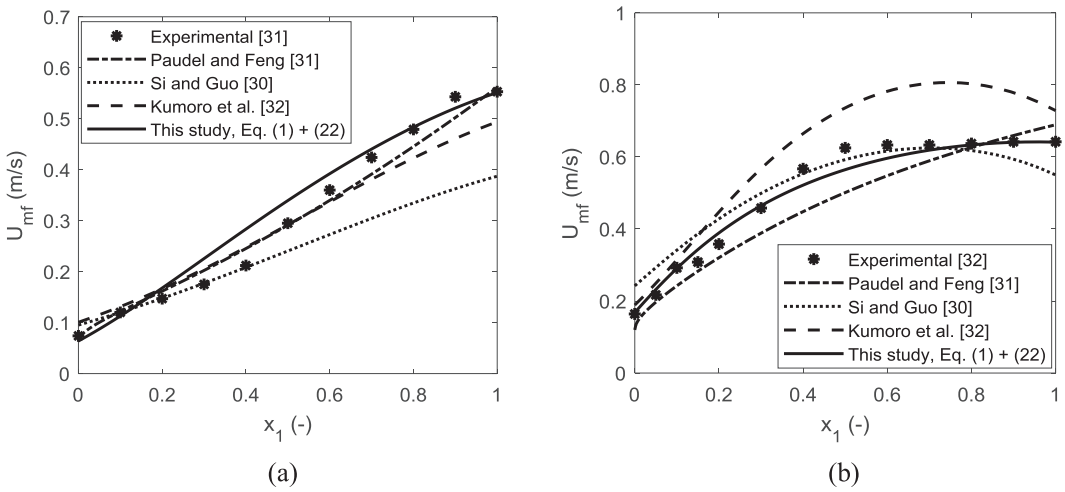

Fig. 7. Variation of minimum fluidization velocity comparing predicted results with experimental data for a binary mixture involving biomass particles (a) 856 μm walnut shell/241 μm sand particles [31] (b) 1560 μm rice husk/350 μm sand particles [32].

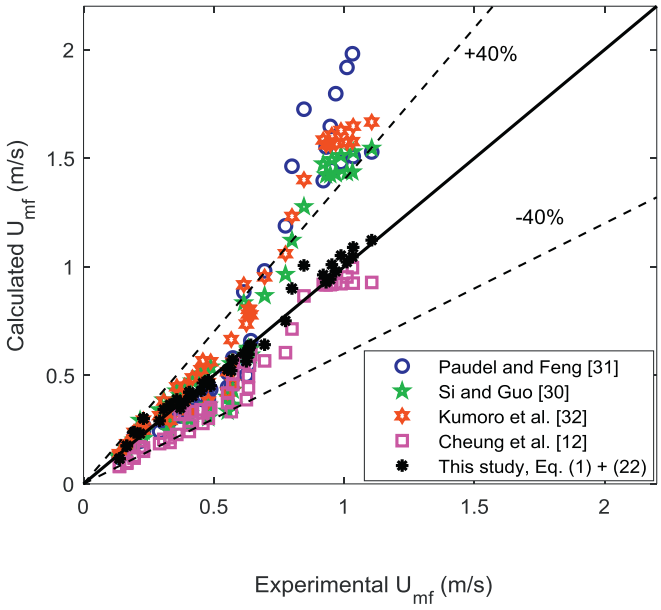

Fig. 8. Parity plot comparing the predicted minimum fluidization velocity with the experimental values for different beds of biomass and inert particles; mixtures: VII – XIII; see Table 3.

In summary, the accuracy of Eq. (22) in predicting the void fraction of a binary mixture depends on the value of the interaction parameter, β used. As shown in Figs. 2 and 6, Eq. (22) can predict the experimental data with a very good accuracy if a correct value of β is assigned. For the results shown in Figs. 4–8, Eq. (23) was used to estimate the values of β. Although the figures show that the U_{mf} values of the binary mixtures are predicted to a reasonable accuracy, the results can also be better with an improvement in the correlation for β. In its current form, Eq. (23) was derived from data of six binary pairs of solids. If a larger data set is analysed, the model for the interaction parameter can be improved.

4. Conclusion

In a binary mixture, the difference in properties between the two different particle types greatly influences the bed behaviour. For this reason, accurate prediction of minimum fluidization velocity of binary mixtures, especially those involving biomass particles, has been a challenge. This paper presents a new model for predicting the bed void fraction and its application to predicting the minimum fluidization velocity of a binary mixture.

For prediction of the bed void fraction, the proposed model requires the void fractions of the pure components in the mixture. However, with known values of minimum fluidization velocities of the different particles in the mixture, the approach presented in this paper avoids the challenge in determining the bed voidage.

For a completely mixed system involving two inert materials, the proposed model can predict the minimum fluidization velocity with a mean error of 15.2%. For a bed mixture of biomass and inert materials, the model can predict the minimum fluidization velocity with an error of 7.0%.

Finally, for accurate prediction of the voidage and minimum fluidization velocity in a partly mixed bed of two types of particles, further work is required to establish a correlation for the binary interaction parameter as well as the mixture composition at the transition to the segregation behaviour.

Nomenclature

A	Bed cross-sectional area, m^2
Ar	Dimensionless particle Archimedes number
a	Solid specific surface area,$^{-}$ 1/m
D_h	Hydraulic diameter, m
d	Diameter, m
g	Acceleration due to gravity, m/s^2
m	Mass, kg
N	Number
Re	Dimensionless Reynolds number
U	Superficial gas velocity, m/s
V	Volume, m^3
v	Dimensionless specific volume
x	Dimensionless mass fraction of a species in a mixture
y	Dimensionless volumetric fraction of a species in a mixture

Greek symbols

α	Dimensionless solids volume fraction
β	Dimensionless interaction parameter
ε	Dimensionless Void Fraction
θ	Dimensionless packing factor
μ	Dynamic viscosity, Pa.s
ρ	Density, kg/m3
φ	Dimensionless particle sphericity

Subscripts

b	Bed
f	Fluid
i, j	Indices
L	Particles of Larger Size
m	Mixture
mf	Minimum fluidization
S	Particles of Smaller Size
s	Solid
(zero)	Initial state or entry positionw

Funding sources

This research did not receive any specific grant from funding agencies in the public, commercial, or not-for-profit sectors.

References

[1] B.T. Vilches, E. Sette, H. Thunman, Behaviour of biomass particles in a large scale (2-4 MWth) bubbling bed reactor, WIT Trans. Eng. Sci. 89 (2015) 151.
[2] M. Fiorentino, A. Marzocchella, P. Salatino, Segregation of fuel particles and volatile matter during devolatilization in a fluidized bed reactor – II. Experimental, Chem. Eng. Sci. 52 (1997) 1909.
[3] R. Solimene, A. Marzocchella, P. Salatino, Hydrodynamic interaction between a coarse gas-emitting particle and a gas fluidized bed of finer solids, Powder Technol. 133 (2003) 79.
[4] D. Kunii, O. Levenspiel, Fluidization Engineering, 2nd ed. Butterworth – Heinemann, Washington Street, 1991.
[5] C.Y. Wen, Y.H. Yu, A generalized method for predicting the minimum fluidization velocity, AICHE J. 12 (1966) 610.
[6] S.P. Babu, B. Shah, A. Talwalkar, Fluidization correlations for coal gasification materials – minimum fluidization velocity and fluidized bed expansion ratio, AIChE Symp. Ser. 74 (1978) 176.
[7] D.C. Chitester, R.M. Kornosky, L.-S. Fan, J.P. Danko, Characteristics of fluidization at high pressure, Chem. Eng. Sci. 39 (1984) 253.
[8] S. Ergun, Fluid Flow through Packed Column, Chem. Eng. Prog. 48 (1952) 89.
[9] W.R.A. Goossens, G.L. Dumont, G.J. Spaepen, Fluidization of binary mixtures in laminar flow region, Chem. Eng. Symp. Ser. 67 (1971) 38.
[10] V. Thonglimp, N. Hiquily, C. Laguerie, vitesse minimale de fluidisation et expansion des couches de melanges de particules solids fluidisees par un gaz, Powder Technol. 39 (1984) 223.
[11] J. Reina, E. Velo, L. Puigjaner, Predicting the minimum fluidization velocity of polydisperse mixtures of scrap-wood particles, Powder Technol. 111 (2000) 245.
[12] L. Cheung, A.W. Nienow, P.N. Rowe, Minimum fluidization velocity of a binary mixture of different sized particles, Chem. Eng. Sci. 29 (1974) 1301.
[13] J. Rincon, J. Guardiola, A. Romero, G. Ramos, Predicting the minimum fluidization velocity of multicomponent systems, J. Chem. Eng. Jpn 27 (1994) 177.
[14] Z. Li, N. Kobayashi, A. Nishimura, M. Husatani, A method to predict the minimum fluidization velocity of binary mixtures based on particle packing properties, Chem. Eng. Commun. 192 (2005) 918.
[15] M. Asif, Minimum fluidization velocity of binary-solid mixtures: method comparison, IJCME 4 (2010) 243.
[16] A.E.R. Westman, The packing of particles: empirical equations for intermediate diameter ratios, J. Am. Ceram. Soc. 19 (1936) 127.
[17] T. Stovall, F. de Larrard, M. Buil, Linear packing density model of grain mixtures, Powder Technol. 48 (1) (1986).
[18] A.B. Yu, R.P. Zou, N. Standish, Modifying the linear packing model for predicting the porosity of nonspherical particle mixtures, Ind. Eng. Chem. Res. 35 (1996) 3730.
[19] F. De Larrard, Concrete Mixture Proportioning: A Scientific Approach, E&FN Spon, London, 1999.
[20] A.K.H. Kwan, K.W. Chan, V. Wong, A 3-parameter particle packing model incorporating the wedging effect, Powder Technol. 237 (2013) 172.
[21] K.W. Chan, A.K.H. Kwan, Evaluation of particle packing models by comparing with published test results, Particuology 16 (2014) 108.
[22] B. Formisani, R. Girimonte, T. Longo, The fluidization process of binary mixtures of solids: development of the approach based on the fluidization velocity interval, Powder Technol. 185 (2008) 97.
[23] A. Marzocchella, P. Salatino, V. Di Pastena, L. Lirer, Transient fluidization and segregation of binary mixtures of particles, AICHE J. 46 (2000) 2175.
[24] S. Uchida, H. Yamada, I. Tada, Minimum fluidization velocity of binary mixtures, J. Chin. Inst. Chem. Eng. 14 (1983) 257.
[25] A.B. Yu, N. Standish, A. McLean, Porosity calculation of binary mixture of nonspherical particles, J. Am. Ceram. Soc. 76 (1993) 2813.
[26] H.J. Finkers, A.C. Hoffmann, Structural ratio for predicting the voidage of binary particle mixture, AICHE J. 44 (1998) 495.
[27] B. Cluet, G. Mauviel, Y. Rogaume, O. Authier, A. Delebarre, Segregation of wood particles in a bubbling fluidized bed, Fuel Process. Technol. 133 (2015) 80.
[28] R.K. Thapa, C. Rautenbach, B.M. Halvorsen, Investigation of flow behaviour in biomass gasifier using electrical capacitance tomography (ECT) and pressure sensors, Proc. International Conference on Polygeneration Strategies (ICPS) 2011, p. 97.
[29] T.R. Rao, J.V.R. Bheemarasetti, Minimum fluidization velocities of mixtures of biomass and sands, Energy 26 (2001) 633.
[30] C. Si, Q. Guo, Fluidization characteristics of binary mixtures of biomass and quartz sand in an acoustic fluidized bed, Ind. Eng. Chem. Res. 47 (2008) 9773.
[31] B. Paudel, Z.-G. Feng, Prediction of minimum fluidization velocity for binary mixtures of biomass and inert particles, Powder Technol. 237 (2013) 134.
[32] A.C. Kumoro, D.A. Nasution, A. Cifriadi, A. Purbasari, A.F. Falaah, A new correlation for the prediction of minimum fluidization of sand and irregularly shape biomass mixtures in a bubbling fluidized bed, IJAER 9 (2014), 21561. .
[33] W. Zhong, B. Jin, Y. Zhang, X. Wang, R. Xiao, Fluidization of biomass particles in a gas-solid fluidized bed, Energy Fuel 22 (2008) 4170.

Article 9 (A9)

Measurement and characterization of biomass mean residence time in an air-blown bubbling fluidized bed gasification reactor

By

Cornelius E. Agu, Christoph Pfeifer, Marianne Eikeland, Lars-Andre Tokheim, Britt M.E. Moldestad

Published in

Fuel 253 (2019) 1414 – 1423

Fuel 253 (2019) 1414–1423

Contents lists available at ScienceDirect

Fuel

journal homepage: www.elsevier.com/locate/fuel

Full Length Article

Measurement and characterization of biomass mean residence time in an air-blown bubbling fluidized bed gasification reactor

Cornelius E. Agu[a,*], Christoph Pfeifer[b], Marianne Eikeland[a], Lars-Andre Tokheim[a], Britt M.E. Moldestad[a]

[a] Department of Process, Energy and Environmental Technology, University of South-Eastern Norway, 3918 Porsgrunn, Norway
[b] Department of Material Sciences and Process Engineering, University of Natural Resources and Life Sciences, 1190 Vienna, Austria

ARTICLE INFO

Keywords:
Biomass gasification
Residence time
Char accumulation
Bubbling bed
Devolatilization

ABSTRACT

Gasification of biomass in bubbling fluidized beds can be limited by accumulation of unconverted char particles during the process. The amount of unconverted biomass depends on the residence time of the fuel particles. This study demonstrates a method for measuring the biomass residence time over the conversion period at a given air flowrate and a given amount of biomass in a bubbling bed using the variation of bed temperature and fluid pressure recorded over time. The results show that biomass conversion is characterized by the devolatilization and extinction times. The two biomass residence times increase with decreasing air flowrate and increasing amount of biomass charged in the bed. The amount of unconverted char between the two characteristic times also increases with decreasing air flowrate and increasing biomass load. The total heat loss during the devolatilization is observed to increase with increasing air flowrate and amount of biomass in the bed. Correlations are proposed for predicting the mean biomass residence time, the amount of unconverted char particles and the devolatilization heat loss at a given operating condition. The results of this study can be used in determining the bubbling bed properties and solid circulation rate required to decongest the accumulated char particles in the bed.

1. Introduction

Fluidized bed reactors can be operated under bubbling or circulating bed regimes for chemical conversion and synthesis. In biomass gasification for example, a combination of these regimes in so-called dual-fluidized bed reactors can be used to ensure efficient utilization of the carbon content of the fuel particles [1]. However, application of a single bubbling or circulating bed reactor offers simpler process design and depending on the utilization route of the producer gas, the type of reactor has to be chosen. In a fluidized bed reactor, an inert bed material is used to aid the fluidization quality of biomass, which is usually difficult to fluidize due to its peculiar shape, size and cohesiveness. Bed fluidization helps to achieve uniform material and heat distribution, thereby enhancing the reaction rates in the reactor. The fluidization also influences the residence time distribution [2,3] and the conversion efficiency of the fuel particles [4]. In addition, the distribution of biomass in a fluidized bed depends on a number of factors including the biomass type, gas velocity and reactor design.

There are different studies on biomass residence time in fluidized beds. The definition of the particle residence times covered in literature depends on the purpose and thus must be clear for its application. The biomass residence time can be determined on the basis of its transport time between two reference positions in the bed, on the basis of the relative amount participating in reactions and on the basis of the time elapsed before complete conversion of the particles has been achieved. Although the later definition is implied in this study, the different types of biomass residence time are interrelated. The fuel conversion time may be longer if it does not receive adequate heat and gasification agent within the bed. The biomass particles can be transported to the surface or bottom of the bed due to segregation effect [5], and thus have limited contact time with the bed material supposed to provide the heat required for the reaction. The particle segregation can be brought about by the density difference between biomass and the bed material particles [6], and by the rise of gas bubbles formed around the particles as biomass undergoes devolatilization [7,8]. The mean residence time and residence time distribution characterize the degree of mixing in a non-catalytic fluidized bed reactor [9]. Gao et al. [10] concluded that the particle flow pattern in a bubbling fluidized bed lies between those

* Corresponding author.
E-mail addresses: cornelius.e.agu@usn.no, agumech@yahoo.com (C.E. Agu), christoph.pfeifer@boku.ac.at (C. Pfeifer), Marianne.Eikeland@usn.no (M. Eikeland), Lars.A.Tokheim@usn.no (L.-A. Tokheim), britt.moldestad@usn.no (B.M.E. Moldestad).

https://doi.org/10.1016/j.fuel.2019.05.103
Received 18 January 2019; Received in revised form 22 April 2019; Accepted 21 May 2019

Nomenclature

Symbols

A [m^2]	cross-sectional area
a [−]	dimensionless fitting parameter
D [m]	bed diameter
d [m]	particle diameter
h_0 [m]	initial bed height
m [kg]	mass
$\dot{m}$ [kg/s]	mass flowrate
p [Pa]	fluid pressure
$\dot{q}_L$ [K/s]	heat loss
T [K]	temperature
t [s]	time
t_* [s]	mean residence time
U [m/s]	superficial air velocity
x [−]	solid fuel to bed material mass ratio
y_{char} [−]	char mass fraction in a bed
Y [−]	volume fraction of solid component

Greek letters

α [−]	degree of conversion completeness
ε [−]	void fraction of bulk material
ρ [kg/m^3]	density
σ	standard deviation
φ [−]	particle sphericity
γ_{char} [−]	characteristic fraction of unconverted char particles

Subscripts

b	biomass
c	complete
p	particle/pressure
mf	minimum fluidization
s	sand
0	initial/bottom reference

of the ideal plug flow and perfectly stirred reactor. Zou et al. [2] showed that an increase in the feed rate of solid particles makes the solids flow pattern closer to plug flow. As reported in different studies, different factors influence the residence time of biomass in fluidized beds. An increase in gas velocity and bed height leads to a wider residence time distribution of solid particles [2]. Larger particles have longer mean residence time [2,3] and lower descending vertical velocity [2]. The mean residence time of solid particles also increases with increasing bed height and decreasing gas velocity in bubbling beds [3].

In addition to distribution of biomass particles, the amount of biomass residing in the bed at a given operating condition determines its conversion efficiency. The conversion efficiency can be measured by the relative flow of carbon entering as solid and leaving the reactor as gas [4]. Before being completely converted, char particles can be reduced to elutriable sizes by attrition, fragmentation or both. Particle elutriation reduces the amount of active carbon for efficient conversion. When the elutriation effect is reduced, the char residence time can be longer, increasing the char conversion efficiency due to increased chemical kinetics rates [11–13]. The carbon conversion can be increased by improving the biomass devolatilization process since elutriation of char particles increases with the amount in the bed [14]. Although it is usually believed that devolatilization is a fast process, completing in few seconds depending on the particle size [15], heating rate [16,17] and the final temperature [16–19], Gable and Brown [20] clearly showed that this process can take more than 40 s to be essentially complete. Higher temperature and heating rate will for the same fuel particles result in a higher amount of volatiles and a lower amount of char in the bed. Moreover, a complete conversion of char in a bed may also not be possible due to a number of factors including the deactivation (thermal and graphitization) effect [21–23], competing reactions within the vicinity of the char particles that may result in reducing the availability of the gasifying agent, and the competing rates between the mass transfer and reaction rate.

In addition to thorough studies on the distribution of biomass in fluidized bed reactors, this paper is aimed at presenting the measurement of the total time required for a given type and amount of biomass to be completely converted in a conventional air-blown bubbling fluidized bed reactor, assuming no elutriation of the fuel particles. Before biomass particles are completely converted, they usually undergo different reaction phases such as devolatilization and partial oxidation. By tracking the changes in the reaction phases, the amount of biomass unconverted over time can be determined. The fraction of biomass in a bed under a specific condition is a useful parameter for design purpose. For a mixture of bed material and biomass particles, the prediction of minimum fluidization velocity [24,25], minimum slugging velocity and bed expansion [26] depends on the proportion of biomass in the bed. With the knowledge of rate of accumulation of char particles, the solid circulation rate applicable in dual fluidized bed reactors can also be determined.

For measurement of biomass residence time based on the relative movement of particles in the bed, different techniques are used. The most common of these techniques are based on single particle tracing [3] and on stimulus responses from chemical differences [27], radioactivity measurements [28] or phosphorescence [29]. The char yield during devolatilization is usually obtained by cooling and weighing method for a given measurement condition. By noting that the pressure drop increases linearly with the amount of char in a bubbling bed, Xu et al. [30] applied the measurement of bed pressure drop to determine the char yield at a given temperature under the atmosphere of nitrogen.

In this study, the experiments are conducted in batches in a non-transparent reactor using air as the fluidizing gas. The technique employed involves measurement of fluid pressure and temperature in the bed over a period of time. As the fluid pressure increases upon introducing biomass in the bed, the fractional change in the pressure indicates the amount of biomass consumed. The peak temperature recorded over the conversion period gives an indication about the completeness of the reaction. Due to partial oxidation with the available oxygen, the amount of char obtained in this study may be lower than that obtained when nitrogen is used as the fluidizing gas. However, the measured char yield still stands a chance of representing the true value when using air for biomass conversion. The detailed experimental procedure is presented in the following section. The results of the data obtained at different biomass loads and air flowrates are presented, analysed and discussed in the subsequent sections. The method developed and described here allows a quick and relatively easy determination of biomass conversion characteristics as well as char residence time in fluidized bed without complex and costly measurement procedure. The findings are based on comprehensive measurements under hot-flow conditions, analyses of cold-flow model results and mathematical modelling.

2. Experimental procedures

To gain in-depth understanding of how much time it takes a given amount of biomass to be completely converted at a given air flowrate, a batch process was used. This section presents a brief description of the bubbling fluidized bed reactor used, and also the detailed procedure employed in measuring the biomass residence time over the reaction

period and the amount of unconverted biomass particles as the reaction goes.

2.1. Experimental setup

As shown in Fig. 1, the experimental setup consists of a stainless-steel cylindrical column with 10 cm internal diameter, thickness of 4 mm and height of 1.0 m above the distributor. Three electric heating elements attached externally along the column wall are used to supply heat to the reactor up to 1000 °C. To minimize the heat loss, the inner side of the reactor is coated with a refractory material while the outer part is insulted with 200 mm thick fiberglass. The behaviour in the reactor is monitored with five different thermocouples and five different pressure sensors located along the vertical axis as shown. Each pressure sensor consists of a pressure tube connected to a pressure transducer through a 4 mm flexible tube, and measures the gauge pressure (i.e. the fluid pressure in excess of the atmospheric pressure) in the given location. The fuel supply is through a screw feeder, which is calibrated for each fuel applied. Air is supplied through two 10 mm-steel pipes positioned 27.5 mm from the column base. The mass flow-rate of air is measured with a BROOK air flowmeter (3809 series) operating in the range, 0.48–4.7 kg/h. Above the reactor column, a gas sampling point is installed. The product gas from the reactor is passed through a flare before being discharged to the atmosphere.

In the experiments, compressed air was used as the fluidizing gas and oxygen carrier. Sand particles with mean particle size of 293 μm were used as the bed material. The mass of the bed material maintained throughout the experiments was 2.2 kg. Two different types of woody biomass were used; wood pellets and wood chips. The properties of the biomass and sand particles at the ambient condition are shown in Table 1, where ρ_p is the particle density, d_p the volume-equivalent spherical diameter, φ_p is the particle sphericity and ε is the void fraction of the bulk material. The wood pellets are cylindrical with diameter 6 mm and length in the range 5–30 mm. The wood chips are considered rectangular with variation in length, width and height in the range of 5–12 mm, 5–12 mm and 1–5 mm, respectively. The sand particle size was obtained by sieve analysis and the volume-equivalent spherical diameter of the biomass particles were computed from the particle geometry.

The experiments were conducted in batches using five different biomass loads in the range 90–450 g. The proportion of biomass in the total solid mixture is given in Table 2, where m_b is the initial mass of biomass loaded in the bed, x_b is the mass ratio between biomass and sand particles, and Y_b is the volume percentage of biomass in the total bed mixture. For each biomass load, six different air flowrates in the range 0.5–2 kg/h were used.

It should be noted that in a continuous process, the amount of air supply is related to the biomass feed rate, where for a typical woody biomass, the minimum air–fuel ratio (AFR) to achieve a complete combustion is about 6. To achieve a gasification, AFR$\ll$ 6. In a batch process, the AFR criterion is not applicable since the amount of biomass in the bed decreases with time. However, in addition to minimizing the particle elutriation, the range of air flowrates applied in this study is based on the amounts that promote gasification at the initial stage assuming that the rate of mass loss is constant over the conversion period. As reported in Tran and White [31], the mass loss during conversion of redwood is in the range 2.92–6.25 g/m^{2}s depending on the ignition heat flux. Assuming a value of 3.0 g/m^{2}s, the estimated air–fuel ratio over the range of biomass loads and air flowrates used in this study is within 0.2–1.4, which is in the range applied for a gasification process.

In each experiment, the sand bed was initially heated up at the applied air flowrate using the reactor heater. When the desired temperature 830 ± 20 °C was achieved, the heater was turned off and the required amount of biomass was then loaded. The temperatures and pressures at different bed positions 1–5 were captured at 1 sec intervals. The product gas was also sampled at 5 min intervals for offline analysis using the SRI gas chromatography (GC). The GC uses a TCD detector and helium as carrier gas with an installed column comprising a packed Molecular Sieve 13x. The GC operates at 10 psi in the temperature range −15 to 120 °C, and provides the composition of the major fuel gases: carbon monoxide (CO), hydrogen (H_2) and methane (CH_4) as well as nitrogen and oxygen in each gas sample by the gradient-method. Each experiment was performed twice to confirm the repeatability, and the two data sets were averaged and recorded.

2.2. Measurement of devolatilization and char residence times

Fig. 2 shows the variations of pressure drop measured at the base (position 1) and the temperature measured at the position 2 located 14.3 cm from the base of the bed containing 26.4 vol% wood pellets at 1.0 kg/h air flowrate. These temperature and pressure curves are also similar for all other biomass loads and air flowrates, and thus are described as the characteristic curves for a batch biomass conversion in the pilot plant which is typical for a bubbling bed. As shown in the figure, the bed pressure increases rapidly shortly after the required amount of biomass is introduced at point **A**. The peak pressure marked **O** increases with the amount of biomass charged in the bed. As the biomass undergoes conversion, the pressure first drops rapidly until a point **D**, then gently to point **E** and finally levels off to a value the same as that at the initial state. The rapid drop in pressure to point **D** indicates that most of biomass in the bed has been released as gas due to drying and devolatilization. Fig. 2(b) shows that the devolatilization begins as soon as biomass is introduced in the bed. After point **D**, the mole fraction of CH_4 in addition to that of H_2 becomes insignificant ($< 0.5\%$). At point **D**, the concentration of CO is also very low while the N_2 mole fraction is close to 70%. In addition, the temperature decreases below the initial bed temperature and becomes minimum at point **D**, showing that the biomass devolatilization effectively completes at point **D**. During the devolatilization phase, the temperature first slightly drops below point **O** and then sharply to point **D**. The time variation of temperature within the bed may depend on the biomass load and axial position as shown in Fig. 3.

Beyond point **D**, the temperature increases almost linearly until point **P** owing to oxidation of residual fuel gases and char particles. With further increase in time, the temperature increases but at a lower rate as there are little or no more amount of combustible gases in the

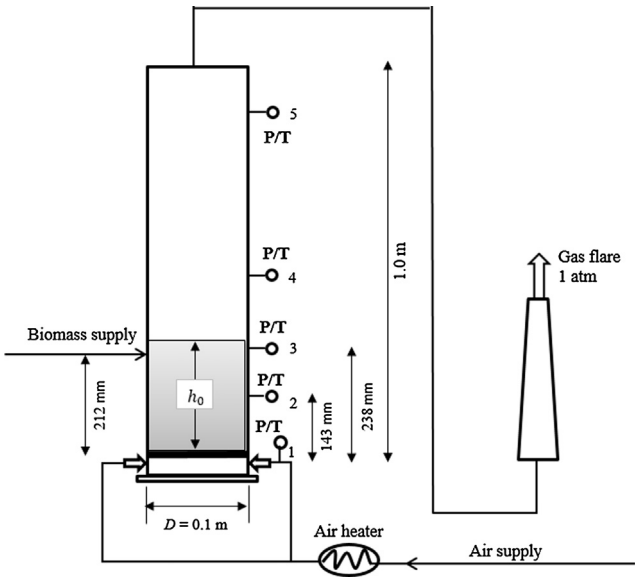

Fig. 1. Schematic illustration of the biomass gasification reactor used for tests. Symbols **P/T** indicate pressure and temperature sensor probes; h_0 is the initial bed height above the air distributor.

Table 1
Biomass and sand particle properties at ambient condition.

Materials	Shape	ρ_p [kg/m^3]	d_p [mm]	φ_p [−]	ε [−]
Wood pellets	Cylindrical	1139	8.96	0.82	0.43
Wood chips	Rectangular	423	6.87	0.75	0.49
Sand	Angular	2650	0.293	0.86	0.42

Table 2
Initial amount and proportion of biomass in the bed solids mixture.

Biomass type	m_b [kg]	x_b [−]	Y_b [vol. %]
Wood pellets	0.230	0.109	20.2
	0.326	0.154	26.4
	0.435	0.206	32.4
Wood chips	0.091	0.043	21.3
	0.156	0.074	31.7

bed. At this stage, the increase in temperature is due to oxidation of char particles in the parts of the bed with available oxygen. When the temperature reaches the peak value at point **E**, almost all the char particles are consumed, resulting in the levelling-off of the pressure in the bed. The temperature decreases beyond point **E** as the heat released from any residual char is significantly lower than the heat loss from the cold air that flows continuously through the bed. As shown in Fig. 3, the temperature is approximately uniform along the reactor after point **E**, suggesting a complete consumption of fuel species in the bed. However, below this point, the figure shows that the temperatures at positions 4 and 5 are higher compared to those in the bed, possibly due to oxidation of fuel gases in the freeboard.

As can be seen in Fig. 2, the biomass conversion process is characterized by two residence times, noted as the devolatilization time, t_d and extinction time, t_e. The devolatilization time is measured at the inflection point on the pressure while the extinction time is measured at the peak of the temperature curve. Within the time interval $[0.t_d]$, the product gas exiting the reactor consists of combustible gases as can be seen in Fig. 2(b). Beyond the time t_d, little or no combustible gas components are present in the exit gas. When the time is increased to the value t_e, the biomass particles are almost completely consumed. The time difference, $(t_e - t_d)$ measures the mean effective char residence time. The mean biomass residence time, t_* can be obtained at the point of intersection between the horizontal line drawn through point **E** and the line of best fit drawn through points **D** and **P** as shown in Fig. 2. The value of t_* is significant when considering a continuous flow process where there is always some amount of unconverted char in the bed.

2.3. Measurement of char yield and heat loss at completion of devolatilization

The peak of the pressure curve is proportional to the amount of biomass charged into the bed at the same air flowrate. The fractional change in the pressure drop as the conversion is going on can thus be used to estimate the change in the amount of biomass consumed in the bed. Between point **D** and **E**, the amount of char released in the bed can be obtained by considering a mass balance across the bed assuming that the pressure drop is related to the amount of solid particles in the bed.

By definition, the char yield γ_{char} at the completion of devolatilization is given by

$$\gamma_{char} = \frac{m_{char}}{m_{bio}} \tag{1}$$

Since the peak pressure drop is proportional to the mass of biomass m_{bio} in the bed, then by the mass balance

$$m_{bio} = \frac{A(p_O - p_s)}{g} \tag{2}$$

$$m_{char} = \frac{A(p_D - p_s)}{g} \tag{3}$$

here, g is the accerelation due to gravity and A is the cross-sectional area of the bed. For the same air flowrate, p_s is the pressure drop in the bed containing only the sand particles, p_O is the peak pressure drop after the biomass is introduced and p_D is the pressure drop recorded at the end of devolatilization. Substituting Eqs. (2) and (3) in Eq. (1), the char yield can be measured from

$$\gamma_{char} = \frac{p_D - p_s}{p_O - p_s} \tag{4}$$

The mean pressure drop in the pure sand bed is shown in Fig. 4(a) for the range of air flowrates used in this study. The error bar indicates the standard deviation of the mean pressure over the 120 s measurement interval. As shown in the figure, the pressure drop is close to the bed weight per unit area, indicating that the bed is in fluidized state at each air flowrate.

Due to the bed fluctuation, it will be difficult to obtain the pressures at points **O** and **D** directly from the pressure curve. It should be noted that the required values of p_D and p_O are at the indicated time instances unlike the pressure drop in the pure sand bed that is measured as an average value over a time interval with measurement uncertainty σ_s^2, where σ_s is the standard deviation of the measurement. For the bed containing biomass, a linear line drawn through point **O** and **D** is introduced as shown in Fig. 4(b). From the line, an average pressure drop

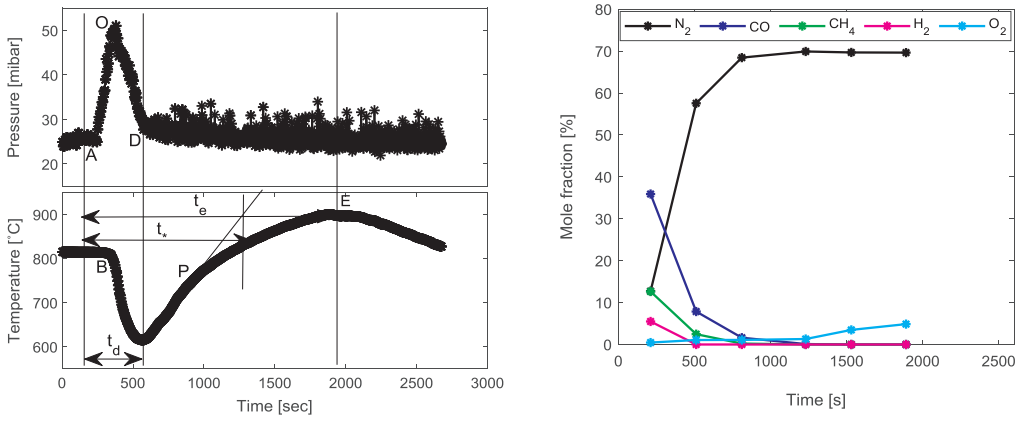

(a) (b)

Fig. 2. Phases of biomass conversion in a bubbling bed containing 26.4 vol% wood pellets at air flowrate of 1.0 kg/h (a) pressure drop and temperature (b) composition of the product gas.

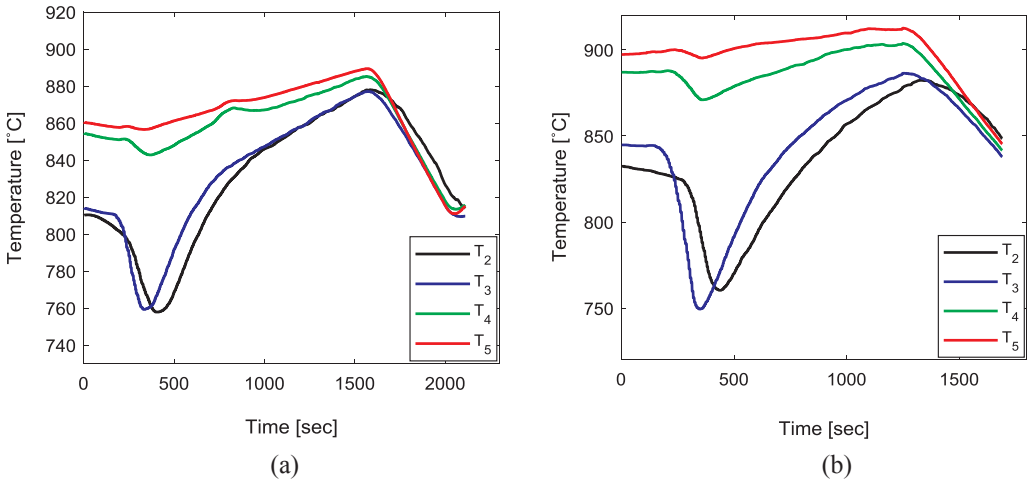

Fig. 3. Temperature variation along the reactor axis for two different beds at 1.2 kg/h air flowrate (a) 20.2 vol% wood pellets (b) 21.3 vol% wood chips.

at a given time between **O** and **D** can be approximately estimated. Assuming that the variance is uniformly distributed over the measurement interval, the uncertainty σ_p^2 in the pressure drop measurement can be computed from

$$\sigma_p^2 = \left(\sqrt{\frac{1}{N} \sum_i (p_i - \bar{p_i})^2} - \sigma_s \right)^2 \tag{5}$$

here, $\bar{p_i}$ is the pressure drop estimated from the linear model and p_i is the actual pressure drop measured at the same time. Applying the differential method, the uncertainty σ_{char}^2 in the measurement of the char yield can be determined from

$$\sigma_{char}^2 = \left(\frac{\partial \gamma_{char}}{\partial p_D} \right)^2 \sigma_p^2 + \left(\frac{\partial \gamma_{char}}{\partial p_O} \right)^2 \sigma_p^2 \tag{6}$$

which leads to

$$\frac{\sigma_{char}^2}{\gamma_{char}^2} = \left[\frac{1}{(\bar{p_D} - p_s)^2} + \frac{1}{(\bar{p_O} - p_s)^2} \right] \sigma_p^2 \tag{7}$$

At the completion of the devolatilization, the total heat loss Q_L can be obtained from the difference between the heat content of the bed before the temperature begins to drop significantly and the heat content at the end of the devolatilization as expressed below

$$Q_L = -m_S c_{p,S} (T_D - T_B) \tag{8}$$

where T_B is the bed temperature before the significant drop is observed and T_D is the temperature at the completion of devolatilization. m_S is the total mass of solid between point **B** and **D** neglecting the mass loss and $c_{p,S}$ is the specific heat capacity of the bed. It should be noted that Q_L is the net heat loss in the bed, which also accounts for the sensible heat loss by the flowing gas and the heat loss through the reactor walls. Dividing Eq. (8) through with $m_S c_{p,S}(t_D - t_B)$, the specific rate of heat loss $\dot{q}_L$, can then be obtained as

$$\dot{q}_L = \frac{T_B - T_D}{t_D - t_B} \tag{9}$$

Since the value of $\dot{q}_L$ determined from Eq. (9) may change along the bed axis as can be seen in Fig. 3, the average value between points 2 and 3 in the bed is computed and recorded for each experimental run.

3. Results and discussion

The analysis and results of the experimental data from conversion of the five different biomass loads at different air flowrates are presented in this section. Fig. 5 shows the temperature curve for the bed containing 20.2 vol% wood pellets compared to that of wood chips of approximately equal volume at the same air flowrate, 1.5 kg/h. It should be noted that on an equal volume basis, the two different beds contain approximately the same number of biomass particles. However, on the basis of equal mass, the difference between the hydrodynamic behaviour of the two different beds will be very large since the number of

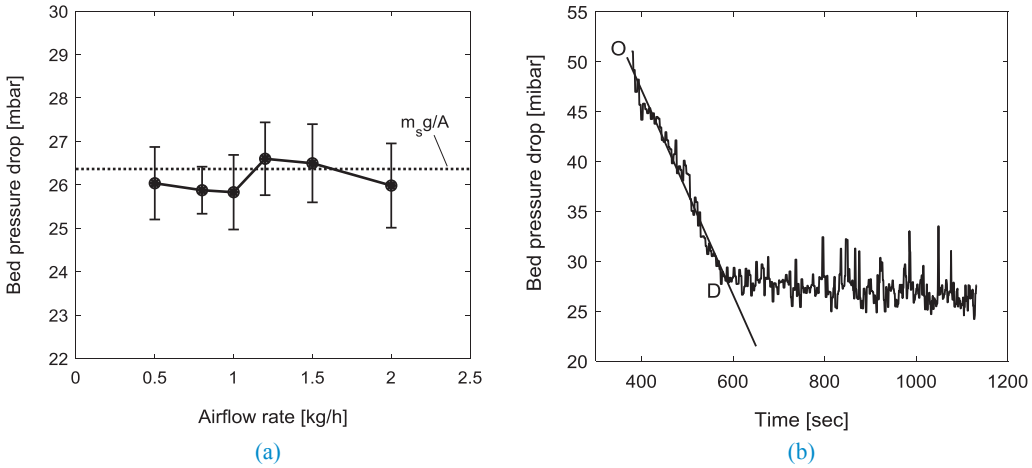

Fig. 4. (a) Pressure drop in the bed of pure 293 μm sand particles at 830 ± 20 °C and different air flowrates (b) linear model illustrating the measurement of pressure drops at points **O** and **D** in a bed containing biomass.

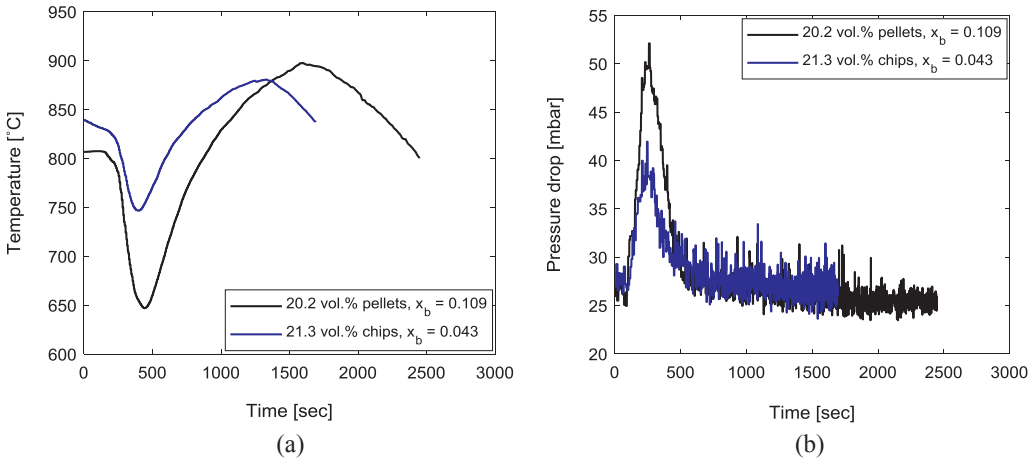

Fig. 5. (a) Temperature curves in the bed of wood chips (21.3 vol%) and pellets (20.2 vol%) at 14.3 cm from the bed base and air flowrate of 1.5 kg/h (b) pressure drops over the two different beds.

biomass particles in the bed of wood chips will be approximately three times as large as that in the pellet bed. Although the trends in Fig. 5(a) are similar for both beds, the results show that the initial mass fraction of biomass in the bed influences the extent to which the bed transits from one stage to another as discussed in Section 2.2. Due to higher mass percentage, the temperature drop during the heating up and devolatilization is higher in the bed with wood pellets. Both the devolatilization and extinction times are also higher in the pellet bed. The peak bed temperature is higher in the bed with pellets due to larger amount of char present after the time, t_d compared to the amount present in the bed with wood chips. Moreover, the peak pressure in the wood chip bed is lower due to the smaller biomass mass load compared to that of the pellet bed as shown in Fig. 5(b).

3.1. Devolatilization and char residence times

Fig. 6 shows the variation of the residence times with the applied air flowrate at different biomass loads. The char residence time, $(t_e - t_d)$ is considerably higher than the corresponding value of t_d at a given gas flowrate in both types of biomass. Both values of $(t_e - t_d)$ and t_d decrease with an increase in air flowrate. As the two biomass loads, x_b for the wood chips are lower than those of the pellets, it is clear that at the same air flowrate, the corresponding residence time increases with increasing amount of biomass in the bed despite the biomass type. However, the dependency of the devolatilization time on the value of x_b is less clear as can be seen in the figures.

3.2. Char yield and heat loss at completion of devolatilization

The amount of unconverted biomass, γ_{char} at the completion of devolatilization is shown in Fig. 7(a) as a function of initial biomass load and air flowrates. The error bar represents the uncertainty σ^2_{char} in the measurement where the mean value over the 29 experimental runs is $\pm$ 8.8x10^{-4}. For both types of biomass, the value of γ_{char} decreases with an increase in air flowrate and a decrease in the value of x_b. As shown in Fig. 7(b), the heat loss increases with increasing air flowrate and biomass load owing to the increasing sensible heat loss from the larger mass flowrate of gas and larger amount of cold biomass introduced in the bed. With a higher heat loss, the final temperature at the completion of devolatilization decreases, resulting in a higher char yield. However, with an increase in air flowrate, partial oxidation of the char particles is enhanced due to higher availability of oxygen. This thus decreases the char yield at increasing air flowrate even though the heat loss is increased.

3.3. Correlations of the experimental data

As discussed above, the characteristic residence time depends on the air flowrate and the initial amount of biomass in the bed. The reaction time parameters are important for ensuring efficient conversion of biomass, particularly during the gasification process. Correlating the data obtained in this study can be useful when scaling up the bed. For the behaviour to be applied to larger beds, the flow variables need to be

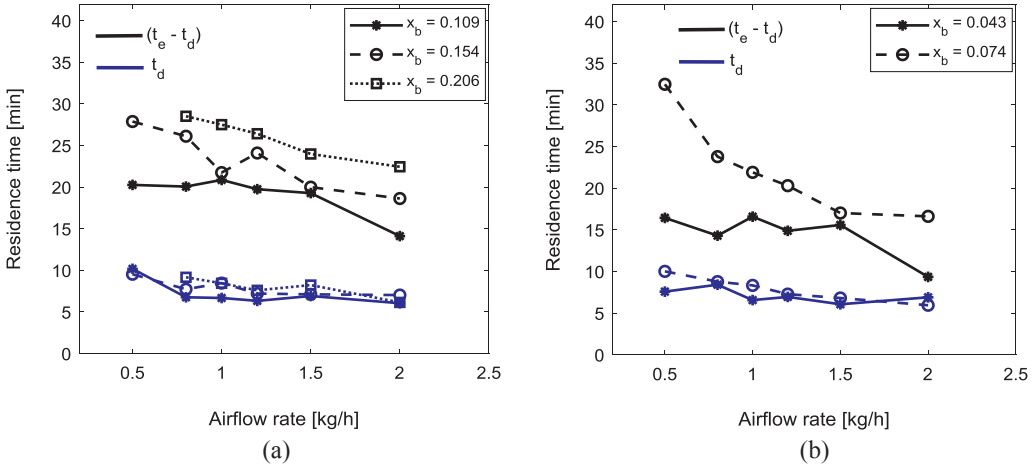

Fig. 6. Comparison between the devolatilization time and char residence time at different biomass loads (a) wood pellets (b) wood chips.

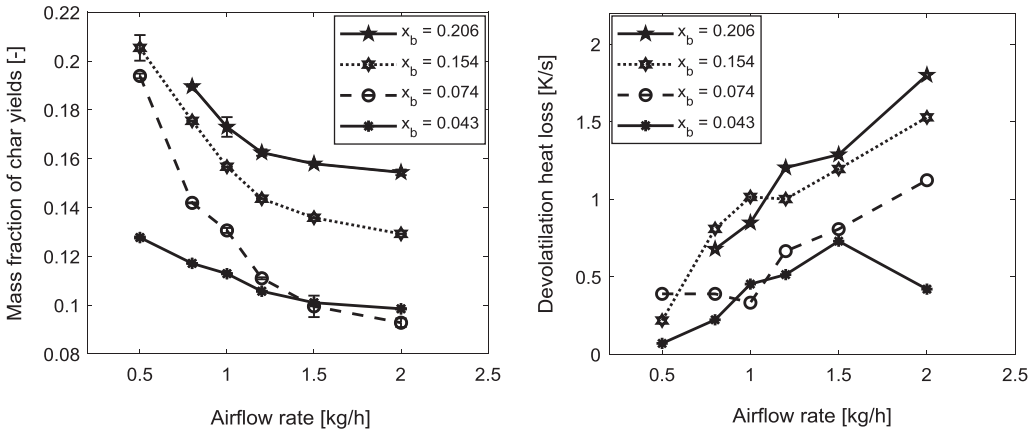

Fig. 7. Effect of biomass load and air flowrate on the biomass devolatilization (a) char yield (b) heat loss.

scaled in a similar manner to the amount of biomass added in the bed. The effect of the bed material needs to be considered also since the degree of fluidization at a given air flowrate depends on the particle properties (size, shape and density). To correctly scale the bed behaviour, the values of t_d and t_e are compared at different values of x_b and U_0/U_{mf}, where $U_0 = \dot{m}_{air}/(\rho_{air}A)$ is the superficial air velocity for a given air flowrate $\dot{m}_{air}$, and U_{mf} is the minimum fluidization velocity of the bed material at the operating conditions.

Fig. 8(a) shows the plot of $\log_{10}(x_b^a t_d)$ against $\log_{10}(U_0/U_{mf})$ while the corresponding plot for the value of t_e is shown in Fig. 8(b). With reference to the points **D** and **E** shown in Fig. 2, the value ofU_0 at each air flowrate is obtained at the temperature corresponding to the respective points while the corresponding value of U_{mf} is predicted using the Wen and Yu [32] correlation. For each plot in Fig. 8, the value of a is obtained by minimizing the mean square error between the fitting line and the experimental data. The results show that both values of $\log_{10}(x_b^a t_d)$ and $\log_{10}(x_b^a t_e)$ decrease linearly with increasing value of $\log_{10}(U_0/U_{mf})$ with correlation coefficients (R^2-values) of 0.64 and 0.73, respectively. Thus, from the fitting lines, t_d [min] and t_e [min] can be modelled as

$$t_d = 11.35x_b^{0.028}\left(\frac{U_0}{U_{mf}}\right)^{-0.3} \tag{10}$$

$$t_e = 67.58x_b^{0.278}\left(\frac{U_0}{U_{mf}}\right)^{-0.185} \tag{11}$$

The accuracies of the models described by Eqs. (10) and (11) are demonstrated in Fig. 9. Fig. 9(a) and Fig. 9(b) display the calculated versus the measured biomass residence time for the devolatilization and char extinction, respectively. As can be seen, the uncertainties in the model predictions are ± 10% for both t_d and t_e, where the mean absolute errors are 7.7% and 7.6%, respectively. The higher range of errors are still within acceptable limits for initial design phase and validation of CFD models.

Similarly, Eqs (12) and (13) give the correlations of the char yields and heat losses at different biomass loads and air flowrates. The overall error in the prediction of γ_{char} includes the uncertainty in the experimental data as described in Section 2.3. Both equations can be applied in modelling an air-biomass gasification process to account for the initial char yield and heat loss during the devolatilization.

$$\gamma_{char} = 0.414x_b^{0.245}\left(\frac{U_0}{U_{mf}}\right)^{-0.463} \pm 18\% \tag{12}$$

$$\dot{q}_L = 1.664\left(\frac{U_0}{U_{mf}}x_b\right)^{0.767} \pm 25\% \tag{13}$$

3.4. Application to a continuous gasification process

To apply Eqs. (12) and (13) to a continuous process, the biomass load x_b in the bed at the given operating conditions is required. As an approximation, a plug flow process can be considered over a cycle period, t_e at the given biomass and air flowrates. By plug flow, it is assumed that all particles have the same residence time thereby reducing the instability that arises due to gas flow [33,34]. Given a constant mass flow of biomass $\dot{m}_b$ and a fixed mass of the bed material, m_p, the

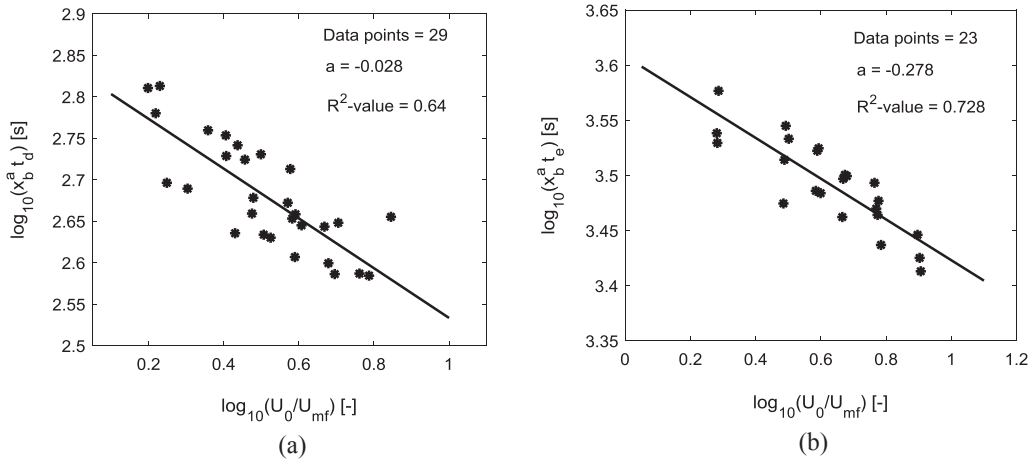

Fig. 8. Correlation of the characteristic residence time for biomass conversion (a) devolatilization (b) extinction.

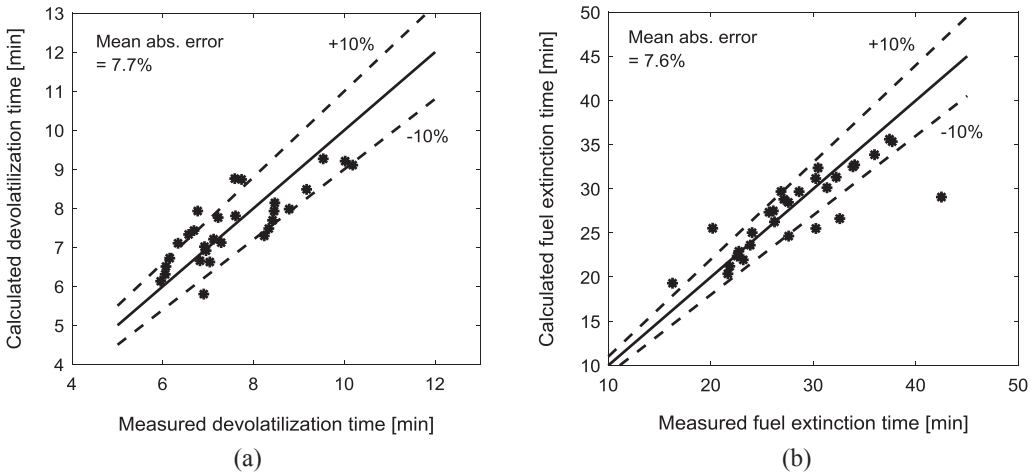

Fig. 9. Computed versus measured biomass characteristic residence time (a) devolatilization (b) extinction, showing the accuracy of the models given by Eqs. (10) and (11), respectively. The experimental data are those obtained in this study from the five different biomass loads at the six different air flowrates for each load.

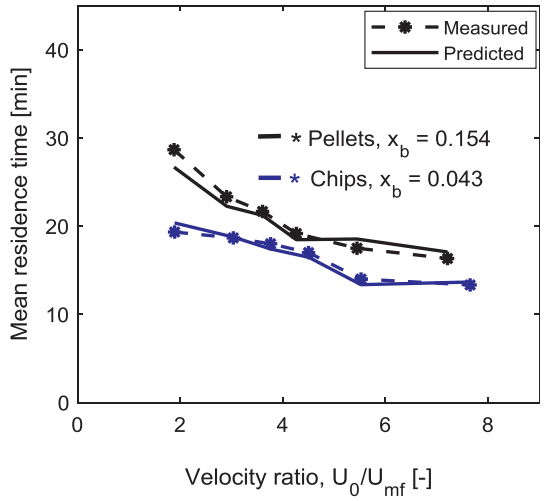

Fig. 10. Biomass mean residence time comparing the predicted results with the measured data.

value of x_b can be obtained from the following expression derived from Eq. (11).

$$x_b = \left[4055\frac{\dot{m}_b}{m_p}\left(\frac{U_0}{U_{mf}}\right)^{-0.185}\right]^{1.385} \tag{14}$$

Moreover, $(t_e - t_d)/t_d > 1.0$ at any given biomass load and air flowrate as shown in Fig. 6. For a continuous flow of biomass in a bubbling fluidized bed, this means that there will be excessive pressure build-up due to biomass accumulation when the residence time of the fuel particles is in the order of t_d. To obtain a stable process where the pressure in the bed is relatively low over an operating period, the biomass residence time must lie between t_d and t_e. Supposing t_* is the operating mean residence time, the degree of char conversion or reaction completeness α can be obtained as

$$\alpha = \frac{t_* - t_d}{t_e - t_d} \tag{15}$$

The value of α ranges from 0 to 1. When $\alpha = 0$, the amount of char in the bed grows at the rate γ_{char} kg/kg raw biomass and no steady state can be attained, although the product gas will be rich in combustible gases. When $\alpha = 1$, the biomass particles in the bed will be reduced to approximately zero, and the exit gas will contain, beside nitrogen and unconverted oxygen, mostly CO_2 and H_2O. However, by assessing the

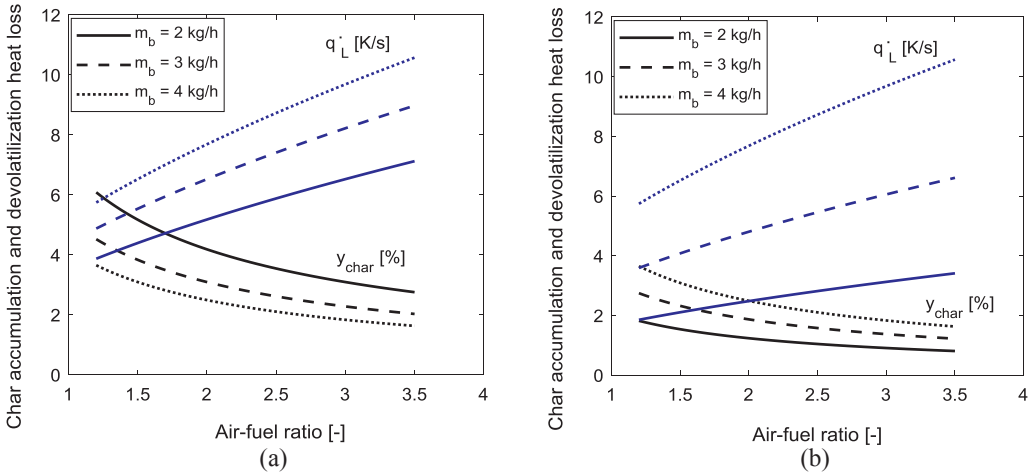

Fig. 11. Computed amount of accumulated char particles based on Eq. (17) and heat loss based on Eq. (13) in a bubbling fluidized bed for a continuous flow of biomass, showing the effect of bed solid loading ratio at different air–fuel ratios (a) constant biomass flowrate to bed material mass ratio $\dot{m}_b/m_p = 1.0$ 1/h (b) constant bed material mass $m_p = 4$ kg. $T = 800$ ℃, bed particle size = 300 μm and the bed diameter = 0.15 m.

temperature profile for a typical biomass conversion as shown in Fig. 2, it is clear that $0 < \alpha < 1$ will always be true for any given continuous process. The operating value of α can be taken as that corresponding to the mean residence time t_* as indicated in Fig. 2. The analysis shows that α varies within 0.45–0.7 for both types of biomass. The mean value of α for the wood pellets is 0.55 while that for the wood chips is 0.6.

Fig. 10 compares the mean residence time, t_* obtained as described in Fig. 2 with the values predicted using a combination of Eq. (10), Eq. (11) and the conversion factor α for different biomass loads. The superficial air velocity U_0 and the minimum fluidization velocity U_{mf} of the 293 μm sand particles are evaluated at the temperature measured at the time, $t = t_*$ during the conversion period, and the value of α is based on the value corresponding to each air flowrate in the respective beds. As can be seen in Fig. 10, the computed values of t_* are closer to the measured values, despite the temperature difference at the devolatilization and extinction times, t_d and t_e. This therefore shows that for subsequent applications, the values of t_d and t_e can be obtained at the given bed operating temperature.

Based on the degree of conversion, the amount of unconverted char particles x_{char} within the period $(t_e - t_d)$ can be thus predicted from

$$x_{char} = (1 - \alpha)\gamma_{char}(t_e - t_d)\frac{\dot{m}_b}{m_p} \tag{16}$$

where x_{char} is the mass ratio of the unconverted char to the bed material. t_d and t_e can be computed using Eqs. (10) and (11). As a percentage y_{char} of the total solids in the bed, Eq. (16) can be re-expressed as

$$y_{char} = \frac{x_{char}}{x_{char} + 1}100\% \tag{17}$$

Using the value of y_{char} estimated from Eq. (17), the minimum fluidization velocity, the minimum slugging velocity and other bubble-induced properties in a biomass bubbling fluidized bed gasifier can be predicted. In addition, with the value of x_{char}, the solids circulation rate, $\dot{m}_{sc}$ required for a dual fluidized-bed biomass gasifier can also be determined as described below:

$$\dot{m}_{sc} = \frac{m_p}{(1 - \alpha)(t_e - t_d)}(x_{char} + 1) \tag{18}$$

Although dual fluidized-bed gasifiers are originally operated for steam-biomass gasification [1], applying this technology in an air-blown gasifier can also help to achieve gasification at low air–fuel ratios, thereby achieving higher CO and H_2 yields in the syngas as for a single bubbling or circulating fluidized bed under autothermal operation (air-blown).

The application of the above correlations in a continuous biomass gasification process is illustrated in Fig. 11. For the same biomass and air flowrates, the figure compares the values of $\dot{q}_L$ and y_{char} at different loadings of the bed material. The mass loading ratio $\dot{m}_b/m_p = 1.0\ \mathrm{h}^{-1}$ is constant in Fig. 11(a), giving different values of m_p at different biomass feeds, while in Fig. 11(b), the mass of the bed material $m_p = 4$ kg is constant. The gasification temperature is 800 ˚C, the particle size is 300 μm and the degree of conversion $\alpha = 0.6$ in all the plots. With an increase in the air–fuel ratio at the same biomass flowrate, the relative amount of char accumulated in the bed decreases and the heat loss during the devolatilization increases due to the increase in gas velocity, U_0/U_{mf}. The figures also show that the value of $\dot{q}_L$ increases with increasing biomass feed rate. At the constant mass load ratio, the char accumulation decreases with increasing biomass flowrate due to the increasing mass of the bed material. Comparing Fig. 11(a) and (b), it can be seen that the heat loss decreases as the mass of the bed material increases, which can be connected to the increasing heat-holding capacity of the bed. With the lower heat loss, the char yield decreases, which can also explain the increasing char accumulation shown in Fig. 11(b) as the biomass supply increases.

In addition to air–fuel ratio, the results described above show that the gas velocity ratio U_0/U_{mf} is an important parameter that influences the extent of biomass conversion in a fluidized bed. Since the rates of particle entrainment and elutriation also depend on U_0/U_{mf} and on the amount of char present, the gas velocity ratio must be selected with caution for successful operation of a fluidized bed gasifier. Moreover, the value of x_{char} obtained from the proposed model is not a steady state value at the given biomass flowrate and gasification conditions since it is based on t_e, a time value very small to achieve a steady state in a gasifier. As shown in Timmer and Brown [4], it can take over 12 h for a steady state condition to be achieved under elutriation effect. Without particle elutriation, this condition will take several more hours if it exists. The value of t_e can be larger than 20 min, which is sufficiently long for successful control of a biomass gasification process. In addition, the proposed model for x_{char} is developed based on the ideal plug flow which gives the desirable flow pattern for any continuous fluidized bed [33,34]. Hence, Eq. (16) gives a more reliable information for successful design and operation of a bubbling fluidized bed gasifier than any steady state value.

4. Conclusions

This study presented a method for obtaining the residence time required for complete conversion of biomass in a bubbling fluidized bed using the time-variation of temperature and pressure in the bed. At any given biomass load and air flowrate, two characteristic times described as devolatilization and extinction times, were observed. The devolatilization time denotes the end of the conversion phase below which the exit gas contains combustible gases such as CO, H_2 and CH_4 while the extinction time marks the time over which nearly all the biomass charged in the bed is completely consumed. Both characteristic times decrease with increasing air flowrate and decreasing initial amount of biomass in the bed. In addition, the amount of char released and the total heat loss during the devolatilization were also measured and characterized.

Based on the data obtained in this study, different correlations were proposed for estimation of the mean biomass residence time, the amount of unconverted char particles and the devolatilization heat loss at a given operating condition. The prediction of the amount of biomass accumulated in the bed can be used in determining the minimum fluidization velocity, slugging velocity and other bubble-induced bed properties as well as the solids circulation rate desired for decongesting the accumulated biomass particles. The developed tools can provide a fast and accurate prediction of fluidized bed behaviour for biomass gasification.

Funding sources

This research did not receive any specific grant from funding agencies in the public, commercial, or not-for-profit sectors.

References

[1] Corella J, Toledo JM, Molina G. A review on dual fluidized-bed biomass gasifiers. Ind Eng Chem Res 2007;46:6831.
[2] Zou Z, Zhao Y-L, Zhao H, Zhang L-B, Xie Z-H, Li H-Z, et al. Hydrodynamic and solids residence time distribution in a binary bubbling fluidized bed: 3D computational study coupled with the structure-based drag model. Chem Eng J 2017;321:184.
[3] Ghaly AE, MacDonald KN. Mixing patterns and residence time determination in a bubbling fluidized bed system. Am J Eng Appl Sci 2012;5:170.
[4] Timmer KJ, Brown RC. Transformation of char carbon during bubbling fluidized bed gasification of biomass. Fuel 2019;242:837.
[5] Di Renzo A, Di Maio FP, Girimonte R, Vivacqua V. Segregation direction reversal of gas-fluidized biomass/inert mixtures – experiments based on Particle Segregation Model predictions. Chem Eng J 2015;262:727.
[6] Goldschmidt MJV, Link JM, Mellema S, Kuipers JAM. Digital image analysis measurements of bed expansion and segregation dynamics in dense gas-fluidized beds. Powder Technol 2003;138:135.
[7] Fiorentino M, Marzocchella A, Salatino P. Segregation of fuel particles and volatile matter during devolatilization in a fluidized bed reactor – II. Experimental. Chem Eng Sci 1909;1997:52.
[8] Solimene R, Marzocchella A, Salatino P. Hydrodynamic interaction between a

coarse gas-emitting particle and a gas fluidized bed of finer solids. Powder Technol 2003;133:79.
[9] Werther J, Hirschberg B. Solids motion and mixing. In: Grace JR, Avidan AA, Knowlton TM, editors. Circulating fluidized bed. London: Chapman and Hall; 1997. p. 119–48.
[10] Gao W, Zhang J, Wang Y, Huang B, Xu G. Residence time distribution of particles in a bubbling fluidized bed with their continuous input and output. Chin J Process Eng 2012;12:9.
[11] Li XT, Grace JR, Lim CJ, Watkinson AP, Chen HP, Kim JR. Biomass gasification in a circulating fluidized bed. Biomass Bioenergy 2004;26:171.
[12] Gomez-Barea A, Arjona R, Ollero P. Pilot-plant gasification of olive stone: a technical assessment. Energy Fuels 2005;19:598.
[13] Lv PM, Xiong ZH, Chang J, Wu CZ, Chen Y, Zhu JX. An experimental study on biomass air-steam gasification in a fluidized bed. Bioresour Technol 2004;95:95.
[14] Brown RC, Ahrens J, Christofides N. The contributions of attrition and fragmentation to char elutriation from fluidized beds. Combust Flame 1992;89:95.
[15] Gaston KR, Jarvis MW, Pepiot P, Smith Jr. KM, Frederick WJ, Nimlos MR. Biomass pyrolysis and gasification of varying particles sizes in a fluidized-bed reactor. Energy Fuels 2011;25:3747.
[16] Zanzi R, Sjostrom K, Bjornbom E. Rapid pyrolysis of agricultural residues at high temperature. Biomass Energy 2002;23:357.
[17] Zanzi R, Sjostrom K, Bjornbom E. Rapid high-temperature pyrolysis of biomass in a free-fall reactor. Fuel 1996;75:545.
[18] Mathieu P, Dubuisson R. Performance analysis of a biomass gasifier. Energy Convers Manage 2002;43:1291.
[19] Scott DS, Piskorz J, Bergougnou MA, Graham R, Overend RP. Role of temperature in the fast pyrolysis of cellulose and wood. Ind Eng Chem Res 1988;27:8.
[20] Gable P, Brown RC. Effect of biomass heating time on bio-oil yields in a free fall fast pyrolysis reactor. Fuel 2016;166:361.
[21] Bar-Ziv E, Kantorovich II. Mutual effects of porosity and reactivity in char oxidation. Prog Energy Combust Sci 2001;27:667.
[22] Henrich E, Buerkle S, Meza-Renken ZI, Rumpel S. Combustion and gasification kinetics of pyrolysis chars from waste and biomass. J Anal Appl Pyrol 1999;49:221.
[23] Wornat MJ, Hurt RH, Yang NYC, Headley TJ. Structural and compositional transformations of biomass chars during combustion. Combust Flame 1995;100:131.
[24] Paudel B, Feng Z-G. Prediction of minimum fluidization velocity for binary mixtures of biomass and inert particles. Powder Technol 2013;237:134.
[25] Kumoro AC, Nasution DA, Cifriadi A, Purbasari A, Falaah AF. A new correlation for the prediction of minimum fluidization of sand and irregularly shape biomass mixtures in a bubbling fluidized bed. IJAER 2014;9:21561.
[26] Agu CE, Tokheim L-A, Eikeland M, Moldestad BME. Improved models for predicting bubble velocity, bubble frequency and bed expansion in a bubbling fluidized bed. Chem Eng Res Des 2019;141:361.
[27] Viitanen PI. Tracer studies on a riser reactor of a fluidised catalytic cracking plant. Ind Eng Chem Res 1993;32:577.
[28] Helmrich H, Schugerl K, Janssen K. Decomposition of $NaHCO_3$ in laboratory and bench scale circulating fluidized bed reactors. In: Basu P, editor. Circulating fluidized bed technology. New York: Pergamon Press; 1985. p. 161–6.
[29] Kojima T, Ishihara K, Guilin Y, Furusawa T. Measurement of solids behaviour in a fast fluidised bed. J Chem Eng Jpn 1989;22:341.
[30] Xu R, Ferrante L, Briens C, Berruti F. Bio-oil production by flash pyrolysis of sugarcane residues and post treatments of the aqueous phase. J Anal Appl Pyrol 2011;91:263.
[31] Tran HC, White RH. Burning rate of solid wood measured in a heat release rate calorimeter. Fire Mater 1992;16:197.
[32] Wen CY, Yu YH. A generalized method for predicting the minimum fluidization velocity. AIChE J 1966;12:610.
[33] Chandran AN, Rao SS, Varma YBG. Fluidized bed drying of solids. AIChE J 1990;36:29.
[34] Raghuraman J, Varma YBG. An experimental investigation of the residence time distribution of solids in multistage fluidisation. Chem Eng Sci 1975;30:145.

Article 10 (A10)

Detailed One-Dimensional Model for Biomass Gasification in a Bubbling Fluidized Bed

By

Cornelius E. Agu, Christoph Pfeifer, Marianne Eikeland, Lars-Andre Tokheim, Britt M.E. Moldestad

Submitted and currently under review in

Energy & Fuels

Detailed One-Dimensional Model for Steam-Biomass Gasification in a Bubbling Fluidized Bed

[*]Cornelius E. Agu[a], Christoph Pfeifer[b], Marianne Eikeland[a], Lars-Andre Tokheim[a], Britt M.E. Moldestad[a]

[a]*Department of Process, Energy and Environmental Technology, University of South-Eastern Norway, 3918 Porsgrunn, Norway*

[b]*Department of Material Sciences and Process Engineering, University of Natural Resources and Life Sciences, 1190 Vienna, Austria*

**cornelius.e.agu@usn.no; christoph.pfeifer@boku.ac.at; Marianne.Eikeland@usn.no; Lars.A.Tokheim@usn.no; britt.moldestad@usn.no*

Abstract

A one-dimensional unsteady state model is developed for simulation of biomass gasification in a bubbling fluidized bed. The proposed model accounts for the effect of hydrodynamic behaviour of the fluidized bed by incorporating the momentum equations of fluid and fuel particles. The model results are validated against experimental data in the literature as well as the results from existing models. The proposed model is capable of predicting the total gas yield and composition of the product gas at different operating conditions. The effect of biomass feeding position is investigated, and the performance of a reactor under non-isothermal condition is compared with its performance under an isothermal operation. As the developed model is computationally less demanding, it can be used to improve design and operational control of bubbling fluidized bed gasifiers.

Keywords: Biomass; Bubbling bed; One-dimensional; Steam gasification; Unsteady state

1 Introduction

Modelling and simulation of biomass gasification reactors is still a growing research interest. For a continuous process and a steady product quality, biomass gasification can be carried out in a bubbling fluidized bed [1, 2] or a circulating fluidized bed reactor [3, 4]. An entrained flow reactor can also be applied using a pulverized feedstock [5]. Moreover, the so-called dual fluidized bed systems are available, which combine two circulating beds or one bubbling and one circulating bed. Depending on the desired product gas composition, biomass gasification can be achieved using air (or pure oxygen), steam or carbon dioxide as the gasifying agent. For a higher energy efficiency, it is advantageous to apply a combination of steam and air [6]. Gonzalez-Vazquez et al. [6] showed that an optimum syngas yield of 2.0 m^3/kg biomass containing 35% (H_2 + CO) can be obtained in an atmospheric wood gasifier when the steam to air ratio of 3.0 is used.

Due to experimental setup limitations, different models have been developed to investigate the effect of different process parameters and operating conditions on the syngas production rate, composition and energy value. Modelling of a fluidized bed biomass gasifier is a multi-task due

to different phase interactions (solid-gas and solid-solid interactions) in the bed. Mazaheri et al. [7] suggested a procedure for achieving a successful model for biomass gasification at different operating conditions. A gasification model can be based on a thermodynamic equilibrium assumption or on chemical reaction kinetics. While the former does not provide information about the reactor design and can only be applied for a specific reaction route, a model based on the chemical kinetics accounts for the reactor geometry and is also flexible to accommodate as many different reactions as possible. A thermodynamic equilibrium model is usually based on minimization of Gibbs free energy, and it gives the maximum theoretical gas yields under a given operating condition [8]. The most complex and reliable kinetic models are those based on the conservation of mass, momentum and energy of fluid and particles. A combination of thermodynamic equilibrium and kinetic models has also been demonstrated in different studies [9]. Pauls et al. [9] incorporated the reaction kinetics and the bed hydrodynamics to enhance CO and H_2 production.

Computational fluid dynamics (CFD) and computational particle-fluid dynamics (CPFD) can be used to model the biomass reactor behaviour. CFD is based on the Euler- Lagrangian or Euler-Euler modelling approach assuming that the bulk solid particles flow continuously in a fluid-like manner [10], and can be developed for one, two and three-dimensional flows. Moreover, CPFD is developed for multiphase flows where the particle motion is described by the Lagrangian particle tracking method [11]. Depending on the solution method, results from different studies using the 3D [1, 2, 4, 12 - 14] and 2D [15, 16] versions of the models agree very well with experiments. However, the complexities arising from the multi-dimensional models limit their applications. The models are computationally time demanding, requiring several days to obtain a solution in 1 hr simulation time.

To combat the gasification modelling challenges, different versions of 1D (steady and unsteady state) models have been proposed [17 - 21]. Most of these models are based on the two-phase theory [22]. The two-phase theory models solve only the mass and energy balances in two separate phases (bubble and emulsion) coupled with the exchange of the conserved variables at the interface between the two phases. The hydrodynamics of the bed are captured by the use of bubble velocity, bubble volume fraction and bed voidage in the interface transfer models. In some studies [21], attempts are made to incorporate the fluid velocity model due to change of mass of each species in the bed. Hejazi et al. [21] also included an expression for solid circulation rate in the model developed for a dual fluidized bed biomass gasifier. To minimize the potential effect of reverse reactions, Inayat et al. [23] implemented a CO_2 adsorbent in their kinetic model, which enhances the production of hydrogen. As most of the available models are based on the assumption of a uniform distribution of the fuel particles, the two-phase models fail to properly account for the axial distribution of temperature and materials in the reactor.

Moreover, extensive one-dimensional models based on conservation of mass, momentum and energy have also been demonstrated for simulation of fluidized bed reactors [24, 25]. These 1D models include the equations for the inert particle momentum and solid fraction propagation, increasing their complexities.

To further enhance the modelling and simulation of biomass gasifiers for efficient design and operation, a more simplified but realistic one-dimensional unsteady state model is developed in

the present study. The proposed model includes the momentum equations of the fluid and fuel particles to capture the effect of particle properties on the bed behaviour. In the model development, it is assumed that the bed inert particles have zero mean velocity over the bed height. This assumption helps to eliminate the complexities in decoupling the particle motion from the rest of the bed. To account for the effects of rising bubbles, correlations for predicting the bed expansion, bubble velocity and bubble volumetric flux are incorporated. The fluid is modelled based on the Eulerian approach while the fuel particle motion is assumed dispersed. The effects of the kinetic energy change, and the impact of bubble flow and resistance due to collision with the bed inert particles are considered in the solid fuel motion. The developed model can be used to investigate the behaviour of a gasifier at different operating conditions and design choices. In the subsequent sections, the detailed development of the model is presented and the model results are validated against experimental data from the literature and results from some existing models.

2 Gasification and reaction kinetics

Biomass gasification depends on temperature and time, and proceeds after pyrolysis where the fuel particles are thermally broken down into volatiles, tar and char [26]. For a lignin-based biomass, the pyrolysis takes place within 250 – 500 ˚C [26]. The biomass conversion in a fluidized bed increases the total gas flow rate and the solids inventory in the bed, which can be obtained at a given temperature by considering the reaction kinetics. There are several kinetic models for biomass pyrolysis [27, 28], but the parallel kinetic model shown in Fig. 1 can be applied.

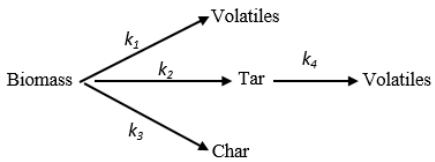

Fig. 1. Illustration of the three parallel steps in biomass pyrolysis [29, 30].

The kinetic rate constant k for the different stages in the pyrolysis phase can be expressed in the Arrhenius form.

$$k_i = A_i \exp\left(-\frac{E_i}{RT}\right). \quad (1)$$

Here, $i = 1,2,3,4$ is the index indicating each of the parallel reactions involved in the pyrolysis. Values of the frequency factor A and the activation energy E can be obtained from Chan et al. [31] as shown in Table 1. The biomass pyrolysis can also be assumed endothermic with a reaction enthalpy of 64 kJ/kg [21].

The mole fraction ϑ_j of the volatiles j $\in (H_2, CO, CO_2, CH_4)$ in the primary pyrolysis ($i = 1$) can be obtained from Eq. (2) [16].

$$\vartheta_j = \frac{\Lambda_j}{\sum_j \Lambda_j};\ \Lambda_j = c_j T^{\alpha_j} \quad (2)$$

Here, T is the mean temperature of the bed, and c_j and α_j are model fitting parameters for each gas species as outlined in Table 2. The correlation in Eq. (2) for the uncorrected gas mole fraction Λ_j was obtained in the temperature range 1000 – 1070 K based on the experimental data from pine wood pellets [16]. The mass fraction γ_j of each component resulting from the tar cracking ($i = 4$) is also given in Table 2 [31].

Table 1. Parameters for kinetic rate constant in the biomass pyrolysis [31].

Pyrolysis Step, i	A_i (1/s)	E_i (J/mol)
1	$1.30\text{x}10^{8}$	$1.40\text{x}10^{3}$
2	$2.00\text{x}10^{8}$	$1.33\text{x}10^{3}$
3	$1.08\text{x}10^{7}$	$1.21\text{x}10^{3}$
4	$1.00\text{x}10^{5}$	$9.34\text{x}10^{1}$

Table 2. Parameters for the light gases from biomass pyrolysis [16, 31].

Gas species, j	c_j	α_j	γ_j
H_2	$1.34\text{x}10^{-16}$	5.73	0.02
CO	$1.80\text{x}10^{7}$	-1.87	0.56
CO_2	$2.48\text{x}10^{3}$	-0.70	0.11
CH_4	$4.43\text{x}10^{5}$	-1.50	0.09
Inert	-	-	0.22

Beyond the pyrolysis, the resulting char particles react with the available gasifying agent including oxygen, steam and carbon dioxide. Moreover, the permanent gas components in the volatiles also act as gasifying agents. A number of gas phase (homogeneous) reactions also take place in the reactor. Different kinetic rate constant models are available for each of the reactions depending on the available gasifying agents. For a steam biomass gasification, Table 3 describes some of the most favourable reactions with their kinetic rate constants taken from different publications.

Table 3. Kinetic rate constants for different reactions in a steam-biomass gasification.

i	Reactions	ΔH_{ri}^{0} (kJ/mol)	Rate constant, r_i (mol/m^3.s)	Ref.
			Heterogeneous	
1	$C+H_2O \rightarrow CO+H_2$	+131	$r_1 = \frac{k_{r1,1}x_{H_2O}}{1/p + k_{r1,2}x_{H_2} + k_{r1,3}x_{H_2O}}(1-X_c)[C]$ $k_{r1,1} = 1.25\text{x}10^5 \exp\left(-\frac{28000}{T}\right)$ $k_{r1,2} = 3.26\text{x}10^{-4}$ $k_{r1,3} = 0.313 \exp\left(-\frac{10120}{T}\right)$	[32]
2	$C+CO_2 \rightarrow 2CO$	+172	$r_2 = \frac{k_{r2,1}}{1+\frac{x_{CO}}{k_{r2,2}x_{CO_2}}}[C]$ $k_{r2,1} = 3.6\text{x}10^5 \exp\left(-\frac{20130}{T}\right)$ $k_{r2,2} = 4.15\text{x}10^3 \exp\left(-\frac{11420}{T}\right)$	[33]
3	$C+2H_2 \rightarrow CH_4$	-75	$r_2 = 6.11\text{x}10^{-3} \exp\left(-\frac{80333}{RT}\right)[H_2][C]$	[34]
			Homogeneous	
4	$CO+H_2O \leftrightarrow CO_2+H_2$	-41	$r_4 = 0.278 \exp\left(-\frac{12560}{RT}\right)\left\{[H_2O][CO] - \frac{[H_2O][CO]}{k_{eq,4}}\right\}$ $k_{eq,4} = 0.022 \exp\left(\frac{34730}{RT}\right)$	[35]
5	$CH_4+H_2O \rightarrow CO+3H_2$	+206	$r_5 = 312 \exp\left(-\frac{15098}{T}\right)[CH_4]$	[36]

[ ] = molar concentration (mol/m^3), p (Pa) = pressure and X_c = char conversion factor.

3 Model development

The distribution of temperature and materials in a bubbling fluidized bed reactor depends on the hydrodynamic behaviour of the bed. To account for this behaviour, both the solid and gas

momentum equations are considered in addition to the mass balance of each phase in the flow direction. Modelling of gas flow is based on the Eulerian approach while the particle motion is based on the dispersed flow behaviour. Due to changes in the mass of the fuel particles, the kinetic energy change along the flow direction is incorporated in the particle flow model. The particle-particle collisions and dragging of particles by the bubbles are also accounted for. Fig. 2 describes the flows of gas and fuel particles within the bed and across their respective boundaries. u_b is the bubble rise velocity, and u and v are the gas and solid fuel velocities, respectively. $\dot{m}_{g,in}$ and $\dot{m}_{b,in}$ are the respective gas and biomass mass flowrates at the inlets with $T_{g,in}$ and $T_{b,in}$ the corresponding boundary temperatures. D is the reactor diameter, l_{sb} is the biomass feeding position above the bed base, and L and l_f are the total reactor height and bed height at the fluidized state, respectively.

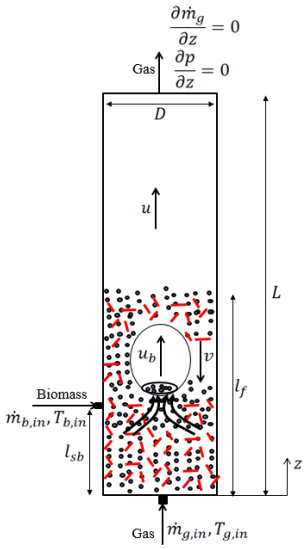

Fig. 2. Illustration of a bubbling fluidized bed behaviour in a binary solid mixture (red = biomass, black = bed material), showing biomass and gas boundary conditions and drag of solids into the bubble wake.

In addition to the assumptions outlined below, the necessary simplifications introduced in developing the gasifier model are given in the relevant sections.

- There are no variations of temperature and species in the radial directions. Hence, the model is one-dimensional, i.e. there are only gradients in the axial direction.
- The bed expands uniformly, resulting in an even distribution of the bed material particles. With this assumption, the complex computation of mass flow of the particles can be eliminated while the average solids fraction of the bed can be obtained from the available empirical correlations.
- The bed material remains inert over a clearly defined volume, and there is no mass loss due to elutriation. Hence, the net velocity of the particles is considered zero over one cycle of the solids circulation.
- The ash content of biomass is negligible.
- The unconverted tar is in vapour phase.
- The gas species move upwards while the fuel solids move downwards.

3.1 Species mass balance

Considering a continuum flow of solid fuel particles, the rate of change in the concentration of the particles within a given volume can be described by

$$\frac{\partial \bar{\rho}_{s,j}}{\partial t} = -\frac{\partial (v\bar{\rho}_{s,j})}{\partial z} + S_{s,j} \tag{3}$$

where $\bar{\rho}_{s,j}$ is the mass concentration of the solid species $\mathrm{j} \in (\mathrm{b}, \mathrm{c})$, with $'\mathrm{b}'$ and $'\mathrm{c}'$ denoting biomass and char, respectively, and $S_{s,j}$ is the rate of generation of mass of the species.

Similarly, the mass balance for each of the gas species $\mathrm{j} \in (\mathrm{H_2}, \mathrm{CO}, \mathrm{CO_2}, \mathrm{CH_4}, \mathrm{H_2O}, \mathrm{tar})$ is as described below.

$$\frac{\partial \bar{\rho}_{g,j}}{\partial t} = -\frac{\partial (y_j \dot{m}''_g)}{\partial z} + S_{g,j} \tag{4}$$

$$y_j = \frac{\bar{\rho}_{g,j}}{\bar{\rho}_g} \tag{5}$$

Here, $S_{g,j}$ is the rate of generation of the gas species per unit volume and $\dot{m}''_g = u\bar{\rho}_g$ is the mass flux of the bulk gas. The mass concentration of the gas mixture $\bar{\rho}_g$ is given by

$$\frac{\partial \bar{\rho}_g}{\partial t} = -\frac{\partial (\dot{m}''_g)}{\partial z} + \sum S_{g,j} \tag{6}$$

3.2 Momentum balance

The velocities of the solid particles and gas species can be obtained by balancing the forces across the control volume for each phase. The Lagrangian approach is considered for the solid fuel where the motion of each particle is assumed to be independent of the others. The gas flow follows the continuum mechanism, and thus the Eulerian approach is used for this phase.

3.2.1 Solid phase

With the assumption that the solid fuel particles are dispersed within the bed, the single particle downward motion is described as follows:

$$\rho_s \frac{\partial v}{\partial t} = -2\rho_s v \frac{\partial v}{\partial z} + g(\rho_s - \rho_g) + F'_b + \beta_{g,s}(-u - v) + \beta_{p,s}(-v) + v \sum S_{s,j} \tag{7}$$

where ρ_s and ρ_g are the solid and gas densities, respectively, g is the acceleration due to gravity and F'_b is the force per unit volume exerted on the fuel particles by the bed material due to flow of bubbles. $\beta_{g,s}$ and $\beta_{p,s}$ are the momentum transfer coefficients due to drag by the gas and collision with the bed material particles, respectively.

$$\beta_{g,s} = \frac{6D_R}{\pi d_s^3} \tag{8}$$

The drag resistance D_R, and the average diameter d_s and density ρ_s of the fuel particles are given by

$$D_R = \frac{1}{8}\pi d_s^2 \rho_g c_d |u + v| \tag{9}$$

$$d_s = \frac{d_b}{\left[1+\left(1.25\sqrt[3]{n_1 \Psi(1-X_c)}-1\right)y_{s,c}\right]} \tag{10}$$

$$\rho_s = \left(\frac{y_{sc}}{\rho_c} + \frac{(1-y_{sc})}{\rho_b}\right)^{-1} \tag{11}$$

The gas-solid drag coefficient c_d can be obtained as described in Kunii and Levenspiel [22]. Eq. (10) is derived considering the shrinkage of biomass particles during devolatilization [37], where d_b is the Sauter mean diameter of the raw biomass, Ψ is the biomass shrinkage factor, n_1 is the factor accounting for primary fragmentation of the particles and X_c is the char conversion factor. $y_{s,c}$ as expressed in Eq. (12) describes the mass fraction of char particles in the solid fuel mixture.

$$y_{s,c} = \frac{\bar{\rho}_{s,c}}{\bar{\rho}_s}; \quad \bar{\rho}_s = \bar{\rho}_{s,c} + \bar{\rho}_{s,b} \tag{12}$$

The solid contact coefficient $\beta_{p,s}$ in Eq. (7) depends on the volume and particle size of the solid fuel relative to the bed material. Noting that the particle velocity of the bed material is zero, $\beta_{p,s}$ can be derived from the model given in Chang et al. [38] based on the collision theory between two different bulks of solid particles in a mixture. Assuming that the momentum change of the bed particles as they are dragged into the bubble wake is transferred to the fuel particles within the bubble vicinity, F_b' can be modelled as

$$F_b' = -(1-\varepsilon_{mf})\rho_p \theta_w G_b \frac{\partial u_b}{\partial z} \tag{13}$$

where ε_{mf} is the void fraction at minimum fluidization, ρ_p is the density of the bed material, θ_w is the bubble wake fraction [22] and G_b is the bubble volumetric flux.

3.2.2 Gas phase

The flow of gas through a bed is resisted by interactions with the bulk of different solid materials (bed material and fuel particles) as well as with the reactor walls. Assuming that the fluid pressure drop over the bed is hydrostatic and that the contribution of the fuel particles on the solid mixture density is negligible, the momentum balance for the gas phase is given by

$$\frac{\partial \dot{m}_g''}{\partial t} = -\frac{\partial(\dot{m}_g''.u)}{\partial z} + g\left[\varepsilon_f\left(1-\varepsilon_f\right)\rho_p - \bar{\rho}_g\right] - \frac{\bar{\rho}_s}{\rho_s}\beta_{g,s}(-u-v) - \frac{2f_g\bar{\rho}_g}{D}u.|u| - u\left(\beta_{g,p} - \sum S_{gj}\right) - \varepsilon_f \frac{\partial p}{\partial z} \tag{14}$$

where ε_f is the bed voidage at the fluidized state, f_g is the wall frictional factor as given in Gidaspow [39] and $\beta_{g,p}$ is the momentum transfer coefficient between the gas and the bed material. The gas-particle momentum transfer coefficient can be obtained from different correlations [40, 41]. Since in a typical bubbling bed, $\varepsilon_f < 0.8$, the value of $\beta_{g,p}$ can be determined from Eq. (15) as proposed by Gidaspow [39].

$$\beta_{g,p} = 150\frac{(1-\varepsilon_f)^2}{\varepsilon_f(\varphi_p d_p)^2}\mu_g + 1.75\frac{(1-\varepsilon_f)}{\varphi_p d_p}\rho_g|u| \quad (15)$$

Here, φ_p and d_p are the bed particle sphericity and diameter, respectively, and μ_g is the gas dynamic viscosity. The gas density ρ_g is given by Eq. (16) and the fluid pressure p is modelled as in Eq. (17), assuming the ideal gas behaviour, where R is the universal gas constant and M_g is the gas molecular weight. The pressure term in Eq. (14) is included to convey the mass generated in the bed appropriately along the reactor axis.

$$\rho_g = \frac{\bar{\rho}_g}{\varepsilon_f} \quad (16)$$

$$p = \frac{\rho_g R T_g}{M_g} \quad (17)$$

3.3 Energy balance

The thermochemical processes in a gasifier involves exchange of heat between the gas and solids, the fuel particles and the bed material, the solids and the reactor walls and between the reactor walls and the environment. As gas flows through the reactor, there is a continuous heat loss. Hence, a continuous heat supply is required to keep the reactions as desired. Accounting properly the flow of heat within and across the reactor will provide a better model for predicting the reactor performance. The necessary equations proposed for solving the energy balance are detailed in the following subsections.

3.3.1 Solid phase (fuel particles)

Since the distribution of fuel particles may not be uniform due to flow of cold biomass at the inlet port and due to variation in concentration of the gasifying agent over the bed height, the sensible heat transferred by the flow of the bulk material is essential to accurately predict the heat distribution. Neglecting the contact and radiation exchange with the walls, the net heat transferred to the solid particles in a unit volume includes the convective term due to gas flow, the collision and radiation exchange with the bed material and the generated heat due to reactions of the particles. The distribution of the solid temperature T_s over the bed height at a given time is therefore modelled by

$$\bar{\rho}_s\bar{c}_{p,s}\frac{\partial T_s}{\partial t} = -\bar{\rho}_s\bar{c}_{p,s}v\frac{\partial T_s}{\partial z} + \frac{6}{d_s}\left(\frac{\bar{\rho}_s}{\rho_s}\right)\left[h_{g,s}(T_g - T_s) + \epsilon_s\sigma\left(T_p^4 - T_s^4\right)\right] + h'_{p,s}(T_p - T_s) - \left(\sum r_i\Delta H^0_{ri} + r_{pyr}\Delta H^0_{pyr}\right) \quad (18)$$

where, $\bar{c}_{p,s}$ is the specific heat capacity of the solid, ϵ_s is the average emissivity of the fuel particles and σ is the Stefan-Boltzmann constant. T_p is the bed particle temperature and $h_{g,s}$ is the single particle convective heat transfer coefficient between the gas and the solid fuel, and it can be obtained as given in Ranz [42]. The particle-particle heat transfer coefficient $h'_{p,s}$ per unit volume is as described in Chang et al. [38]. The last term in Eq. (18) is the net heat generated during the conversion of the particles in the heterogeneous reactions (i = 1, 2, 3) and in the devolatilization (pyrolysis) stage, where $r_{pyr} = \bar{\rho}_{s,b}\sum k_i$.

3.3.2 Gas phase

For the gas phase, the heat balance also includes the convective heat exchange with the bed material due to a possible temperature difference between the two media. Assuming that the reactor walls are in thermal equilibrium with the gas, the energy balance is thus given by

$$\bar{\rho}_g \bar{c}_{p,g} \frac{\partial T_g}{\partial t} = -\bar{\rho}_g \bar{c}_{p,g} u \frac{\partial T_g}{\partial z} - \frac{6}{d_s}\left(\frac{\bar{\rho}_s}{\rho_s}\right) h_{g,s}\left(T_g - T_s\right) - \frac{6}{\varphi_p d_p}\left(1-\varepsilon_f\right) h_{g,p}\left(T_g - T_p\right) - K_r \sigma\left(T_w^4 - T_p^4\right) - \frac{4}{D} U_a (T_w - T_a) - \sum\left(r_i \Delta H^0_{r,i}\right) \quad (19)$$

where, $\bar{c}_{p,g}$ is the gas specific heat capacity and $h_{g,p}$ is the convective heat transfer coefficient between the gas and the bed material in fluidized state as expressed in Gunn [43]. U_a is the overall heat transfer coefficient between the walls and the surroundings at ambient temperature T_a. The last term includes only the homogeneous reactions (i = 4, 5 in Table 3). $T_w = T_g$ is the wall temperature under the gas-wall thermal equilibrium. Assuming that the bulk solid material is a cylinder concentric with the reactor walls (cylinder), Eq. (20) can be derived for the effective radiation coefficient K_r, where ϵ_p and ϵ_w are the emissivity of the bed particle and the reactor wall materials, respectively.

$$K_r = \frac{4}{D}\left[\frac{1-\epsilon_p}{\epsilon_p\left(1-\varepsilon_f\right)^2} + \frac{1}{\epsilon_w}\right]^{-1} \quad (20)$$

3.3.3 Solid phase (inert bed particles)

With the assumption that the mean velocity of the inert particles is zero, T_p can be obtained from Eq. (21), where $\bar{c}_{p,p}$ is the specific heat capacity of the bed material.

$$\left(1-\varepsilon_f\right)\rho_p \bar{c}_{p,p} \frac{\partial T_p}{\partial t} = \frac{6}{\varphi_p d_p}\left(1-\varepsilon_f\right) h_{g,p}\left(T_g - T_p\right) - \frac{6}{d_s}\left(\frac{\bar{\rho}_s}{\rho_s}\right) \epsilon_s \sigma\left(T_p^4 - T_s^4\right) - h'_{p,s}\left(T_p - T_s\right) + K_r \sigma\left(T_w^4 - T_p^4\right) \quad (21)$$

3.4 Bubble properties and bed expansion

The gasification model outlined in the previous section requires accurate prediction of the bubble properties (diameter, volumetric flux and bubble velocities) and bed expansion. There are several models for predicting the bubble diameter [44 - 46] and bubble velocity [47 - 50]. The most common methods for the prediction of bubble volumetric flux G_b and bed voidage ε_f at fluidized state are those based on the two-phase theory as described in Kunii and Levenspiel [22]. The inaccuracy in predicting the bed voidage and expansion can affect the model global accuracy. A higher bed voidage indicates flow of faster and larger bubbles as well as a lower gas-solid contact time due to a reduced pressure drop. On the other hand, the distributions of heat and materials will be poor when the bed is not well expanded. For the particles within the Geldart B solid groups, the bubble velocity u_b, the bed voidage (with the bed expansion Δe) and the bubble volumetric flux can be computed using the correlations [47, 51] given in Eq. (22) – Eq. (26).

$$u_b = 12.51(u_0 - u_{mf})^{0.362}\left(\frac{d_b}{D}\right)^{0.52} D \quad (22)$$

$$\Delta e = \left[1 - 0.103\left(u_0 - u_{mf}\right)^{-0.362}\left(\frac{\bar{d}_b}{D}\right)\right]^{-1} - 1 \quad (23)$$

$$\varepsilon_f = 1 - \frac{1-\varepsilon_{mf}}{1+\Delta e} \quad (24)$$

$$l_f = \frac{1-\varepsilon_0}{1-\varepsilon_f} l_0 \quad (25)$$

$$G_b = 1.285\left(\frac{d_b}{D}\right)^{1.52} D \quad (26)$$

Here, u_0 is the superficial gas velocity at the inlet boundary condition, u_{mf} is the particle minimum fluidization velocity, d_b is the bubble diameter at any position z along the bed axis and $\bar{d}_b$ is the average bubble diameter over the bed height. l_f is the total bed height at fluidized state, and ε_0 and l_0 are the voidage and bed height at fixed state, respectively. While the bubble diameter depends on the bed particles, it is also affected by temperature. For fine particles, the bubble diameter decreases with increasing temperature [22]. However, most of the available models for bubble diameter give the opposite trend at a given value of u_0 since u_{mf} decreases with increasing temperature. The correlation proposed by Agu et al. [51] for predicting the average bubble diameter over the bed height can account for the effects of particle and fluid properties, but it is limited to only large particles for which the Archimedes number, $A_r > 400$. Nevertheless, to close the proposed gasifier model, the values of d_b and $\bar{d}_b$ can be evaluated based on the Werther [48] correlation as given in Eq. (27) while the other correlations required to completely solve the balance equations are shown in Table 4.

$$d_b = 0.00853\left[1 + 27.2\left(u_0 - u_{mf}\right)\right]^{1/3}(1 + 6.84z)^{1.21} \quad (27)$$

In Table 4, M_j is the molecular weight of the gas species, x_j is the gas mole fraction and n is the number of species in the gas phase. Pr is the Prandtl number at the gas flow condition. The specific heat capacity $\bar{c}_p$, dynamic viscosity μ and thermal conductivity λ of each gas species are correlated with temperature as documented in Coker [52]. The gas mixture viscosity and thermal conductivity are obtained by the Wilke [53] mixing rules whereas other properties are based on the linear mixing rule. The correlation of $\bar{c}_p$ with temperature for the biomass and char particles can also be obtained from literature [26].

4 Model numerical solution

The set of nonlinear partial differential equations proposed for a gasification process can be discretized into a number of ordinary differential equations using the finite volume method. Like many other numerical solutions, the grid size and size distribution affect the accuracy of the model; the finer the grid, the better the solution but longer the computational time. For the present study, the gasifier model is discretized into 110 grid points along the reactor axis comprising 80 grid points within the bed (50 below the biomass feeding position and 30 above) and 30 grid points in the freeboard to ensure that the numerical solution is closer to the possible analytical solution. The resulting equations are solved in MATLAB using the ode 23tb solver with adaptive time-step. The inlet gas flow is given at the bottom of the bed while the zero pressure gradient is defined at the exit as shown in Fig. 2. The model stability depends on the treatment of the internal

boundary where the biomass feed is located, and on the interface boundary between the bed and the freeboard due to the coupling effect between the gas momentum and continuity equations.

Table 4. Algebraic equations and mixing rules for different mixtures.

Expressions	Units
$\bar{c}_{p,k} = \sum y_j \bar{c}_{pj}$ k∈(s, g)	J/(kg.K)
$M_g = \sum x_j M_j$	kg/kmol
$x_j = \frac{y_j}{M_j \sum \left(\frac{y_j}{M_j}\right)}$	-
$\mu_g = \sum_{i=1}^{n} \left(\frac{x_i \mu_i}{\sum_{j=1}^{n} x_j \emptyset_{ij}} \right)$	Pa.s
$\lambda_g = \sum_{i=1}^{n} \left(\frac{x_i \lambda_i}{\sum_{j=1}^{n} x_j \emptyset_{ij}} \right)$	W(/m.K)
$\emptyset_{ij} = \frac{\left[1 + \left(\frac{\mu_i}{\mu_j}\right)^{0.5} \left(\frac{M_j}{M_i}\right)^{0.25}\right]^2}{\sqrt{8\left(1 + \frac{M_i}{M_j}\right)}}$	-
$Pr = \frac{\bar{c}_{pg} \mu_g}{\lambda_g}$	-

j or i is the species in the respective phase k (solids or gas)

When biomass is fed into a bed from the side, an internal boundary condition is defined as given in Eq. (28), where v_{in} is the solid velocity evaluated at the biomass feeding position. The biomass concentration at the boundary is split into upwards and downwards flows to ascertain the initial distribution of the fuel particles.

Biomass inflow boundary: $\bar{\rho}_{b,in} = \frac{4\dot{m}_{b,in}}{\pi D^2 v_{in}}$ (28)

For all the results presented, the computation of the kinetic rate constants for the pyrolysis is at the solid fuel temperature T_s while that for the different heterogeneous reactions are at the film temperature, $\bar{T}_s = 1/2(T_s + T_g)$ since gasification takes place on the surface of the fuel particles. The instantaneous superficial gas velocity u_0 for estimating the bubble properties is based on the inlet gas flowrate and on the fluid properties evaluated at the mean temperature over the bed.

The steady state solution of the model depends on a combination of different factors including the bed temperature, feed rate, particle properties and the position in the reactor. To achieve a steady state at a given operating condition, each simulation was run for 30000 s.

5 Model validation

The model results are compared with the experimental data in the literature to ascertain its accuracy. Based on biomass gasification with steam, the data presented in Li et al. [54] and Gopalakrishnan [16] are used. Both studies were conducted using two different dual fluidized bed reactors. In Li et al. [54], the diameter of the gasifier is 0.28 m and the bed contained 120 kg silica sand of mean particle size 143 μm, initially loaded to a height of 1.27 m. Softwood pellets were applied at a feed rate of 10 kg/h. The gasifier in the Gopalakrishnan [16] study was rated 100 kW at a biomass feed rate of 15 kg/h using sawdust pellets as the feedstock. The biomass was fed at a position 0.2 m above the base of a bed containing greywacke sand particles with a mean size of 275 μm and an initial height of 0.24 m.

These two reactors have also been modelled in different studies as can be found in Hejazi et al. [21] and Gopalakrishnan [16]. Both reactor models are one-dimensional and were developed based on the two-phase theory. The experimental data from these two reactors can therefore be used to compare the performance of the proposed model with the existing ones [16, 21]. The proposed model results are also compared with the simulated results from a 2D hydrodynamic model also outlined in [16].

The biomass feeding position in the Li et al. [54] study is not clearly defined, but it is well inside the bed. For the preliminary model validation, $l_{sb} = 0.63$ m is assumed. The effect of biomass feeding position will be further discussed based on this gasifier.

In a steam biomass gasification process, the heat required is usually supplied by the circulated sand particles between a bubbling bed gasifier and a circulating fluidized bed combustor as is also the case in the above mentioned studies. The operation of the combustor is controlled to maintain the gasification temperature within the bubbling bed, often the same as the temperature of the incoming superheated steam, leading to an isothermal operation. It should be noted that the model developed in this study does not include circulation of the bed material. The heat flow into the gasifier is therefore from the incoming steam and the possible exothermic reactions in the bed, giving room for a non-isothermal process. To achieve an isothermal behaviour, the bed temperature is assumed the same as the temperature of the incoming steam in the simulations. The non-isothermal behaviour of the model is compared with the behaviour under isothermal condition in later discussions.

Fig. 3(a) shows the composition of the product gas obtained from the experimental setup of Gopalakrishnan [16] at 780 ºC and the steam-biomass ratio (S/B) of 0.53. In the figure, the predictions based on the present model are compared with the experimental data and also with those based on the 1D and 2D models presented in Gopalakrishnan [16]. As can be seen, the results from the three models agree reasonably well with the experimental data. With the proposed model, the agreement is better for the H_2, CH_4 and H_2O mole fractions. For the mole fractions of

CO and CO_2, the predictions from the present model are closer to those of the 2D model, which gives a better prediction of CH_4 than the Gopalakrishnan [16] 1D model. The predicted distribution of the gas species along the bed axis, as shown in Fig. 3(b), is also in agreement with that given by the 2D model [16]. Fig. 3(a) also shows that the present model predicts the sum of the mole fractions of H_2 and H_2O in a good agreement with the experiment (2% error), which is also true for the sum of CO and CO_2 (-2% error). However, the Gopalakrishnan [16] 1D model over predicts the (CO + CO_2) value by 19% and under predicts that of (H_2 + H_2O) by 17%. With the 2D model, the predictions of the different sums are also closer to the experiment, where the error for the (CO + CO_2) value is 2% and that for the (H_2 + H_2O) value is -1%. These results thus show that the proposed model can predict the gas yields obtained from an experiment quite well.

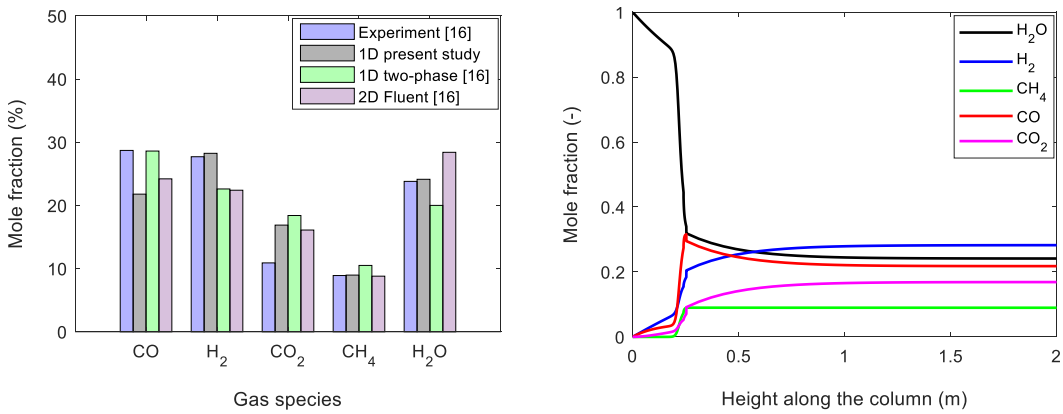

(a) (b)

Fig. 3. Predicted gas composition at 780 ºC and S/B = 0.53 (a) compared with experimental data and with results from existing models [16] (b) showing the axial distribution of the gas species based on the present model.

Fig. 4 compares the gas composition predicted at different temperatures with the experimental data from Li et al. [54]. Above 690 ºC, the model results agree quite well with the experiments, especially for the CH_4 and CO_2 mole fractions. The scattered behaviour of the experimental data is due to variation of the steam-biomass ratio in the range 0.94 – 1.05 as noted in the literature [54]. Comparing with the results from the 1D model presented in Hejazi et al. [21], the present model has a better prediction accuracy for the experimental data. Based on the present study, the mean absolute errors over the temperature range of the experiments shown in Fig. 4 are 12, 8, 11 and 9% for H_2, CO, CO_2 and CH_4, respectively, whereas the corresponding values are 67, 40, 17 and 72% based on the Hejazi et al. [21] 1D model.

6 Discussion

Since the accuracy of the proposed model is reasonably good, the model can be used to investigate different operating parameters and design choices on the gasification behaviour. In this study, the effect of biomass feeding position on the gas composition and that of temperature on the total gas yield are discussed using the gasifier described in Li et al. [54] as a case study. In addition, a comparison between the isothermal and non-isothermal modes of operation is discussed.

6.1 Effect of biomass feeding position on the gas composition

The gas compositions predicted at different biomass feeding positions are shown in Fig. 5. In the result, the distribution of the grid size along the reactor column is kept constant for all the biomass feeding points. The figure shows that moving the feeding position towards the bed surface increases the amounts of H_2 and CO_2 and decreases those of CO and CH_4 in the product gas. With biomass fed close to the bottom of the bed, char conversion through reaction route 1 in Table 3 is favoured due to higher availability of steam and char particles as well as their increased contact time. This leads to a reduced amount of H_2O available for the freeboard reactions, thereby reducing the yields of H_2 and CO_2. Supplying biomass near the bed surface leads to a lower char conversion and a higher availability of H_2O in the freeboard. The exothermic water gas shift dominates the process, leading to higher H_2 and CO_2 concentrations. The steam-methane reaction is also enhanced, resulting in a decrease in the

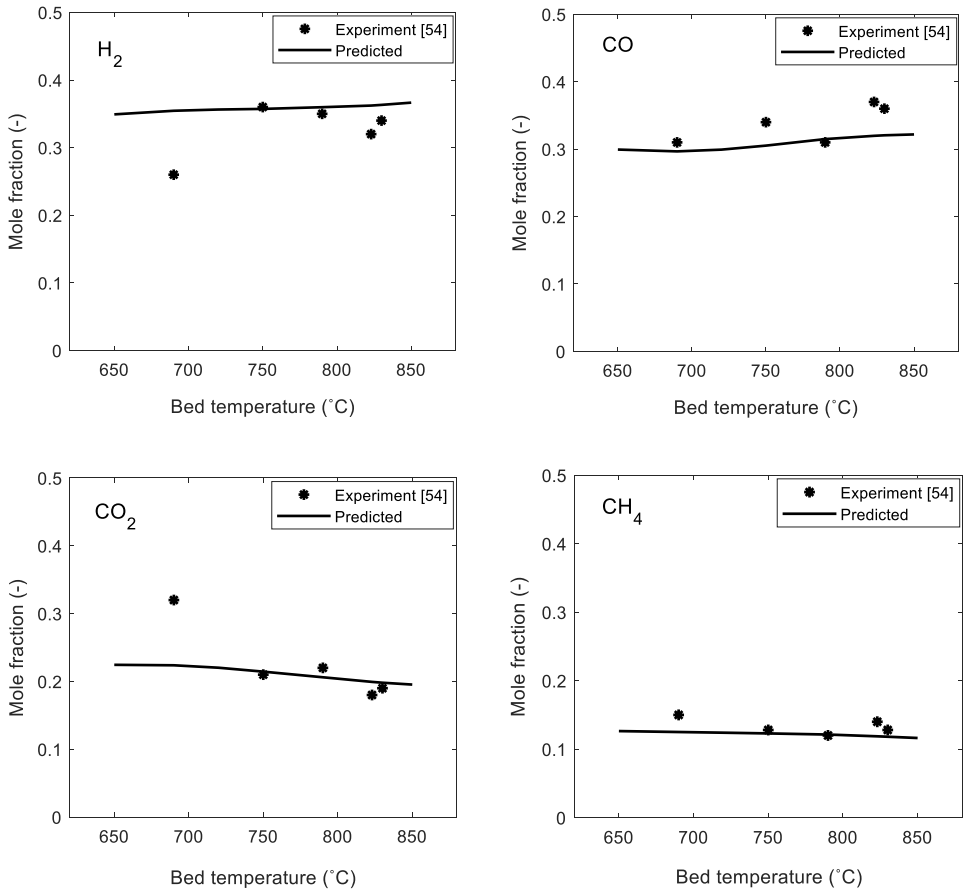

Fig. 4. Predicted gas composition (dry basis) compared with experimental data [54] (l_{sb} = 0.63 m, S/B = 1.0) at different bed temperatures.

CH_4 mole fraction. Moreover, due to the low density of the char particles, their poor sinking behaviour into the bed also influences the poor conversion of the fuel particles at increasing biomass-feeding position. Lowering the feeding position to about 0.3 m, Fig. 5 shows that the predicted gas composition is consistent with the experimental data reported at about 830 ºC [54]. The trends of the results in Fig. 5 are also similar to those observed by Radmanesh et al. [18] whose experimental data were compared with data from Narvaez et al. [55]. However, the 1D

two-phase model presented in [18] showed poor predictions of CO and H_2 compared to the experimental data [55] obtained when the biomass is fed close to the bottom of the bed.

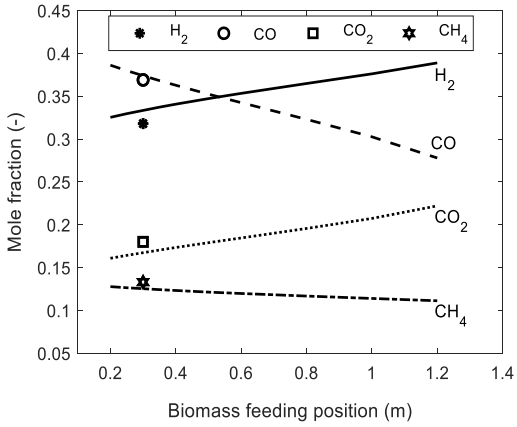

Fig. 5. Predicted gas composition, showing the effect of biomass feeding position on gasification behaviour. S/B = 1.0 and $T = 830$ ºC: data points = experiment [54], lines = predicted values.

6.2 Effect of temperature on the total gas yield

In addition to the product gas composition, an important output from the proposed model is the cold gas production rate (gas yield), Y determined from the following equation.

$$Y = \frac{\pi D^2}{4} \frac{(1-x_{\mathrm{H2O}})}{\dot{m}_{b,in}(1-y_{\mathrm{moist}})} \left(\frac{T_{std}}{T_g}\right) \left(\frac{\dot{m}_g''}{\bar{\rho}_g}\right) \tag{29}$$

Here, $T_{std} = 273.15$ K is the standard temperature and y_{moist} is the weight fraction of moisture in the raw biomass. The term $\dot{m}_g''/\bar{\rho}_g$ is the gas velocity evaluated at the gas exit temperature T_g and x_{H2O} is the mole fraction of water in the product gas. As shown in Fig. 6(a), the gas velocity increases with an increase in the temperature due to increasing amount of pyrolysis gas above the biomass feeding position. Above the bed surface, the velocity decreases to a constant value as the gas bulk density is increased in the absence of solid particles. In practice, the high gas velocity at the bed surface would result in splash of particles into the freeboard. However, as this splash zone is not considered in the developed model (cf. section 4), the decrease in the gas velocity is relatively sharp. The profile of the gas velocity could have been improved by properly accounting for the bed-freeboard interface conditions. One possibility is to calculate the splash zone height based on the momentum balance of the solids carried in the wake of erupting bubbles.

Fig. 6(b) shows that the gas yield increases with increasing temperature owing to the increase in the conversions as well as the gas specific volume. The value of Y predicted is comparable with those obtained from the thermodynamic equilibrium model [56] and from the experiments [57, 58], which although is difficult to be measured. As expected, the value of Y predicted at 830 ºC is higher than the experimental value of 1.03 Nm^3/kg-dry biomass reported in the literature [54]. In the model predictions, all the char particles are available for the gasification reactions, leading to a higher gas yield. In the experimental reactor, some of the char particles are burned off in the combustor while some are entrained from the reactor, resulting in a lower gas yield. The predicted

gas yield is also in agreement with the yield measured when biomass is gasified with air/oxygen in a bubbling bed where there is a lower char loss in the absence of bed material circulation [57].

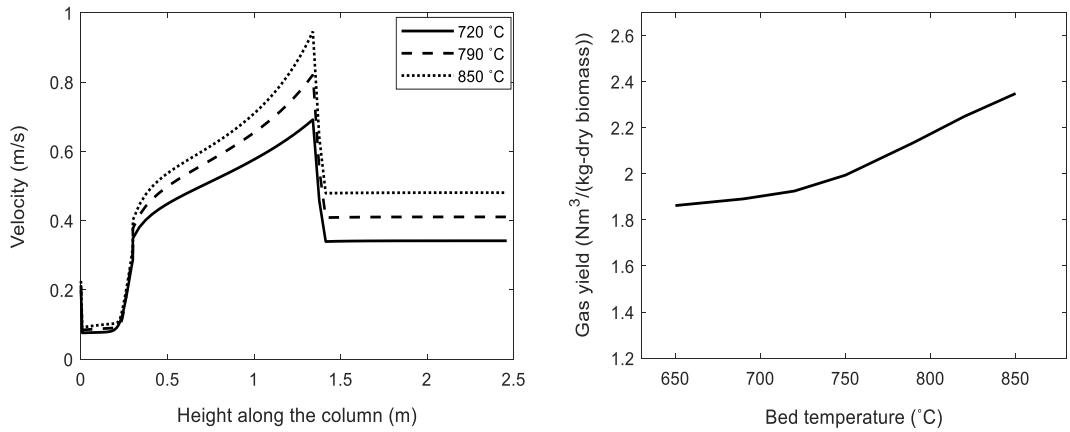

(a) (b)

Fig. 6. Predicted (a) gas velocities (b) total gas yield on dry basis at different temperatures based on the gasifier described in [54]; S/B = 1.0, $l_{sb} = 0.3$ m.

6.3 Comparison between isothermal and non-isothermal operations

In an isothermal gasification process, the temperature of the bed material is the same as that of the incoming steam whereas the two temperatures differ in the non-isothermal case. To simulate the gasification process under the non-isothermal condition, all the heat equations described in Section 3.3 are applied at a given incoming steam temperature. The performance of the gasifier [54] under the two different modes of operations are compared in this section.

6.3.1 Temperature distribution

Fig. 7 shows that in the isothermal operation, the gas temperature is the same over the bed but slightly increases in the freeboard due to the water-gas shift (WGS) reaction. In the non-isothermal case, the bed temperature increases from a point near the biomass feeding position. The decrease in temperature in the lower part of the bed enhances the exothermic reactions, which increases the bed temperature in the upper part. The maximum temperature drop in the bed increases with increasing steam temperature. The figure also shows that within the steam temperature 720 – 850 ºC, the difference in temperature in the freeboard is less than 20 ºC, suggesting that the non-isothermal process gives sufficient freedom for equilibrium to be reached in the freeboard at the given biomass and steam flowrates. The temperature profile in the non-isothermal process is similar to those experimentally observed [59, 60]. As the heat loss is neglected in the simulations, the temperature remains high over the length of the freeboard in both operations. In practice however, the gas temperature may be lower and may also decrease along the freeboard due to heat loss and possibly significant endothermic reactions.

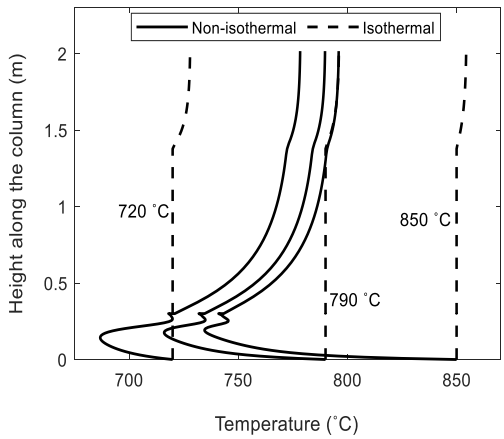

Fig. 7. Predicted axial temperature distribution (l_{sb} = 0.3 m, S/B = 1.0), comparing isothermal and non-isothermal gasification processes at different steam temperatures.

6.3.2 Distribution of gas species

Fig. 8 shows that the conversion of steam in the bed increases with increasing temperature, and is better under the isothermal condition owing to the higher temperature shown in Fig. 7. The difference in the gas composition between the two processes is more pronounced in the bed but diminishes in the freeboard as the temperature is increased. The higher CO_2 concentration compared to CO as can be clearly seen in Fig. 8(b) indicates that the water gas shift reaction is also favoured in the lower part of the bed in both types of operation. Above the fuel feeding position, the results show that the WGS reaction dominates the process. The mole fraction of CO decreases below the value in the bed while the mole fractions of H_2 and CO_2 increase significantly. The concentration of methane is invariant between the two processes as the reaction of the species with steam is quite slow. Moreover, the CH_4 yield below the feeding position is negligible because biomass devolatilization is complete before the bottom of the bed in addition to the slow reaction rate of char with H_2.

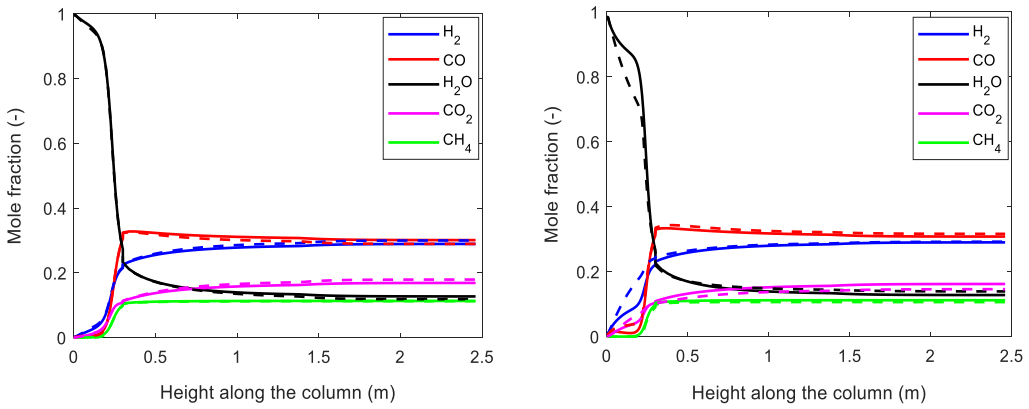

(a) (b)

Fig. 8. Predicted axial distribution of gas species (l_{sb} = 0.3 m, S/B = 1.0), comparing isothermal (dashed line) and non-isothermal (solid line) gasification processes at different temperatures (a) T = 720 ºC (b) T = 850 ºC.

6.3.3 Product gas composition at different temperatures

As the reactions tend towards the equilibrium condition, Fig. 9 shows that there is no significant difference in the product gas composition at different temperatures when the process is operated in the non-isothermal mode. However, in the isothermal mode, the gas composition varies significantly with changes in the bed temperature. The amounts of H_2 and CO_2 decrease with an increase in temperature under this condition. The increasing CO and H_2O mole fractions suggest that the water gas shift reaction is less favoured as the temperature is increased. As there is no absolute isothermal condition in reality, a slightly lower congruence as presented in Fig. 9 should be expected.

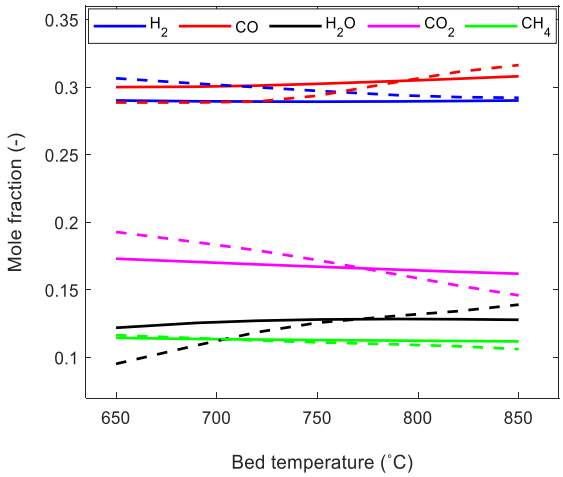

Fig. 9. Product gas composition (l_{sb} = 0.3 m, S/B = 1.0), comparing isothermal (dashed line) and non-isothermal (solid line) gasification processes at different temperatures.

7 Conclusions

A model for simulating a bubbling fluidized bed gasifier was developed. The model includes the fluid and particle momentum equations to account for the effect of bed material properties on the flow behaviour. The proposed one-dimensional unsteady state model was used to investigate the performance of steam gasifiers with different biomass feeding positions and different modes of operation (isothermal and non-isothermal processes with respect to steam temperature and gasifier temperature).

The results show that the model can predict the total gas production rate depending on the reactor design and operating conditions. Increasing the biomass feeding position towards the bed surface decreases the CO mole fraction and increases that of H_2 in the product gas due to a reduced char conversion effect and an enhanced water gas shift reaction. The water gas shift reaction is also favoured greatly when operating the reactor isothermally in a deep bed.

The proposed model can be applied to any bubbling fluidized bed reactor, and it is computationally less demanding, thus can be used to improve the design and operational control. The model can be developed further to include circulation of bed material and integration with a circulating fluidized bed combustor.

8 Funding sources

This research did not receive any specific grant from funding agencies in the public, commercial, or not-for-profit sectors.

9 References

[1] Chen, J.; Yu, G.; Dai, B.; Liu, D.; Zhao, L. CFD simulation using a bubble-based drag model. *Energy Fuels* **2014**, *28*, 6351.

[2] Nardo, A.D.; Calchetti, G.; Stendardo, S. Modeling and simulation of an oxygen-blown bubbling fluidized bed gasifier using the computational particle-fluid dynamics (CPFD) approach. *J. Appl. Fluid Mech*. **2018**, *11*, 825.

[3] Juhui, C.; Weijie, Y.; Shuai, W.; Guangbin, Y.; Jiuru, L.; Ting, H.; Feng, L. Modelling of coal/biomass co-gasification in internal circulating fluidized bed using kinetic theory of granular mixture. *Energy Convers. Manage*. **2017**, *148*, 506.

[4] Liu, H.; Elkamel, A.; Lohi, A.; Biglari, M. Computational fluid dynamics modeling of biomass gasification in circulating fluidized-bed reactor using the Eulerian-Eulerian approach. *Ind. Eng. Chem. Res*. **2013**, *52*, 18162.

[5] Gao, X.; Zhang, Y.; Li, B.; Yu, X. Model development for biomass gasification in an entrained flow gasifier using intrinsic reaction rate submodel. *Energy Convers. Manage*. **2016**, *108*, 120.

[6] Gonzalez-Vazquez, P. M.; Garcia, R.; Pevida, C.; Rubiera, F. Optimization of a bubbling fluidized bed plant for low-temperature gasification of biomass. *Energies* **2017**, *10*, 306.

[7] Mazaheri, N.; Akbarzadeh, A.H.; Madadian, E.; Lefsrud, M. Systematic review of research guidelines for numerical simulation of biomass gasification for bioenergy production. *Energy Convers. Manage*. **2019**, *183*, 671.

[8] Mahishi, M.R.; Goswami, D.Y. Thermodynamic optimization of biomass gasifier for hydrogen production. *Int. J. Hydrogen Energy* **2007**, *32*, 3831.

[9] Pauls, J.H.; Mahinpey, N.; Mostafavi, E. Simulation of air-steam gasification of woody biomass in a bubbling fluidized bed using Aspen Plus: A comprehensive model including pyrolysis, hydrodynamics and tar production. *Biomass Bioenergy* **2016**, *95*, 157.

[10] Versteeg, H.K.; Malalasekera, W. *An Introduction to Computational Fluid Dynamics: Finite Volume Method*, second ed., Pearson Education Limited, Edinburgh Gate Harlow Essex CM20 2JE, England, 2007.

[11] Andrews, M.J.; O'Rourke, P.J. The multiphase particle-in-cell (MP-PIC) method for dense particulate flows. *Int. J. Multiph. Flow* **1996**, *22*, 379.

[12] Eri, Q.; Peng, J.; Zhao, X. CFD simulation of biomass steam gasification in a fluidized bed based on a multi-composition multi-step kinetic model. *Appl. Therm. Eng.* **2018**, *129*, 1358.

[13] Thapa, R.K.; Pfeifer, C.; Halvorsen, B.M. Modeling of reaction kinetics in bubbling fluidized bed biomass gasification reactor. *Int. J. Energy Environ.* **2014**, *5*, 35.

[14] Kraft, S.; Kirnbauer, F.; Hofbauer, H. CPFD simulations of an industrial-sized dual fluidized bed steam gasification system of biomass with 8 MW fuel input. *Appl. Energy* **2017**, *190*, 408.

[15] Gungor, A.; Yildirim, U. Two dimensional numerical computation of a circulating fluidized bed biomass gasifier. *Comput. Chem. Eng.* **2013**, *48*, 234.

[16] Gopalakrishnan, P. *Modelling of biomass steam gasification in a bubbling fluidized bed gasifier*. PhD. Thesis, The University of Canterbury, 2013.

[17] Fiaschi, D.; Michelini, M. A two-phase one-dimensional biomass gasification kinetics model. *Biomass Bioenergy* **2001**, *21*, 121.

[18] Radmanesh, R.; Chaouki, J.; Guy, C. Biomass gasification in a bubbling fluidized bed reactor: Experiments and modeling. *AIChE J*. **2006**, *52*, 4258.

[19] Petersen, I.; Werther, J. Experimental investigation and modeling of gasification of sewage sludge in the circulating fluidized bed. *Chem. Eng. Process* **2005**, *44*, 717.

[20] Champion, W.M.; Cooper, C.D.; Mackie, K.R.; Cairney, P. Development of a chemical kinetic model for a biosolids fluidized-bed gasifier and the effects of operating parameters on syngas quality. *J. Air Waste Manage. Assoc.* **2014**, *64*, 160.

[21] Hejazi, B.; Grace, J.R.; Bi, X.; Mahecha-Botero, A. Kinetic model of steam gasification of biomass in a dual fluidized bed reactor: Comparison with pilot-plant experimental results. *Energy Fuels* **2017**, *31*, 12141.

[22] Kunii, D.; Levenspiel, O. *Fluidization Engineering*, second ed., Butterworth – Heinemann, Washington Street, USA, 1991.

[23] Inayat, A.; Ahmad, M.M.; Yusup, S.; Mutalib, M.I.A. Biomass steam gasification with in-situ CO_2 capture for enriched hydrogen gas production: A reaction kinetics modelling approach. *Energies* **2010**, *3*, 1472.

[24] Solsvik, J.; Chao, Z; Jakobsen, H.A. Modeling and simulation of bubbling fluidized bed reactors using a dynamic one-dimensional two-fluid model: The sorption-enhanced steam methane reforming process. *Adv. Eng. Softw.* **2015**, *80*, 156.

[25] Silva, J.D. Numerical Modelling of the Fluid Dynamics in a Bubbling Fluidized Bed Biomass Gasifier. *J. Petroleum Gas Eng.* **2012**, *3*, 35.

[26] Basu, P. *Biomass Gasification, Pyrolysis, and Torrefaction – Practical Design and Theory*, second ed., Elsevier Inc., London NW1 7BY, UK, 2013.

[27] Blasi, C. D. Modeling chemical and physical processes of wood and biomass pyrolysis. *Prog. Energy Combust. Sci*. **2008**, *34*, 47.

[28] Yu, J.L.; Strezov, V.; Lucas, J.; Liu, G.S.; Wall, T. A mechanistic study on char structure evolution during coal devolatilization – experiments and model predictions. *Proc. Combust. Inst.* **2002**, *29*, 467.

[29] Shafizadeh, F.; Chin, P.P.S. Thermal deterioration of wood. *ACS Symp Ser* **1977**, *43*, 57.

[30] Hejazi, B.; Grace, J.R.; Bi, X.; Mahecha-Botero, A. Coupled reactor and particle model of biomass drying and pyrolysis in a bubbling fluidized bed reactor. *J. Anal. Appl. Pyrolysis* **2016**, *121*, 213.

[31] Chan, W-C. R.; Kelbon, M.; Krieger, B. B. Modelling and experimental verification of physical and chemical processes during pyrolysis of a large biomass particle. *Fuel* **1985**, 64, 1505.

[32] Matsui, I.; Kunii, D.; Furusawa, T. Study of fluidized bed steam gasification of char by thermogravimetrically obtained kinetics. *J. Chem. Eng. Jpn.* **1985**, *18*, 105.

[33] Braun, R.L.; Mallon, R.G.; Sohn, H.Y. Analysis of Multiple Gas-Solid Reactions during the Gasification of Char in Oil Shale Blocks. In Proceeding, *14th Oil Shale Symposium*, Colorado School of Mines Press, Golden, Colo. 1981, p 289.

[34] Babu, B.; Sheth, P. Modeling and simulation of reduction zone of downdraft biomass gasifier: effect of char reactivity factor. *Energy Convers. Manage.* **2006**, *47*, 2602.

[35] Bıba, V.; Macak, J.; Klose, E.; Malecha, J. Mathematical model for the gasification of coal under pressure. *Ind. Eng. Chem. Process Des. Dev*. **1978**, *17*, 92.

[36] Zahradnik RL, Grace RJ. Chemistry and physics of entrained coal gasification. *Ind. Eng. Chem. Proc. Des. Dev.* **1974**, *126*, 203.

[37] Bates, R.B.; Altantzis, C.; Ghoniem, A.F. Modeling of biomass char gasification, combustion and attrition kinetics in fluidized beds. *Energy Fuels* **2016**, *30*, 360.

[38] Chang, J.; Yang, S.; Zhang, K. A particle-to-particle heat transfer model for dense gas-solid fluidized bed of binary mixture. *Chem. Eng. Res. Des.* **2011**, *89*, 894.

[39] Gidaspow, D. *Multiphase Flow and Fluidization: Continuum and Kinetics Theory Descriptions*, Academic Press Inc., San Diego, California, USA, 1994.

[40] Taghipour, F.; Ellis, N.; Wong, C. Experimental and computational study of gas-solid fluidized bed hydrodynamics. *Chem. Eng. Sci*. **2005**, *60*, 6857.

[41] Li, P.; Lan, X.; Xu, C.; Wang, G.; Lu, C.; Gao, J. Drag models for simulating gas solid flow in the turbulent fluidization of FCC particles. *Particuology* **2009**, *7*, 269.

[42] Ranz, W.E. Friction and transfer coefficients for single particles and packed beds. *Chem. Eng. Prog*. **1952**, *48*, 247.

[43] Gunn, D.J. Transfer of heat or mass to particles in fixed and fluidized-beds. *Int. J. Heat Mass Transfer* **1978**, *21*, 467.

[44] Choi, J. H.; Son, J. E.; Kim, S. D. Bubble Size and Frequency in Gas Fluidized Beds. *J. Chem. Eng. Jpn*. **1988**, *21*, 171.

[45] Mori, S.; Wen, C. Y. Estimation of Bubble Diameter in Gaseous Fluidized Beds. *AIChE J*. **1975**, *21*, 109.

[46] Werther, J. Effect of gas distributor on the hydrodynamics of gas fluidized beds. *Ger. Chem. Eng.* **1978**, *1*, 166.

[47] Agu, C. E.; Tokheim, L.-A.; Eikeland, M.; Moldestad, B. M.E. Improved models for predicting bubble velocity, bubble frequency and bed expansion in a bubbling fluidized bed. *Chem. Eng. Res. Des*. **2019**, *141*, 361.

[48] Werther, J. Influence of the bed diameter on the hydrodynamics of gas fluidized beds. *AIChE Symp. Ser*. **1974**, *70*, 53.

[49] Davidson, J.F.; Harrison, D. *Fluidized Particles*, Cambridge University Press, London, 1963.

[50] Hilligardt, K.; Werther, J. Local bubble gas hold-up and expansion of gas/solid fluidized beds. *Ger. Chem. Eng*. **1986**, *9*, 215.

[51] Agu, C. E.; Pfeifer, C.; Eikeland, M.; Tokheim, L.-A.; Moldestad, B. M.E. Models for predicting average bubble diameter and volumetric bubble flux in deep fluidized beds. *Ind. Eng. Chem. Res*. **2018**, 57, 2658.

[52] Coker, A.K. *Ludwig's Applied Process Design for Chemical and Petroleum Plants*, Vol. 1, fourth ed., 2007, p 827 – 862.

[53] Wilke, C.R. A Viscosity Equation for Gas Mixtures. *J. Chem. Phys.* **1950**, *18*, 517.

[54] Li, Y.H.; Chen, Z.; Watkinson, P.; Bi, X.; Grace, J.; Lim, C.J.; Ellis, N. A novel dual-bed for steam gasification of biomass. *Biomass Conv. Bioref.* **2018**, *8*, 357.

[55] Narvaez, I.; Orio, A.; Aznar, M.P.; Corella, J. Biomass gasification with air in an atmospheric bubbling fluidized bed. Effect of six operational variables on the quality of the produced raw gas. *Ind. Eng. Chem. Res.* **1996**, *35*, 2110.

[56] Sreejith, C. C.; Muraleedharan, C.; Arun, P. Performance prediction of steam gasification of wood using an ASPEN PLUS thermodynamic equilibrium model. *Int. J. Sustain. Energ*. **2014**, *33*, 416.

[57] Gil, J.; Corella, J.; Aznar, M.P.; Caballero, M.A. Biomass gasification in atmospheric and bubbling fluidized bed: Effect of the type of gasifying agent on the product distribution. *Biomass Bioenergy* **1999**, *17*, 389.

[58] Jand, N.; Brandani, V.; Foscolo, P.U. Thermodynamic limits and actual product yields and compositions in biomass gasification processes. *Ind. Eng. Chem. Res*. **2006**, *45*, 834.

[59] Wilk, V.; Schmid, J.C.; Hofbauer, H. Influence of fuel feeding positions on gasification in dual

fluidized bed gasifiers. *Biomass Bioenergy* **2013**, *54*, 46.

[60] Kern, S.; Pfeifer, C.; Hofbauer, H. Gasification of wood in a dual fluidized bed gasifier: Influence of fuel feeding on process performance. *Chem. Eng. Sci*. **2013**, *90*, 284.

Nomenclature

Symbols

A [1/s]	frequency factor
c [K$^{-\alpha}$]	fitting coefficient
c_d [-]	drag coefficient
$\bar{c}_p$ [J/kg-K]	specific heat capacity
D [m]	vessel diameter
d [m]	diameter
$\bar{d}$ [m]	height-averaged diameter
E [J/mol]	activation energy
Δe [-]	bed expansion
F [N]	force
F' [N/m^3]	force per unit volume
f [-]	friction factor
G_b [m/s]	bubble volumetric flux
g [m/s^2]	acceleration due to gravity
ΔH_r^0 [J/kg]	reaction enthalpy change
h [W/m^2-K]	unit area heat transfer coefficient
h' [W/m^3-K]	unit volume heat transfer coefficient
K_r [1/m]	effective radiation coefficient

k [1/s]	rate constant
L [m]	Total column height
l [m]	height above bed base
M [kg/kmol]	molecular weight
$\dot{m}$ [kg/s]	mass flowrate
$\dot{m}''$ [kg/s-m^2]	mass flux
n [-]	number
n_1 [-]	fragmentation factor
Pr [-]	Prandtl number
p [Pa]	fluid pressure
R [J/mol-K]	universal gas constant
r [mol/m^3-s]	reaction rate constant
S [kg/m^3-s]	mass generation rate
T [K]	temperature
t [s]	time
U [W/m^2-K]	overall heat transfer coefficient
u [m/s]	gas velocity
v [m/s]	solids velocity
X_c [-]	char conversion factor
x [-]	mole fraction
Y [Nm^3/kg]	cold gas yield
y [-]	mass fraction
z [m]	axial position

Greek letters

α [-]	fitting index
β [N.s/m^4]	momentum transfer coefficient

ϵ [-]	emissivity
ε [-]	void fraction
Λ [-]	uncorrected pyrolysis gas mole fraction
λ [W/m-K]	thermal conductivity
σ [W/m^2-K^4]	Stefan Boltzmann constant
ρ [kg/m^3]	density
$\bar{\rho}$ [kg/m^3]	mass concentration
θ_w [-]	bubble wake fraction
ϑ [-]	pyrolysis gas mole fraction
μ [Pa.s]	dynamic viscosity
Ψ [-]	shrinkage factor
φ [-]	particle sphericity
γ [-]	mass fraction of tar components

Subscripts

a	ambient
b	bubble/biomass
c	char
f	fluidized state
g	gas
i	step/species
j	species
k	phase
m	mixture
mf	minimum fluidization
p	particle
r	reaction

s	solids
w	wall
0	initial/bottom reference

Other presentations include

Article 11 (A11)

C.E. Agu, R.K. Thapa, B.M. Halvorsen, Simulation of simplified model for kinetics of biomass gasification, 56th SIMS Conference on Simulation and Modelling, SIMS 2015, Linkoping, Sweden, 7 – 9 October, 2015

Article 12 (A12)

K.-A. Solli, C.E. Agu, Evaluation of drag models for CFD simulation of fluidized bed biomass gasification, 58th SIMS Conference on Simulation and Modelling, SIMS 2017, Reykjavik, Iceland, 25 – 27 September, 2017.

Article 13 (A13)

C. Agu, B. Moldestad, Distribution of solids in a fluidized bed operated without a gas distributor, 59th International Conference of Scandinavian Simulation Society, Oslo, Norway, 26 – 27 September, 2018.

Article 14 (A14)

R. Jaiswal, C.E. Agu, B.M.E. Moldestad, R.K. Thapa, Study of fluidized bed regimes using computational particle fluid dynamics, 59th International Conference of Scandinavian Simulation Society, Oslo, Norway, 26 – 27 September, 2018.

Doctoral dissertation no. 35
2019
—

Bubbling Fluidized Bed Behaviour for Biomass Gasification
Dissertation for the degree of Ph.D
—

Cornelius Emeka Agu
—

ISBN: 978-82-7206-526-2 (print)
ISBN: 978-82-7206-527-9 (online)

usn.no